Thèse de doctorat
de l'Université Pierre et Marie Curie

Ecole Doctorale 398 Géosciences, Ressources Naturelles et Environnement

Spécialité: **Hydrology and water resources / remote sensing**

Global-scale evaluation of a hydrological variable measured from space: SMOS satellite remote sensing soil moisture products

Présentée par Amen Mohammed Al-YAARI

Laboratoires:
UMR 7619 METIS
INRA, UMR 1391 ISPA Interactions Sol Plante Atmosphère

Pour obtenir le grade de:
Docteur de l'Université Pierre et Marie Curie

Présentée et soutenue publiquement le 14/11/2014
devant le jury composé de:

M. Le Treut Hervé	Professeur à l'Université Pierre et Marie Curie	Président
M. Polcher Jan	Directeur de recherche, CNRS, LMD	Rapporteur
M. Zribi Mehrez	Directeur de recherche, CNRS, CESBIO	Rapporteur
M. Kerr Yann	Directeur de recherche CNES, CESBIO	Examinateur
Mme De Rosnay Patricia	Chargée de recherche CNRS, ECMWF	Examinatrice
Mme Ducharne Agnès	Directrice de recherche, CNRS, METIS	Directrice de thèse
M. Wigneron Jean-Pierre	Directeur de recherche, INRA Bordeaux	Directeur de thèse

Université Pierre & Marie Curie - Paris 6
Bureau d'accueil, inscription des doctorants et base de données
Esc G, 2ème étage
15 rue de l'école de médecine
75270-PARIS CEDEX 06

Tél. Secrétariat : 01 42 34 68 35
Fax : 01 42 34 68 40
Tél. pour les étudiants de A à EL : 01 42 34 69 54
Tél. pour les étudiants de EM à MON : 01 42 34 68 41
Tél. pour les étudiants de MOO à Z : 01 42 34 68 51
E-mail : scolarite.doctorat@upmc.fr

Dédicace/ Dedication

To my Mother and my late Father (God bless his soul)

Remerciements/Acknowledgements

Three years have passed since my arrival at the Institut National de la Recherche Agronomique (INRA) in Bordeaux to pursue a Ph.D. This period was extremely rewarding experience for me scientifically and personally. While this chapter of my life is about to finish, I want to express my sincere gratitude to all those who have directly or indirectly made it possible.

A few words are not enough to acknowledge all the people who helped me to have this Ph.D. research work done. Nevertheless, I will try to do my best to express my sincere thanks and extend my great appreciation to everyone who made it possible. I will begin with God the Almighty Allah: without the will of Allah, I would have never found the right path. Allah's mercy was with me throughout my life and ever more in this doctoral study.

First and foremost, I would like to express my sincere and deepest gratitude to my advisors Dr. Jean-Pierre WIGNERON and Dr. Agnes DUCHARNE for their excellent guidance, friendship, patience, and most importantly providing me with an excellent atmosphere and inspiration for doing research during my Ph.D. research work at INRA and Université Pierre et Marie Curie (UPMC), respectively. This Ph.D. research work would never have been completed without their guidance. Dr. Jean-Pierre WIGNERON and Dr. Agnes DUCHARNE, I thank you for everything you've done for me.

I am very pleased and honored to have Hervé LE TREUT, Professor at UPMC, as the president of the jury of my PhD thesis defense. I am so grateful to Dr. Jan Polcher and Dr. Mehrez Zribi to have accepted the role of rapporteur. I would also like to thank Dr. Yann Kerr and Dr. Patricia de Rosnay for their acceptance to be members of the jury of my PhD thesis defense.

I feel obligated to mention the names of a few colleagues: Françoise PRUDHOMME, Patricia BRACONNIER, Valérie SAVORNIN, Anne-Marie BOUCHON, and Dovy TRISTANI (UPMC) for helping me with the administrative side of this Ph.D. research work, Barry GARDINER and Lisa WINGATE for helping me to revise the English of my published articles, Ajit GOVIND, Dominique GUYON, and Jean-Pierre LAGOUARDE for giving me a lot of insightful suggestions and invaluable comments during my research, Christophe MOISY, Tovo RABEMANANTSOA, Guy PRACROS, Alain MOLLIER, Sandra DEBESA, and Didier GARRIGOU for their technical assistance, and Clement DUFFOUR,

Damien COMMANDOIRE, Jean-Charles SAMALENS, Joana JORLY, Sylvio LAVENTURE, Julien KAMMER, and others for teaching me French. I would also like to thank all of the members of the Interactions Sol Plante Atmosphère (ISPA) and Centre d'Etudes Spatiales de la Biosphère (CESBIO) research group for their help, availability, and kindness.

Last but not certainly least, and most importantly, I thank my Mother and sibling, for supporting me with all what I needed as well as providing me with the opportunity to be where I am today. Mother, you were with me at every step of the way even though you were physically thousands of kilometers away. I would like also to thank my beautiful wife for her unwavering love, support, encouragement, and tolerance of my occasional vulgar moods throughout this Ph.D... I also dedicate this Ph.D. thesis to my two lovely children, Yousef and Fatima who are the pride and joy of my life.

Finally, this Ph.D. research work was financially supported by a Merit Scholarship Programme for High Technology, the Islamic Development Bank (IDB) - Saudi Arabia.

Global-scale evaluation of a hydrological variable measured from space: SMOS satellite remote sensing soil moisture products

Abstract

Soil moisture (SM) plays a key role in meteorology, hydrology, and ecology as it controls the evolution of various hydrological and energy balance processes. The community of scientists involved in the field of microwave remote sensing has made considerable efforts to build accurate estimates of surface SM (SSM), and global SSM datasets derived from active and passive microwave instruments have recently become available. Among them, SMOS (Soil Moisture and Ocean Salinity), launched in 2009, was the first ever passive satellite specifically designed to measure the SSM, at L-band (1.4 GHz), at the global scale. Validation of the SMOS SSM datasets over different climatic regions and environmental conditions is extremely important and a necessary step before they can be used. A better knowledge of the skill and uncertainties of the SSM retrievals will help not only to improve the individual products, but also to optimize the fusion schemes required to create long-term multi-sensor products, like the essential climate variable (ECV) SSM product generated within the European Space Agency's (ESA's) Climate Change Initiative (CCI) program. After the introductory Chapters I to III, this dissertation consists of three main parts. Chap. IV of the dissertation evaluates the passive SMOS level 3 (SMOSL3) SSM products at L-band against the passive AMSR-E SSM at C-band by comparing them with a Land Data Assimilation System estimates (SM-DAS-2) produced by the European Centre for Medium Range Weather Forecasts (ECMWF). This was achieved over the common period 2010-2011 between SMOS and AMSR-E, using classical metrics (Correlation, RMSD, and Bias). In parallel, Chap. V of the dissertation evaluates the passive SMOSL3 products against the active ASCAT SSM at C-band by comparing them with land surface model simulations

(MERRA-Land) using classical metrics, advanced statistical methods (triple collocation), and the Hovmöller diagram over the period 2010-2012. These two evaluations indicated that vegetation density (parameterized here by the leaf area index LAI) is a key factor to interpret the consistency between SMOS and the other remotely sensed products. This effect of the vegetation has been quantified for the first time at the global scale for the three microwave sensors. These two chapters also showed that both SMOS and ASCAT (AMSR-E) had complementary performances and, thus, have a potential for datasets fusion into long-term SSM records. In Chap. VI of the dissertation, with the general purpose to extend back the SMOSL3 SSM time series and to produce an homogeneous SM product over 2003-2014 based on SMOS and AMSR-E, we investigated the use of a multiple linear regression model based on bi-polarization (horizontal and vertical) brightness temperatures (TB) observations obtained from AMSR-E (2003 - 2011). The regression coefficients were calibrated using SMOSL3 SSM as a reference over the 2010-2011 period. The resulting merged SSM dataset was evaluated against an AMSR-E SSM retrievals and modelled SSM products (MERRA-Land) over 2007-2009. These first results show that the multi-linear regression method is a robust and simple approach to produce a realistic SSM product in terms of temporal variation and absolute values. In conclusion, this PhD showed that the potential synergy between the passive (AMSR-E and SMOS) and active (ASCAT) microwave systems at global scale is very promising for the development of improved, long-term SSM time series at global scale, such as those pursued by the ESA's CCI program. It also provides new ideas on the way to merge the different SSM datasets with the aim of producing the CCI (phase 2) long-term series (a coherent "SMOS-AMSR-E" SSM time series for the period 2003 -2014), that will be evaluated further in the framework of on-going ESA projects.

Keywords: Soil moisture, Global-scale, Hydrology, Microwave remote sensing, SMOS, ASCAT, AMSR-E, Statistical evaluation

Évaluation à l'échelle globale d'une variable hydrologique mesurée par télédétection: les produits d'humidité du sol du satellite SMOS

Résumé en Français

L'humidité du sol (SM) contrôle les bilans d'eau et d'énergie des surfaces continentales et joue ainsi un rôle clé dans les domaines de la météorologie, l'hydrologie et l'écologie. La communauté scientifique en télédétection micro-ondes a fait des efforts considérables pour établir des bases de données globales de l'humidité du sol en surface (SSM) découlant d'instruments micro-ondes actifs et passifs. Parmi ces instruments, SMOS (Soil Moisture and Ocean Salinity), lancé en 2009, est le premier satellite passif conçu spécifiquement pour mesurer SSM à partir d'observations en bande L (1.4 GHz) à l'échelle globale. La validation des données SMOS SSM sur différentes régions climatiques et pour des conditions environnementales variées est une étape indispensable avant qu'elles soient utilisées de manière opérationnelle. En effet, une meilleure connaissance de la précision des estimations de SSM et des incertitudes associées permettra non seulement d'améliorer les produits SMOS SSM, mais aussi d'optimiser les approches de fusion de données utilisées pour créer des produits multi-capteurs long terme. De tels produits sont développés dans le cadre du programme Climate Change Initiative (CCI) de l'Agence spatiale européenne (ESA) pour l'ensemble des variables climatiques essentielles (ECV), dont SSM. A la suite des chapitres d'introduction I à III, les résultats de cette thèse sont présentés en trois chapitres. Le chapitre IV présente une comparaison des produits SSM issus des capteurs passifs SMOS (bande L) et AMSR-E (bande C) en prenant pour référence les estimations SSM du système d'assimilation SM-DAS-2 du Centre Européen pour les Prévisions Météorologiques à Moyen Terme (CEPMMT). Cette évaluation est menée sur la période d'observation commune à SMOS et AMSR-E (2010- 2011), en utilisant des indicateurs classiques (corrélation, RMSD,

Biais). En parallèle, le chapitre V présente une comparaison des produits SMOS SSM avec les produits SSM issus du capteur actif ASCAT en bande C en utilisant comme référence les simulations SSM d'un modèle des surfaces continentales (MERRA-Land), et en utilisant des indicateurs classiques, des méthodes statistiques avancées (triple collocation), et des diagrammes de Hovmöller sur la période 2010-2012. Ces deux évaluations ont montré que la densité de la végétation (paramétrée ici par l'indice foliaire LAI) est un facteur clé pour interpréter la cohérence entre le produit SMOS et les produits AMSR-E et ASCAT. Cet effet de la végétation a été quantifié pour la première fois à l'échelle globale pour les trois capteurs micro-ondes. Ces deux chapitres ont également montré que les trois capteurs SMOS, AMSR-E et ASCAT ont des performances complémentaires selon la densité de végétation et qu'il y a ainsi un potentiel intéressant en terme de fusion des jeux de données micro-ondes passifs et actifs. Dans le chapitre VI, avec l'objectif général d'étendre vers le passé les séries de données SSM de SMOSL3 et de développer un jeu de données SSM homogène sur 2003-2014, nous avons évalué l'utilisation d'une approche de régression linéaire multiple appliquée aux mesures de températures de brillance de AMSR-E (2003 - 2011). Les coefficients de régression ont été calibrés avec les produits SSM issus de SMOS sur 2010-2011. Le produit SSM résultant, qui fusionne les observations SMOS et AMSR-E, a été évalué par comparaison avec un produit SSM AMSR-E et les produits SSM MERRA-Land sur 2007-2009. Ces résultats préliminaires montrent que la méthode de régression linéaire est une approche simple et robuste pour construire un produit SSM réaliste en termes de variations temporelles et de valeurs absolues. En conclusion, cette thèse a montré que le potentiel de synergie entre les systèmes micro-ondes passifs (AMSR-E et SMOS) et actifs (ASCAT) est très prometteur pour le développement et l'amélioration de longues séries temporelles SSM à l'échelle mondiale, telles que celles produites dans le cadre du programme CCI de l'ESA. Elle a également fourni de nouvelles idées sur la façon de fusionner les différents ensembles de données de SSM dans le but de produire une série CCI SSM (Phase 2) long terme (une série cohérente combinant SMOS et AMSR-E sur la période 2003-2014), qui va être évaluée dans le cadre de projets ESA en cours.

Mots-clés: Humidité du sol, Échelle globale, Hydrologie, Télédétection micro-ondes, SMOS, ASCAT, AMSR-E, Évaluation statistique

Table of Contents

Chapter I

1. Introduction

1.1 Background and Motivation

Soil moisture (SM) is a key variable in better understanding of the land-atmosphere interactions because it influences the partitioning of precipitation into infiltration and runoff and the partitioning of energy into sensible and latent heat (Daly & Porporato, 2005; Pielke & Niyogi, 2010; Western et al., 2002). Spatio-temporal variabilities of SM are critical and have direct applications in hydrology, agronomy, water resources managing (Blöschl et al., 2009; Dobriyal et al., 2012), weather prediction and climate change studies (Leese et al., 2001; Seneviratne et al., 2010), flood analyses and drought monitoring (Bolten et al., 2010; Michele & Salvadori, 2002), irrigation operation, and soil erosion studies (Fu et al., 2000; Luk, 1985). In addition, SM initial conditions are crucial for the quality of hydrological models and Numerical Weather Prediction (NWP) at all range, including short range, monthly, and seasonal forecasts (Beljaars et al., 1996; de Rosnay et al., 2012; Drusch, 2007; Koster et al., 2004a; Koster et al., 2006; Panegrossi et al., 2001).

Consequently, there have been broad efforts to estimate SM in numerous research areas. Researchers have tried to estimate SM as accurately as possible using in situ observations (Dirmeyer et al., 2006; Robock et al., 2000), land surface models (wherein the accuracy of SM estimates depends on the forcing datasets and construction of the model), and Remote Sensing. Remote Sensing with high spatio-temporal coverage overwhelms the limitations and weakness of the other sources of information. Remote Sensing is an interesting source of information about SM as it offers the opportunity to obtain global and repetitive surface SM (SSM) estimates derived from satellite-based microwave sensors (Bartalis et al., 2007a; Kerr et al., 2001; Njoku et al., 2003; Owe et al., 2008). The main disadvantages of the remotely sensed datasets are their limitation to the top few centimeters of soil and the spatial and temporal gaps in dense vegetation and high surface roughness regions. Two types of microwave sensors offer the opportunity to retrieve SSM information:

radiometers (passive) and radar (active) sensors (scatterometers or SAR system). Radar and radiometers sensors measure surface backscatter and brightness temperatures (TB) signals, respectively, which are mainly determined by the soil dielectric constant, from which SSM can be derived (Njoku et al., 2002; Ulaby et al., 1996). Various radiometer and radar sensors have been used to measure SSM, and space-borne missions with new radiometer and radar sensors are presently being developed (Bartalis et al., 2007a; Entekhabi et al., 2010; Kerr et al., 2001; Njoku et al., 2003). Historically, passive microwave sensors were first used, starting with the Scanning Multichannel Microwave Radiometer (SMMR; 6.6, 10.7 , 18.0 21, and 37 GHz channels; (Wang, 1985)), which operated on Nimbus-7 between 1978 and 1987, then the Special Sensor Microwave Imager (SSM/I; 19.4, 22.2, 37.0, and 85.0 GHz channels) of the Defense Meteorological Satellite Program which started in 1987. Later passive sensors include: the microwave imager from the Tropical Rainfall Measuring Mission (TRMM; 10, 19 and 21 GHz channel; (Bindlish et al., 2003; Gao et al., 2006)), the Advanced Microwave Scanning Radiometer on Earth Observing System (AMSR-E; from 6.9 to 89.0 GHz; (Njoku & Li, 1999)) which operated on the AQUA satellite between 2002 and 2011, and Coriolis Windsat which started in 2003 (Parinussa et al., 2011b). More recently, the Soil Moisture and Ocean Salinity (SMOS) was launched on November 2, 2009 (Kerr et al., 2012) and the upcoming SMAP (Soil Moisture Active/Passive) mission is scheduled for launch in November 2014 (Entekhabi et al., 2010).

Besides passive microwave sensors, active microwave sensors are also useful to retrieve SSM including, but are not limited to, the European Remote Sensing (ERS-1) Scatterometer which is operated since 1992, and its copy on ERS-2 which started collecting data from March 1996, and the Advanced Scatterometer (ASCAT) on board the Meteorological Operational satellite programme (METOP), METOP-A was launched in 2006 (Bartalis et al., 2007a) followed by METOP-B in 2012.

The (European Space Agency) ESA's Programme on Global Monitoring of Essential Climate Variables (ECV), known as the Climate Change Initiative (CCI), and the European Space Agency's Water Cycle Multi-mission Observation Strategy (WACMOS) merged several active and passive i.e. SMMR, SSM/I, TMI, AMSR-E, ERS-1/2, and ASCAT data (Liu et al., 2011) to produce long-term and consistent time series of SSM (1978-2010), with a spatial resolution of 0.25° x 0.25°. This product has been available since June 2012 and has been of interest for researchers to study the long-term trends of SSM (Albergel et al., 2013b; Seneviratne et al., 2010).

The SMOS satellite, among all the aforementioned passive microwave sensors, is the first ever satellite dedicated and specifically designed to measure SSM, over the land surfaces, and surface ocean salinity (SSS) at L-band on a global basis (Kerr et al., 2010). L-band (1.4 GHz), within the microwave bands protected for remote sensing applications, has been recognized to be well-suited to monitoring SSM owing to better penetration through vegetation and reduced atmospheric effects on their signals (Kerr et al., 2001; Njoku & O'Neill, 1982; Wang & Schmugge, 1980). As the attenuation effects of the vegetation layer overlaying the ground decrease with increasing wavelength, L-band is theoretically more optimal for sensing SSM than C-band (4–8 GHz) or higher frequencies. Furthermore, the effective SSM sampling depth at L-band (~0-3cm; Escorihuela et al., 2010) is larger than at C-band (~0-1cm). In the literature, the compared capabilities of remote sensing at C-band and L-band to monitor SSM were established from in situ observations and theory (Ulaby et al., 1986; Wigneron et al., 1993). Therefore, it is likely the SMOS SSM products are useful and of high priority in most operational hydrologic models for agricultural applications, flood forecast and water quality management.

Two SSM products have been released since the launch of SMOS: (i) the Level 2 SMOS SSM products (SMOSL2), distributed by the ESA, which is derived from the multi-

angular and fully polarized bi-polarization SMOS TB observations and provided as swath-based products and more recently (ii) the Level 3 SMOS SSM products (SMOSL3), distributed by the Centre Aval de Traitement des Données SMOS (CATDS), which is a gridded product computed from the SMOS TB observations (Jacquette et al., 2010). The general principle of the algorithm used to compute SSM in both SMOSL2 and SMOSL3 is almost similar (Jacquette et al., 2010). However, in the SMOSL3, the quality of SSM products is enhanced by using multi-orbit retrievals (Kerr et al., 2013b), and provided as global maps in a more friendly format (NetCDF) for the final users. Evaluation of both SMOSL2 and SMOSL3 SSM products, as for any remote sensing products, is needed to guide their correct use, and to improve our understanding of their strengths and weaknesses over a large spectrum of climate and environmental conditions across the world. Evaluation not only assesses the accuracy and reliability of the estimates and their scientific utility, but also defines possible limits of satellite instruments.

Several studies have evaluated SMOSL2 SSM products over different regions using in situ observations, model-based data, and remote sensing products at the local, continental, and global scales (Al Bitar et al., 2012; Albergel et al., 2011; Albergel et al., 2012; Collow et al., 2012; Dall'Amico et al., 2012; Dente et al., 2012; Jackson et al., 2012; Kaihotsu et al., 2013; Lacava et al., 2012; Leroux et al., 2013a; Leroux et al., 2013b; Parrens et al., 2012; Peischl et al., 2012; Pierdicca et al., 2013; Sanchez et al., 2012; Wigneron et al., 2012). Nevertheless, there is no evaluation was done to evaluate the newly re-processed SMOSL3 SSM products, due to their recentness, with the exception of (Su et al., 2013) who evaluated SMOSL3 with AMSR-E and ASCAT against in-situ observations from the Murrumbidgee Soil Moisture Monitoring Network for the 2010-09/2011 period.

At the local scale, for instance, Lacava et al. (2012) have assessed SMOSL2 SSM products through a comparison with modelled SSM and in situ observations from three sites

situated in Luxemburg and Italy. Collow et al. (2012) and Jackson et al. (2012) have performed an evaluation of the SMOSL2 SSM products over the central USA and four watersheds located in the USA, respectively. Leroux et al. (2013b) compared the SMOSL2 SSM products with AMSR-E, ASCAT, and the European Centre for Medium range Weather Forecasting (ECMWF) SSM products, for the year 2010, against in situ observations over four watersheds located in the USA. Sanchez et al. (2012) and Wigneron et al. (2012) have evaluated the SMOSL2 SSM products with SSM observations obtained from the REMEDHUS Network and the VAS (Valencia Anchor Station) site, respectively, located in Spain. Dente et al. (2012) have validated SMOSL2 SSM products over the Maqu region on the Tibetan Plateau in China and the Twente region in The Netherlands. Peischl et al. (2012) have evaluated SMOSL2 SSM products with SSM observations obtained from the Australian Airborne Experiments for SMOS (AACES) located in South-East Australia. More recently, Kaihotsu et al. (2013) have evaluated SMOSL2 SSM products using in situ observations on the Mongolian Plateau for the 2010-2011 period. Most of these studies came to almost the same conclusion that SMOS had a Root Mean Square Error (RMSE) close to the accuracy requirement of SMOS i.e. 0.04 m^3/m^3, the SSM dynamics were well captured by SMOS, and the SMOS was a bit dryer than the other datasets.

At the regional and continental scales, for instance, Albergel et al. (2012) have evaluated the SMOSL2 SSM products, together with ASCAT and SM-DAS-2 SSM products (produced at ECMWF) against in situ observations from several stations located in Australia, Africa, the USA, and Europe during 2010. Albergel et al. (2012) concluded that ASCAT and SMOS had a an average correlation of 0.55 with in-situ datasets. Parrens et al. (2012) have compared SMOSL2 SSM products with land surface model simulations (ISBA LSM) over the whole of France. Al Bitar et al. (2012) have evaluated SMOSL2 SSM products using in situ observations obtained from the Soil Climate Analysis Network (SCAN) and the Snowpack

Telemetry (SNOTEL) sites located in North America. More recently, Pierdicca et al. (2013) have compared SMOSL2 SSM products with only ASCAT SSM products over Europe and extreme North Africa during the 2010 - 03/2012 period. Pierdicca et al. (2013) have demonstrated that the two products correlated fairly to each other and their consistency depends on season and surface land cover.

At the global scale, there is only, to date, one dedicated SSM study that has been conducted to evaluate the SMOSL2 SSM products. Leroux et al. (2013a) performed, at the global scale, a comparison between the SMOSL2 SSM products against AMSR-E and ASCAT SSM products taking ECMWF model simulations as a benchmark for the year 2010. This study showed that SMOS was better in terms of RMSE values than ASCAT and AMSR-E datasets over Australia, North America, and Central Asia.

Four issues can be identified in the review of the existing evaluations of SMOS SSM products, summarized in the previous paragraphs:

(i) The evaluations and comparisons were generally made with observations from in situ networks, which are limited in space and time. In the natural environment, there is a large spatio-temporal variability of SM, which depends on the combined influence of hydrometeorology, soil hydraulic properties, climate, and vegetation. In situ observations have a low spatial density so that point-based observations cannot represent accurately the spatial distribution of SSM (Dorigo et al., 2011), therefore inadequate to carry out a global evaluation and draw global conclusions. In contrast, land-surface models are able to simulate global SSM products (Dirmeyer et al., 2006; Georgakakos & Carpenter, 2006) and their spatial resolutions are often in agreement with the resolution of the remotely sensed products. For instance, several global SSM datasets produced from modelling or assimilation approaches are becoming

readily available (e.g., SM-DAS-2, MERRA-Land which is a NASA atmospheric reanalysis) in 2013. However, little is known about the reliability of those products at the global scale and how they compare to the remote sensing datasets (Draper et al., 2009b; Reichle et al., 2007; Sabater et al., 2007). Hence, more research is required to advance our understanding of the capabilities of SSM products from remote sensing and from models to assess the uncertainties associated with them.

(ii) The evaluations and comparisons were only based on the SMOSL2 SSM retrievals. However, as already mentioned, new recently re-processed 1-day global SSM product i.e. SMOSL3 provided by the CATDS with enhancement of better SSM estimations at revisited locations and increasing of SMOS retrieval coverage (Jacquette et al., 2010) has been released.

(iii) Most of the aforementioned studies addressed the evaluation only in the year 2010, evaluation should include longer period so that the temporal span can be more reasonable to draw any conclusive statistics.

(iv) None of the aforementioned studies compared the capabilities of remote sensing at C-band and L-band to monitor SSM at the global scale.

The motivation for this doctoral research work relies on the fact, discussed above, that there has been limited evaluation of the state of the art SMOS SSM product, using SSM products retrieved from other active or passive microwave sensors or simulated from land surface models. It is crucial to evaluate their accuracy at the global scale and for a range of climate and environmental conditions across the world before developing operational applications based on the SMOS observations, thereby improving the knowledge of errors in the satellite data across space and time. In addition, the inter-comparisons of SMOS SSM products with other satellite and model SSM products at the global scale help in

understanding the similarities and differences between the various products and in learning the regions where they agree or differ. Moreover, a successful evaluation of the SMOS SSM datasets at the global scale would be a significant contribution to improving the prediction capability of hydrologic models, thus, leading to improvement in SM estimation through data assimilation (Reichle et al., 2008).

Furthermore, SSM sensors do not deliver decadal homogeneous products. SMOS SSM products, for instance, are only available since 2010; whereas AMSR-E SSM products are only available from 2002 to 2011. Nevertheless, for several applications such as climate change trend analysis, flood analysis, and drought monitoring, a historical record is required. The latest CCI program SSM product did not consider SMOS in its first phase programme, due to its recentness. However, SMOS presents an innovative interferometric antenna concept, dedicated for SSM monitoring, which is a promising technology for SSM retrievals. Therefore, SMOS should be considered to be merged with the other existing microwave remotely sensed products to produce long-term SSM time series.

1.2 Dissertation objectives

The main science objectives in the context of the global evaluation of SMOS SSM products have been already raised in the motivation of this doctoral dissertation. Very little research has been done to evaluate the performance of the newly reprocessed SMOSL3 SSM retrievals at the global and regional scales. The overall goal of this doctoral dissertation is to complement the existing assessment and evaluations of the global SMOSL3 SSM estimates by carrying out a comprehensive evaluation using longer time series (2010-2012) that also include modelling products. This study is expected to contribute to the evaluation/validation activities of SMOS SSM products via SM-DAS-2 and MERRA-Land SSM products. In

connection to the above introduction, the following research objectives have been addressed in this doctoral dissertation:

(i) Conducting global comparisons between SMOS (L-band) SSM products and other existing microwave passive (AMSR-E; C-band) and active (ASCAT; C-band) SSM products using models SSM simulations (MERRA-Land and SM-DAS-2) as benchmarks with the following purposes:

   a. A better understanding of the quality of the SSM products retrieved from passive and active techniques at L- and C-bands at the global scale.

   b. Evaluating their ability to capture the spatial and temporal dynamics of SSM at the global scale (where are the significant differences and consistencies in the performances between the different satellite SSM products?).

   c. Evaluating the effects of the biome types and vegetation density, parameterized here by the leaf area index (LAI), on the different SSM retrievals (how the accuracy of the SSM retrievals is impacted by vegetation?).

(ii) Developing a global and a long record i.e. 2003-2014 of SSM dataset which is coherent across different sensors (more specifically: Are statistical regression approaches a good tool to merge the AMSR-E and SMOS SSM data to produce realistic and long term SSM time series in terms of variations and absolute values?).

These objectives are accomplished as separate studies resulting in journal articles. A brief description of each paper follows in the next Section.

1.3 Dissertation outline

This doctoral dissertation consists of seven chapters, which are organized as follows: Chapter I has just given brief background and the motivation, objectives, and scope of this research work.

Chapter II gives the theoretical background regarding SM. It covers aspects such as: SM definition, its importance, different types of measurements (including in situ, remote sensing, models, and assimilation techniques).

Chapter III gives an overview on the SMOS mission and its products. It describes shortly the basics of the SSM retrieval algorithm and the main types of existing SMOS products. This chapter includes also a brief overview of the AMSR-E and ASCAT missions and their SSM products.

Chapter IV performs a comparative analysis of the SMOSL3 SSM products along with another SSM product derived from the observations of the AMSR-E at C-band (this latter product is referred to as AMSRM). The AMSRM product is to date the reference SSM product produced from passive microwave remotely-sensed sensors (Owe et al., 2008). SM-DAS-2, a SSM product produced by ECMWF Land Data Assimilation System was used as an independent reference to monitor the quality of both SMOSL3 and AMSRM SSM products. The present study was carried out from 03/2010 to 09/2011, a period during which both SMOS and AMSR-E products were available at the global scale. Three statistical metrics (considering both original SSM data and anomalies) used for the evaluation were the correlation coefficient (R), the Root Mean Squared Difference (RMSD), and the bias. In this chapter, the impact of the biome types and vegetation density on the performance of the SMOS and AMSR-E retrievals was analyzed at the global scale.

In Chapter V, the performance of the SMOSL3 dataset is further evaluated against SSM retrievals made by an active C-band system. This chapter performs a global-scale

evaluation of the SMOSL3 SSM products and a satellite-based active microwave SSM datasets (ASCAT) with respect to modelled surface SSM simulated by MERRA-Land. The SSM time series retrieved from ASCAT is to date the reference product used in the CCI project. The evaluation period in Chapter IV was extended to 3 years (2010–2012) in this Chapter. The relationship between the global-scale SSM products was studied using (1) a time series statistics (considering both original SSM data and anomalies), (2) a space-time analysis using Hovmöller diagrams, and (3) a triple collocation error model. Chapter IV and V both have in common that the remotely sensed data were compared to a land surface model.

In Chapter VI, the complementary performances between AMSR-E and SMOS shown in Chapter IV motivated us to produce a merged SSM dataset. For that purpose, this Chapter investigates the use of physically based multiple-linear regressions to retrieve a global and long term SSM record based on a combination of bi-polarization (horizontal and vertical) TB observations from the AMSR-E and SMOS sensors. Chapters IV to VI address the three major research objectives mentioned earlier. Each chapter is considered as an independent study having its own introduction to conclusion, but they are all connected under the umbrella of SMOS SSM data evaluation. Some overlap exists between the Chapters IV-VI, this was unavoidable since each chapter is a self-explanatory based manuscript that has been or will be published in scientific journals.

Finally, Chapter VII concludes this dissertation and summarizes the results obtained from all the chapters. Limitations encountered in this research are discussed and some directions/recommendations for the future research are provided.

Chapter II

2. Soil moisture and its importance/measurements

2.1 Soil moisture and its importance

2.1.1 Soil moisture

The soil medium is often divided into three phases consisting of liquid, gaseous, and solid phases. Soil matter, the sum of the mineral matter and the organic matter, represents the solid phase amounting about to 50 % of the entire soil medium (Hillel, 1980). Pore space represents the other 50 %, which consists of the liquid phase (i.e., the soil water) and the gaseous phase (i.e., the soil atmosphere) (Hillel, 1980). The components of the soil medium are displayed in Fig. 2.1. Pore spaces between soil particles can be filled by air or water, the latter is often referred to as soil moisture and is also known as soil water content. In other words, the quantity of water that is present in the unsaturated zone, held in the soil between the surface and the groundwater level, is known as soil moisture. The soil water moves freely down by gravity and up by capillary force. It is then extracted by plant roots, evaporates at the surface, or recharges the groundwater (Strangeways, 2000). It is a small fraction of the world's fresh water supply (Dingman, 2002), and it is generally expressed in gravimetric units (g/cm^3), volumetric units (m^3/m^3; m^3 water per m^3 bulk soil volume) or percent (% vol.) (Dingman, 2002; Smith & Mullins, 2000).

Soil is saturated when the pore spaces between the soil particles are totally filled by water without any air pockets (See Fig. 2.1). This water, within a day or longer, drains-with the exception if the water table is within the soil which occurs quite often- downwards and away under gravity and leaves the soil at the so called “field capacity” with certain quantity of water that holds against gravity (Twarakavi et al., 2009; Veihmeyer & Hendrickson, 1931). At this point, the spaces between the soil particles are filled with a mixture of water and air pockets (see Fig. 2.1). When the plants can no longer extract the necessary water for growth

and therefore suffer and they start to wilt before dying, the soil is described as at "wilting point" (see also Fig. 2.1) (Briggs & Shantz, 1912).

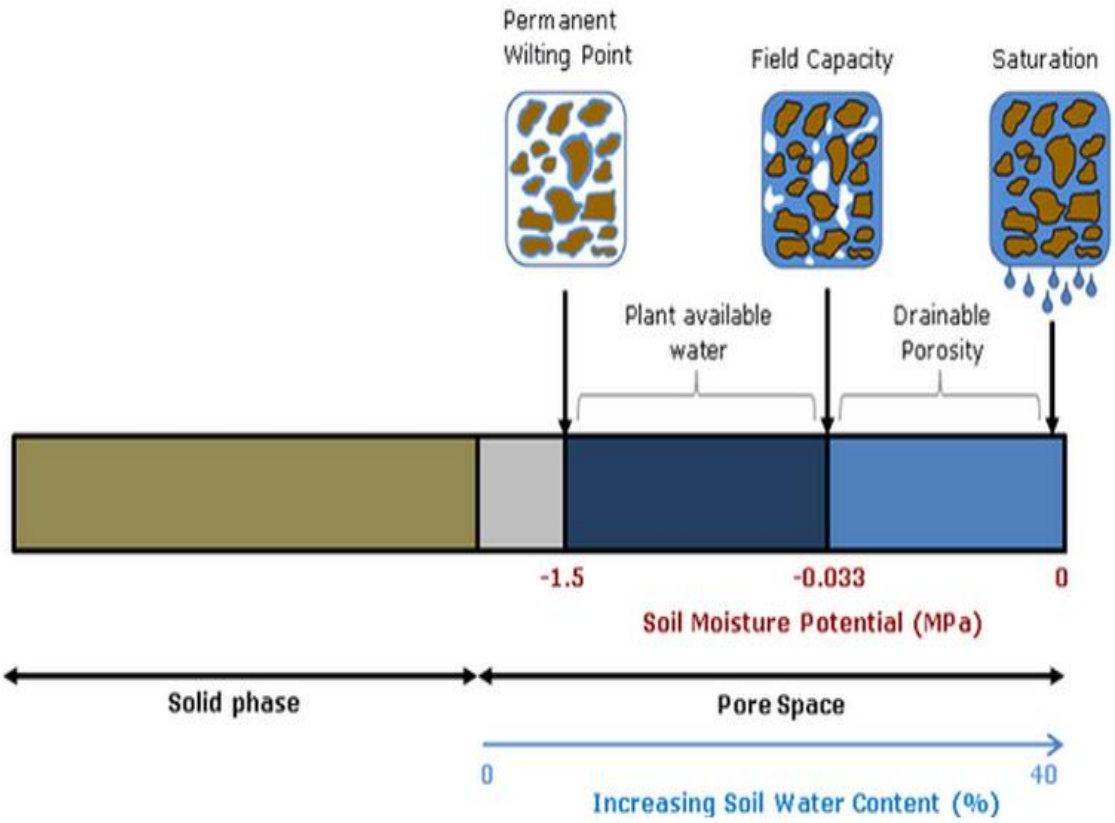

Fig. 2 - 1 *Components of soil medium (After O'Geen, 2012).*

The capacity of the soil to store water depends on the size, type, shape, the properties of the solid phase (in particular its electrical charges), and the continuity of the pores of the soil. Temporal variations and spatial distribution of soil moisture can be influenced by precipitation, soil texture, topography, organic matter content, porosity, soil structure, and vegetation and land cover. Soil texture (i.e. percentage of clay, sand, and silt) and soil structure control the water-holding capacity while topography (i.e. variations in slope and aspect) affects soil moisture distribution i.e. soil moisture movements. Table 2.1 presents the influence of the relief elements (aspect & slope) on the spatial distribution of soil moisture.

The soil moisture values represent the ratio of soil moisture on a slope and soil moisture on a flat surface with the same type of soil and vegetation for four aspects (North, South, East and West) and for four slope parts(upper, middle, lower and the foot of a slope) for summer period of the year (Svetlitchnyi et al., 2003). Soil, for instance, is dryer at flat surface than at foot of slop, and the slopes face west and south are dryer than the slopes which face east and north, this may be explained by the relatively high radiation exposure of the sun (Svetlitchnyi et al., 2003). The effects of north and south may be not equal in the Northern and Southern Hemisphere.

Table 2 - 1 Typical effects of slope and aspect on soil moisture values (relative units) in the upper soil layer (After Svetlitchnyi et al., 2003)

Relief elements	**Convex slope (Aspect at)**				**Straight or concave slope (Aspect at)**			
	North	East	South	West	North	East	South	West
Flat surface	1.00	1.00	1.00	1.00	1.00	1.00	1.00	1.00
Upper part of a slope	1.10	1.10	0.95	0.95	1.00	0.83	0.56	0.61
Middle part of a slope	1.00	1.00	0.79	0.79	1.00	1.00	0.80	0.80
Lower part of a slope	1.00	1.00	0.63	0.66	1.17	1.17	1.00	1.00
Foot of a slope	1.50	1.50	1.24	1.24	1.61	1.61	1.30	1.30

Vegetation (i.e. vegetation type and density) influences infiltration, runoff, and evapotranspiration, thus, influences the variations of soil moisture at different space and time-scales (English et al., 2005). In addition, climate (i.e. precipitation, solar radiation, wind, and humidity) controls the dynamics of soil moisture. Precipitation is the most important climatic forcing for soil moisture content and its distribution, which induces along with evaporation the trends in aridity and saturation of soil (D'Odorico & Porporato, 2004; Koster et al., 2003).

2.1.2 General importance of soil moisture for the environment and our climate system

Water is a vital source of all life on Earth's climate system. It circulates continuously between oceans, the atmosphere, and land surface due to the solar energy. This circulation and conservation of the Earth's water, known as the water cycle (see Fig. 2.2), is a critical component for our climate system.

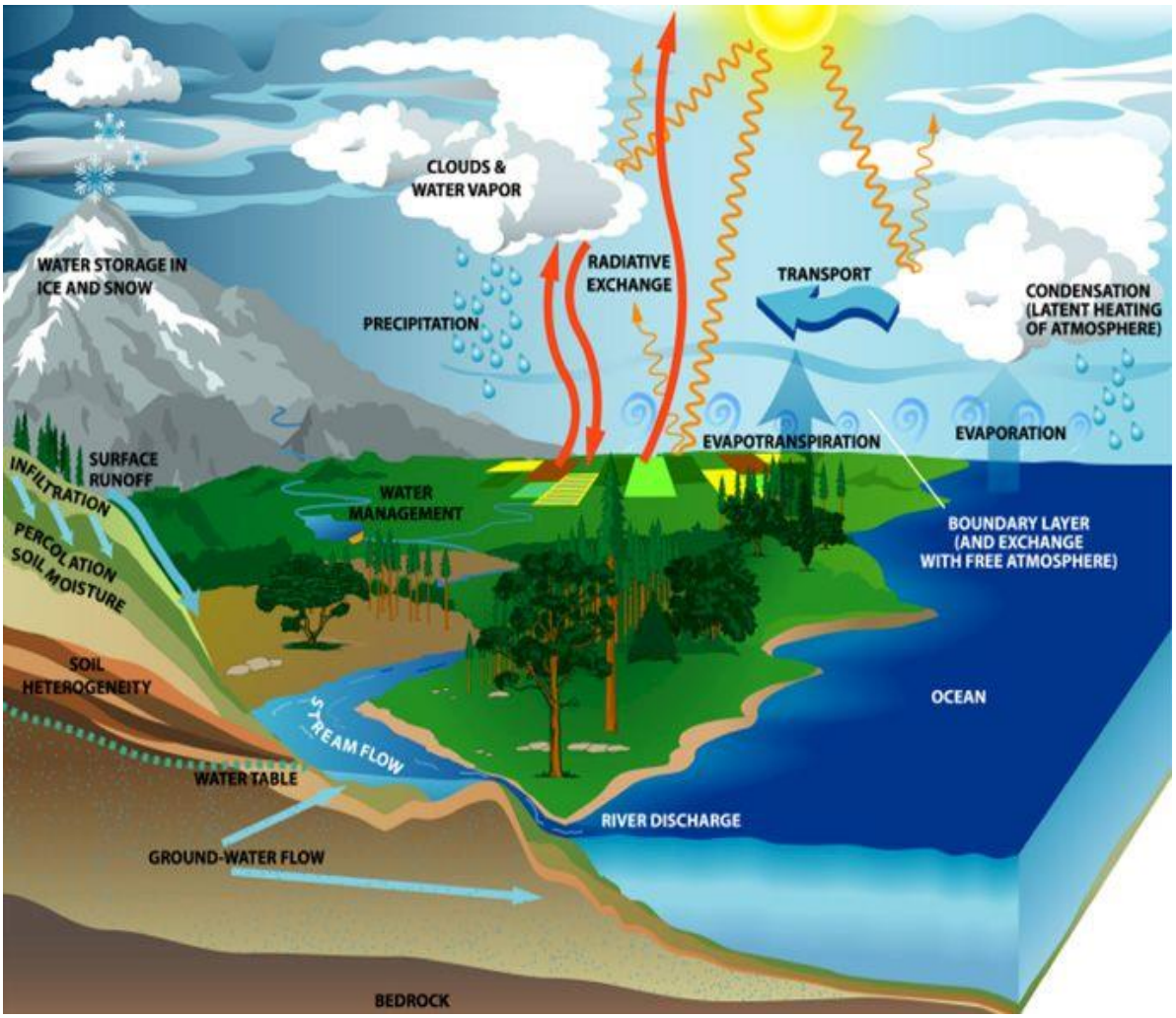

Fig. 2 - 2 *The Global Water Cycle. Adapted from* Houser et al. *(2007).*

A schematic diagram of this global water cycle with the quantities of water volumes and fluxes are shown in Fig. 2.3. Fig. 2.3 illustrates the qualitative proportions of the global water reservoirs and transports. However, precise values are not known yet; therefore, the specified numbers can differ from others given in the literature.

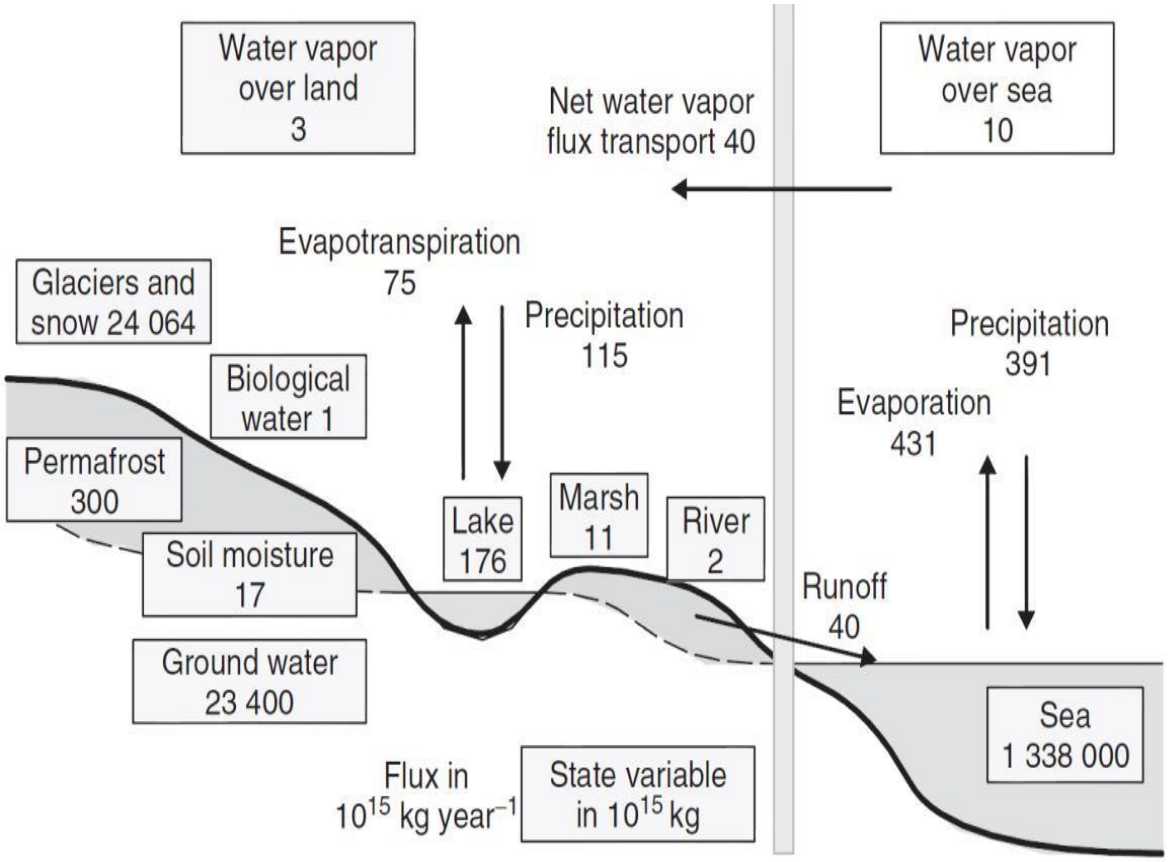

Fig. 2 - 3 *Schematic diagram of the Earth's water cycle. Reservoir volumes (boxes) are stated in 10^3 km^3, water fluxes (arrows) in 10^3 km^3 per year. Adapted from* Oki *(1999).*

Although the soil moisture only represents a small proportion (0.05 %) of the total of fresh water volume, as can be seen in Fig. 2.3 compared to the other components, its influence on the global water cycle is of great importance and it plays a major role in the water cycle. Soil moisture is a key variable in the exchanges of water, energy, carbon between the land

surface interface and the atmosphere. It is also an important factor in many fields: in atmospheric circulation (Walker & Houser, 2004), as soil moisture influences energy and mass transfer across the landscape boundary (Arora & Boer, 2006; Findell & Eltahir, 2003), in water resources management, for instance in flood analyses and drought monitoring (Michele & Salvadori, 2002), in agricultural management, by defining appropriate irrigation amounts and intervals (Hanson et al., 2000), in soil science, it is a key parameter in ecology and biogeochemistry to determine potential land slide and can help in soil erosion's predictions in semi-arid areas (Kiome, 1992), and in plant biology, soil moisture is the key factor for plant water stress (Veihmeyer & Hendrickson, 1950).

More specifically, soil moisture can be of significant importance resource for plants as well as for human activities:

a) The soil moisture of the root zone is a limiting factor for plant growth, and it is optimal when not too dry and not too wet over a long time period for plants to survive. Therefore, information of the appropriate amount of soil water is essential for cultivation of plants and agriculture in general. This helps in irrigating crop fields more efficiently. Furthermore, information of soil moisture patterns helps agronomist to enhance irrigation's scheduling and better crop yield predicting in arid and semi-arid areas (Tao et al., 2003).

b) The soil moisture is a variable of major importance to assess the potential for risks in the case of extreme events. Soil moisture conditions (excessively saturated or dry) can be signs of warning of subsequent flooding (as the occurrence and intensity of flooding are strongly influenced by the soil's ability to take up a certain amount of water) or drought (Dingman, 2002; Richter & Semenov, 2005).

c) Soil moisture plays an important role in the hydrological models, as it controls the re-distribution of the precipitation into runoff and infiltration. Therefore,

accurate observations of soil moisture are essential before estimating water fluxes (Parajka et al., 2006).

d) Soil moisture plays an important role in meteorological and climate models, as its temporal variation and spatial distribution play a major role in the partitioning of the solar energy into sensible and latent heat fluxes at both global and local scales (Robock et al., 1998). Soil moisture availability plays a significant role in the biases of surface temperature in climate models (Cheruy et al., submitted for publication). Accurate estimates of soil moisture are necessary for improving numerical weather predictions, whereas inaccurate soil moisture initialization leads to large errors in climate predictions (Robock et al., 1998; Rowntree & Bolton, 1983).

e) Soil moisture spatio-temporal variations over land influence runoff, inflow, controls evaporation and transpiration, thus regulates the extent of groundwater recharges (Mohanty & Skaggs, 2001). More generally, soil moisture influences the discharge which is the most accessible fresh water resource.

2.2 Measurements of soil moisture

There are different methods for soil moisture measurements employed for different applications. These include measurements techniques: (i) direct and indirect in-situ measurements (e.g. radiological methods, neutron attenuation, gamma absorption, soil-water dielectrics, microwave probe, etc.) and (ii) emerging technologies (remote sensing), and estimation techniques: (i) land surface models and (ii) integration of the previous methods in the so called assimilation. All these methods differ significantly by the accuracy, complexity, technique, and spatio-temporal scales. These methods are briefly presented in the following sections.

2.2.1 In-situ measurements

In-situ measurements methods have several common advantages including, but not limited to, relatively accurate for the sampling point and measurements of soil moisture could be taken at several depths. On the other hand, there are common disadvantages including, but not limited to, local scale and thus cannot be representative for larger scales, time consuming, and costly. Nevertheless, models and remote sensing up to date use in-situ measurements to calibrate and validate their predictions and observations, respectively.

Thermogravimetric method (Marshall & Holmes, 1988) is the most common classical method to measure volumetric water content. The equation used to compute the water content ($\emptyset_m$) on a mass basis can be written as follows:

$$\emptyset_m = \frac{m_w}{m_s} \qquad 2-1$$

where:

m_w is mass of water lost upon a sample 24 hour drying in an oven at 105 °C and

m_s is a constant mass of the sample before drying.

Whereas the equation used to compute the water content on a volumetric basis ($\emptyset_v$), most commonly used, can be written as follows (Smith & Mullins, 2000):

$$\emptyset_v = \emptyset_m \frac{\rho_b}{\rho_w} \qquad 2-2$$

where:

ρ_b is the dry bulk density of the soil (kg/m^3) and

ρ_w is the density of the water (1000 kg/m^3).

If the volume of soil is known (sampled by coring), volumetric water content ($\emptyset_v$) can be computed as follows (Smith & Mullins, 2000):

$$\emptyset_v = \frac{mass\ of\ wet\ soil - mass\ of\ dry\ soil}{soil\ volume * the\ density\ of\ the\ water} \qquad 2-3$$

This method has several advantages being simple, reliable, inexpensive (but not for regional or global scales), and can be easily calculated. This method is, however, not free error as some clay soils still contain water after oven drying which leads to an underestimation of water content. Similarly, some organic soils loose some weight due to organic matter changes during heating, which leads to an overestimation of water content (Smith & Mullins, 2000).

Other indirect methods have been developed to overcome the limitations of thermo-gravimetric method with more advantages such as repetitiveity, quickness, and less disruption (Schmugge et al., 1980). The basic principle of these methods is that certain characteristics of the soil are functions of the soil moisture, thus monitoring these properties leads to soil moisture measurements (Strangeways, 2000). Some of these methods are briefly summarized in Table 2.2.

Table 2 - 2 Types of in situ soil moisture measurement techniques (Schmugge et al., 1980; Smith & Mullins, 2000; Walker et al., 2004; Zazueta & Xin, 1994)

Technique	Measurement of SM	Strengths	Weaknesses
Thermo-gravimetric	This method involves taking a volume of soil, accurately weighing it, completely drying it out in an oven, re-weighing the dry sample, and calculating soil moisture percentage from the weight loss.	Accurate measurements - simple procedure to compute soil moisture- not costly - and not dependent on salinity and soil type.	Time consuming and pain staking procedure - difficult and destructive sampling - inapplicable to repetitive measurements and to automatic control - must know dry bulk density to transform data to volume moisture content- costly for regional and global scales.
Nuclear techniques (Neutron scattering)	Based on the relationship between the emitted neutrons with the hydrogen nuclei in the soil water.	Average soil moisture with depth can be obtained - reliable - automatic readings - non-destructive - water can be measured in any phase.	Poor depth resolution - costly - radiological safety procedures (radiation hazard) required - special measures necessary to deal with readings in surface soil - care required in access tube installation - must calibrate for different types of soils - access tubes must be installed and removed - measurement partially dependent on physical and chemical soil properties - depth probe cannot measure soil water near soil surface.
Soil dielectric method (1)Time Domain Reflectrometry (TDR)	This method involves measuring the dielectric constant which is a function of soil moisture.	Can be installed easily and at any depth - applicable for automatic monitoring - possible to perform long-term in situ measurements - portable - independent of soil texture, temperature, and salt content.	Small zone of influence of TDR probes - the electronics to control and interpret the measurements are rather costly - high cost of equipment - only sensitive to the moisture around the probe - attenuation of the signal caused by salinity or highly conductive heavy clay soils.
Soil dielectric method (2) Capacitance probes	This method involves measuring the dielectric constant which is a function of soil moisture (Probes are inserted into the soil to the required measurement depth and the measurement can either be displayed on a meter or can be recorded using a	Rapid and easy measurements - very sensitive to small changes in soil moisture - readings are instantaneous - precise resolution - theoretically, can provide absolute soil water content - water content can be determined at any depth.	Small zone of influence for capacitance probes - high sensitivity to air gaps and regions surrounding the probes - long-term stability questionable.

Technique	Measurement of SM	Strengths	Weaknesses
	data logger).		
Thermal conductivity	This method involves measuring the rate of heat dissipation which decreases with decreased water content.	-	This is only possible in soils with extreme salinity.
Gamma ray attenuation	Based on the scattering and absorption of the radiation which is related to the density of the matter.	Not destructive - very good depth resolution with attenuation method but poor with backscatter techniques - can determine mean water content with depth - can be automated for automatic measurements and recording - can measure temporal changes in soil water.	Costly - difficulty of use - radiological safety procedures necessary - Gamma ray scanners of the gamma ray method are only used in laboratory situations - restricted to soil thickness of 2.54 cm or less - affected by soil bulk density changes.
Electrical Conductivity Probes and resistance Blocks	Generally, soil conductivity decreases with decreasing soil moisture. Resistance or gypsum block sensors measure soil conductivity.	Not costly and simple to use and install.	Conductivity of the soil water is different in different soil types (alkaline or acid soils) and can change according to the sprays or fertilizers applied - resistance block sensors are generally used for trends in soil moisture changes only - sometimes requires calibration.
Tensiometer (Soil Suction technique)	This method involves measuring the water availability to plants and on the measurement of the capillary tension.	Easy to design, install, and maintain - low-cost - readings are in units of negative pressure (suction) expressed as kilo Pascals - it is preferred for agriculture and irrigation of crops - provide additional information (water table elevation - the direction of fluxes in soil profile - and soil moisture tension) - operates for long periods if properly maintained, can be adapted to automatic measurement with pressure transducers - can be operated in frozen soil with ethylene glycol.	Indirect measurements - very weak instrument - only measures soil water suction - predetermination of soil water characteristics essential - inaccuracies due to hysteresis of water content/potential relationship - limit range of 0 to -0.8 bar not adequate for sandy soil - difficult to translate data to volume water content - automated systems costly and not electronically stable.
Hygrometric techniques	Based on the relationship between moisture content in porous materials and the relative humidity.	Low-cost - low maintenance - wide soil matric potential range - well suited for automated measurements and control of irrigation systems.	Declination of the sensing element through interactions with the soil components and a special calibration is required for the tested material.

It is noticed from Table 2.2 that whatever the method used to measure the soil moisture, the common issue is the high cost and effort of setting up the network stations and they are only point measurements. Several researchers attempted to gather all available in situ soil moisture measurements in one database such as the Global Soil Moisture Data Bank developed by (Robock et al., 2000) which was transferred and extended recently to the International Soil Moisture Network (ISMN; Dorigo et al., 2011) which is available at https://ismn.geo.tuwien.ac.at/. Fig. 2.4 shows the geographical distribution of the available in situ networks at ISMN. It can be seen that most of the network stations are located in the Northern Hemisphere. Consequently, they are not sufficient to study soil moisture at the global scale.

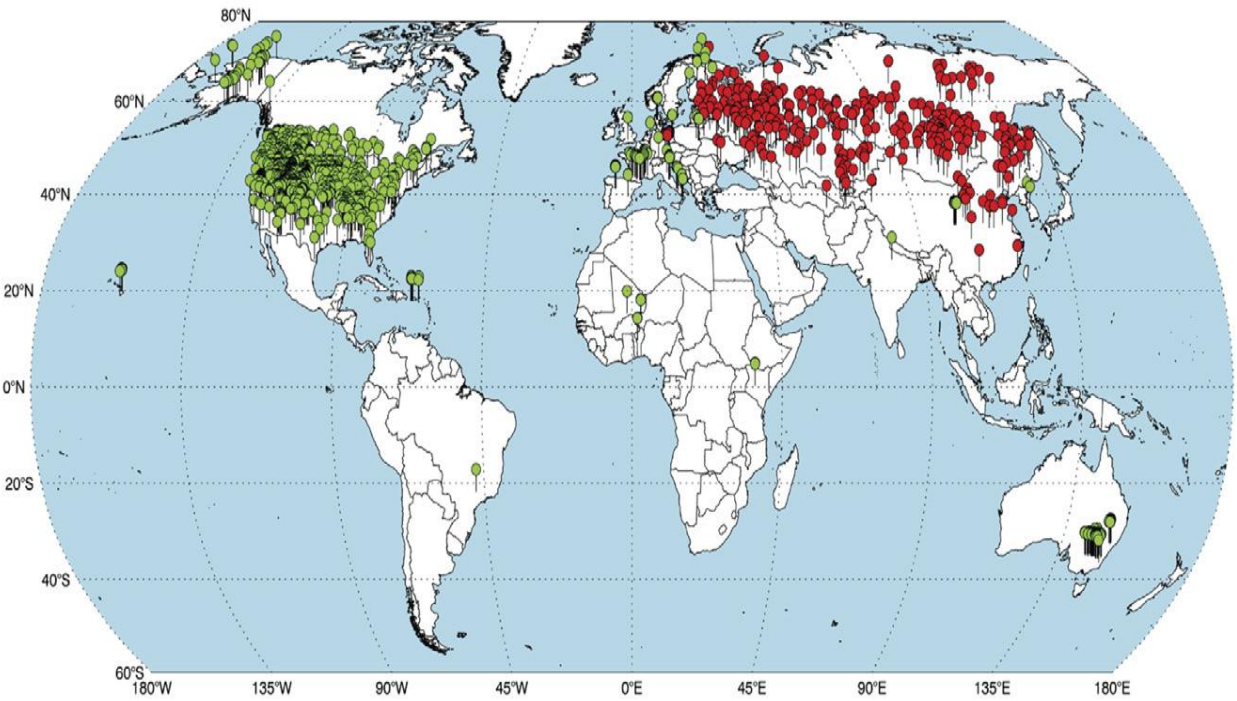

Fig. 2 - 4 *Overview of soil moisture in situ network stations available at ISM. Adapted from* Ochsner et al. *(2013).*

2.2.2 Remote sensing of soil moisture

Remote sensing techniques are being widely used to monitor most kinds of environmental issues, from local to original and global scales. Information about the land and water surfaces on Earth can be derived using images of the electromagnetic radiations acquired from space, reflected or emitted from the Earth's surface (Campbell, 1996). Information over large areas can be obtained rapidly and repetitively thanks to remote sensing techniques for making it possible to distribute information through sensors mounted on satellites, which operate in several spectral regions (from the optical to microwave regions) (Jeyaseelan, 2004). A satellite, launched into special orbit, mostly takes a few days to explore the whole surface of the Earth and repeats its path at regular intervals (Jeyaseelan, 2004). Most of the electromagnetic spectrum (e.g., optical, infrared and microwave, Fig. 2.5) has been used in recent years with different sensors which can provide unique information about properties of the surface of the Earth or subsurface soil layers (e.g., albedo, surface temperature, soil moisture, etc.).

Remote sensing is the most appropriate technique to provide global maps of soil moisture, and recently, has been providing soil moisture using various techniques (Sandholt et al., 2002). In general, soil moisture can be estimated from remote sensing data especially from: (i) visible/near-infrared remote sensing, (ii) thermal infrared remote sensing, and (iii) microwave remote sensing which includes both passive microwave remote sensing and active microwave RS. Table 2.3 summarizes the characteristics and advantages as well as the limitations of each category. For more information on the principles of estimating near-surface soil moisture from remote sensing data, advantages and limitations, the reader is directed to (Nichols et al., 2011; Wang & Qu, 2009; Wang & Zhang, 2005).

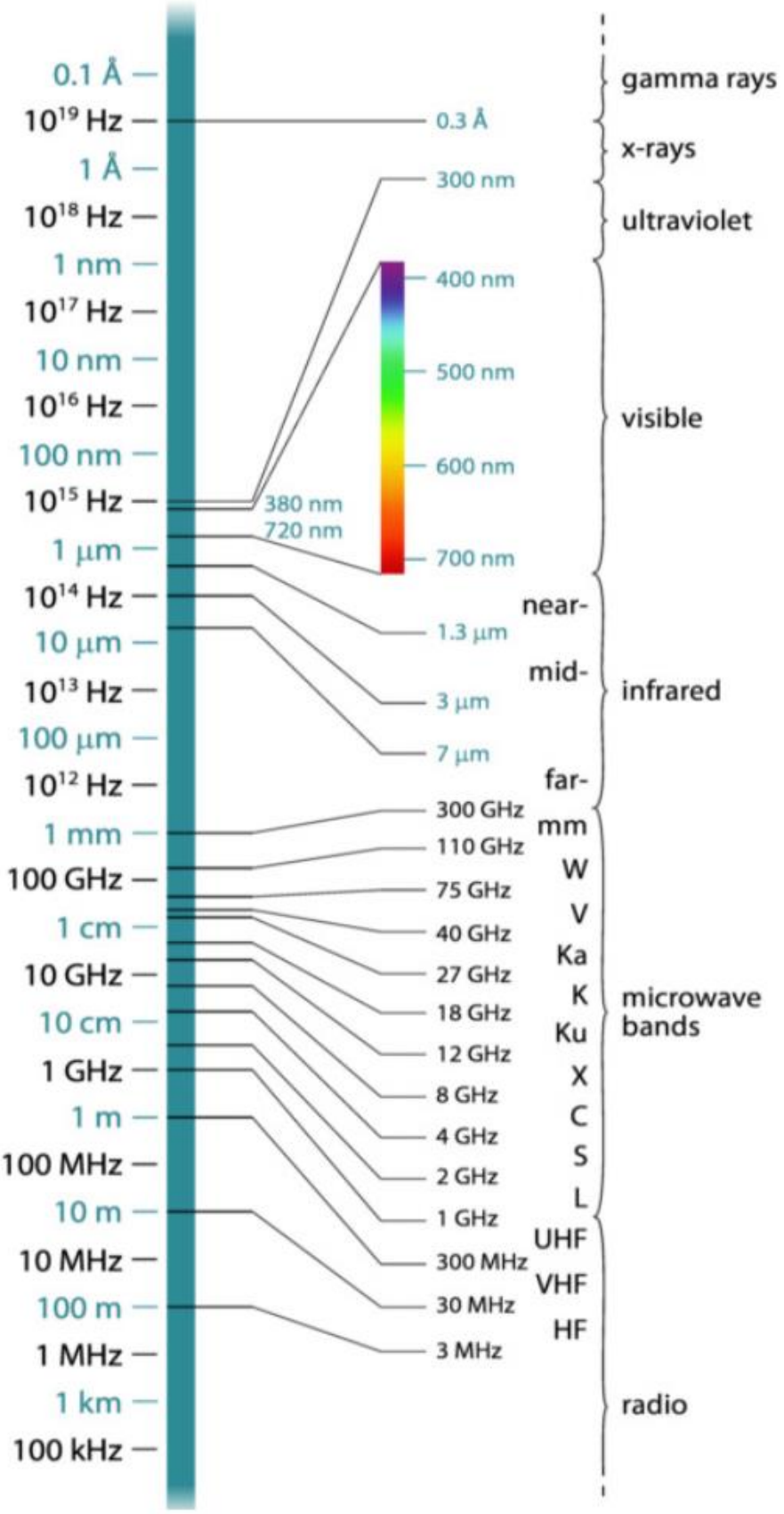

Fig. 2 - 5 *Electromagnetic spectrums (including the entire range of radiations, which are measured either as waves or frequencies) (From Bartalis et al., 2009).*

Table 2 - 3 Comparison of different remote sensing techniques. Adapted from Kong (2006).

Sensor type	Wavelengths	Property observed	Sensors	Advantages	Limitations
Visible	Red: 610 - 700 nm Orange: 590 - 610 nm Yellow: 570 - 590 nm Green: 500 - 570 nm Blue: 450 - 500 nm Indigo: 430 - 450 nm Violet: 400 - 430 nm	Soil albedo ; Index of refraction	NOAA AVHRR Landsat TM Terra MODIS Envisat MERIS AATSR SPOT	High /medium resolution.	Influenced by various factors: Cloud effects, soil texture, structure, illumination geometry, and atmospheric conditions.
Infrared	Near Infrared (NIR): 0.7 to 1.5 µm. Short Wavelength Infrared (SWIR): 1.5 to 3 µm. Mid Wavelength Infrared (MWIR): 3 to 8 µm. Long Wavelength Infrared (LWIR): 8 to 15 µm. Far Infrared (FIR): longer than 15 µm.	Surface temperature	GOES TIR NOAA AVHRR Terra MODIS Landsat TM Envisat AATSR	High /medium resolution Large swath Physics are well understood.	Influenced by Cloud effects, vegetation, topography, and meteorological conditions. Limited frequency of coverage;
Passive microwave	L band: 1 - 2 GHz (15 - 30 cm) S band: 2 - 4 GHz (7.5 - 15 cm) C band: 4 - 8 GHz (3.8 - 7.5 cm) X band: 8 - 12.5 GHz (2.4 - 3.8 cm) Ku band: 12.5 - 18 GHz (1.7 - 2.4 cm) K band: 18 - 26.5 GHz (1.1 - 1.7 cm) Ka band: 26.5 - 40 GHz (0.75 - 1.1 cm)	Brightness temperature; Dielectric properties; Soil temperature	SMMR SSM/I AMSR-E SMOS AMSR2 AQURIES WindSat SMAP	Penetrate cloud, rain, smoke and smog; Vegetation semi-transparent; Measurements are directly sensitive to	Low spatial resolution; Influenced by roughness, vegetation cover, and soil temperature.

Sensor type	Wavelengths	Property observed	Sensors	Advantages	Limitations
				changes in surface soil moisture; high temporal resolution; Low cloud and atmospheric noise. Detect only naturally occurring energy	
Active microwave	L band: 1 - 2 GHz (15 - 30 cm) S band: 2 - 4 GHz (7.5 - 15 cm) C band: 4 - 8 GHz (3.8 - 7.5 cm) X band: 8 - 12.5 GHz (2.4 - 3.8 cm) Ku band: 12.5 - 18 GHz (1.7 - 2.4 cm) K band: 18 - 26.5 GHz (1.1 - 1.7 cm) Ka band: 26.5 - 40 GHz (0.75 - 1.1 cm)	Backscatter coefficient; Dielectric properties; change detection	ERS1/ERS2 SAR Radarsat Envisat ASAR ASCAT	penetrate cloud, rain, smoke and smog; Vegetation semi-transparent; Independent of solar illumination; High spatial resolution; Low atmospheric noise. Act as their own energy source	Low temporal resolution More roughness and vegetation and topography effects than passive microwave sensors.

2.2.2.1 Optical remote sensing (Visible and near-infrared)

The visible/near-infrared remote sensing is mainly used to study land cover and vegetation at the present. Nevertheless, measurements of surface reflectance of radiation of the sun in the visible and near-infrared (from 350 nm to 800 nm) regions (Fig. 2.5) have been also used to retrieve surface soil moisture (Gillies et al., 1997; Kaleita et al., 2005; Whiting et al., 2004). The basic principle is that it was found that the reflectance at visible and infrared wavelengths increased as the moisture content decreased (wet soils are darker in color on the image than dry soils and reflectance values are generally low for wet surfaces and high for dry surfaces)(Kaleita et al., 2005; Planet, 1970; Weidong et al., 2002). Nevertheless, retrieving soil moisture from these data has some limitations and difficulties, as the reflectance of a soil is not just a function of soil moisture but is strongly influenced by other soil factors (e.g., amount of organic matter, surface roughness, angle of incidence, color of soil elements, texture, and mineral composition) (Gascoin et al., 2009a; Gascoin et al., 2009b; Muller & Decamps, 2001). In addition optical sensors can only be used to monitor soil moisture over bare soil, due to the low penetration depth of the signal through clouds. There are two independent problems: (i) clouds and (ii) bare soil only as vegetation reflects light before the soil does.

2.2.2.2 Thermal Infrared remote sensing

Thermal infrared remote sensing, operating in a wavelength region of approximately 3 to 14 μm (Fig. 2.5), measures the soil surface temperature which could be used to infer near-surface soil moisture content (Curran, 1985; Hain et al., 2009; Rahimzadeh-Bajgiran et al., 2013). Several researchers found that land surface temperature, in the thermal infrared, is strongly dependent on the soil moisture as areas having higher soil moisture content are cooler during the day and warmer at night (Hain et al., 2009; van de Griend & Engman,

1985), because cooler areas are the ones that evaporated more, and evaporation is water limited. Earlier studies have shown that the amplitude of the diurnal range of soil surface temperature has been found to have a good correlation with the near-surface soil moisture (Schmugge et al., 1980). Limitations to this type of measurement are due to effects of cloud cover, soil types, and vegetation and meteorological factors (Wetzel & Woodward, 1986).

2.2.2.3 Microwave remote sensing

Microwave remote sensing systems use electromagnetic radiation in the frequency range of about 0.3 to 30 GHz, with wavelengths of about 1mm to 1m (Fig. 2.5). Satellites operating in the microwave domain have unique capabilities, over the higher frequencies, such as atmosphere transparency, cloud penetration, day and night capability (independency of solar illumination), vegetation semi-transparency, strong dependency on the dielectric properties of the soil (which is a function of the soil moisture), and soil penetration (to a certain extent) (Schmugge et al., 2002; Ulaby et al., 1981). The microwave remote sensing is categorized into active and passive systems (see Fig. 2.6). Active sensors emit electromagnetic pulses and measure the radiation back-scattered from the surface, whereas passive systems (radiometers) record the natural radiation of the earth's surface. Fig. 2.6 illustrates the differences between passive and active microwave remote sensing.

Although active and passive systems have different recording techniques, there is a close connection using Kirchhoff's law of thermal radiation, which states that the emissivity of a body is equal to its absorptivity under thermodynamic equilibrium (Schanda, 1986).

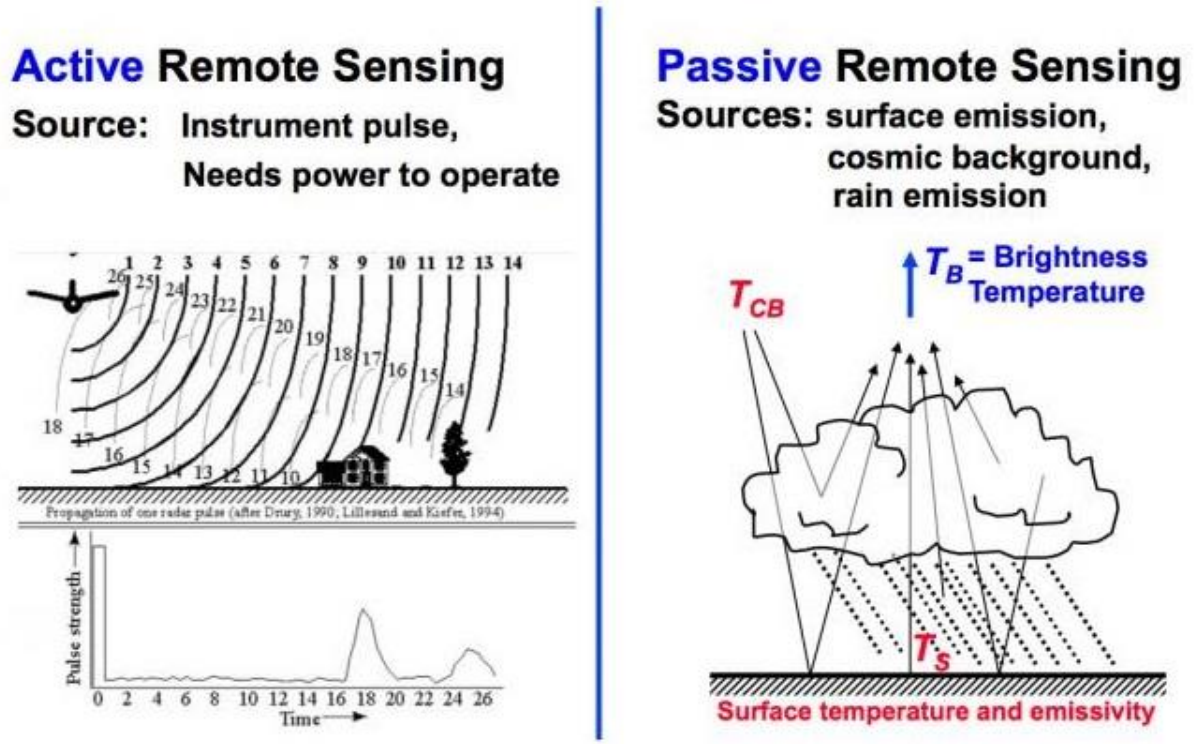

Fig. 2 - 6 *Scheme of active and passive microwave remote sensing principles. Source: [http://pmm.nasa.gov/node/345].*

Passive microwave sensors do not directly measure the soil moisture but brightness temperatures (TB), which allows for retrieving bio-geophysical variables including the soil moisture. TB for a non-black body can be computed using the inverse of Planck function:

$$TB = \frac{D_2}{\lambda \, ln[1 + \frac{D_1}{\lambda^5 I_\lambda}]} \qquad 2-4$$

where:

D_1 = 1.1911x10^8 [W m^{-2} sr^{-1} μm^5],

D_2 = 1.4388x104 [K μm],

I_λ is the measured intensity (radiance) [W m^{-2} sr^{-1}], and

λ is the s the wavelength [μm].

It should be noted that TB, in the infrared domain, is equal to kinetic temperature for a black body but for a natural material:

$$TB^4 = e_p T^4 \qquad 2-5$$

where the emissivity (e_p) is a dimensionless value (0 < e <1) and a function of a number of factors.

Planck function in the microwave domain can be further simplified using the Rayleigh –Jeans approximation, which gives:

$$TB = e_p T \qquad 2-6$$

The emissivity of a soil varies greatly according to its water content, which can be described as (Njoku & Li, 1999):

$$e_p = 1 - r_{sp} \qquad 2-7$$

where r_{sp} is the surface reflectivity, which can be computed for smooth soil using Fresnel laws (Njoku & Li, 1999). The Fresnel reflection coefficients r_{bH} and r_{bV} at horizontal (H) and vertical (V) polarizations, respectively, can be written as:

$$r_{sH}(\theta) = \left| \frac{\cos(\theta) - \sqrt{\mu_s \varepsilon_b - sin^2(\theta)}}{\cos(\theta) + \sqrt{\mu_s \varepsilon_b - sin^2(\theta)}} \right|^2 \qquad 2-8$$

$$r_{sV}(\theta) = \left| \frac{\varepsilon_b \cos(\theta) - \sqrt{\mu_s \varepsilon_b - sin^2(\theta)}}{\varepsilon_b \cos(\theta) + \sqrt{\mu_s \varepsilon_b - sin^2(\theta)}} \right|^2 \qquad 2-9$$

where

ε_b is the complex soil dielectric constant,

θ is the incidence angle, and

b subscript stands for bare soil.

The basic concept for retrieving surface soil moisture from passive measurements is based on the large contrast of the dielectric constant values of the soil, which is ~4 for dry soil, ~80 for water, and from ~4 to ~40 for soil-water mixtures in the microwave region (Njoku & Entekhabi, 1996; Schmugge et al., 1986). The dielectric constant is an electrical property of the material which is a measure of the response of a medium to an applied electric

field. It is a complex number, consisting of a real part (determines the propagation characteristics of the passed energy into the soil) and an imaginary part (determines the energy loose) (Schmugge et al., 1986). In an inhomogeneous medium, such as the soil, the complex dielectric constant is a combination of the individual dielectric constants of its components (air, water, and stone). Fig. 2.7 illustrates the relationship between the dielectric constant of the soil and water content, which is almost linear.

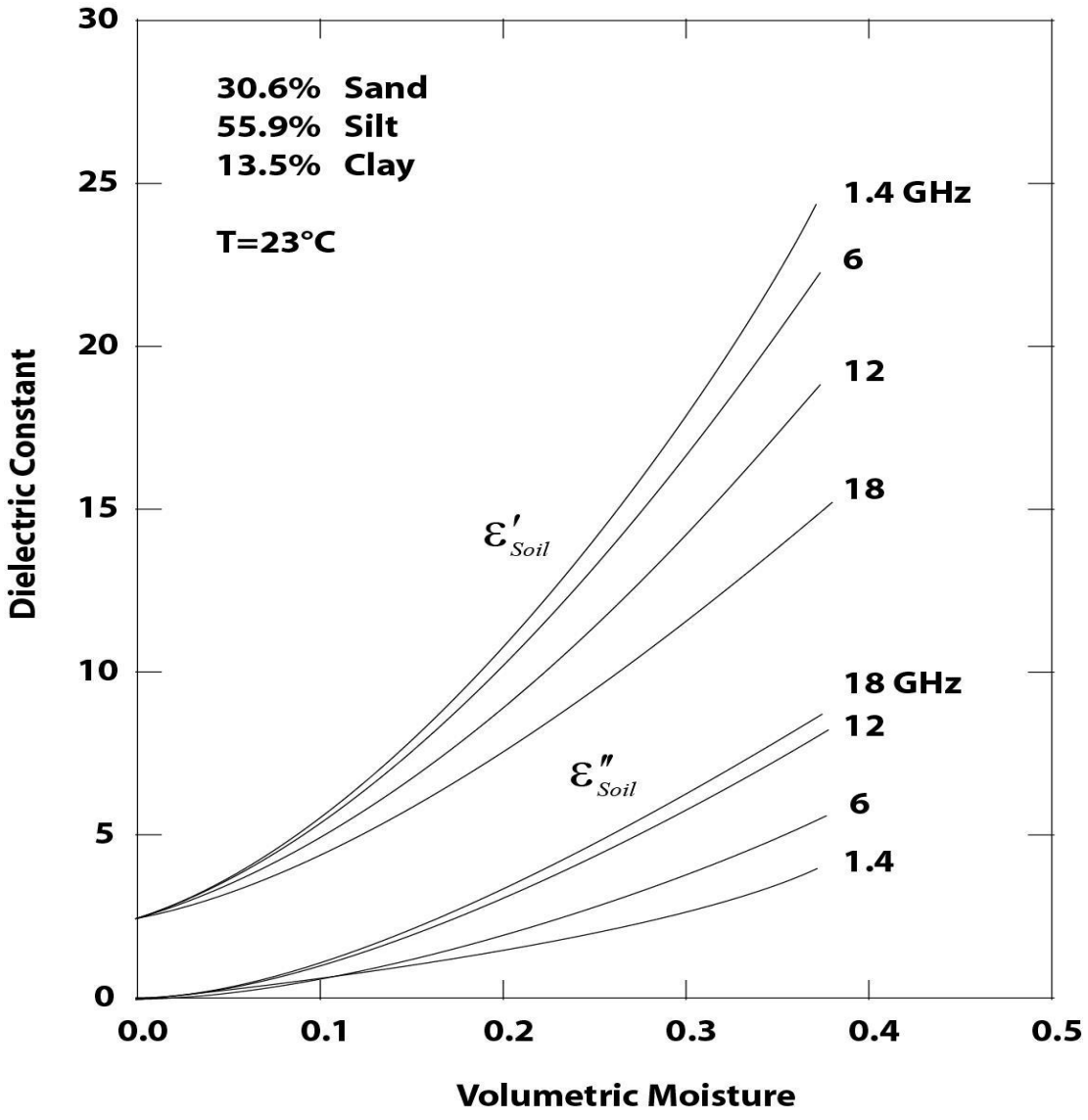

Fig. 2 - 7 *Relationship between The real ε′ and imaginary ε′′ components of the dielectric coefficient for different types of soils and soil moisture (Ulaby et al., 1986).*

The dielectric constant can be measured in the ground using Capacitance or Time-domain reflectometer (TDR) probes. However, these probes are expensive and require

specific and careful calibrations (Dobriyal et al., 2012). Alternatively, several dielectric models have been developed to calculate the dielectric constant such as: semi-empirical model (Dobson et al., 1985; Peplinski et al., 1995), the Wang & Schmugge empirical mixing model (Wang & Schmugge, 1980), and more recently the semi-physical model (Mironov et al., 2012), which is formally known as the Mineralogy-Based Soil Dielectric Model (MBSDM). It should be noted that all these models depend on frequency, soil texture, and soil moisture though they differ in analytical forms. Readers are directed to (Mironov et al., 2009) for more details about the description of these different models.

Similarly, active sensors do not directly measure the soil moisture but the radar scattering cross section (σ), measured in m^2, from the surface which is mainly influenced by the soil moisture. The radar scattering cross section is a function of the angle of incidence, the frequency of operation, polarization, electrical properties of soil (e.g., dielectric constant and conductivity), and the physical properties (e.g., texture, surface type, etc.). The radar scattering cross section is given by the general radar equation (e.g. Ulaby et al., 1981):

$$\sigma = \frac{(4\pi)^3 R^4 P_r}{G^2 \lambda^2 P_t} \qquad 2-10$$

where:

P_r is the received power at receiver [W],

P_t is the transmitted power [W],

λ is the wavelength [m],

R is the range or distance of target [m], and

G is the antenna power gain [-].

There are several active (ASCAT, etc.) and passive (SMOS, AMSR-E, etc.) microwave sensors, as already mentioned in the Introduction, that have been used to observe the Earth emissions and backscatter from various targets for several decades. However,

several factors affect the sensitivity of these microwave sensors to soil moisture, that should be accounted for when retrieving soil moisture from microwave observations, including (Choudhury et al., 1979; Choudhury, 1993; Ferrazzoli et al., 1992; Njoku & Entekhabi, 1996; Njoku & Li, 1999; Schmugge et al., 1986; Schmugge, 1985; Ulaby et al., 1986; Wang et al., 1983; Wigneron et al., 1993; Wigneron et al., 1998):

- Microwave sensors have different soil penetration capabilities which depend on the frequency used. The performance of microwave sensors operating at low frequencies is less affected by the atmospheric effects. The frequencies above 30 GHz, for instance, are strongly affected by water clouds, whereas the effects are negligible for frequencies below 15 GHz. Also, the effect of intense rain is more pronounced for frequencies above 10 GHz (Ulaby et al., 1981).
- The penetration depth in the surface is strongly related to the frequency/ wavelength. Microwave sensors operating at longer wavelengths penetrate deeper in the soil surface and/or vegetation canopy. Therefore, the C ($\lambda \sim 3.8$ - 7.5 cm) and L-band ($\lambda \sim$ 15 - 30 cm) are commonly used for sensing soil moisture but L-band is more preferred as the sampling depth is larger, ~ 3 cm (Escorihuela et al., 2010).
- The signal of microwave sensors is also influenced by the incidence angle; it becomes less sensitive to soil moisture when the incidence angle increases. At lower incidence angles, the attenuation of vegetation and the effect of surface roughness are minimized. Therefore, lower incidence angles are optimal for sensing soil moisture (Ulaby et al., 1986).
- Active and passive microwave sensors measure the backscatter and surface's emission, respectively, using different polarizations. Active sensors can measure backscatter in HH, VV, HV, and VH polarizations, whereas passive sensors measure

the emission in V or H polarizations. The vertical polarization signal is less sensitive to the soil moisture than horizontal polarization (Njoku & Li, 1999).

- The surface roughness, which is a measure of the irregularities of the surface geometry, has a significant effect on the variation of backscatter and TB, as it increases the surface area. Passive microwave sensors are, in most cases, less sensitive to surface roughness than active microwave sensors (Schmugge, 1985). However, a recent study found that the sensitivity of the passive observations to surface roughness was relatively similar for all the frequencies i.e. 1.4, 10.65, 23.8, 36.5, and 90 GHz (Montpetit et al., 2014).
- Vegetation cover attenuates the soil emission and its influence increases as the frequency increases (Ferrazzoli et al., 1992; Wigneron et al., 1993).
- Other factors such as the soil temperature (Raju et al., 1995), topography (Mialon et al., 2008), soil texture (Mironov et al., 2012), have a small influence on the microwave observations but should be taken into consideration (Njoku & Entekhabi, 1996).

It can be summarized that the negative effects of these factors, generally, increase with increasing frequency (Njoku & Entekhabi, 1996) within the microwave domain. Besides, atmosphere and ground penetration is deeper at lower frequencies. This makes the observations at low-frequency bands (1-3 GHz i.e. ~30-10 cm wavelength) more optimal for sensing soil moisture (Kerr et al., 2001; Njoku & Entekhabi, 1996; Schmugge et al., 1986).

Table 2.4 shows passive sensor frequency allocations. Some of the passive sensors, such as the AMSR-E, operate in unprotected frequency bands i.e., 6.925 GHz (C-band), 10.65 GHz (X-band), and 18.7 GHz (K-band) which are used also in satellite communications, whereas other passive sensors, such as the SMOS and SMAP, operate in protected bands i.e. 1.4 GHz (L-band).

Table 2 - 4 Passive sensor frequency allocations (GHz). Adapted from Ulaby et al. (1981).

Protected for radio astronomy - no transmitters allowed	**Shared primary use for services having transmitters**	**Shared secondary use for services having transmitters**
0.404-0.406	1.6605-1.6684	1.370-1.400
1.400-1.427	2.690-2.700	2.640-2.600
10.68-10.70	10.60-10.68	4.2-4.4
15.35-15.40	21.2-21.4	4.80-4.99
23.6-24.0	31.5-31.8	6.425-7.250
31.3-31.5	36- 37	15.20-15.35
89.92	50.2-50.4	18.6-18.8
-	-	22.21-22.5

2.2.3 Soil moisture modelling

In order to overcome the limitations of ground based measurement, several dynamic models can be used to predict and model the spatio-temporal variations of soil moisture over large areas. Models have the advantage, in comparison to in situ, that they can provide soil moisture in different spatial and temporal resolutions from local to global and from hours to days, respectively. Notwithstanding, models require knowledge of other estimated or measured parameters and have a disadvantage of requiring several dynamic and statics inputs (e.g., a digital terrain model, soil type, soil texture, land cover, climate forcings, etc.), due to the complexity of the hydrologic cycle and the heterogeneity of the land surface. Consequently, models vary in the level of complexity of details they use in representing the physical system, temporal and spatial scales, variation of the driving forces, and the number of soil layers used (Schmugge et al., 1980).

All above dynamic models predict soil moisture among other components of the water cycle such as runoff, rainfall, and evapotranspiration. This is true for hydrological models (e.g. TOPMODEL, a TOPography based hydrological MODEL (Beven & Kirkby, 1979)), and land surface models (LSMs), whether used alone or within weather or climate models. Among the various state-of-the-art LSMs, one finds: the Interactions Soil-Biosphere-Atmosphere (ISBA; (Noilhan & Planton, 1989)), ORCHIDEE (Organizing Carbon and Hydrology In Dynamic Ecosystems) (de Rosnay & Polcher, 1998; Krinner et al., 2005), MERRA-Land (NASA's Modern-Era Retrospective Analysis for Research and Applications) (Reichle et al., 2011), HTESSEL (Hydrology Tiled ECMWF Scheme for Surface Exchange over Land (Balsamo et al., 2009), etc. Note that the Global Soil Wetness Project (GSWP-2) (Dirmeyer et al., 2002) is aiming at producing a global soil moisture datasets from a multi-land surface models ensemble to serve as a benchmark production. Readers are directed to (Pitman, 2003; Singh & Woolhiser, 2002) for a detailed review of land surface and distributed hydrological models, as this topic is beyond the scope of this doctoral dissertation.

As stated before, soil moisture plays a major role in the water cycle by influencing the soil-vegetation-atmosphere interactions through influencing water and energy exchanges. It can be said that the two fundamental equations for soil moisture modelling are represented by the water and energy balance equations as follows:

The water balance is commonly expressed as follows (Dingman, 2002; Schmugge et al., 2002):

$$\frac{\Delta S}{\Delta t} = P - ET - Q \qquad 2-11$$

where the variables are expressed as volume of water per unit system area per unit time:

S is soil water or soil moisture [L],

t is time [T] (e.g. h, day),

Δt is the time step,

P is the precipitation [L/T],

$\Delta S/\Delta t$ is the change in storage in the soil [L/T],

ET is the evapotranspiration [L/T], and

Q is the runoff [L^3/T].

The energy balance is commonly expressed as follows (Schmugge et al., 2002):

$$R_n - G = H + LE \qquad 2-12$$

Where:

R_n is the net radiation [W/m^2],

G is the soil heat flux [W/m^2],

H is the sensible heat flux [W/m^2], and

LE is the latent heat flux [W/m^2].

The quantity R_n-*G* is the available energy for the turbulent fluxes (LE and H).

In hydrological models, *ET* is often expressed as a depth of water over daily (mm/day) or longer time scales (Schmugge et al., 2002). It is often deduced from the so-called "reference evapotranspiration", ET0, which corresponds to ET from a well-watered "reference" grass (uniform short grass of 0.12 m, with a fixed surface resistance of 70 s m^{-1} and an albedo of 0.23), that would not suffer from any water stress, thus evaporate at its potential rate. In this framework, actual ET (AET), i.e. the amount of ET that actually occurs when the water is limited (Ward & Trimble, 2004), can be deduced from a water stress factor multiplied to potential ET (PET), which can itself be deduced from ET0 by means of a crop coefficient, accounting for the differences in PET between the reference grass and the selected vegetation/crop. The Penman-Monteith equation (Monteith, 1965), as proposed by the FAO

(United Nations Food and Agricultural Organization), has been widely used to calculate ET0 , using readily available meteorological data (Allen, 1998):

$$ET_0 = \frac{0.408\Delta(R_n - G) + [\gamma u\,(e_a - e_d)\frac{900}{T+273}]}{\Delta + \gamma(1 + 0.43u)} \qquad 2-13$$

Where ET_0 is evaporation (kg/m^2/d), G is soil heat flux (MJ/m^2/d), R_n is the net radiation flux density at the surface (MJ/m^2/d), $c_p$is the specific heat of moist air, $e_a$is the saturation vapour pressure of the air (kPa), e_d is the mean actual vapour pressure of the air (kPa), $(e_a - e_d)$ is the vapour pressure deficit of the air, u is wind speed at 2 m height (m/s), Δ is the slope of the saturation vapor pressure curve, γ is the psychometric constant (kPa°C^{-1}), and ρ is the atmospheric density (kg/m^3). Basically, the Penman-Monteith approach is a way to implicitly use the energy budget without explicitly solving it. It is used in most hydrological models, including TOPMODEL (Beven & Kirkby, 1979).

In contrast, LSMs use the energy budget equation and diffusive equations to calculate E and H (Barella-Ortiz et al., 2013). LSMs use turbulent diffusive equations because of high time step required to solve it jointly with the surface energy budget, which needs to be small enough (typically half-hourly) to account for the pronounced diurnal cycle of the involved energy fluxes. A diffusive equation was introduced by Budyko (1956) to estimate PET:

$$PET = \frac{\rho}{r_a}[q_s T_w - q_a] \qquad 2-14$$

where:

ρ is the air density,

r_a is the aerodynamic resistance,

q_s is the saturated specific humidity,

T_w is the virtual temperature, and

q_a is the specific humidity of the air.

2.2.3.1 MERRA-Land

MERRA-Land is an enhanced product to the hydrological fields in the NASA MERRA atmospheric reanalysis (Reichle et al., 2011). MERRA uses Version 5.2.0 of the Goddard Earth Observing System model (GEOS-5) and its associated data assimilation system, covering the period 1979-present period (Rienecker et al., 2011). The reader is directed to Rienecker et al. (2011) for more details on MERRA reanalysis and products, which can be obtained from the M-DISC (http://disc.sci.gsfc.nasa.gov/mdisc/) (Reichle, 2012).

MERRA-Land, which is a land-only ("off-line"), introduced some enhancements to MERRA including (Reichle et al., 2011): (ii) enhancing the MERRA-Land precipitation forcing by merging MERRA precipitation with a gauge-based data product from the NOAA Climate Prediction Center and (ii) updating the catchment land surface model by using the "Fortuna-2.5" version instead of the "MERRA" version. These two changes were evaluated by Reichle et al. (2011) and was found that these changes improved the quality model in various ways.

Other characteristics of MERRA-Land data include (Reichle, 2012): (i) this product can be freely obtained from the Goddard Earth Sciences (GES) Data and Information Services Center (DISC) (ii) this product is provided as hourly averages (iii) this product is described as a simulation product and there is no assimilation of model state variables (such as soil moisture or snow) (iv) Leaf area index and greenness in this product are prescribed as a monthly climatology based on AVHRR (Advanced Very High Resolution Radiometer) observations, and (v) this product is provided with a horizontal resolution of 1/2° latitude by 2/3° longitude. This is the same as in the standard MERRA product (Reichle, 2012).

Fig. 2.8 displays the surface below each atmospheric column in GEOS-5 which consists of a set of tiles: Ocean, Land, (land) Ice, or Lake. A catchment model is used to

simulate these sub-tile fractions, which vary with time (Reichle, 2012). For further details on the catchment model, the readers are directed to (Ducharne et al., 2000; Koster et al., 2000).

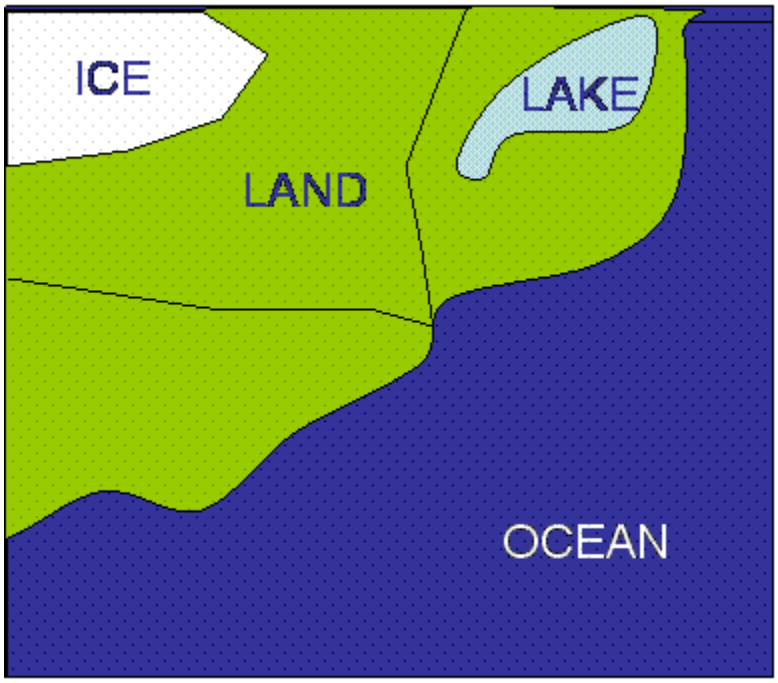

Fig. 2 - 8 *Land surface representation in GEOS-5. Adapted from (Reichle, 2012)*

The land surface water balance equation is described, in GEOS-5, as follows (Reichle, 2012)

$$\frac{\partial W}{\partial t} = P_l + P_s - E_l - R_l + R_w \qquad 2-15$$

where:

W is the total water held in all land surface reservoirs (comprising the soil, the interception reservoir, and the snowpack),

P_l the liquid rain,

Ps "snowfall" rates,

E_l is the total evapotranspiration rate,

R_l is the total runoff–surface (or overland) plus baseflow, and

R_w is a spurious water source

The balance equation for total land surface energy is described, in GEOS-5, as follows (Reichle, 2012):

$$\frac{\partial \varepsilon}{\partial t} = SW_l + LW_l - SH_l - L_v E_l - L_f \Delta SWE + R_l \qquad 2-16$$

where:

ε is the total heat content (in the soil, canopy, and snowpack) relative to liquid water

SW_l is the net shortwave radiation,

LW_l is the net long wave radiation,

L_v is the latent heat of vaporization (from liquid),

E_l is the total evaporation from the land surface,

SH_l is the sensible heat flux from the land surface,

L_f is the latent heat of fusion,

R_l is the spurious snow energy source, and

ΔSWE is the change in the snow water equivalent.

2.2.4 Soil moisture data assimilation

Forecasts (predictions) are made using numerical models, and different models are used depending on the target forecasted variables. Forecast of state variables can be improved by optimally integrating model predictions with observations through data assimilation techniques. Soil moisture data assimilation has been applied in hydrology since the eighties and with a recent rapid progress thanks to remote sensing (Ni-Meister, 2008). The recent availability of surface soil moisture from remote sensing enables, for instance, hydrologists to obtain more accurate values of the root zone soil moisture through data assimilation of remotely sensed near-surface soil moisture into land surface models (Draper et al., 2009b; Draper et al., 2012; Hoeben & Troch, 2000; Reichle et al., 2007; Scipal et al., 2008).

There are several data assimilation techniques in soil moisture fields: (i) the Kalman Filter (Crosson et al., 2002; Walker et al., 2001), (ii) direct insertion method (Heathman et al., 2003; Walker et al., 2001), (iii) extended Kalman Filter (Reichle et al., 2002a), and (iv) Ensemble Kalman Filter (Reichle et al., 2002b). The Ensemble Kalman Filter (EnKF) is the most widely used due to its strength in handling non-linear systems and computational efficiency (Crow & Wood, 2003). More recently, satellite-based active microwave near-surface soil moisture observations (0-2 cm) from the ASCAT have been integrated with land surface models (ECMWF) through land data assimilation system and produced SM-DAS-2 soil moisture product (de Rosnay et al., 2013). This recent later product was used in this doctoral dissertation as a benchmark and it is briefly described in Chapter IV.

2.2.4.1 SM-DAS-2

SM-DAS-2 is a near real time (NRT) root zone soil moisture index generated by assimilating the ASCAT surface soil moisture index in the improved, Hydrologically, ECMWF HTESSEL (Tiled ECMWF Scheme for Surface Exchanges over Land, Balsamo et al., 2009) land surface model (PUM, 2012). SM-DAS-2 soil moisture product is assimilation product produced based on a simplified Extended Kalman Filter (EKF) to propagate the ASCAT surface soil moisture index observation towards the root region down to 2.89 m below surface (PUM, 2012). Fig. 2-9 shows SM-DAS-2 production chain based on the ECMWF HTESSEL land surface model.

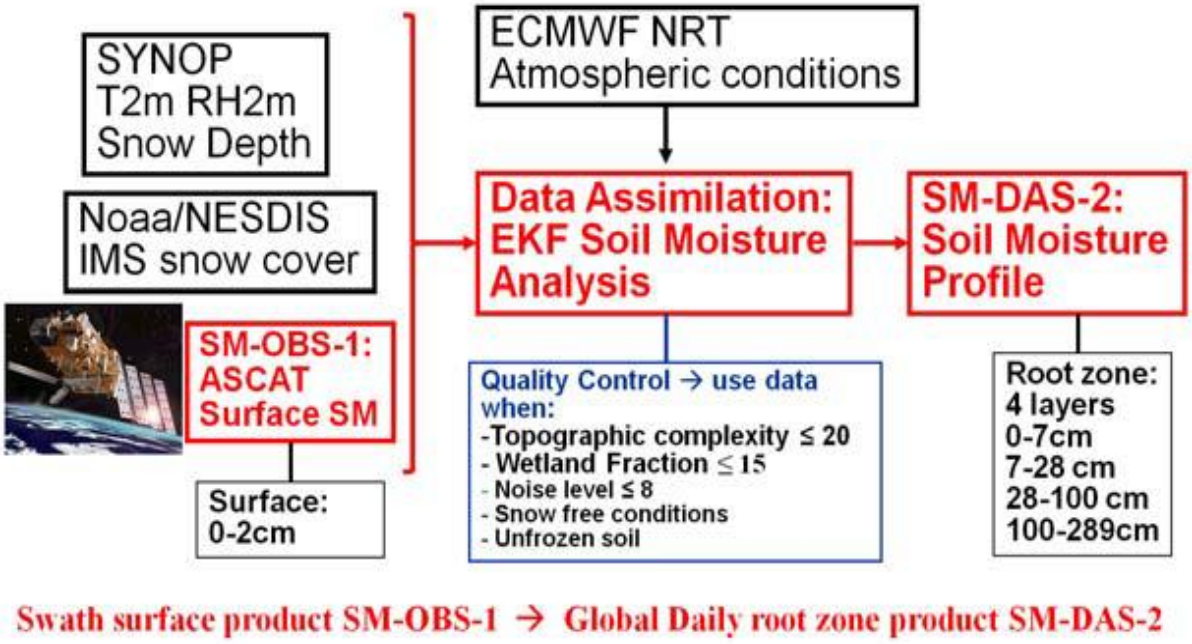

Fig. 2 - 9 *SM-DAS-2 production chain. Adapted from* (PUM, 2012).

The scheme of the last version of HTESSEL is displayed in Fig 2-10. The HTESSEL has six tiles over land (low and high vegetation, bare ground, shaded and exposed snow, and intercepted water), two over water (open and frozen water), and four layers (from top to down: 0.07, 0.21, 0.72 and 1.89 m) for each grid cell with separate energy and water balances (PUM, 2012). HTESSEL recently accounts for vegetation seasonal cycle described by Leaf Area Index (LAI) monthly climatology data sets, and recently considered improved bare soil evaporation parameterization (Balsamo et al., 2011). The vegetation information and LAI climatology is based on the Global Land Cover Characteristics (GLCC) and MODIS datasets, respectively (de Rosnay et al., 2013). Richards's equation and Darcy's law are used to compute the vertical movement of water in the unsaturated zone. The dominant soil texture class for each grid point is adopted by HTESSEL and taken from the FAO (FAO, 2003) available at a resolution of 5'x5' (about 10 km) (de Rosnay et al., 2013).

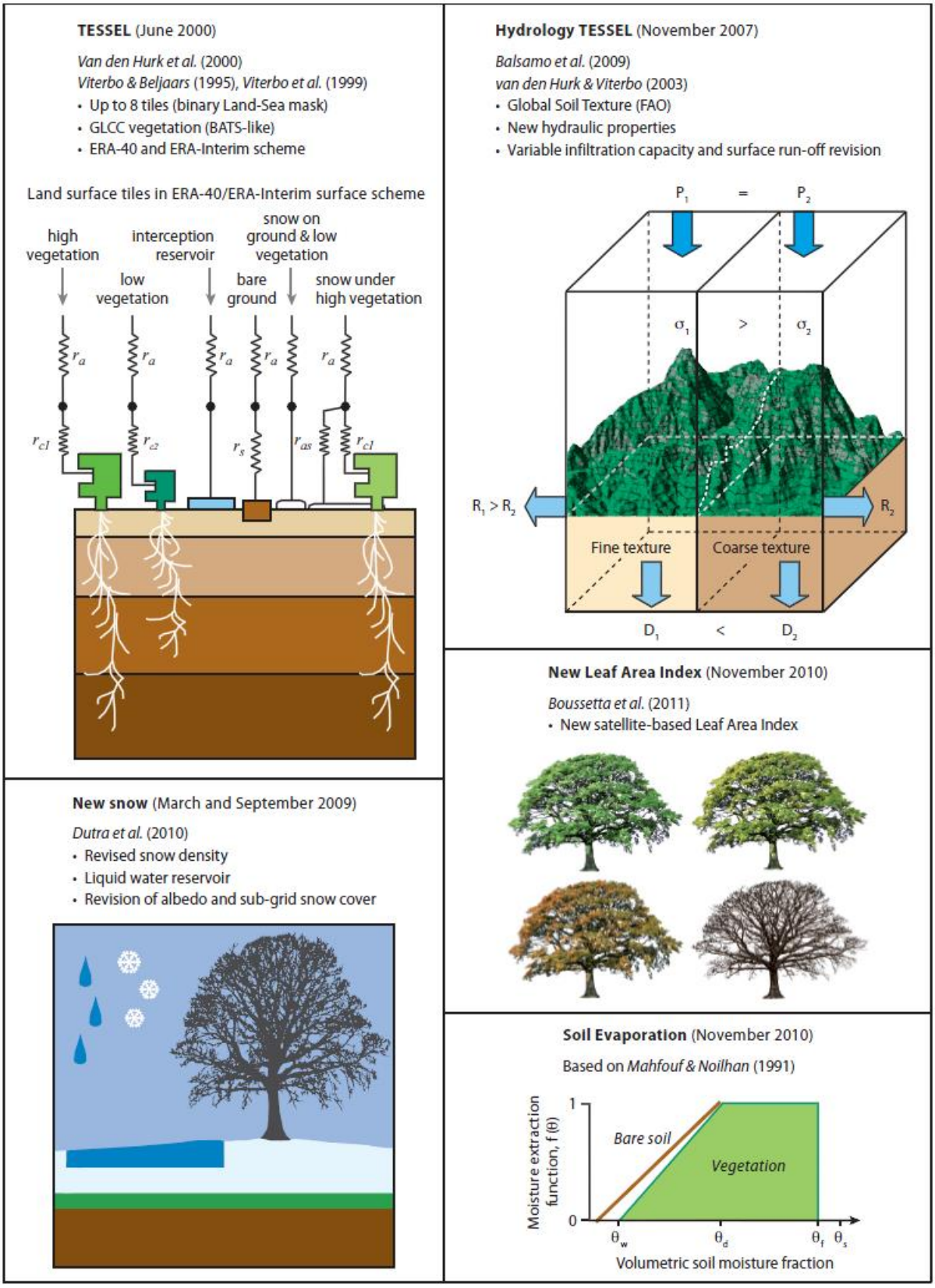

Fig. 2 - 10 *The scheme of HTESSEL and the recent revisions in the land surface model. Adapted from (Balsamo et al., 2011)*

For each tile the energy balance, in HTESSEL, is calculated separately as follows (Wipfler et al., 2011):

$$(1-\alpha i)R_s\downarrow+\downarrow R_l - R_l\uparrow - G_i = H_i + \lambda E_i \qquad 2-17$$

where:

R*s* is the flux density of short wave (W/m^2)

R*l* is the flux density long wave radiation (W/m^2), the arrows refer to incoming (↓) and outgoing (↑) flux densities,

αi is albedo,

H*i* is the sensible flux density of tile I (W/m^2)

λE*i* is the latent flux density of tile I (W/m^2)

G*i* is the soil heat flux density of tile I (W/m^2) ,

λ is the specific latent heat of vaporization (J/kg), and

E is the mass flux density of evaporation (kg /m^2/s).

The water balance (mm/d) at the land surface, in HTESSEL, is calculated as follows (Wipfler et al., 2011):

$$\Delta W + \Delta S = P - E - R \qquad 2-18$$

where:

ΔW is the change in water storage of the soil moisture and interception reservoir,

ΔS is the change in accumulated snowpack,

P is the precipitation,

E is the evaporation of soil, vegetation and intercepted water,

R is the surface and subsurface runoff.

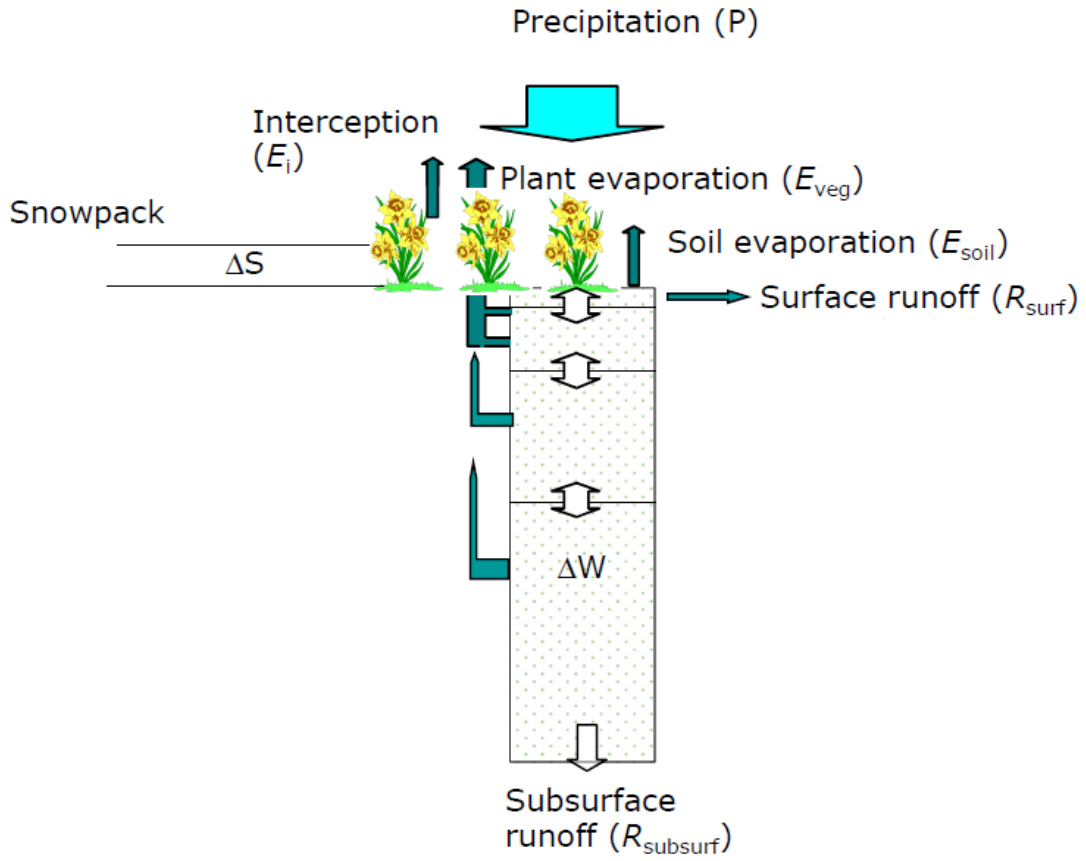

Fig. 2 - 11 *Water balance representation in HTESSEL. Adapted from (Wipfler et al., 2011).*

SM-DAS-2 soil moisture datasets were validated against soil moisture measurements from in situ data from more than 200 stations across four continents (PUM, 2012). Albergel et al. (2012) gathered ground-based soil moisture measurements from 295 stations (France, Spain, Germany, Italy, Denmark, Luxembourg, Finland, Poland, Australia, the United States, and Western Africa), for the year 2010. Albergel et al. (2012) compared SM-DAS-2 product with these in situ datasets along with SMOS and ASCAT soil moisture products and found that SM-DAS-2 was closer to the in situ datasets, in terms of correlation, than the other datasets.

Other characteristics of SM-DAS-2 include: (i) this product is available at a 24-hour time step (ii) this product has a horizontal resolution of ~ 25 km (a Gaussian reduced grid at

T799), (iii) this product is available online on ftp://ftp.meteoam.it, (iv) this product is provided either as digital data (GRIB1 format) or images (PNG format) (PUM, 2012).

Chapter III

3. SMOS/ASCAT/AMSR-E Mission overview

This chapter gives an overview on the current state of the art in the SMOS, as well as shortly ASCAT and AMSR-E, mission. It also describes shortly the basics of surface soil moisture (SSM) retrievals from these sensors and the types of existing SSM products. The main characteristics of SMOS, ASCAT, and AMSR-E missions and their SSM products are listed in Table 3.3 at the end of this chapter.

3.1 SMOS

3.1.1 SMOS mission overview

The SMOS mission (see SMOS satellite in orbit in Fig. 3.1), known as the European Space Agency (ESA's) water mission, was proposed by the CESBIO (Centre d'Etudes Spatiales de la BIOsphère) – CNES (Centre national d'études spatiales) in 1993 and then to ESA in 1999 as a response to the needs of weather and climate modelling, where surface soil moisture (SSM) is involved in the water cycle. The ESA collaborated with the CNES and CDTI (the Centre for the Development of Industrial Technology) in Spain to conduct the SMOS satellite as part of its Living Planet program as the second of seven Earth Explorer missions (Kerr et al., 2001; Kerr et al., 2010). The SMOS satellite was launched in November 2009 by a Rocket launcher in Northern Russia at 01:50 UTC. It is the first ever passive satellite specifically dedicated to monitor two geophysical variables (ocean salinity and soil moisture) at the global scale (Kerr et al., 2001; Kerr et al., 2010). The SMOS satellite has a revisit frequency of ~ three days and has two overpass times, from South Pole to North Pole (the so-called ascending) at 06:00 local time and from North Pole to South Pole (the so-called descending) at 18:00, displayed in Fig. 3.1. The SMOS satellite measures the Earth's emissions (brightness temperatures) that originate from the top 5 cm of soil at L-band (1.4 GHz). L-band provides the best sensitivity to variations in surface soil moisture (SSM) and ocean salinity contents as it is not much sensitive to perturbing factors from weather, atmosphere, and vegetation (Kerr et al., 2001; Njoku & Entekhabi, 1996; Pellarin et al., 2003).

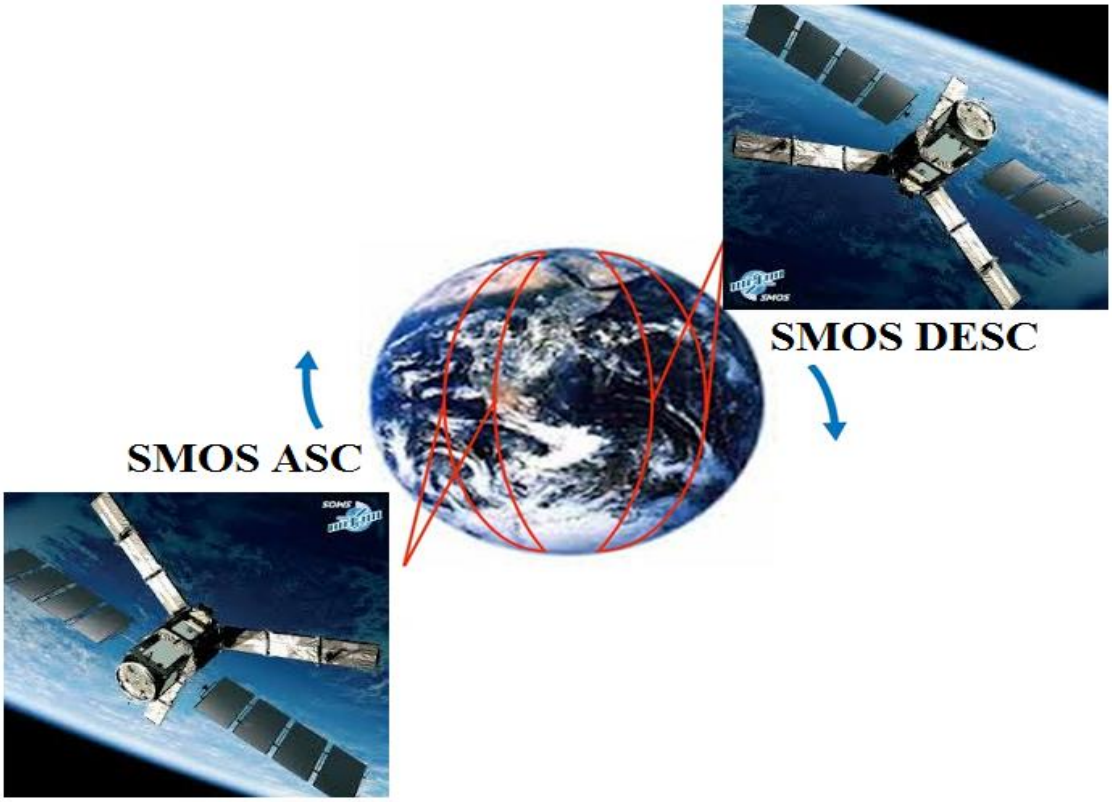

Fig. 3 - 1 *SMOS satellite with ascending (ASC) and descending (DESC) orbits. Source: [www.esa.int].*

The SMOS mission has two primary objectives (Kerr et al., 2001; Kerr et al., 2010):

(i) To accurately provide space-borne brightness temperatures (TB) observations from which global maps of SSM and Sea Surface Salinity (SSS) can be retrieved, which in turn enhance the understanding of climate change, improve weather forecasts, and make better hydrological models predictions, and

(ii) To contribute to cryosphere studies by providing observations over snow and ice regions and improving snow mantle monitoring and multilayer ice structure.

A unique aspect of this mission is that the SMOS satellite carries a novel and innovative payload adopting a completely different approach in the field of remote sensing.

This technique is based on a new passive instrument which is capable of recording TB at 1.40-1.427 GHz frequencies (L-band) in two polarizations (H & V) and multi-angular angles (McMullan et al., 2008). This new instrument is called the Microwave Imaging Radiometer by Aperture Synthesis (MIRAS), which is a two-dimensional passive microwave interferometry radiometer (McMullan et al., 2008), see Fig. 3.2. To achieve an adequate spatial resolution for passive imaging from space by SMOS at L band (= 21 cm), large rotating antenna (several meters) is required. However, it will be too big to be carried by a satellite and costly, therefore it is a major challenge. To overcome this problem, antenna apertures for which thinned arrays using synthetic aperture principles were adopted for SMOS mission (Kerr et al., 2001).

The main characteristics and features of MIRAS, which has a Y-shaped deployable structure, are listed below (McMullan et al., 2008):

I. A central hub to which 3 straight arms are connected and are equally separated, 120° apart each other with an arm length of 4.5 m and are spaced d = 0.875 wavelengths (Fig. 3.2). The Nyquist criterion is not satisfied here as for hexagonal sampling necessitates that the antenna separation should be d $=1/\sqrt{3}$ wavelengths to avoid aliasing in the unit circle (Camps et al., 1997). Consequently the reconstructed 2-D TB images (i.e. the microwave radiation emitted from the Earth's surface) suffer from aliasing (see Fig. 3.3) (Camps et al., 2005).

II. Each arm comprises three segments with six L-band radiometers on each segment

III. 54 radiometers on the arms and 12 in the hub (a total of 66 radiometers).

IV. 3 noise injection radiometers (NIRs) placed in the central hub.

V. 69 small receivers and uniformly distributed antennas, the antennas are separated by a distance of 18.37 cm, with a diameter of each antenna of 165 mm, with a height of 19 mm and a weight of 190 grams.

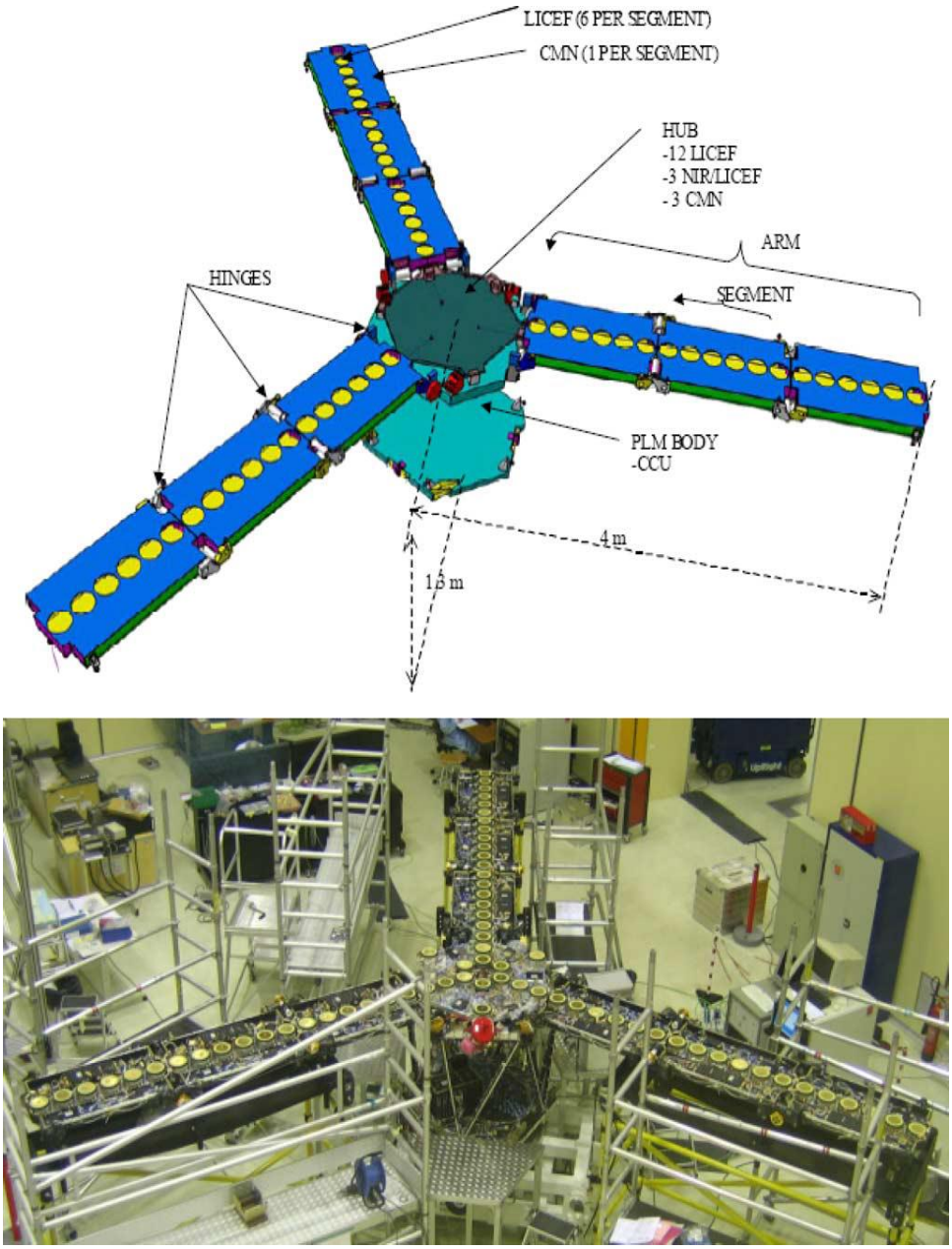

Fig. 3 - 2 *MIRAS instrument configuration diagram (upper panel) and during its assembly and integration (bottom panel) (McMullan et al., 2008).*

The MIRAS instrument, on-board the SMOS satellite, has been measuring the TB at L-band since 2010 within a wide field of view (FOV; see Fig. 3.3 (a)) and range of incidence angles spanning from 0° to 65°. Fig. 3.3 (a-c) shows the observation geometry of SMOS (a), which is a hexagon-like shape about 1000 km across called the "alias-free zone" (www.esa.int; Camps et al., 2005), an example (b) over the Baltic Sea area in Northern

Europe, and each pixel in the Alias-free-FOV (c) as it is seen at a different radiometric sensitivity, spatial resolution, and incidence angle (Camps et al., 2005). The spatial resolution of the TB measurements depends on the incidence angle (Kerr et al., 2010), which is maximum (~ 50 km; at incidence angles of 65) at the edge of the FOV and minimum (~ 35 km; at nadir) at the center of the FOV (Maaß et al., 2013).

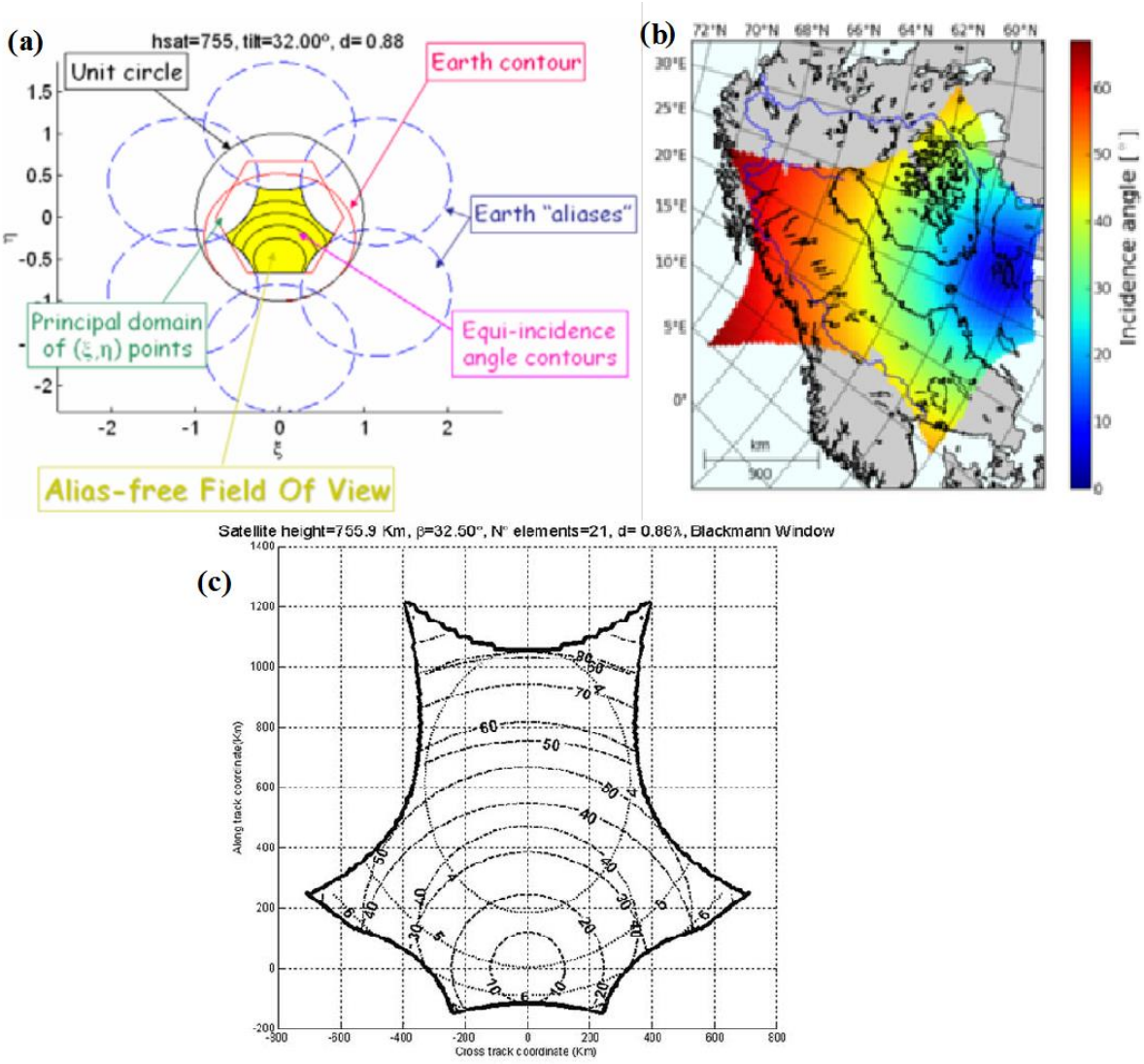

Fig. 3 - 3 *SMOS observation geometry (a), an example of the hexagon-like shaped 'alias free' SMOS snapshot over the Baltic Sea area in Northern Europe (b), and incidence angle (dashed lines from 10 to 60, circles cantered at (0, 0)); spatial resolution (dash-dot lines from 40 to 80 km); and radiometric sensitivity (dotted lines from 4 to 6 K) (c). (www.esa.int; Camps et al., 2005).*

3.1.2 SMOS products overview

SMOS SSM datasets are produced and distributed in different levels (Level 0 to Level 4) according to different levels of processors (www.esa.int). Level 0 (L0) to Level 2 (L2) are produced and distributed by the ESA, whereas Level 3 (L3) and Level 4 (L4) are produced and distributed by national centers in France and Spain (Jacquette et al., 2010). SMOS products are classified as follows (www.esa.int;Jacquette et al., 2010):

1- L0 processor and L0 products: the L0 products are obtained by formatting the SMOS Payload raw data (i.e. sorted in their original format as received from the satellite) in source packets with added Earth Explorer product headers.

2- Level 1: the TB are constructed in this level which is subdivided into three levels:

   (i) Level 1A (L1A) processor and L1A products: the L1A processor converts and calibrates all data coming from the spacecraft into engineering units. L1A products are, scientifically, called “Calibrated visibilities”.

   (ii) Level 1B (L1B) processor and L1B products: the L1B processor converts the L1A products into Fourier components of the TB using the so-called image reconstruction process. The L1B products are arranged as snapshots and not geographically sorted.

   (iii) Level 1C (L1C) processor and L1C products: the L1C processor reprocesses L1B products and provides swath-based maps of TB in the antenna polarization reference frame, which are geographically sorted as the so-called swath-based multi-angular TB maps. The L1C data are geolocated in the Icosahedral Snyder Equal Area projection (ISEA).

   (iv) Level 1 (L1) near real time (NRT) processor and L1 NRT products: L1 NRT processor converts the extracted L0 data into TB swaths. These

datasets are delivered to the users within three hours from sensing time and are used as inputs for weather models such as the ECMWF.

3- Level 2 (L2) processor and L2 products: the L2 processor applies the L-MEB (L-Band Emission of the Biosphere) model, which is shortly described in the next Section, to derive the global SSM swath-based maps. Quality indicators such as theoretical uncertainties of adjusted parameters and flags are also computed by L2 processors. The version number of SMOS L2 (SMOSL2) SSM operational processor (e.g., v4.2, v5.00, v5.51, v6.0, etc.) deployed in the SMOS processing has changed several times. The latest and current stable version available version is V6.0 which implemented substantial corrections and improvements (e.g., improved RFI detection, the change of the dielectric constant model from the Dobson model (from v5.51 onward) to the Mironov formulation, etc.). More details on the SMOSL2 processor and products can be found in (Kerr et al., 2012), ARRAY (www.array.ca/smos), ESA (http://earth.esa.int/smos), or through the CESBIO blog (www.cesbio.ups-tlse.fr/SMOS_blog/).

4- Level 3 (L3) processor and L3 products: the SMOS L3 (SMOSL3) products are global gridded maps of SSM produced with improved characteristics through temporal and spatial resampling and processing. They are provided by the CATDS (Centre Aval de Traitement des Données SMOS) center, which is a ground segment developed by the CNES since June 2011. The SMOSL3 SSM products are provided at different temporal resolutions: daily products, 3 day (a complete coverage of the Earth surface), 10-day composite products, and monthly averaged products (Jacquette et al., 2010). The CATDS center provides the SMOSL3 SSM products in the NetCDF format on the EASE (Equal Area Scalable Earth) grid with a ~25 km cylindrical projection (Jacquette et al., 2010). The SMOSL3 SSM products can be easily downloaded from the CATDS

website (http://catds.fr). This product was used throughout this Ph.D. research work. The SMOSL3 has, similar to the SMOSL2, several changes in the products for each update of the version and this depends on the period: SMOSL3 version v2.45 and v2.4X is from Jan. 2010 to Oct. 2012, SMOSL3 version v2.5X is from Nov 2012 to June 2013, SMOSL3 version v2.6 is from July 2013 to Dec. 2013, and SMOSL3 version 2.7X is from Jan. 2014 (corresponding to SMOSL2 V6) onwards. All SMOSL3 SSM products produced at CATDS from 2010 to 2013 are tagged RE01. However, a complete reprocessing is being done at the CATDS to produce a homogeneous time series (2010 – present) and this will be released very soon with the latest version 2.72 of the L3 processor and this reprocessed product will be tagged RE02.

5- Level 4 (L4) products: the L4 product is a combination of SMOS data with external datasets (from sensors or models) under development at the CATDS. The L4 products, include, for instance, root zone moisture (1 meter deep), enhanced resolution products through a combination of optical, thermal and microwave remote sensing products, thickness of the ice, and extreme event products and prevention of natural risks (e.g., global drought index, fire, and flood prediction).

3.1.3 SMOS SSM algorithm

The basic theory of passive microwave remote sensing has been described in detail by a number of researchers (e.g., Ulaby et al., 1986). The general principal of the SMOS algorithm relies on the measurements of the TB, corresponding to various contributions, from the surface of the Earth (Kerr et al., 2001). The TB observations are largely determined by the physical temperature and the emissivity of the radiating object. Wigneron et al. (1993; 1998; 2000) have demonstrated the possibility to perform 2-parameter retrievals (soil moisture and optical depth) from multi-angular TB observations. A theoretical representation of the TB is

given by a radiation equation of the black body. The concept of a perfect emitter is only theoretical. At microwave wavelengths the Rayleigh -Jeans is valid, and the emissivity (*e*) can be expressed as the ratio between the TB (K) and the physical temperature (Njoku & Entekhabi, 1996), as shown in Eq. (2.6) in Section 2.2.2 in Chapter II.

3.1.3.1 Input datasets

The SMOSL2 and SMOSL3 retrieval algorithms use, as inputs, the following datasets (Kerr et al., 2012):

(i) The SMOS L1C TB observations.

(ii) Static datasets i.e. do not vary over time such as: the soil texture, the land cover (ECOCLIMAP), soil bulk density (the Global Gridded Surfaces of Selected Soil Characteristics), sand and clay fraction (the FAO datasets), the topography index, etc.

(iii) Dynamic datasets i.e. vary over time such as: the Leaf Area Index (LAI; the MODerate Resolution Imaging Spectroradiometer (MODIS)), initial soil moisture (ECMWF), snow, soil and surface temperatures, etc.

3.1.3.2 The SMOSL2 algorithm

A flow chart showing the entire algorithm of SMOSL2 is displayed in Fig. 3.4 (Kerr et al., 2012). The SMOSL2 algorithm, in general, is based on a forward model and iterative inversion process. The forward model simulates the TB emitted by land nodes of SMOS using initial estimates of soil moisture obtained from the ECMWF forecasts, auxiliary datasets, surface temperature, etc. The inversion process estimates the actual soil moisture by minimizing the Root Mean Square Difference ("Cost Function") between the forward model simulations and the measured multi-angular TB (L1C data) (Kerr et al., 2012).

The L1c products are delivered on the icosahedral Snyder equal area Earth fixed (ISEA-4H9) grid known as the discrete global grid (DGG). Each DGG node is subdivided

into discrete fine flexible grids (DFFG) of approximately 4 km^2 each (Kerr et al., 2013a). The collective contributions from these DFFG cells form the upwelling TB signal measured by the SMOS satellite (Kerr et al., 2013a). This upwelling TB is inversed using the L-Band Microwave Emission of the Biosphere (L-MEB; Wigneron et al., 2007) model. The L- MEB model, with the help of auxiliary datasets (e.g., soil texture, land cover), is able to simulate TB for all incidence angles. The L-MEB model is the output of a broad review of knowledge of the microwave emission of a variety of land cover types (Wigneron et al., 2007). The L-MEB model is continuously improved based on several ground and air-borne L-band radiometer experimental campaigns over different regions (e.g., de Rosnay et al., 2006; Grant et al., 2007; Saleh et al., 2009).

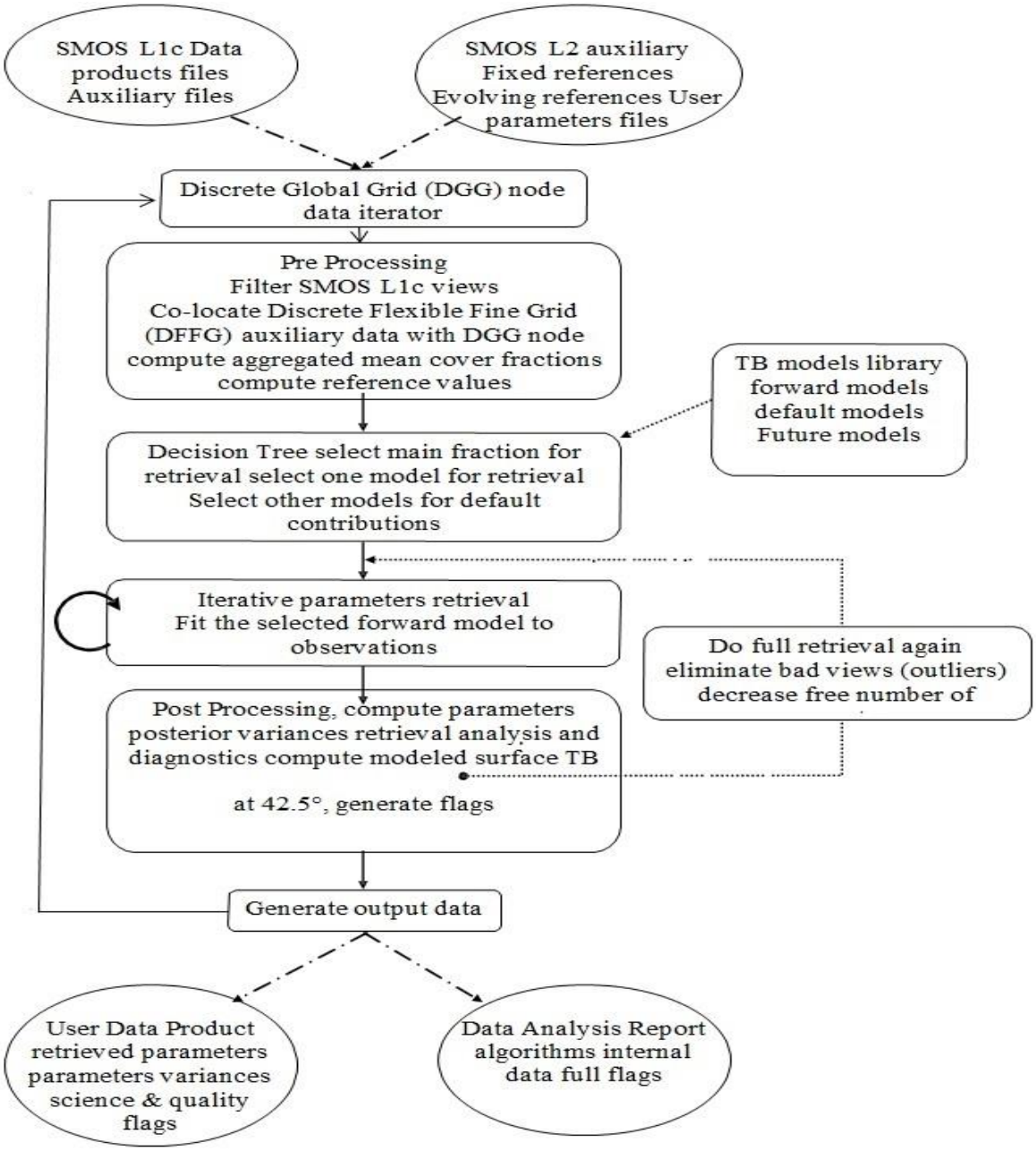

Fig. 3 - 4 *Schematic diagram of the SMOSL2 SSM algorithm. Adapted from* Kerr et al. *(2012).*

The L-MEB algorithm is based on an iterative optimization method, which aims at minimizing a cost function consisting on the sum of the squared weighted differences between TB simulated by L-MEB and measured by SMOS. This is achieved by guessing and adjusting the states of geophysical variables (including SSM and vegetation optical thickness) until the distance between the TB observed by SMOS and simulated by L-MEB is minimized (Kerr et al., 2013a; Kerr et al., 2012).

The SMOS TB signal observed at the antenna, shown in Fig. 3.5, can be formulated in the general radiative transfer equation as follows (Kerr et al., 2012):

$$TB_p = TB_{atmu} + TB_{sp}\exp(-\tau_{atmu}) + (TB_{atmd} + TB_{sk}\exp(-\tau_{atmd}))\, r_{sp} exp(-\tau_{atmu}) \qquad 3-1$$

where:

TB_{atmu} is the up-welling atmospheric emission,

TB_{atmd} is the down-welling atmospheric emission reflected (scattered) at the surface,

TB_{sp} is the Earth's surface emission, attenuated by the atmosphere,

TB_{sk} is the cosmic background emission attenuated by the atmosphere, reflected /scattered at the surface,

r_{sp} is the surface reflectivity,

τ_{atd} is the downward path atmospheric opacity,

τ_{atu} is the upward path atmospheric opacity, which depends on the gaseous and liquid droplet attenuating constituents (primarily oxygen, water vapor, and clouds),

$_p$ subscript indicates the polarization, and

$_s$ subscript stands for a combination of surface and near surface layers.

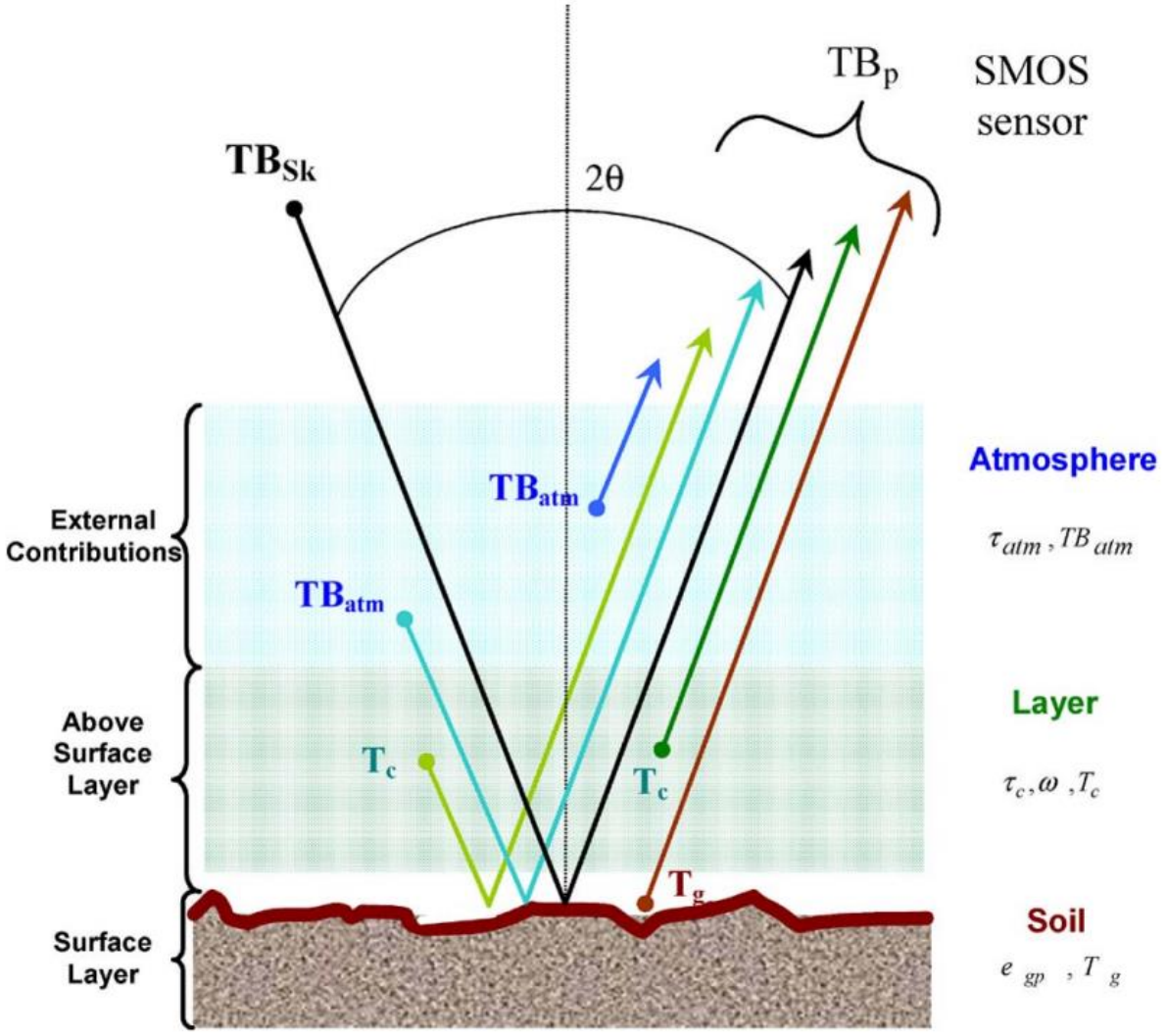

Fig. 3 - 5 *Components of the general radiative transfer equation (Kerr et al., 2012).*

The SMOS satellite operates at L-band, so τ_{atu} and τ_{atd} can be considered equal. Also, the atmospheric radiation components (TB_{atmd} and TB_{atmu}) are small and can be considered equal. The spatial resolution of the SMOS is about 45 km in average, so a pixel represents various surface types such as rural areas, snow, forests, bare fields, fallow land, woodland, ponds, etc. Therefore, the total TB is the sum of various classes of emitters, which are aggregated by the L-MEB model to obtain a composite TB (Kerr et al., 2013a; Kerr et al., 2012). The most important classes are shortly presented in the following (Kerr et al., 2013a; Kerr et al., 2012):

1- Bare soil:

The SMOS satellite operates at low frequency (L-band) so Rayleigh–Jeans approximation can be used. Therefore, the upwelling TB measured from the surface of bare soils is simply the product of the soil effective temperature, T_g and the soil emissivity of the radiating body e_p:

$$TB_p = T_g\, e_p \qquad 3-2$$

p subscript stands for either vertical or horizontal polarization, e_p can be further described as:

$$e_p = 1 - r_{sp} \qquad 3-3$$

where r_{sp} is the surface reflectivity, which can be computed for smooth soil using Fresnel laws (Eqs. (2.8) & (2.9) in Section 2.2.2 in Chap. II).

The basic concept for retrieving SSM from the SMOS TB observations, as for the other passive measurements, is based on the large contrast of the dielectric constant values of the soil (see Section 2.2.2 in Chap. II). The Dobson dielectric model was used in previous releases of the SMOSL2 SSM algorithm and was later replaced by the Mironov model, which results in more accurate and higher retrieved SSM at the global scale (Mialon et al., 2014).

The effective soil temperature is computed following a simplified formulation developed by (Wigneron et al., 2008):

$$T_g = T_{soil\ depth} + C_t\left(T_{soil\ surf} - T_{soil\ depth}\right) \qquad 3-4$$

where:

C_t is a parameter depending mainly on frequency and SSM,

$T_{soil\ depth}$ is the soil temperature at depth (between ~ 0.5 and 1m), and

$T_{soil\ surf}$ is the surface soil temperature (between ~ 1 and 5 cm).

$T_{soil\ depth}$ and $T_{soil\ surf}$ can be obtained from land surface models. $T_{soil\ depth}$ and $T_{soil\ surf}$ in the SMOSL2 algorithm are obtained from the ECMWF. According to (Choudhury et al., 1982), C_t is a constant (~ 0.246 at L-band) that depends only on frequency. However

Wigneron et al. (2008) found that C_t depends also on soil moisture. When the soil is very dry, soil layers deeper than 1 m for dry sand contribute significantly to the soil emission, and the value of C_t is lower than 0.5. When the soil is very wet, the soil emission originates mainly from layers at the soil surface, and $C_t \approx 1$. C_t can be computed using a simplified formulation, which is used in the L-MEB model, developed by Wigneron et al. (2001):

$$C_t = \left[\frac{ws}{w0}\right]^{bw0} \qquad 3-5$$

where:

ws is the surface soil moisture at about 0–2 cm, and

w0 and bw0 are semi-empirical parameters depending on specific soil characteristics (e.g., texture, structure, and density). The values w0 = 0.3 m^3/m^3 and bw0 = 0.3 are used as default values in the L-MEB model.

When the bare surface is not flat, Fresnel law (Eqs (2.8) & (2.9) in Section 2.2.2 in Chap. II) should be corrected for surface roughness with a purpose to account for the effects of surface scattering as follows (Kerr et al., 2013a; Wigneron et al., 2007; wigneron et al., 2010):

$$r_{gp}(\theta) = \left((1-Q)r_{bp} + Qr_{bp}\right)\exp\left(-H(SM)cos^{NRp}(\theta)\right) \qquad 3-6$$

where:

r_{gp} is the rough surface reflectivity,

Q is a polarization coupling factor,

H is an effective surface roughness dimensionless parameter which can be computed as: $H = (2\,k\,\sigma)^2$ where k is the wave number and σ is the surface root mean square height,

NRp is an integer (N=2) used to parameterize the dependence of the roughness effects on incidence angle, and

rbq is the smooth surface reflectivity for alternate polarization.

Table 3.1 presents the values of the different parameters used for bare soils (Kerr et al., 2013a) in the SMOSL2 algorithm.

Table 3 - 1 Bare soil parameters (Kerr et al., 2013a).

Surface TB of bare soil	Input	Parameter Name	Range	Units
Dobson or Mironov model to compute soil dielectric constant : εb Note: Mironov model does not require S, ρb , ρ s	S	Sand fraction	0-100	%
	C	Clay fraction	0-100	%
	ρb	Dry bulk soil density	0.5-2.5	g^3/cm^3
	ρ s	Soil particle density	2-3	g^3/cm^3
	SM	Soil moisture	0-0.5	m^3/m^3
	Sal	Soil salinity	0-12	Ppt
	F	Frequency	1.4	Ghz
	Tg	Effective surface-deep soil temperature	250-350	K
Fresnel equations to compute the εb Bare soil dielectric constant [F/m] specular reflectivity H & V for smooth air-soil boundary rbp	εb	Bare soil dielectric constant		F/m
	θ	incidence angle	0-55	Deg
Introduce soil roughness to compute bare soil scattering / reflectivity : rgp	rbp	Specular smooth soil reflectivity	0-0.6	-
	θ	Incidence angle	0-1.25	Rad
	Q	H/V polarization coupling factor	0-0.5	-
	H	Surface roughness parameter	0-5	-
	NRp	Power law of cos (θ)	0-5	-
Computing effective soil temperature	$T_{soil\ depth}$	Soil temperature at depth (~at 46 cm)	250-350	K
	$T_{soil\ surf}$	Soil temperature at surface (~ at 3.5 cm)		K
	W0	Texture parameters used to compute the coupling factor Ct for effective soil	0.05-2	m^3/m^3
	bw0		0-2	-

2- Low vegetation (grassland, crop):

The $\tau - \omega$ model (Mo et al., 1982; Wigneron et al., 2007) is used to approximate the effects of vegetation, which attenuates soil emission and contributes to the emitted radiation, on the satellite signal. This model is mainly based on the optical depth τ, to parameterize the vegetation attenuation properties, and the single scattering albedo ω, to parameterize the scattering effects within the canopy layer. According to the $\tau - \omega$ model, the emission from soil and vegetation is the sum of three components: (i) the direct emission from vegetation, (ii) the direct emission from soil attenuated by the canopy, and (iii) the direct emission from vegetation reflected by the soil and attenuated by the canopy layer (Mo et al., 1982; Wigneron et al., 2007). This is formulated as follows:

$$TB_p = (1 - \omega_p)(1 - \gamma_p)(1 + \gamma_p r_{sp})T_c + (1 - r_{sp})\gamma_p T_g \qquad 3-7$$

where:

T_g is the effective soil temperature [K],

T_c is the effective vegetation temperatures [K],

r_{sp} is the soil reflectivity,

ω_p is the single scattering albedo, and

γ_p is the vegetation attenuation factor (transmissivity), which can be estimated as follows:

$$\gamma_p = \exp\left(\frac{-\tau_p}{cos\,\theta}\right) \qquad 3-8$$

where:

τ_p is the vegetation optical depth and

θ is the observation angle.

More details on the values of the parameters used for low vegetation and the $\tau - \omega$ model can be found in (Kerr et al., 2013a; Wigneron et al., 2007).

3- Forest (coniferous, evergreen, and deciduous):

An algorithm specific for forest is only applied when a large fraction of land is covered by forests. When a large fraction of land is covered by forests, TB is computed as follows (Ferrazzoli et al., 2002):

$$TB_p = (1 - \omega_f)(1 - \gamma)(1 + \gamma_p r_{gp})T_c + (1 - r_{gp})\gamma T_g \qquad 3-9$$

where:

T_g is the effective soil temperature [K],

T_c is the effective vegetation temperatures [K],

r_{gp} is the soil reflectivity,

ω_F is the equivalent albedo, and

γ_p is the vegetation transmissivity, which can be estimated as follows:

$$\gamma = \exp\left(\frac{-\tau_f}{cos\,\theta}\right) \qquad 3-10$$

where:

τ_f represents the contributions due to crown, litter, and understory.

The basic algorithm used for forests is, in general, similar to the one used for low vegetation with some differences:

- A simple τ_f constant (in law vegetation), and
- ω_f (in law vegetation) may be considered constant (i.e., independent on angle, polarization and time), with a value of 0.08.

4- Open water

Contributions from the extended water surfaces (e.g., ocean for coastal pixels, rivers, canals, lakes, ponds, flooding, etc.) are taken into account in the SMOSL2 SSM algorithm. The emission from water bodies is estimated using the Fresnel equations (Eqs.

(2.8) & (2.9) in Section 2.2.2 in Chap. II) with replacing the soil magnetic permeability by the water magnetic permeability. The real and imaginary parts of the complex dielectric constant are computed using the modified Debye equation (Kerr et al., 2013a; Ulaby et al., 1986). For information on how other surface types such as saline water, dry sand, very dry soils, rocks, etc. are dealt with in the SMOSL2 algorithm, readers are directed to (Kerr et al., 2013a; Kerr et al., 2012).

3.1.3.3 The SMOSL3 SSM algorithm

The SMOSL3 algorithm, adopted at the CATDS, is based on the SMOSL2 SSM algorithm, described shortly in the previous Section. The main differences with the SMOSL2 are that SMOSL3 takes into account several revisits simultaneously in a multi-orbit retrieval and are produced as gridded (NetCDF) maps not swath-based maps as the SMOSL2 products. The input datasets for the SMOSL3 algorithm are the same as these used for the SMOSL2 but on a different grid (EASE-Grid). This grid was preferred as it is mostly used by the community (Jacquette et al., 2010).

The SMOSL3 SSM algorithm produces daily products using three multi-angular acquisitions during the synthesis period (Jacquette et al., 2010): One for the product date (the reference day), one before and one after the product date; the data are selected from a search period of 7 days centered on the reference day (Kerr et al., 2013b). This approach increases the number of views available, hence, more nodes are considered for the retrieval, which results in a larger coverage and more geophysical parameters can be derived. An overview of the SMOSL3 SSM processing chain at CATDS is displayed in Fig. 3.6. For a detailed description of the different steps of the algorithm, readers are directed to (Kerr et al., 2013b).

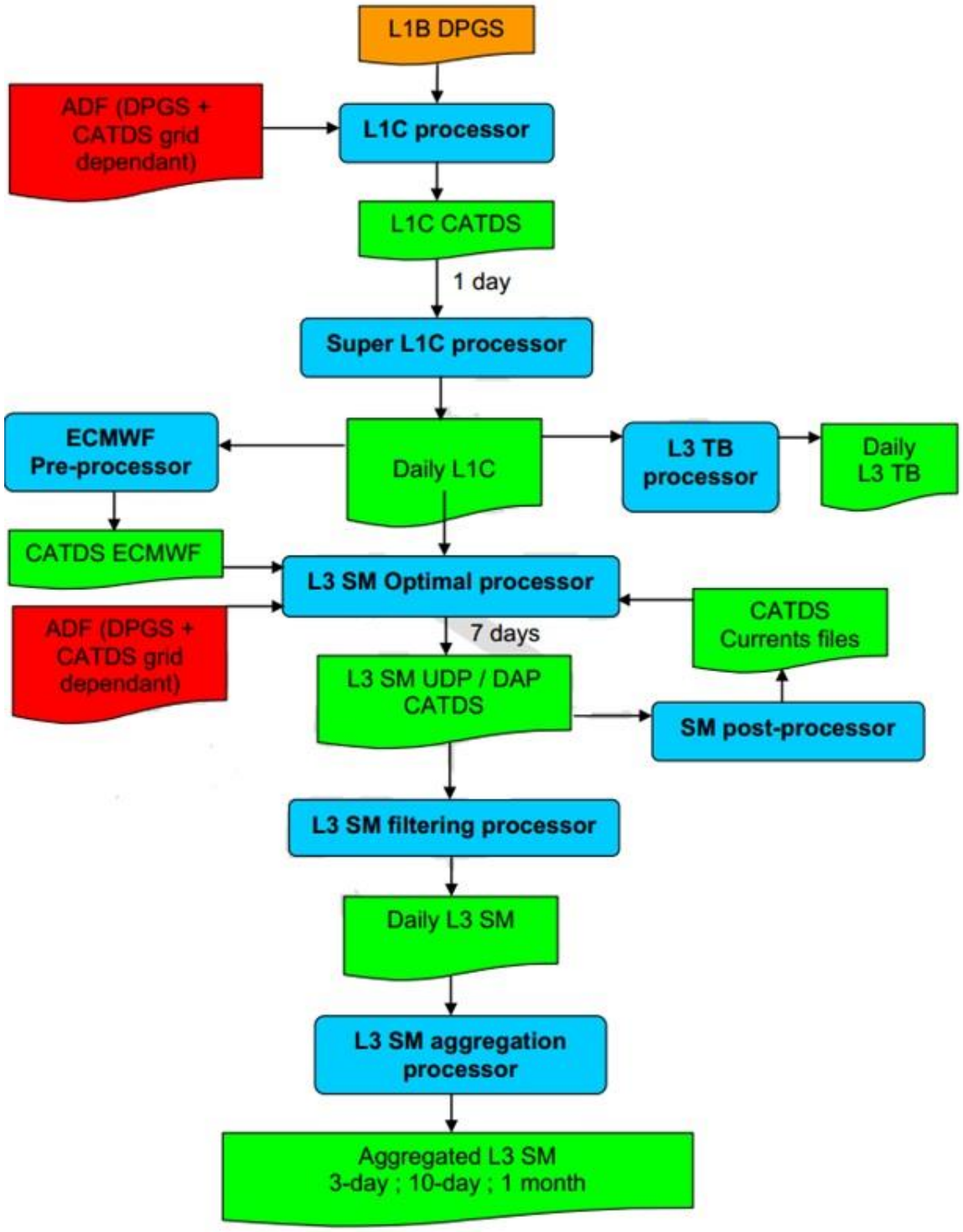

Fig. 3 - 6 *Overview of the CATDS SMOSL3 SSM processing chain (Kerr et al., 2013b). Processors steps are colored in blue and products are colored in green. UDP: User Data Product, DAP: Data Analysis Product, ADF: Auxiliary Data File, and DPGS: Data Processing Ground Segment.*

3.1.4 SMOS RFI issues

The negative impact of RFI (Radio Frequency Interference) on the passive microwave radiometers data has been a serious problem in the last decades (Njoku et al., 2005), which should be well identified and removed in order to maintain the science value of the space-borne observations. Since the launch of the SMOS satellite, it was noticed that the quality of its TB observations is negatively impacted by unnatural emissions, the so-called RFI. Although SMOS measures TB in a protected frequency window of (1.400 -1.427) GHz, preserved by the ITU Radio communication Sector (ITU-R) regulations for radio-astronomy and remote sensing satellite services (see Table 2.4 in Section 2.2.2 in Chapter II), its observations are still impacted by the RFI (Daganzo-Eusebio et al., 2013). The RFI is defined as the TB intensity that exceeds the radiation emitted by natural sources (Daganzo-Eusebio et al., 2013; Oliva et al., 2012) and it is mainly manmade emissions (Oliva et al., 2012):

- TV stations
- Radio transmission
- Global Positioning System (GPS) L3 transmission channel
- Military radars
- Telecommunication and television relays not properly filtering harmonics
- Unauthorized emissions within the protected passive band coming from active sources.

The effects of the RFI can be, generally, classified into three categories (Daganzo-Eusebio et al., 2013; Oliva et al., 2012):

- Low RFI emissions, which are similar to natural levels or below and are very challenging to detect leading to retrieve wrong SSM.
- Moderate RFI emissions, which can be easily detected and, thus, corrected.

- Strong RFI emissions, which influence larger areas. Strong RFI sources distort the whole snapshot's TB and lead to very high TB values, which exceed the naturally observed TB emitted by the Earth's surface. This TB cannot be used to retrieve SSM.

A clear RFI was noticed in the first SMOS products (Camps et al., 2010); consequently the development of effective approaches to mitigate and detect the RFI has been priority since the launch of SMOS. Several algorithms have been and are being developed to deal most effectively with the problems caused by the RFI contamination (Camps et al., 2010; Oliva et al., 2012). A first and simple detection method for the RFI was applied on SMOSL2 which relies mainly on excluding all unreasonable TB values. A natural physical temperature times the emissivity gives directly reasonable TB, so with knowing the ranges of this reasonable TB, other non-natural TB values can be isolated. 338 K is the maximum physical temperature that was ever recorded, so BTs values higher than 340 K originate from man-made transmitters (Daganzo-Eusebio et al., 2013). These conditions enable to build a global probability of RFI occurrences, for a specific time period, based on (Daganzo-Eusebio et al., 2013):

$$p = \frac{\mathrm{NRFIX} + \mathrm{NRFIY}}{\mathrm{NSNAP}p} \qquad 3-11$$

where:

NRFIX are the number of TBs detected as contaminated on X antenna polarization,

NRFIY are the number of TBs detected as contaminated on Y antenna polarization, and

NSNAP_p is the total number of observed TBs.

Fig. 3.7 displays the latest available worldwide probability of RFI occurrences maps for 24-04-2014 ascending and descending (http://www.cesbio.ups-tlse.fr/SMOS_blog/). It can be seen that RFI is not uniformly distributed, with particularly strong RFI over Europe, Japan, India, China, and the Middle East. Nevertheless, there is no or little RFI over most of

America, Australia and south Africa, whereas the ocean is almost free of RFI with the exception of some cases of interferences coming from emitting ships (Daganzo-Eusebio et al., 2013).

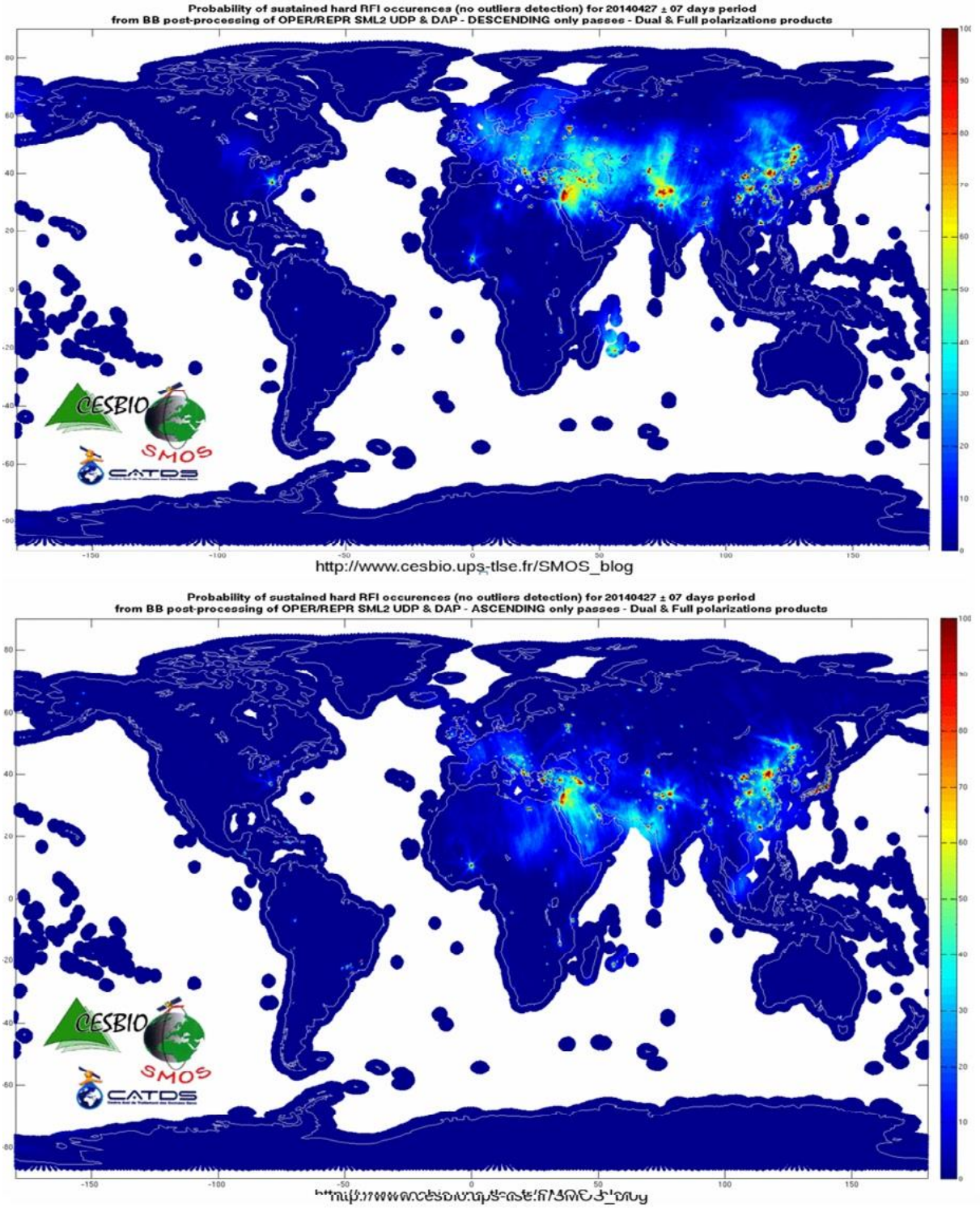

Fig. 3 - 7 *probability of RFI occurrences for 20140427 ascending (bottom) and descending (top). Source: [http://www.cesbio.ups-tlse.fr/SMOS_blog/].*

Several short, medium, and long-term actions and strategies were done since the launch of SMOS to deal most effectively with RFI issues (Daganzo-Eusebio et al., 2013; Oliva et al., 2012):

- Cooperate with the National Spectrum Management Authorities (NSMA) to advance the progress about the investigation of the RFI sources and tracking the illegal transmitters and switching them off.
- Report the detected RFI sources to the NSMA and request for their support to initiate investigations to increase the awareness at the international level to fulfil the ITU Radio-Regulations, aiming at prohibiting any emissions and respecting the maximum levels recommended for unwanted emissions in the passive band.
- Enhance the RFI flagging processes in the data products which prevent retrieving SSM from contaminated regions.
- Develop new RFI mitigation algorithms to filter or remove the RFI impact.

The ESA has made many efforts and succeeded to contact 45 administrations, mostly in Europe and Asia. As a result, 42% of the RFI sources were successfully identified and switched off (Daganzo-Eusebio et al., 2013).

Finally, RFI detection algorithm is progressively improved, therefore, caution should be taken when working with SMOS products by considering the version of the product. In V5.01, for instance, a temperature threshold linked to the surface expected emissivity was considered to filter RFI; whereas in previous versions V4.00, a fixed 340 K threshold was used.

3.2 ASCAT

3.2.1 ASCAT mission overview

The Advanced Scatterometer (ASCAT) is an active microwave sensor that transmits electromagnetic pulses and measures the electromagnetic wave reflected by the surface (Bartalis et al., 2008; Wagner et al., 2013). It was launched in October 2006, following the European Remote-Sensing Satellites 1 and 2 (ERS 1 and 2) launched in 1991 and 1995, respectively, aboard the Meteorological Operational Platforms (METOP–A; Fig. 3.8) and METOP–B since 2012 . METOP-A has a sun-synchronous orbit which crosses the equator at 09:30 and 21:30 local solar time for descending and ascending orbits, respectively (Wagner et al., 2013). The ASCAT instrument operates at C-band (5.3 GHz, wavelength = 5.7 cm) in vertical vertical (VV) polarization, which inherits and continues the role of the ERS1 & 2 scatterometers (Wagner et al., 2013). The ASCAT is a real-aperture radar system, thus it has a lower spatial resolution (25-50 km) compared to other instruments such as the synthetic-aperture radar (Wagner et al., 2013). The main purpose of ASCAT and its first application was to measure wind speed over the oceans (Wagner et al., 2013). Another application of the ASCAT was the SSM retrievals on the mainland, as many studies (Bartalis et al., 2007a; Naeimi et al., 2009) have shown that soil moisture can be related, expressed as percentage, relatively to the historically highest and lowest ASCAT backscatter measurements. See Table 3.3 for more information on the ASCAT and MetOp –A Platform.

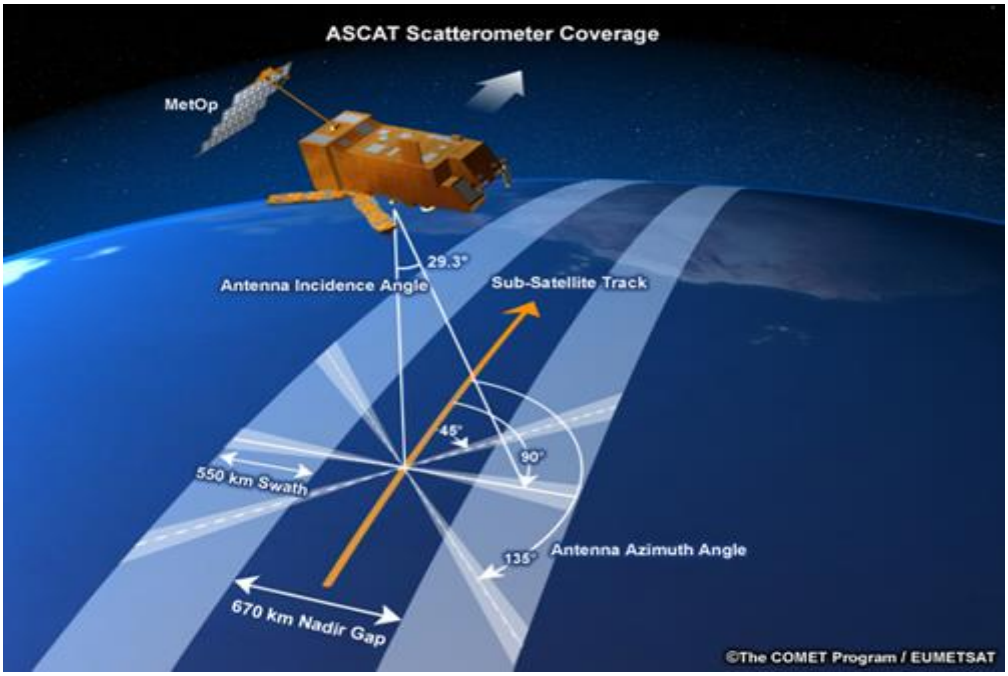

Fig. 3 - 8 *ASCAT on orbit and its geometry. Source: [the European Organization for the Exploitation of Meteorological Satellites (EUMETSAT) website (www.eumetsat.int)].*

3.2.2 ASCAT SSM algorithm

The Vienna University of Technology (TU- Wien) in Austria developed an algorithm to retrieve SSM data from active microwave backscatter measurements, which was initially introduced by (Wagner et al., 1999b) and later improved by (Naeimi et al., 2009). This algorithm relies on several assumptions (Bartalis et al., 2008; Wagner et al., 2013):

(i) There is a linear relationship between the backscattered signal (σ^0 expressed in decibels) measured by ASCAT and the SSM,

(ii) There is a strong dependency between the backscattered signal and the incidence angle, which is illustrated in Fig. 3.9,

(iii) The surface roughness and land-cover patterns do not vary in time (static), and

(iv) The backscattered signal is affected by the vegetation phenology on a seasonal scale and vegetation cycle does not change from year to year.

Fig. 3.9 shows the relationship between the σ0 and the soil moisture and vegetation (Wagner et al., 1999a), where the σ0 may increase or decrease when vegetation grows and there is an incidence angle where the σ0 is stable in spite of seasonal changes in above ground vegetation biomass (Wagner et al., 2013).

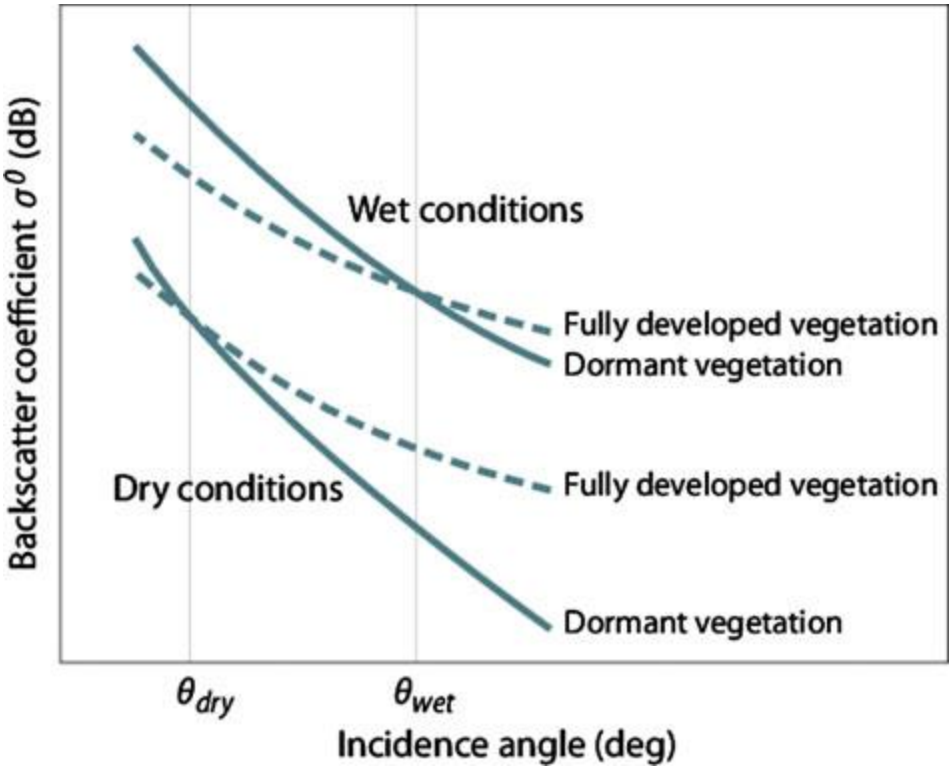

Fig. 3 - 9 *Relationship between the backscatter coefficient (σ0) and the surface soil moisture and vegetation. Adapted from* Wagner et al. *(1999a).*

The soil Water Retrieval Package (WARP) software, realized with the programming language IDL at TU-Wien, is used to generate the ASCAT SSM products. It uses the change detection method (Fig. 3.10) (Wagner et al., 2013), to produce the SSM from the ASCAT σ0 observations at the global scale. Soil moisture retrieval form the ASCAT σ0 measurements involve several processing steps (Bartalis et al., 2008): resampling the ASCAT measurements, using a Hamming weighting function with radius 18 km, in orbit geometry to a fixed Discrete

Global Grid (DGG), normalizing the ASCAT Level 1B backscatter observations based on their acquisition azimuthal angle (applying a correction bias), extrapolating all backscatter observations taken over the entire incidence angle range spanning from 18° to 59° to a reference incidence angle of 40°, which was found optimal for minimum extrapolation errors, and calculate the average σ0 (40°) based on the backscatter triplet, estimating the backscatter noise, correcting for the seasonal effects of the vegetation, determining dry and wet backscatter, and calculating surface soil moisture (%) between the historically wettest (highest) and driest (lowest) reference values σ0(40°).

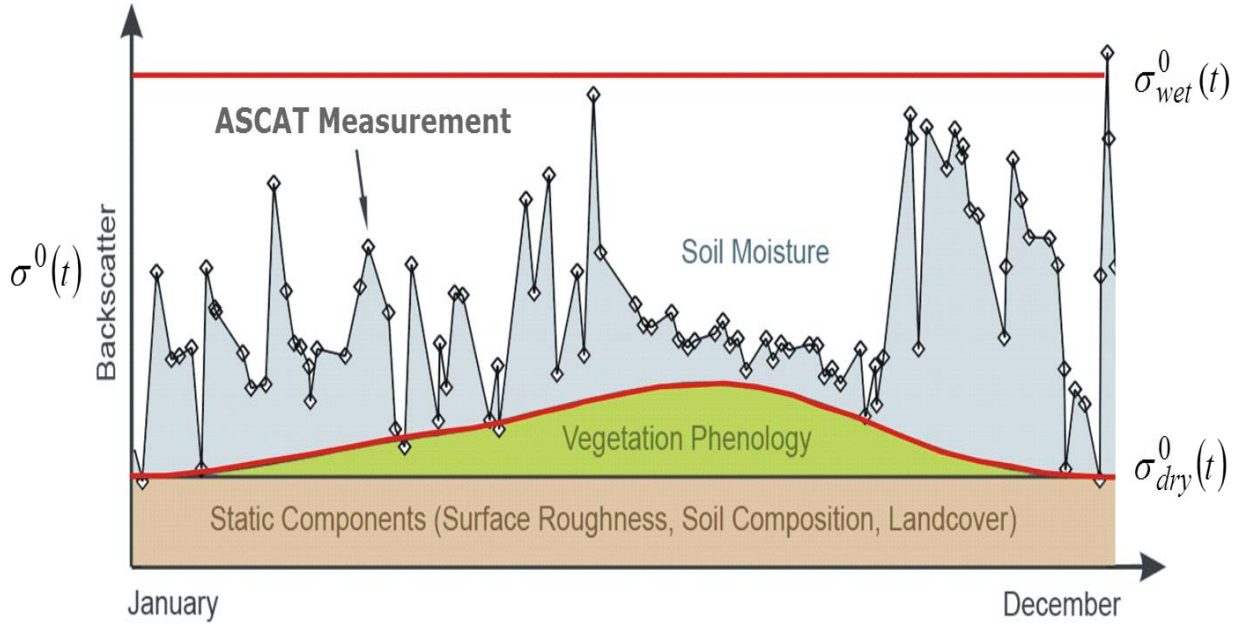

Fig. 3 - 10 *TU-Wien change detection approach for SSM retrieval using radar backscatter signal. After* Verstraeten et al. *(2007).*

The change detection method estimates the SSM index (t) (~ 2 cm) based on scaling the backscatter observations between highest (100% saturation) and lowest (0% driest), in one of the last processing steps, assuming that the soil moisture changes linearly with the σ0 observations, which can be described as (Wagner et al., 2013):

$$SSMindex\ (t) = \frac{\sigma^0(t,i) - \sigma^0_{dry}(i)}{\sigma^0_{wet}(i) - \sigma^0_{dry}(i)} \qquad 3-12$$

where $\sigma^0(t,i)$ is the measured backscatter, given in m^2/m^2 or Decibels (dB), at time t and under incidence angle *i* (40) and is given by:

$$\sigma^0\left[\frac{m^2}{m^2}\right] = \frac{\sigma}{A} \quad or \quad \sigma^0[dB] = 10log\sigma^0\left[\frac{m^2}{m^2}\right] \qquad 3-13$$

where:

A is the geometric antenna area [m^2]

σ is the radar scattering cross section [m^2], which can be found in Section 2.2.2.2 in Chap.II as Eq. (2.10).

Detailed information on these processing steps and mathematical formulations can be found in (Bartalis et al., 2007b; Bartalis et al., 2008).

This algorithm provides a standardized SSM index in a unit of degree of saturation (i.e., the SSM content expressed in percent of porosity (Hillel, 1982)). Multiplying the degree of saturation with the porosity gives a direct estimation of the volumetric water (m^3/m^3) content. Readers are directed to (Wagner et al., 2013) for more details on the physical concept of the TU-Wien SSM algorithm.

There are several versions of the WARP processor; WARP 5.5 is the latest software version available for the retrieval of SSM from ASCAT scatterometer data, which was used in Chap. V. A new version of the WARP processor (WARP 6.0) is to be released in the near future.

3.2.3 ASCAT Products

The ASCAT products, in general, are categorized into different levels (Bartalis et al., 2008):

• Level 0 (L0): raw instrument datasets (unprocessed) transmitted from the spacecraft to the ground stations in binary form,

• Level 1a: reformatted L0 datasets for the successive processing,

• Level 1b (L1b): backscatter coefficients are calibrated and geo-referenced and their quality is controlled in full resolution,

• Level 2 (L2): L1b data are converted to geophysical parameters (SSM), and

• Level 3: L2 data are resampled or gridded.

3.3 AMSR-E

3.3.1 AMSR-E mission overview

In June 2002, the Advanced Microwave Scanning Radiometer (AMSR- E) sensor was launched aboard the AQUA satellite by the National Aeronautics and Space Administration (NASA) (see Fig. 3.11), which, however, due to some problems with rotations of its antenna, stopped working in October 2011. The AQUA satellite is on a sun-synchronous orbit at 705 km equatorial altitude and inclination of 98.2^{o}, with an ascending overpass time around 13:30 hours local at the equator and descending overpass time around 01:30 (Demarest et al., 2001; JAXA, 2006).

Fig. 3 - 11 *AMSR-E aboard AQUA satellite. Source: [http://aqua.nasa.gov/]*

AMSR-E records TB at six frequencies: 6.9 (C-band), 10.65 (X-band), 18.7 (Ku-band), 23.8 (K-band), 36.5 (Ka-band), and 89 (W-band) GHz (horizontal and vertical polarizations) at a single incidence angle of 55°, with a spatial resolutions of 56 km (6.9 and 10.65 GHz), 25 km (18.7 and 23.8 GHz), 15 km (36.5 GHz), and 5 km (89 GHz) (JAXA, 2006). This mission is further detailed on the website of NASA: http://www.ghcc.msfc.nasa.gov/AMSR/index.html and in JAXA (2006), its main characteristics are summarized in Table 3.3 at the end of this chapter.

The AMSR-E TB observations are contaminated by RFI particularly in the C-band frequencies in North America and Japan (Njoku et al, 2005). The RFI problems at C- and X-band in AMSR-E have been already investigated (Kidd, 2006; Li et al., 2004; Njoku et al., 2005). More recently, (Lacava et al., 2013) implemented the Robust Satellite Techniques (RST) approach using AMSR-E data at C-band to identify RFI source locations over land at global scale. Lacava et al. (2013) have confirmed previous studies that large parts of North

America and several zones in India, South America, and Japan are mostly contaminated by the RFI.

There are several algorithms which have been developed in order to retrieve SSM from the AMSR-E TB measurements. The official and first product is the NSIDC (National Snow and Data Centre, (Njoku et al., 2003)), which was shown to be able to reproduce the dynamics of SSM (Rüdiger et al., 2009). Along with the official product and other algorithms, the Vrije Universiteit Amsterdam (VUA) in cooperation with the NASA (VU-NASA) (Owe et al., 2001) developed an algorithm to retrieve SSM, surface temperature, and optical thickness at X and C-bands (the former is used when the latter is contaminated by the RFI) (Owe et al., 2001). The product of this later algorithm was used in Chap. IV and it is briefly described in the following Section.

3.3.2 AMSR-E VU-NASA algorithm:

The VU-NASA algorithm implements the LPRM (Land Parameter Retrieval Model, (Owe et al., 2001; Owe et al., 2008) model to the TB acquisitions from the AMSR-E sensor in order to retrieve the SSM. The diagram displayed in Fig. 3.12 represents the algorithm of the LPRM, which is based on a forward radiative transfer model. The LPRM algorithm consists in five main modules: dielectric mixing model, smooth surface reflectivity, rough surface emissions, vegetation, and radiative transfer model, which are described in details in the Algorithm Theoretical Baseline Document (Chung et al., 2013). These five components are used to simulate a TB which is then compared to the TB acquired by the AMSR-E sensor. SSM is changed (input at the top of Fig. 3.12) until the difference between the TB modelled and observed is at its minimum (weighted measurement accuracy difference). The LPRM algorithm retrieves the SSM and vegetation optical depth (τ_v) simultaneously from the AMSR-E observations at C-and X-band frequencies using iterative optimization technique;

whereas surface temperature is computed from the Ka-band frequency. The vegetation optical depth (τ_v) is computed using the Microwave Polarization Difference Index (MPDI) (Chung et al., 2013).

The TB (Tb in Fig 3.12) observations measured by AMSR-E in LPRM are described using a simple radiative transfer model (Mo et al., 1982):

$$TB_{s,p} = T_s e_{r,p} \Gamma_v + (1-\omega) T_v (1-\Gamma_v) + (1-\omega)\left(1-e_{r,p}\right) T_v (1-\Gamma_v)\Gamma_v \qquad 3-14$$

where:

T_s is the thermodynamic temperatures of the soil [K],

T_v is the thermodynamic temperatures of the vegetation [K],

Γ_v is the vegetation transmissivity, which is assumed to be equal for vertical and horizontal polarization,

e_r is the rough surface emissivity,

TB_u and TB_d are the upwelling and downwelling atmospheric brightness temperatures [K], respectively, and

ω is the single scattering albedo.

The subscript p denotes either horizontal (H) or vertical (V) polarization.

e_r is calculated in LPRM as follows (Wang & Choudhury, 1981):

$$e_r = 1 - Q\left(r_{s,p2} + (1-Q) r_{s,p1}\right) e^{-H cos\theta} \qquad 3-15$$

where:

Q is the polarization mixing factor,

H is the roughness height, and

r_s is the surface reflectivity and p1 and p2 are opposite polarizations (horizontal or vertical).

Γ_v is calculated in LPRM as follows:

$$\Gamma_v = \exp\left(\frac{-\tau v}{cos\theta}\right) \qquad 3-16$$

where τ_v is the optical depth and θ is the incidence angle.

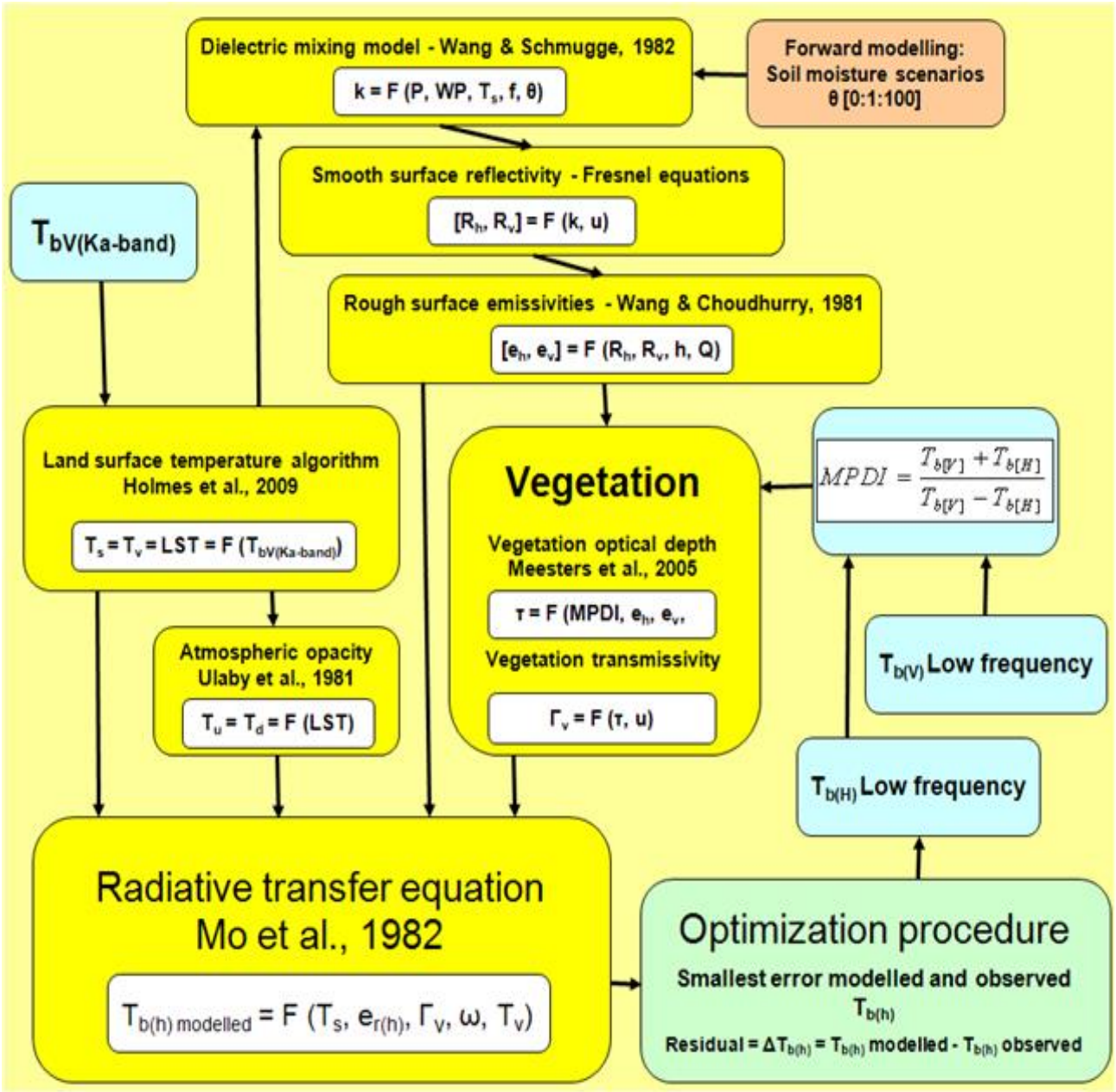

Fig. 3 - 12 *Schematic diagram of the entail methodology of LPRM model. Adapted from* Chung et al. (2013).

Eq. (3.13) consists of three terms: the first term represent the emission (attenuated by the vegetation canopy) from the soil, the second term represents the emission from vegetation, and the third term represents the downwelling radiation from the vegetation and reflected upwelling by the soil (attenuated by the vegetation canopy).

The soil wilting point and porosity information in the LPRM algorithm were obtained from the FAO soil texture map (FAO, 2000); the other parameters (τ_v, ω, H, and Q) were given fixed values. The values of the different parameters used in the LPRM algorithm for the different frequencies are presented in Table 3.2.

Table 3 - 2 Values of the different parameters used in LPRM for the different frequencies. Adapted from Chung et al. (2013).

Parameter	C-band (~6.9 GHz)	X-band (~10.8 GHz)	Ku-band (~19 GHz)
τ_v	0.01	0.01	0.05
ω	0.05	0.06	0.06
H	0.09	0.18	0.13
Q	0.115	0.127	0.14

Finally, in the LPRM algorithm, the RFI is detected based on an index of vertically polarized TB at C-band to vertically TB at X-band (Li et al., 2004). Two important things have to be noted about the AMSR-E VU-NASA SSM datasets:

- The AMSR-LPRM retrieval does not rely on calibration to local site conditions
- The LPRM algorithm does not need ancillary datasets.

3.4 Pre-Processing

Satellite soil moisture retrieved from observed brightness temperature is subject to some factors (strong topography, water bodies, etc.) that can strongly perturb the observed brightness temperature. Brightness temperatures emitted by the Earth surface, as a natural emission, are also affected by artificial sources originating from man-made emissions (e.g. satellite transmissions, FM broadcast, etc.), so called Radio Frequency Interference (RFI) (Njoku et al., 2005; Oliva et al., 2012). Therefore, remotely sensed datasets are often associated with flags to filter these potential effects.

Quality control was applied to SMOSL3, AMSRM, and ASCAT prior to the evaluation based on quality flags associated with the remotely sensed datasets. For SMOSL3, Data Quality IndeX (DQX), index related to the quality of the retrieved parameter and RFI were used in the data selection. SMOSL3 datasets were rejected when DQX > 0.06 m^3/m^3, DQX is equal to fill value (meaning the retrieval has failed), Percentage of RFI > 30% (which is a daily RFI indicator), and Probability of RFI > 30% (which was computed from a moving window average of RFI events over several months). For AMSRM, the soil moisture error (SME), based on error propagation analysis, related to the sensor characteristics and vegetation optical depth, was used in the data selection. AMSRM datasets were rejected when SME > 0.35 m^3/m^3. For ASCAT, a noise error (ERR), which is based on Gaussian error propagation related to the sensor characteristics and incidence angle uncertainty, an estimated standard deviation of the backscatter signal, was used in the data selection. ASCAT datasets were rejected when ERR > 14% (Draper et al., 2012).

Furthermore, all the datasets were re-projected from their original coordinate systems onto a regular 0.25° × 0.25° grid using a nearest neighbor approach (e.g., Draper et al., 2011; Rüdiger et al., 2009; Scipal et al., 2008). Finally, all the remotely sensed datasets (SMOSL3, AMSRM, and ASCAT) were screened, applying additional static masks, to remove grid cells

with (i) steep mountainous terrain (> 10%), (ii) wetland fraction (> 5%) (Draper et al., 2012), and (iii) frozen soil conditions (soil temperatures < 276 K).

In Chapters 4 and 5, we perform global-scale comparisons of three SSM datasets (AMSRM, SMOSL3, and SM-DAS-2 in Chapter 4, and ASCAT, SMOSL3, and MERRA-Land in Chapter 5). In each 0.25° × 0.25° pixel, the selected statistical indicators, detailed in Chapters 4 and 5, were computed only when the compared three SSM products were simultaneously available. Therefore, the number of SSM data elements used in the time series of Chapter 4 was identical for AMSRM and SMOSL3, and the number of SSM data elements used in the time series of Chapter 5 was identical for ASCAT and SMOSL3. This number of data elements is illustrated in Fig. 3.13.

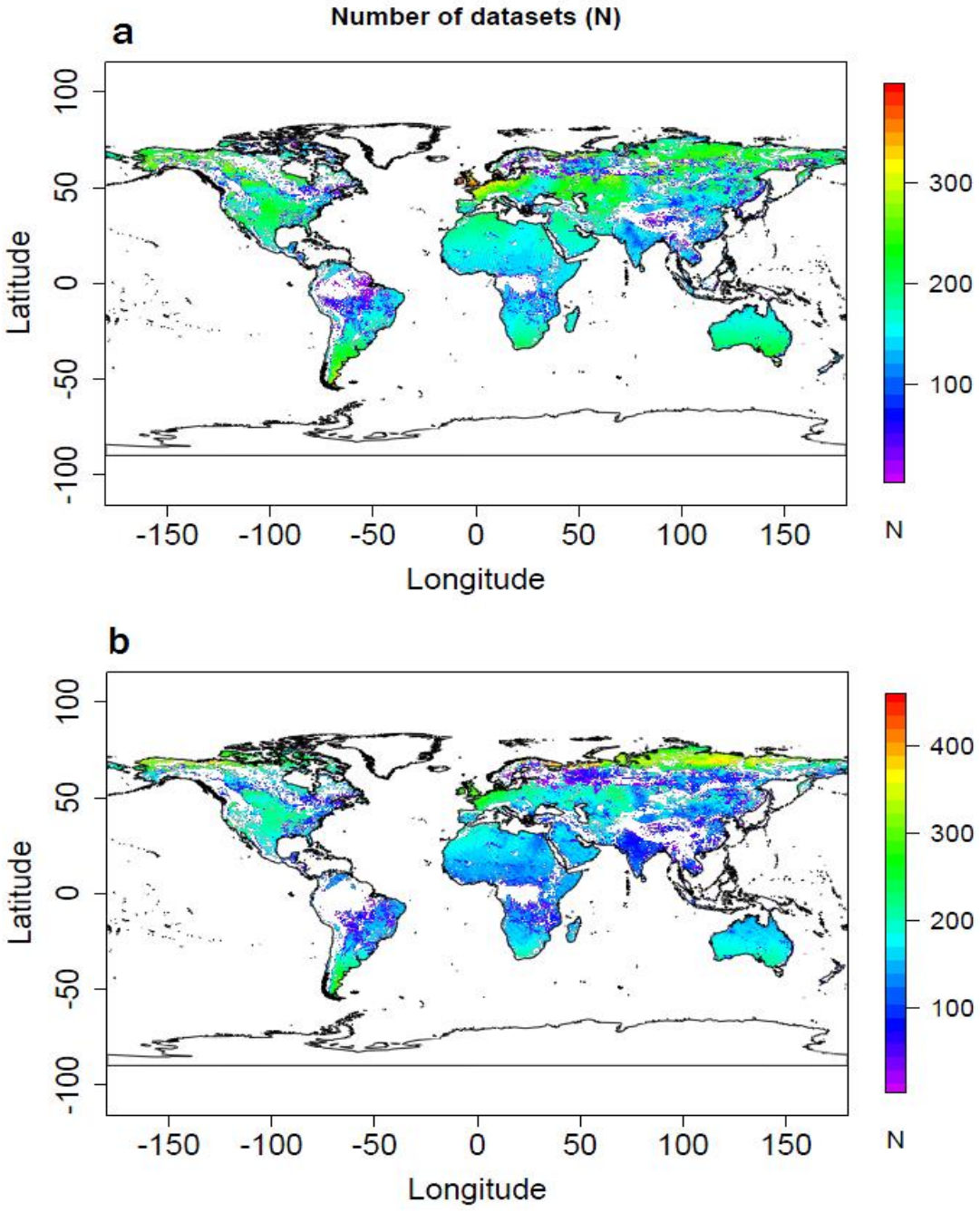

Fig. 3 - 13 *The number of data elements considered for (a) SMOSL3 and AMSR-E in Chapt. 4, (b) SMOSL3 and ASCAT in Chapt.5.*

Table 3 - 3 The main characteristics of SMOS, ASCAT, and AMSR-E missions and SSM products used in this Ph.D. research work.

Mission	SMOS	ASCAT	AMSR-E
Satellite/ Spacecraft	SMOS	METOP - A & B	AQUA
Agency	ESA/CNES	EUMETSAT/ESA	NASA
Sensor	Passive MIRAS	Active ASCAT	Passive AMSR-E
Launch	2nd, Nov. 2009	19th, Oct. 2006	4th, May 2002-1st, Oct. 2011
Design life	Minimum 3 years	5 years	6 years
End of data availability	ongoing	ongoing	09/2011
Orbit	Polar (Sun-synchronous, dawn/dusk, quasi-circular orbit.	Polar (orbit at an angle of 98.7° to the equator, Sun-synchronous)	Polar (Sun-synchronous, near-polar orbit
Equator crossing time (local solar time)	6.00 am for ascending and 18.00 pm for descending	21:30 pm for ascending and 09:30 am for descending	13:30 pm for ascending 01:30 am for descending
Altitude (km)	763	817	705
Spacecraft operations control center	CNES, Toulouse, France	European Meteorological Satellite Organization (EUMESAT)	National Space Development Agency of Japan (NASDA)
Centre frequency (GHz)	1.413 (L-band; 21cm)	5.255 (C-band, 5.7 cm)	6.925 10.65 18.7 23.8 36.5 89.0
Band width (MHz)	24	Microwave radar	350 100 200 400 1000 3000
Polarization	H & V (polarimetric mode optional)	VV	H & V
Incidence angle	0-55 °	25–53° (mid-beam); 34–64° (fore- and at beams)	55 °
Swath width (km)	1000	2* 520	1445

Mission	SMOS	ASCAT	AMSR-E
Spatial resolution (km)	(30-50), Average 35 km at center of field of view	25 & 50	75 × 43 51 × 29 27 × 16 32 × 18 14 × 8 6 × 4
Radiometric resolution	0.8-2.2 K		0.3 0.6 0.6 0.6 0.6 1.1
Temporal resolution (revisit time)	3 days revisit at Equator	~2 days for covering global	~3 days at the equator and more frequently at higher latitudes
Daily global coverage	~82 %	~82 %	90 %
Model for retrieval	L-MEB (Wigneron et al., 2007)	WARP (Bartalis et al., 2007b)	LPRM (Owe et al., 2008)
Forward model	Radiative transfer model	Change Detection	Radiative transfer model
Simultaneous retrievals	Soil temperature Vegetation optical depth Roughness	None	Soil temperature Vegetation optical depth Surface temperature
Soil moisture unit	Volumetric soil moisture (m^3/m^3)	Degree of saturation (0-1 or %) relative value (0 = dry and 100 = saturated)	Volumetric soil Moisture (m^3/m^3)
Grid	Fixed ISEA4-9 Discrete Global Grid (SMOSL2) EASE grid (SMOSL3)	Swath geometry WARP 5 Grid (sinusoidal DGG)	Regular Grid
Spatial coverage	60^oS 180^oW - 80^oN 180^oE	60^oS 180^oW - 90^oN 180^oE	60^oS 180^oW - 90^oN 180^oE
Soil moisture accuracy	0.04 m^3/m^3	-	0.06 m^3/m^3
Pixel spacing	15 km (SMOSL2) 25km (SMOSL3)	12.5 km	0.25°
Auxiliary datasets	Several static and dynamic auxiliary datasets	None	FAO soil texture map (FAO, 2000)

Mission	SMOS	ASCAT	AMSR-E
Quality flags	RFI Prob Data quality index, etc.	Soil moisture error Topography index Wetland fraction etc.	Soil moisture error
Product version used in this Ph.D.	SMOSL3 (RE01, V 2.48 and 2.5)	WARP 5.5	LPRM Level 3
Reference URL	http://www.catds.fr/Products	http://www.ipf.tuwien.ac.at/radar	http://www.falw.vu/~jeur/lprm/

Chapter IV

4. Global-scale evaluation of two satellite-based passive microwave soil moisture datasets (SMOS and AMSR-E) with respect to Land Data Assimilation System estimates[1]

[1] This chapter has been published as: A. Al-Yaari, J.-P. Wigneron, A. Ducharne, Y. Kerr, P. de Rosnay, R. de Jeu, A. Govind, A. Al Bitar, C. Albergel, J. Muñoz-Sabater, P. Richaume, A. Mialon, Global-scale evaluation of two satellite-based passive microwave soil moisture datasets (SMOS and AMSR-E) with respect to Land Data Assimilation System estimates, Remote Sensing of Environment, Volume 149, June 2014, Pages 181-195, ISSN 0034-4257, http://dx.doi.org/10.1016/j.rse.2014.04.006.

4.1 Introduction

Soil moisture (SM) is a key environmental variable, which interacts with vegetation and ecosystem functioning (Bolten et al., 2010; Daly & Porporato, 2005), water resources (Dobriyal et al., 2012), and the climate system. It is central to land–atmosphere interactions due to its positive control on evapotranspiration, with feedback loops that are usually negative on air temperature (Cheruy et al., 2013), and still not well understood on rainfall (Taylor et al., 2012). SM also influences the dynamics of all the above mentioned processes by buffering or memory effects, with consequences on the persistence of extreme events, climate and hydrologic predictability, and even anthropogenic climate change trajectories (Entekhabi et al., 1996; Koster et al., 2004a; Koster et al., 2010; Quesada et al., 2012; Seneviratne et al., 2013; Teuling et al., 2010).

As a result, accurate SM initialization is crucial to the quality of most water-related environmental forecasts up to at least seasonal forecasts, including numerical weather predictions (NWP) (Beljaars et al., 1996; De Lannoy et al., 2013; de Rosnay et al., 2012; de Rosnay et al., 2013; Drusch & Viterbo, 2007; Koster et al., 2006).

In particular, it is important to achieve an accurate SM initialization at the scale of the forecast models, which can exceed 0.5° × 0.5° for NWP and climate models. In situ SM measurements can now be routinely achieved with an accuracy as high as 0.025 m^3/m^3 (Walker et al., 2004). However, considering the high spatial variability of SM and the poor density of in situ measurement sites, it is not possible to produce accurate large-scale estimate of SM from in situ measurement networks (Dorigo et al., 2011; Hollinger & Isard, 1994; Vivoni et al., 2008).

A major alternative to estimate SM at the large scale is to rely on remote sensing satellites, using passive or active microwave sensors, which offer global coverage and good temporal repetitivity, but are only sensitive to a shallow layer of the soil. Historically, passive microwave sensors were first used, starting with the Scanning Multichannel Microwave

Radiometer (SMMR; 6.6, 10.7, 18.0 21, and 37 GHz channels;(Wang, 1985)) which operated on Nimbus-7 between 1978 and 1987, then the Special Sensor Microwave Imager (SSM/I) which started in 1987. Later passive sensors include the microwave imager from the Tropical Rainfall Measuring Mission (TRMM; 10, 19 and 21 GHz channel; (Bindlish et al., 2003; Gao et al., 2006), the Advanced Microwave Scanning Radiometer on Earth Observing System (AMSR-E; from 6.9 to 89.0 GHz; (Njoku & Li, 1999)) which operated on the AQUA satellite between 2002 and 2011, and Coriolis Windsat which started in 2003 (Parinussa et al., 2011b). More recently, the Soil Moisture and Ocean Salinity (SMOS; 1.4 GHz) was launched in 2009 (Kerr et al., 2010) and the upcoming SMAP (Soil Moisture Active/Passive) mission, including a radiometer at L-band, was planned by the National Aeronautics and Space Administration (NASA) and scheduled for launch in 2014 (Entekhabi et al., 2010). Low-resolution active microwave sensors (scatterometers) have also been used (Bartalis et al., 2007a; Wagner et al., 2007).

Among all these microwave sensors, SMOS is the first satellite dedicated and specifically designed to measure directly surface SM (SSM) and sea surface salinity on a global scale (Kerr et al., 2010; Kerr et al., 2012) owing to its polar-orbiting 2-D interferometric radiometer at L-band. The Level 2 SMOS SSM products (SMOSL2) are derived from the multi-angular and fully polarized L-band passive microwave measurements (Kerr et al., 2012). A new global Level 3 SSM dataset (referred to as SMOSL3; (Jacquette et al., 2010)) has been released very recently. The general principle of the algorithm is similar to the one used for producing the standard Level 2 SSM products, but the quality of the SSM product is enhanced by using multi-orbit retrievals (Kerr et al., 2013b).

Another strategy to produce large-scale estimates of SM relies on modelling, either directly using multimodel SM means (Dirmeyer et al., 2006; Georgakakos & Carpenter, 2006), or via assimilation systems, which aim at optimally combining land surface models

and SM related observations (de Rosnay et al., 2012; Drusch & Viterbo, 2007). This strategy has proved to be particularly fruitful and highlighted the need for accurate surface and root zone SM remotely sensed estimates (de Rosnay et al., 2012; de Rosnay et al., 2013; Draper et al., 2009b; Muñoz-Sabater et al., 2007; Reichle et al., 2007). The SM-DAS-2 analysis, for instance, is retrieved by assimilating ASCAT SSM products in the ECMWF (European Centre for Medium-Range Weather Forecasts) Land Data Assimilation System, and the resulting estimates of SM benefit from high quality analyzed atmospheric data (de Rosnay et al., 2011; de Rosnay et al., 2013; Drusch et al., 2009).

Whatever their origin, the evaluation of global SSM products is needed to guide their correct use, and to improve our understanding of their strengths and weaknesses over a large spectrum of climate and environmental conditions across the world. Several studies have evaluated SSM products based on passive microwave sensors against in situ measurements and modelled data over different regions (Al Bitar et al., 2012; Albergel et al., 2012; Brocca et al., 2011; Dall'Amico et al., 2012; Draper et al., 2009a; Jackson et al., 2012; Lacava et al., 2012; Leroux et al., 2011; Mladenova et al., 2011; Sahoo et al., 2008; Su et al., 2011). Although consistent results were generally obtained from the remotely sensed and modelled data, disagreements or biases between the different sources of SSM data were noted depending on the particular regions or time periods. For instance, Albergel et al. (2012) found that the SM-DAS-2 SSM estimates were closer to in situ measurements in terms of correlation than SMOS and ASCAT SSM products, in several stations situated in Africa, Australia, Europe, and the United States.

In this context, we present in this study a global evaluation of two SSM datasets retrieved from passive microwave observations (SMOSL3 and AMSRM, respectively based on SMOS and AMSR-E observations) against the SM-DAS-2 product, which is used here as a reference, because it is the most consistent SM product compared to in situ SM data (Albergel

et al., 2012). In doing so, we have two specific objectives. The first objective is to provide the first assessment of the SMOSL3 product at global scale. The second objective is to compare SSM products retrieved from passive microwave observations at two different frequency bands: L-band (~ 1.4 GHz) for SMOSL3 vs. C-band (~ 5 GHz) for AMSRM. Although the performances of L-band vs. C-band for SSM retrievals have been compared against experimental or simulated data sets (Calvet et al., 2011; Wigneron et al., 1993), no global study based on satellite data has yet been made, to our knowledge. L-band is generally considered to be the optimum frequency band for SM monitoring due to (i) lower attenuation effects by vegetation (ii) lower atmospheric effects and larger effective sampling depth (~ 0–3 cm; (Escorihuela et al., 2010)) than C-band.

The SSM datasets used and the methodology for their evaluation are described in Section 4.2. The results are then presented in Section 4.3. Finally, discussion and conclusions are given in Section 4.4.

4.2 Materials and methods

4.2.1 Global-scale soil moisture datasets

The main characteristics of the three SSM datasets considered in this study are summarized in Table 4.1. The evaluation was performed for the period 03/2010–09/2011, which corresponds to the full period of availability of the two satellite-based products: tests made during the SMOS commissioning phase ended in March 2010 while the AMSR-E spatial mission ended in October 2011.

Table 4 - 1 Main characteristics of the surface soil moisture datasets used in this study. Note that all products are daily and global products re-sampled to 0.25° (~ 25 km).

Soil moisture datasets	Incidence angle (°)	Data type and frequency	Sampling depth and unit	Temporal coverage	Reference
SMOS level 3 (SMOSL3)	0–55	Remotely sensed (L-band, passive)	~ 0–3 cm (m^3/m^3)	2010–present	(Jacquette et al., 2010)
AMSR-E, NASA-VUA Algorithm (AMSRM)	55	Remotely sensed (C-band, passive)	~ 0–1 cm (m^3/m^3)	2002–2011	(Owe et al., 2008)
ECMWF SM-DAS-2 (DAS2)	–	Land Data Assimilation System	0–7 cm (m^3/m^3)	2010–present	(de Rosnay et al., 2013; Drusch et al., 2009)

4.2.1.1 SMOSL3

The SMOS satellite was launched in November 2009 and is operated by the European Space Agency (ESA), as part of its Living Planet Programme, and the Centre National d'Etudes Spatiales (CNES) in France. SMOS operates at L-band with a spatial resolution of 35–50 km (Kerr et al., 2001; Kerr et al., 2010). The SMOS mission aims to monitor SSM at a depth of about 3 to 5 cm and an accuracy of 0.04 m^3/m^3. SMOS provides global coverage with a 3-day revisit at the equator with a morning ascending orbit at 0600 h local time and an afternoon descending orbit at 1800 h (Kerr et al., 2012).

The CATDS Centre (Centre Aval de Traitement des Données; http://catds.ifremer.fr/) recently provided re-processed global maps of SSM at different temporal resolutions: daily products, 3-day global products insuring a complete coverage of the Earth surface, 10-day composite products, and monthly average products, the so-called SMOS level 3 products (SMOSL3). These products are presented in the NetCDF format on the EASE grid (Equal

Area Scalable Earth grid) with a spatial resolution of ~25 km × 25 km. The main principle of the algorithm used to retrieve SSM is the same as the one used by the ESA operational algorithm for producing the standard Level 2 SSM products (Kerr et al., 2012; Wigneron et al., 2007). In both Level 2 (L2) and Level 3 (L3) products, multiangular observations are used to retrieve simultaneously SSM and vegetation optical depth at nadir (τ-NAD) using a standard iterative minimization approach of a cost function (Statistical Inversion Approach as discussed in Wigneron et al. (2003). The main difference with the L2 processing is the fact that the L3 processing takes into account over each pixel several revisits simultaneously in a multi-orbit retrieval approach (Jacquette et al., 2010; Kerr et al., 2013b). In the L2 algorithm, SSM and τ-NAD are retrieved from multiangular observations made using one SMOS overpass at 0600 or 1800 h local time. Conversely, in the L3 algorithm, SSM and τ-NAD are retrieved from multiangular observations made using several overpasses (3 at most) over a 7-day window. Over the short 7-day window, it is considered that optical depth at nadir (τ-NAD) varies slowly in time. In the L3 processor, this is accounted for by assuming that the retrieved values of τ-NAD are correlated using a Gaussian auto-correlation function over the 7-day window (while the SM values are considered as uncorrelated). The multi-orbit retrieval approach was selected to produce the L3 product as it improves the SM retrieval (Kerr et al., 2013b):

I. Increasing the number of overpasses over a given node taking into account several revisits (multi-orbit approach) increases the number of observations available for a node. As the number of observations increases, more nodes are considered in the retrieval process, resulting in a larger coverage. This is mostly significant at the edge of the swath for which a single overpass does not provide enough brightness temperature (TB) data for an accurate retrieval process (Wigneron et al., 2000).

II. Considering that the vegetation optical thickness is correlated over a given period of time adds more constraints in the retrieval process and the robustness of the retrieval is improved.

SMOSL3 (ascending and descending) datasets include flags that can be used to filter out the datasets (Jacquette et al., 2010; Kerr et al., 2013b; Kerr et al., 2008). More details on the flags used to filter SMOSL3 data are given in Section 4.3.

Note that new versions of the SMOSL3 data set will be produced based on re-processing activities in the near future and will lead to improvements in the product accuracy. The version of SMOSL3 used in the present study was the latest version available at CATDS. The version of the processor is V2.48, corresponding to a Level-2 version higher than ~V5.0, although there is not a strict correspondence between Level-2 and Level-3 versions.

4.2.1.2 AMSRM

The Aqua satellite is operated by the National Aeronautics and Space Administration (NASA). It was launched in May-2002 and carries, among others, the AMSR-E radiometer providing passive microwave measurements at six frequencies (6.925, 10.65, 18.7, 23.8, 36.5, and 89.0 GHz) with day-time ascending orbit at 1330 h and night-time descending orbit at 0130 h (Owe et al., 2008). The datasets cover the period from June 2002 to October 2011. On this latter date, AMSR-E on board the NASA Aqua satellite stopped producing data due to a problem with the rotation of its antenna.

The AMSR-E sensor was one of the first sensors to target SSM as a standard product (Njoku et al., 2003; Njoku & Chan, 2006). Various algorithms have been developed to retrieve SSM from the AMSR-E observations. The main ones were developed at (i) NASA which produced the standard AMSR-E-NASA algorithm (Njoku et al., 2003), (ii) the Japan Aerospace Exploration Agency (Koike et al., 2004), and (iii) the "Vrije Universiteit

Amsterdam" in collaboration with NASA, referred to as the NASA-VUA algorithm (Owe et al., 2001; Owe et al., 2008). The NASA-VUA algorithm uses a three-parameter retrieval approach (i.e., SSM, vegetation optical depth, and soil/canopy temperature are retrieved simultaneously) to convert multi-frequency TB measured by AMSR-E to SSM. The retrieved SSM products accuracy was shown to be 0.06 m^3/m^3 for sparsely to moderately vegetated canopies (de Jeu et al., 2008).

A range of studies (Brocca et al., 2011; Draper et al., 2009a; Hain et al., 2011) addressed the evaluation of the NASA-VUA SSM products based on combinations of observations made at different AMSR-E frequencies, mainly using C-band (6.925 GHz) and/or X-band (10.65 GHz). Using in situ observations and/or modelled SM data as reference, these studies showed good performance of the NASA-VUA products in capturing the SSM variability at global scale.

In this paper a version (Level 3 gridded data) of the NASA-VUA product exclusively based on the AMSR-E C-band and descending orbit observations was used. It is referred hereafter to as AMSRM. Descending orbit (night time) SM products were shown in previous studies to be more accurate and less affected by temperature-related errors than ascending orbit (day time) products (Draper et al., 2009a; Jackson et al., 2010; Kerr & Njoku, 1990; Su et al., 2011). The use of C-band (6.925 GHz) data, i.e. the lowest frequency available for the AMSR-E instrument, maximizes the soil sampling depth (~ 0–1 cm) of the retrieved product (Owe et al., 2008) and minimizes the sampling depth mismatch with the SMOSL3 product.

4.2.1.3 ECMWF soil moisture analysis

This study used the SM-DAS-2 SM analysis product as a reference. SM-DAS-2 is produced at ECMWF in the framework of the H-SAF project of EUMETSAT (Satellite Application Facility on support to operational Hydrology and water management; more information at http://hsaf.meteoam.it/). The SM-DAS-2 analysis uses the Hydrology Tiled

ECMWF Scheme for Surface Exchanges over Land (HTESSEL; (Balsamo et al., 2009; van den Hurk & Viterbo, 2003)). HTESSEL is a multilayer model where the soil is discretized in four layers (thickness: 7, 21, 72 and 189 cm). SM-DAS-2 relies on a dedicated advanced Land Data Assimilation System: a simplified Extended Kalman Filter able to ingest information contained in observations close to the surface (temperature and relative humidity at 2 m) as well as ASCAT SM retrieval (de Rosnay et al., 2013; Drusch et al., 2009), which is used to correct the model SM prognostic variable. SM-DAS-2 analysis is available at a spatial resolution of about 25 km (Gaussian reduced grid T799). The first layer (0–7 cm) is considered only, to represent the relatively low sampled soil layer of the SSM estimates derived from microwave remote sensing sensors (~ 0–3 cm at L-band and ~0–1 cm at C-band). SM-DAS-2 was shown to represent SM variability well. For instance, Albergel et al. (2012) have used in situ measurements from more than 200 stations located in western Africa, Australia, Europe, and the United States to determine the reliability of SM-DAS-2 to represent SM over 2010. Correlation values with in situ data were found to be very satisfactory over most of the investigated sites located in contrasted biomes and climate conditions with averaged correlation (R) values of 0.70 and an estimate of the averaged error is about 0.07 m^3/m^3. SM-DAS-2 is produced in the framework of the H-SAF project from EUMETSAT and it benefits from the latest model and analysis developments from ECMWF. This is why it was selected as the benchmarking dataset for this study. However it is important to emphasize that, as shown by the validation statistics above, SM-DAS-2 does not represent the absolute truth. It was used as a reference in this paper because at the time of this study it was the product that best captures the SM dynamics. On the longer term, when the SM retrieval algorithms will be fully calibrated, it is likely that satellite products such as SMOS SM will be used as reference data sets for SM product comparison studies. SM-DAS-2 is a SM index product; however in this study it was converted to volumetric SM (in m^3/m^3)

using global soil texture and hydraulic soil properties derived from the Food and Agriculture Organization digital (FAO) soil map as described in Balsamo et al. (2009). Hereafter, this product will be referred to as "DAS2".

4.2.2 Pre-processing

Quality control was applied to SMOSL3 and AMSRM prior to the evaluation based on quality flags associated with the remotely sensed datasets. The uncertainties associated with the NASA-VUA retrieval algorithm are based on error propagation analysis, related to the sensor characteristics and vegetation optical depth, as described in Parinussa et al. (2011c). AMSRM SSM values with an estimated SSM uncertainty greater than 0.35 m^3/m^3 were rejected. Flags such as Data Quality IndeX (DQX) and Radio Frequency Interferences (RFI) are also associated with the SMOSL3 data and were used in our data selection. The DQX is an index related to the quality of the retrieved parameter. It takes into account the uncertainties associated with the parameter retrievals, depending on the number of multi-angular observations available, the surface conditions (dry or wet soil conditions, dense or sparse vegetation cover, etc.), the TB accuracy, etc. (Kerr et al., 2012; Wigneron et al., 2000). The DQX value is provided in volumetric SSM moisture units between 0 and 0.1 m^3/m^3. In this study, we selected data with a value of DQX lower than 0.06, as we considered this ratio represents a good compromise between the need to keep sufficient data and the need to ensure data quality. Radio Frequency Interferences come from man-made emissions (e.g. satellite transmissions, aircraft communications, radar, TV radio-links, FM broadcast, and wireless camera monitoring systems). It perturbs the natural microwave emission emitted by the Earth surface and measured by passive microwave systems (Njoku et al., 2005; Oliva et al., 2012). With the SMOS interferometric system (based on a three arm Y-shaped antenna array), RFI effects are complex and oscillating interference effects may happen (Oliva et al., 2012). These

effects could not be systematically detected and the SMOS L3 product is still contaminated by RFI effects. To illustrate the spatial patterns of the probability of RFI occurrences on SMOS observations, a map is given in Fig. 4.1. This map represents the three-year (i.e., 2010–2012) average of probability of RFI occurrences and shows the regions where the undetected RFI effects are the most likely. The RFI flags provided in the SMOSL3 data set are given in an attempt to filter out the most significant RFI effects. In the present study, SMOSL3 data were rejected if one of the following conditions was fulfilled:

(i) DQX >0.06 and DQX is equal to fill value (meaning the retrieval has failed),

(ii) Percentage of Radio Frequency Interference (RFI fraction) > 30%, which is a daily RFI indicator, and

(iii) Probability of RFI (RFI Prob) > 30%, which was computed from a moving window average of RFI events over several months.

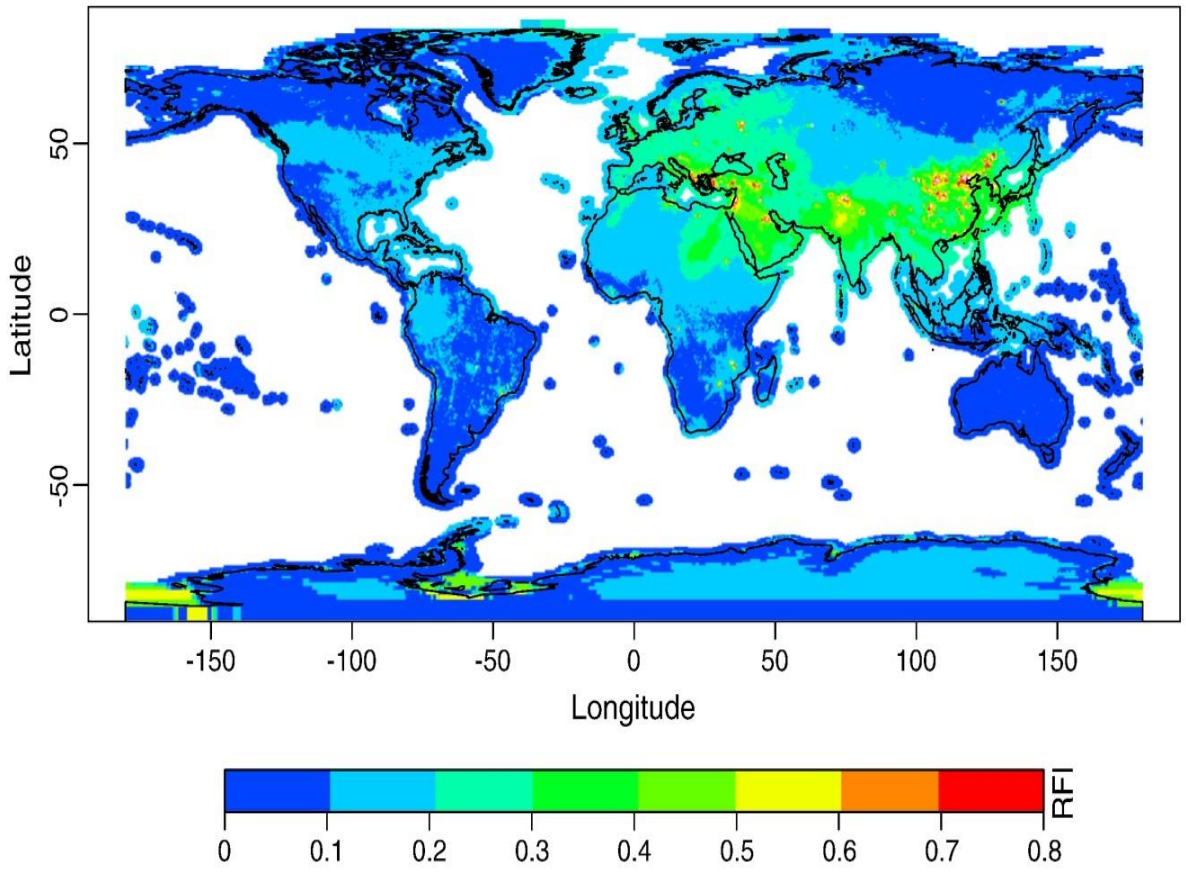

Fig. 4 - 1 *Probability of Radio Frequency Interference (RFI) occurrences in the L-band SMOS observations. The map represents the average probability of RFI occurrences for the period 2010–2012.*

Within the NASA-VUA algorithm for AMSR-E, Radio Frequency Interference is detected according to the method of (Li et al., 2004). This method is based on absolute differences between the different frequencies. In the AMSRM product, the standard configuration of NASA-VUA was used and C-band observations were used generally. Only when an RFI threshold value was reached, NASA-VUA made a switch to X band observations (Chung et al., 2013).

Based on flags, AMSRM and SMOSL3 data were also rejected in regions of strong topography or wetlands. AMSRM, SMOSL3, and the reference DAS2 dataset were provided on different grids and formats. So pre-processing was required to allow a comparison of all products on the same grid. All the datasets were re-projected from their original coordinate

systems onto a regular 0.25° × 0.25° grid using a nearest neighbor approach (e.g., Draper et al., 2011; Rüdiger et al., 2009; Scipal et al., 2008).

4.2.3 Comparison metrics

Three statistical indicators were computed between pairs of the remotely sensed (SSM_{RS}) and reference SSM products (SSM_{REF}). We considered the Pearson correlation coefficient (R), the mean difference (Bias), and the Root Mean Squared Difference (RMSD) between the remotely sensed (SSM_{RS}) and the reference SM products. The equations for the calculation of the three indicators are given as follows (Brocca et al., 2011; CECR, 2012):

$$R = \frac{\sum_{i=1}^{n}(\mathrm{SSM_{REF(i)}} - \overline{\mathrm{SSM_{REF}}})(\mathrm{SSM_{RS(i)}} - \overline{\mathrm{SSM_{RS}}})}{\sqrt{\sum_{i=1}^{n}(\mathrm{SSM_{REF(i)}} - \overline{\mathrm{SSM_{REF}}})^2 \sum_{i=1}^{n}(\mathrm{SSM_{RS(i)}} - \overline{\mathrm{SSM_{RS}}})^2}} \qquad 4-1$$

$$\mathrm{Bias} = \overline{(\mathrm{SSM_{RS}} - \mathrm{SSM_{REF}})} \qquad 4-2$$

$$\mathrm{RMSD} = \sqrt{\overline{(\mathrm{SSM_{RS}} - \mathrm{SSM_{REF}})^2}} \qquad 4-3$$

where the overbar denotes the mean operator, n is the number of SSM data, SSM_{RS} is the satellite-based SSM product (SMOSL3 and AMSRM), and SSM_{REF} is the reference SSM (DAS2). We used RMSD instead of RMSE (Root Mean Squared Error) because the reference SSM values may contain errors and cannot be considered as the "true" SSM values.

4.2.4 Regional-scale analyses

This regional study was made to compare the three different datasets for a variety of conditions. We compared the SSM time series from SMOSL3, AMSRM, and the reference (DAS2) over eight sites which were selected taking into consideration contrasting vegetation types and climate conditions (see Fig. 4.2). A summary of the main characteristics of the eight selected sites is given in Table 4.2.

Table 4 - 2 Locations and type of biome of the eight sites selected to evaluate the SSM time series (Fig. 4.2). All sites have the same surface area (i.e., ~ 360,000 km^2).

	Region	Coordinates (center) (longitude–latitude)	Biome (vegetation)	Köppen–Geiger climate classification
1	Brazil, Amazon Basin	(− 53° W to − 8° S)	Tropical humid (evergreen rain forest)	Af & Am
2	Deccan Plateau Region of India	(78° E–21° N)	Tropical semi-arid (Isolated trees and bush in open grassland)	BSk, Aw, & BSh
3	Central Australia	(133° E to − 23° S)	Desert temperate	BWh
4	North–West America, Great Basin Region (Nevada, Utah, Idaho and Washington)	(− 114° W–40° N)	Desert temperate	BWh & BWk
5	North–East America, Interior Plains Region (Iowa, Illinois, Minnesota, and Wisconsin)	(− 94° W–43° N)	Temperate humid (forest, grass land, agriculture)	Aw & Dfa
6	Sahel, Savanna Region of Nigeria, Cameroon, Central African Republic and Chad	(18° E–89° N)	Tropical semi-arid (isolated trees and bush in open grassland)	Aw
7	Central Europe (Austria, France, Germany and Italy)	(4° E–47° N)	Temperate forest (Deciduous broadleaf forest)	Cfb
8	Argentina, Pampas Region	(− 53° W to −26°S)	Temperate humid (grass land)	Cfa

This evaluation was limited to only eight sites which cannot span the whole range of soil, vegetation, and climate conditions present at global scale. However, this evaluation allowed us to analyze and illustrate some major features of the three datasets. To compare the temporal dynamics of SSM between remotely sensed and reference observations, we removed the systematic differences by matching the remotely sensed time series to the reference time series as discussed by Dorigo et al. (2010). This was done by normalizing the original remotely sensed data (the data referred to as ‘original’ in the following) are the data extracted

directly from the SMOSL3 or AMSRM data set and expressed in volumetric units (m^3/m^3) SSM_{or} so that they have the same mean and standard deviation as the reference SSM dataset SSM_{REF} according to the following equation (Brocca et al., 2010; Draper et al., 2009a):

$$SSM(t) = \overline{SSM_{REF}} + \frac{\sigma(SSM_{or})}{\sigma(SSM_{REF})}\left(SSM_{or}(t) - \overline{SSM_{or}}\right) \qquad 4-4$$

Here, SSM(t) stands for the rescaled remotely sensed retrievals at time steps t = 1,…, n, where n is the total number of observations, $\left(\overline{SSM_{or}}\right)$ *and* $\sigma(SSM_{or})$ are the mean and standard deviation of the original remotely sensed retrievals, respectively, and $\overline{SSM_{REF}}$ and $\sigma(SSM_{REF})$ are mean and standard deviation of the reference dataset, respectively.

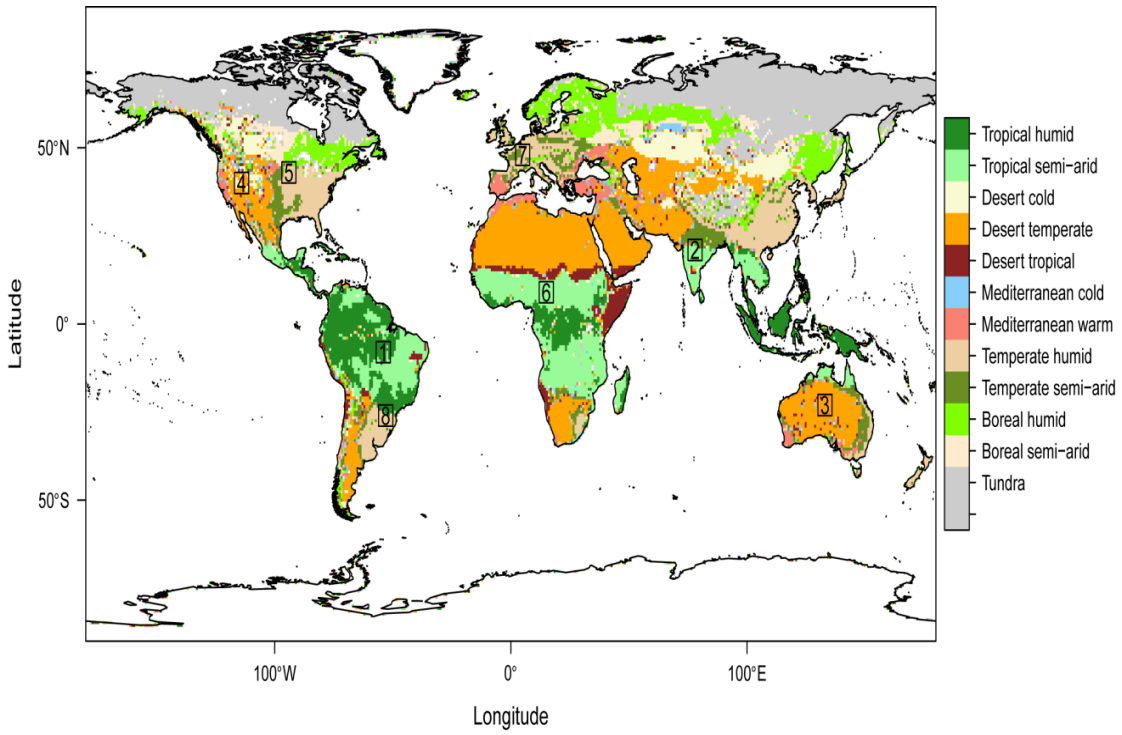

Fig. 4 - 2 *Distribution of major biomes (Chesworth, 2008). The boxes on the map indicate the sites which were selected to illustrate the main features of the SMOSL3, AMSRM and DAS2 products for a variety of vegetation and climatic conditions.*

4.2.5 SSM seasonal anomalies

All the above statistics were calculated for original SSM values, expressed in volumetric units (m^3/m^3). We also applied the above performance metrics to SSM anomalies. The anomaly time-series were calculated in order to avoid seasonal effects that can unrealistically increase the degree of correlation (Scipal et al., 2008) and to analyze the ability of remotely sensed SSM products to capture the day-to-day variability in the SSM time series. We computed the anomalies following the method described by Albergel et al. (2009). The anomalies $SSM_{anom}(t)$ were computed as the difference to the mean for a sliding window of 35 days, which was further scaled using the standard deviation in order to be dimensionless:

$$\mathrm{SSM_{anom}(t)} = \frac{\mathrm{SSM_{or}(t)} - \overline{\mathrm{SSM_{or}(t-17:t+17)}}}{\sigma[\mathrm{SSM_{or}(t-17:t+17)}]} \qquad 4-5$$

where *SSMor*(t) is the original SSM value at time t obtained from the satellite sensor or reference datasets, the over-bar and σ symbols are the temporal mean and standard deviation operators, respectively, for a time window of 35 days corresponding to the time interval [t − 17 days, t + 17 days]. The use of a ~monthly window is a very common approach to compute SM anomalies (Brocca et al., 2011; Draper et al., 2013; Draper et al., 2009b; Reichle et al., 2008).

4.2.6 Global-scale analyses

Global maps of (i) correlations (R), to assess the global consistency in the SSM variability at both long- (original) and short-term (anomaly) scales, (ii) RMSD, and (iii) bias between the reference and the two remotely sensed SMOSL3 and AMSRM SSM time series were computed. The performance indicators were computed for all common pixels on a daily basis. To analyze the effects of the vegetation and climatic conditions and to facilitate the interpretation of the results of the global comparison, the values of the three performance

indexes were averaged for a variety of biomes. These biomes represent different bioclimatic conditions and contrasting vegetation types. In this study we used the classification made by (Chesworth, 2008), illustrated in Fig. 4.2, who distinguished: “tundra”, “boreal semi-humid”, “boreal humid”, “temperate semi-arid”, “temperate humid”, “Mediterranean cold”, “Mediterranean warm”, “desert tropical”, “desert temperate”, “desert cold”, and “tropical humid” biomes.

The analysis of the results was also made accounting for the LAI (mean value computed over the pixel) to evaluate the link between the accuracy of the remotely sensed SSM products and the vegetation effects (in relation with vegetation density and biomass). To investigate this link, the global correlation results (original and anomalies) were averaged according to the global distribution of LAI values. The values of LAI were the long term-mean LAI values taken from the Global Soil Wetness Project (Dirmeyer et al., 2006) illustrated in Fig. 4.3.

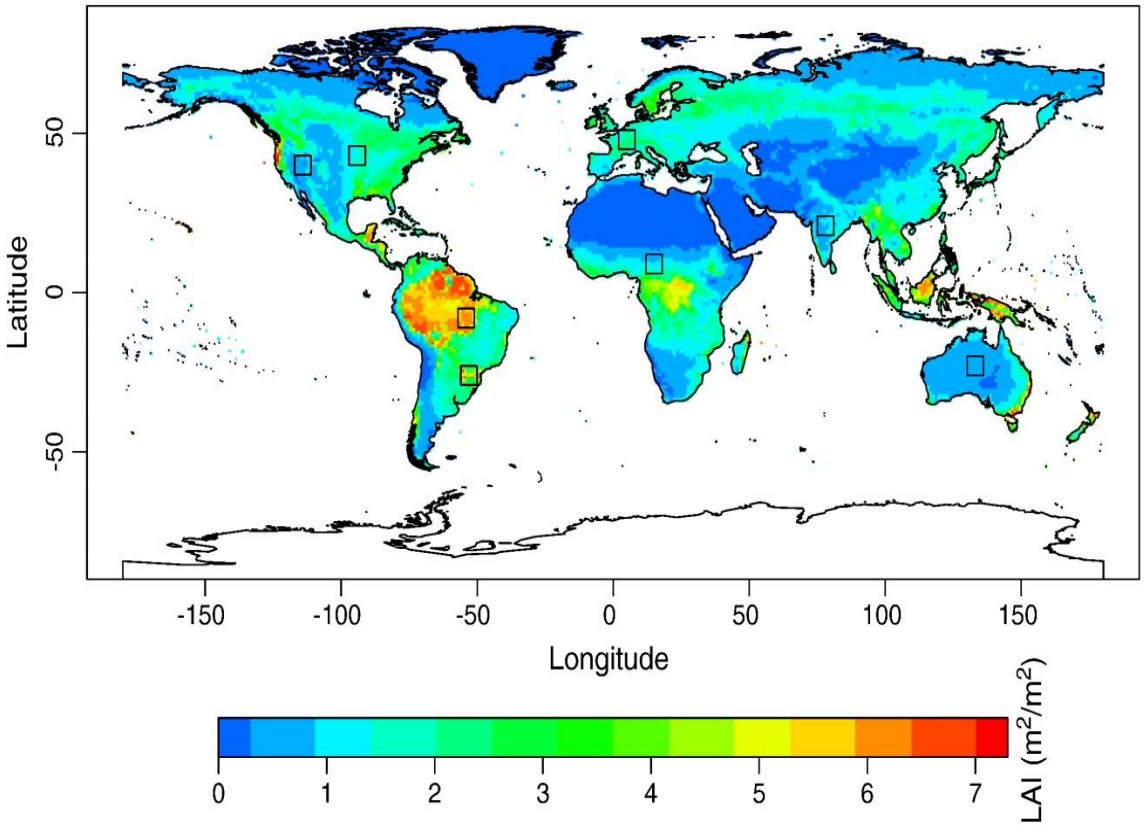

Fig. 4 - 3 *Global map of the long term mean LAI in* $m^2 \cdot m^{-2}$ *(Dirmeyer et al., 2006).*

4.3 Results

4.3.1 Comparison of SMOSL3 ascending and descending overpasses

Original SMOSL3 retrievals obtained from the ascending and descending overpasses were compared to the reference SSM data. In terms of correlation, a better performance of SMOSL3 for ascending orbits compared with descending orbits with respect to the reference can be clearly seen in Fig. 4.4. In much of the world (e.g., central USA, Europe, South America, and South Africa), ascending SMOSL3 retrievals were found to be better correlated to the reference datasets than descending SMOSL3 retrievals. This was expected because at dawn soil is often in near hydraulic equilibrium (Jackson, 1980), and factors affecting SM retrieval, such as vertical soil-vegetation temperature gradients, are minimized. In some

places, however, particularly in India, Eastern USA, Eastern Australia, and the Middle East, descending SMOSL3 retrievals were found to be closer to the reference than the ascending ones. This result could be partly explained by the fact that ascending retrievals over these regions are highly affected by RFI (see Fig. 4.1), which is the main source of errors in the SMOS SSM products (Oliva et al., 2012). As the SMOS antenna is tilted forward by 32°, there is an asymmetry in the patterns of RFI contaminations between ascending and descending passes for a given ground location. For instance, when considering ascending overpasses over a given point in the Central Plains in the USA, the SMOS has a trajectory from South to North. And because the antenna is tilted by 32° toward the North, it picks up RFI emission from the Defense Early Warning (DEW) system in Northern Canada (the DEW line can be seen through the lighter blue band around the USA–Canada border in Fig. 4.1). Conversely, for descending overpasses over the same sites, the tilted antenna is looking in a more southerly direction and is not contaminated by these northern RFI sites. To get a global assessment of the differences between the SSM retrievals for the ascending and descending overpasses, we computed the global averaged value of the RMSD and R coefficient between the SMOSL3 data and the reference; we obtained for ascending: RMSD = 0.18 m^3/m^3 and R = 0.44 and for descending: RMSD = 0.20 m^3/m^3 and R = 0.41. Given that better performances were generally found for ascending retrievals, only SMOSL3 ascending overpasses will be considered in the following.

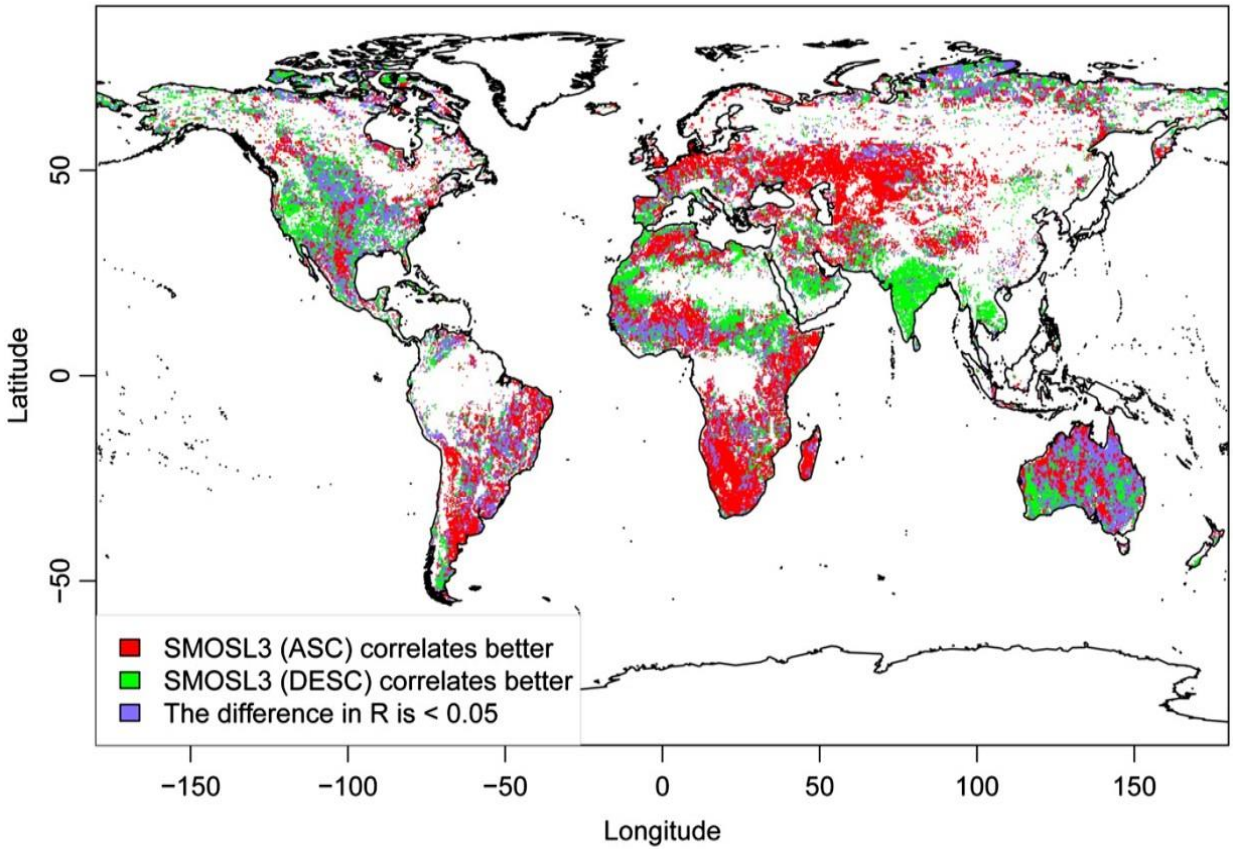

Fig. 4 - 4 *Spatio-temporal comparison between SMOSL3 ascending (ASC) and SMOSL3 descending (DESC) products in terms of correlation with respect to the reference (DAS2) product for the period 03/2010–09/2011. The map shows the areas where either SMOSL3 ASC (red) or SMOSL3 DESC (green) correlates better with the reference. Pixels where ASC and DESC have similar performances (differences in the values of R are lower than 0.05) are shown in blue. Only significant correlations (p-value < 0.05) are presented.*

4.3.2 Comparison of the SSM time series over eight selected sites

The time series of the three SSM products (SMOSL3, AMSRM, and DAS2) are compared in Fig. 4.5 for the eight selected sites described in Table 4.2. The SSM time series were spatially averaged over the whole site and normalized to have the same mean and standard deviation using the method given in Eq. (4.4). The eight sites were selected to illustrate the SSM dynamics in the three products for a variety in vegetation, soil, and climatic conditions (see Fig. 4.2).

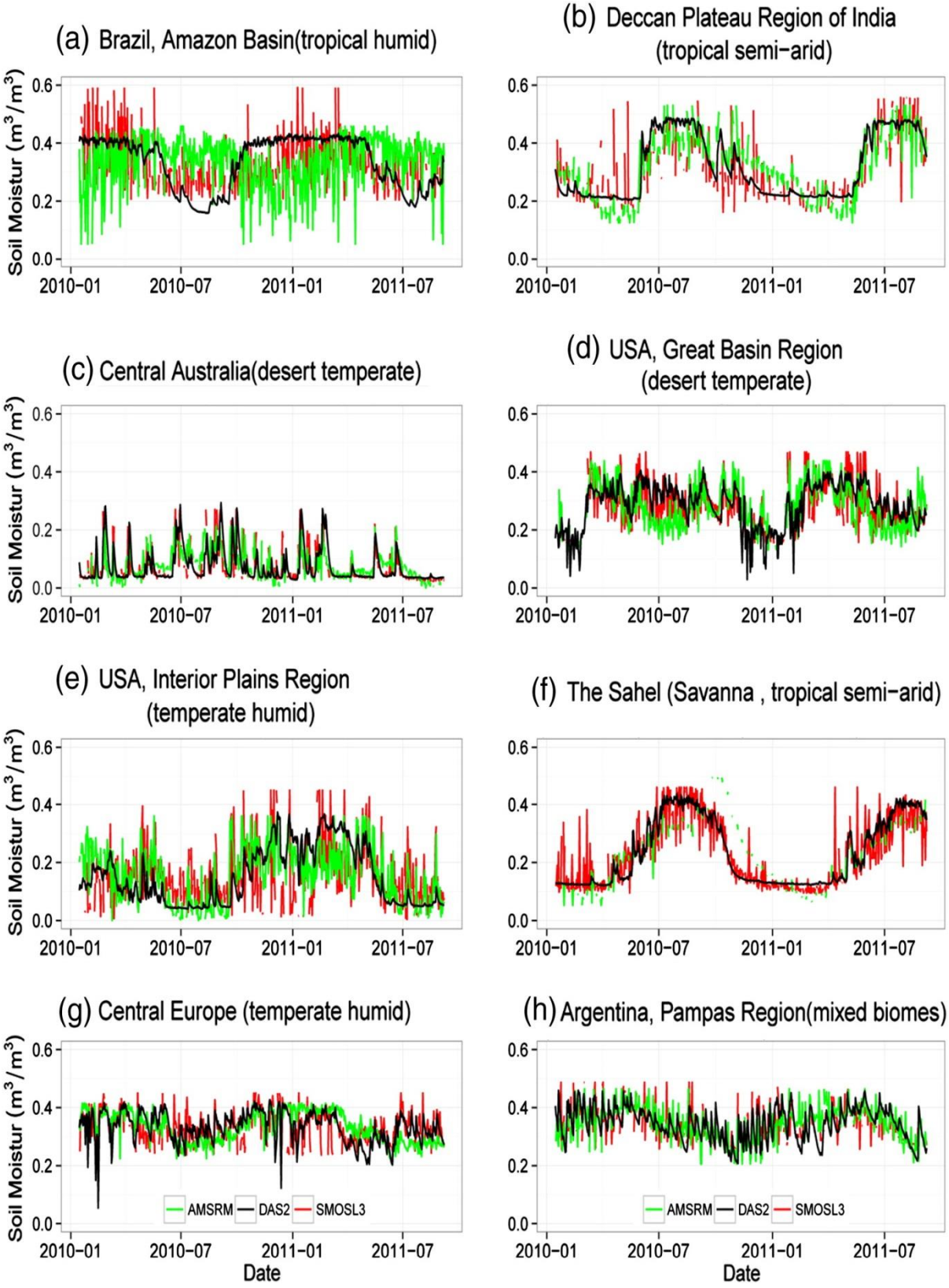

Fig. 4 - 5 *Comparison of the time series of the mean SSM (site averaged) derived from SMOSL3, AMSRM and DAS2 for the period 03/2010–09/2011 for the eight selected sites shown in Fig. 4.2.*

In general, the seasonal dynamics of SSM for the three products were found to be similar. However, over the "tropical humid" site (Fig. 4.5a) the seasonal dynamic of the reference product is better reproduced by the SMOSL3 retrievals. Over this site, it can be seen that the seasonal trend in the AMSRM product is almost opposite to that of the two other products (SMOSL3 and DAS2): increasing trends in AMSRM correspond more or less to decreasing trends in both SMOSL3 and DAS2 and vice versa. Over the same site, it can be seen that there is a large plateau (~ six months from October to April) in the DAS2 values, which cannot be seen for the two other products.

Over the site in India (Fig. 4.5b), a plateau for high values of SSM during the monsoon season can also be seen for DAS2 and not for SMOSL3 and AMSRM, but it is shorter (~ three months) than over the site in the "tropical humid" biome. Also, the transition from wet to dry conditions after the monsoon season is more abrupt for DAS2 than for the remotely sensed SSM values. Over this region, ascending SMOSL3 data are highly impacted by RFI from Northern India and surrounding countries (see Fig. 4.1) but they still reproduce a SSM dynamic, which is in good agreement with the AMSRM and DAS2 datasets.

The site in Central Australia (Fig. 4.5c), is a desert area which has the advantage of being almost free of RFI contaminations at both L- (see Fig. 4.1) and C-bands (Njoku et al., 2005) along with low vegetation and unfrozen conditions in general. In this area, both SMOSL3 and AMSRM were found to be very close to the reference and the very dry conditions were well depicted. There is generally good agreement between all three products in the detection of rain events over this desert area. It should be noted that during the wet season (May, June, July), the declining trend in the SSM time series based on SMOSL3 and DAS2 seems to be slightly steeper than the one retrieved from AMSRM. Also, during rain events, very high values of SSM can be seen for SMOSL3. Such results have already been noted in previous studies and could be explained by water ponding effects when soil is at

saturation during intensive rain events (Al Bitar et al., 2012; Jackson et al., 2012; Wigneron et al., 2012).

Over the two sites in the USA (Fig. 4.5d and e), and in the Sahel (Fig. 4.5f), there is generally good agreement between the three SSM products, but it can be clearly seen that there is a much larger scatter in the remotely sensed products than in the reference one (DAS2). During cold periods in the Great Basin Region in the USA (Fig. 4.5d) very low values can be seen (below 0.1 m^3/m^3). These values can be explained by the effect of soil freezing. In DAS2, the SSM values do not account for the frozen soil water content and its SSM estimates correspond only to the liquid soil water content. These peak values corresponding to "very dry conditions" cannot be seen in SMOSL3 and AMSRM, as frozen soil conditions were flagged and excluded in the remotely sensed products. In the site in Sahel (Fig. 4.4f), there is quite a good agreement between the general seasonal trends of all three SSM products. However, some outliers can be noted for AMSRM, especially when it rains and at the end of the wet season, and the scatter in the SMOSL3 dataset is much larger than that of the two other products.

Finally, results for two sites in wet regions are illustrated in Fig. 4.5g (Central Europe) and Fig. 4.5h (Argentina). Even if the seasonal trend is relatively low over these two sites (SSM varying between 0.3 and 0.4 m^3/m^3), it can be seen that there is good general agreement between all three products. As was found in some previous figures, very high values in SMOSL3 SSM data can be seen in Fig. 4.5g during some rain events and very low values corresponding to freezing conditions can be seen in Fig. 4.5h for DAS2. In summary, all the three products behaved similarly over the different test sites considered in this study, each product having in some cases some caveats either irregular behavior or adversely affected by RFI effects.

4.3.3 Spatial analysis of SSM retrievals at global scale

To get a more global evaluation of the SMOSL3 and AMSRM products, maps of the calculated statistical indicators (correlation coefficient (R) for both original SSM values and anomalies, RMSD and Bias) described in Section 4.3.2 are shown in Fig. 4.6a–h at global scale. In these maps, SMOSL3 and AMSRM were evaluated against the reference dataset (DAS2) for the period 03/2010–09/2011 and only significant correlations are presented. In this study, we consider that the correlation is statistically significant when the p-value is less than the significance level of 0.05 (p-value < 0.05 meaning that the probability of observing such a correlation value by chance is lower than 5%) as considered in several studies in this field (Albergel et al., 2012).

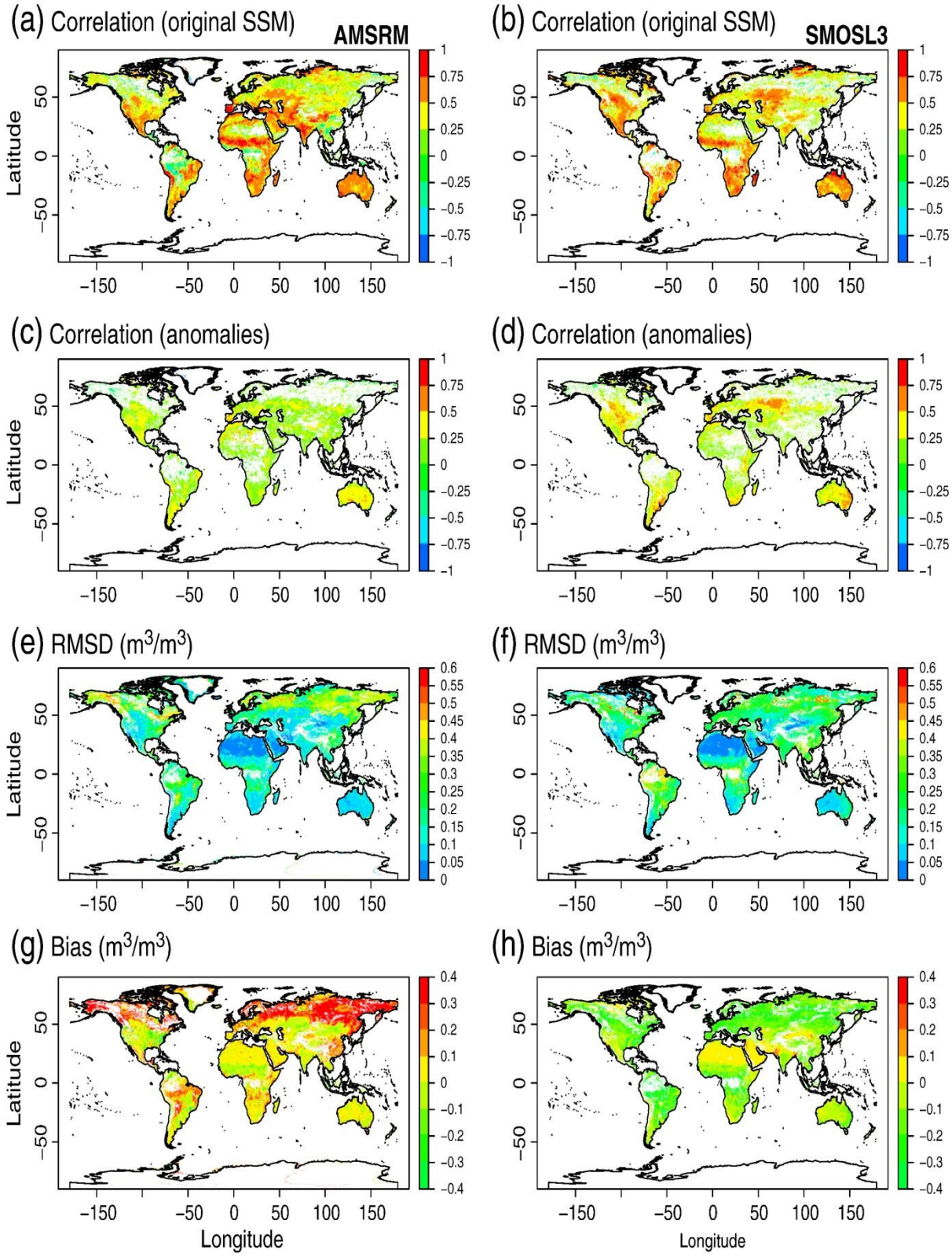

Fig. 4 - 6 *Pairwise comparison between the AMSRM (left panel) and SMOSL3 (right panel) SSM products with respect to the reference DAS2 product in terms of the correlation coefficient (R) based on original SSM data (a and b), the correlation coefficient (R) based on SSM anomalies (c and d), RMSD (m^3/m^3; e and f), and Bias (m^3/m^3; g and h) for the period 03/2010–09/2011. Only significant correlations (p-value < 0.05) are presented.*

In general, it can be seen that the three products have similar spatial patterns over most of the globe, although there are important differences between them in the amplitude of the temporal SSM variations. Fig. 4.6a and b shows that robust correlations between the global remotely sensed and the reference SSM products ($R > 0.5$) were found in the transition zones between wet and dry climates (e.g., Sahel), in the Great Plains (USA), Western Europe, Eastern Australia, India, South Africa, and the south-eastern region of Brazil. This can be explained by the strong seasonal annual cycle of SSM in these regions (Koster et al., 2004b). Conversely, remotely sensed datasets exhibited weak correlations ($R < 0.20$) against the reference in arid regions (e.g., Sahara) due to the small range of variation in the SSM values, which corresponds roughly to the remotely sensed retrieval accuracy (~ 0.04 m^3/m^3). Low correlations in high latitude regions can also be seen in Fig. 4.6a and b, where correlation values (R) drop below 0.25. The significant differences between satellites and model products in high latitude regions may partly be explained by the effect of frozen soil conditions.

Correlation values (R) computed on seasonal anomalies, as described in Section 4.3.4, are shown in Fig. 4.6c and d. It can be seen that the global spatial patterns are relatively similar for both SMOSL3 and AMSRM, with better ability of SMOSL3 to capture the short-term SM variability than AMSRM. The highest values of the R coefficient were found in eastern Australia, extreme South Africa, Western Europe, and Central America while the lowest values were found in the northern tundra region.

A similar distribution of RMSD and bias values was found for both SMOSL3 and AMSRM products (Fig. 4.6e–h). Low RMSD and bias values were found in deserts and semi-arid regions (e.g., the Sahara, the Arabian Peninsula, extreme South Africa, and Central Australia), while high RMSD and bias values were found in high latitude regions (e.g., in Northern Canada, Alaska, Northern Europe, and Siberia). Large differences between the remotely sensed and the reference SSM products were also found in tropical regions. In Fig.

4.6g and h, relatively similar patterns can be noted for both SMOSL3 and AMSRM at global scale but the values of the biases are quite different: a strong overestimation of the reference SSM values can be noted for AMSRM, especially in the high latitude and desert regions, while a strong underestimation can be noted for SMOSL3.

To better identify the spatial differences in the results obtained for SMOSL3 and AMSRM, Fig. 4.7a and b shows the areas where SMOSL3 correlates better with the reference than AMSRM (red), where AMSRM correlates better with the reference than SMOSL3 (green) and where the difference in the correlation coefficient (R) between both SMOSL3 and AMSRM is less than 0.05 (blue). The top panel shows results for the original SSM datasets, while the bottom panel shows results for anomalies, i.e. areas where either SMOSL3 or AMSRM better captured the short-term variability in the reference SSM values. In these maps only significant values are plotted (p-value < 0.05). In general, it can be seen that better correlations with DAS2 were obtained with SMOSL3 over regions with high to moderate vegetation density (e.g., in parts of Amazonia, Eastern Australia and the North-Central US). These latter regions are known to be little contaminated by RFI effects (see Fig. 4.1). On the other hand, it can be seen that AMSRM shows better correlations with DAS2 than SMOSL3 in areas with low to moderate vegetation density and where there is a strong seasonality in the SSM variability (e.g., India, Western Australia, Sahara, and Arabian Peninsula). Poor results were also obtained systematically for SMOSL3 in regions known to be strongly contaminated by RFI effects (Middle East, Southern Europe, China, and India).

When looking at anomalies, AMSRM and SMOSL3 have relatively similar performances over dry regions, but better correlations with the reference were obtained for SMOSL3 over most of the grid cells.

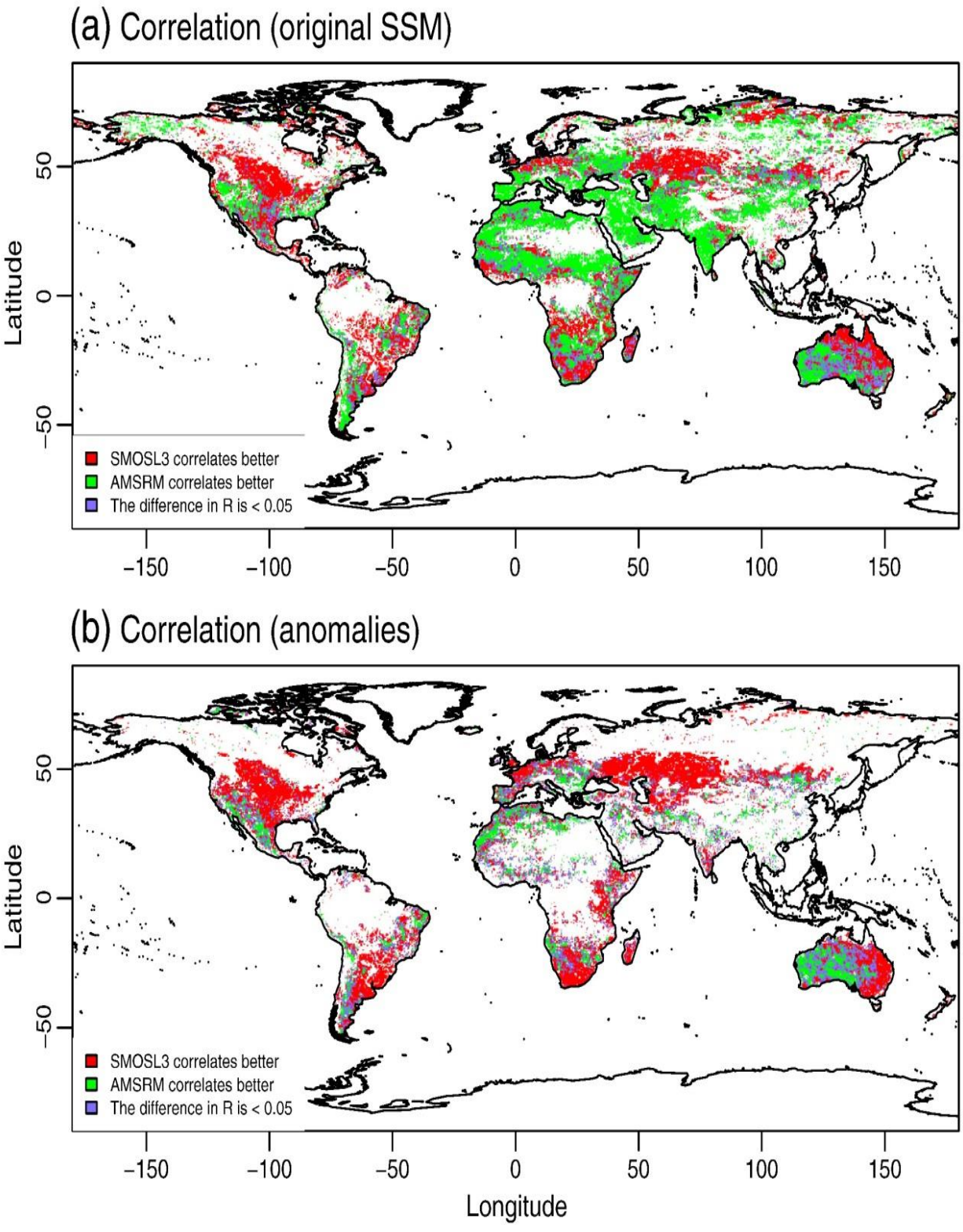

Fig. 4 - 7 *Pairwise comparison between the SMOSL3 and AMSRM SSM products with respect to the reference DAS2 SSM product in terms of correlations based on the original SSM data (a) or on SSM anomalies (b) for the period 03/2010–09/2011. The map show the areas where either SMOSL3 (red) or AMSRM (green) correlates better with the reference. Pixels where SMOSL3 and AMSRM have similar performances (differences in the values of R are lower than 0.05) are shown in blue. Only significant correlations (p-value < 0.05) are presented.*

4.3.4 Biome influence

To investigate more in depth the dependence of the results shown in Fig. 4.6 and Fig. 4.7 on the vegetation and climatic conditions, the statistical indicators were averaged for the twelve types of biomes described in Section 4.3.5 and illustrated in Fig. 4.2. The results are shown in Fig. 4.8a–d in terms of correlation (R) for original SSM data and anomalies, RMSD, and bias.

The distributions of the correlation (R) and RMSD values as a function of biome types are quite similar for both SMOSL3 and AMRSM (Fig. 4.8a–c). In terms of correlation values computed from the original SSM data (Fig. 4.8a), the best results were obtained for biomes with relatively sparse vegetation covers ("Mediterranean warm", "Mediterranean cold", "temperate semi-arid", "tropical semi-arid", etc.), while the poorest results were found in Northern environments ("tundra", "boreal semi-arid", and "boreal humid"). Yet, the results are quite different for the "Tropical humid" biome, where performances of SMOSL3 were more coherent with DAS2 (R = 0.42) compared to the results found for AMSRM (R = 0.15).

Fig. 4.8b shows that the mean correlation coefficients computed from the SSM anomalies are lower than the mean correlation coefficients computed from the original SSM, as the covariations imposed on all three datasets by the seasonal forcing are largely filtered out in SSM anomalies. The general pattern of the distribution of the R values as a function of the biomes is similar to the one obtained for the original SSM data. It seems that the short-term variability in the SSM values is better detected by SMOSL3: better performances were obtained for SMOSL3 over all biomes, even if the correlation values are relatively small.

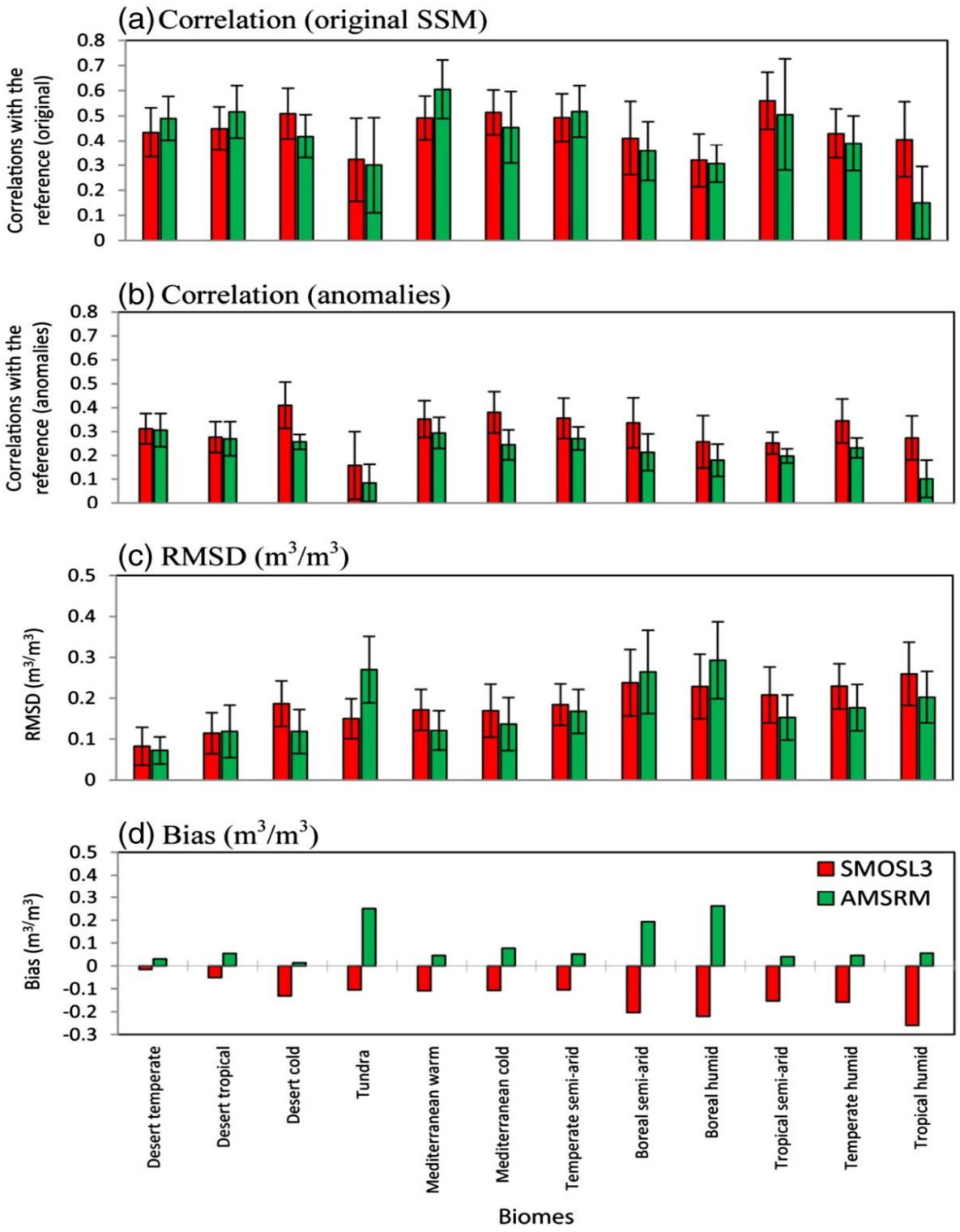

Fig. 4 - 8 *Distribution of the statistical indicators between SMOSL3 (red) and AMSRM (green) and the reference as a function of biome types for the period 03/2010–09/2011. Statistics in terms of correlation coefficient based on original SSM data (a), correlation coefficient based on SSM anomalies (b), RMSD (m^3/m^3; c), and Bias (m^3/m^3; d) are computed at each grid cell and then averaged by biome type. The biome types are defined from the classification given by Chesworth (2008) shown in Fig. 4.2. Error bars represent mean ± standard deviation (SD) and only significant correlations (p-value < 0.05) are considered in the analysis.*

In Fig. 4.8c, confirming previous results, the poorest performances (corresponding to the largest RMSD values), were obtained again in Northern environments (“tundra”, “boreal semi-arid”, and “boreal humid”) for both SMOSL3 and AMSRM, while the best results (smallest RMSD values) were obtained in desert regions (“desert temperate”, “desert tropical”) and in semi-arid regions. As discussed previously, in desert areas, the range in the SSM values simulated in DAS2 is relatively small and this fact partly explains the low values of RMSD computed.

Finally, Fig. 4.8d shows that biases with respect to the reference dataset are opposite for SMOSL3 and AMSRM. In all biomes, AMSRM overestimates SSM DAS2 values while SMOSL3 underestimates them. Moreover, the bias between remotely sensed and reference SSM varies substantially across biomes. The bias is very large in northern environments for both SMOSL3 and AMSRM but it is also large in humid regions (“temperate humid”, “tropical humid”) for SMOSL3. The lowest biases were found in deserts (“desert temperate”, “desert tropical”, and “desert cold”) and in semi-arid regions (“temperate semi-arid”, “Mediterranean warm” and “Mediterranean cold”) for both SMOSL3 and AMSRM.

4.3.5 Influence of leaf area index (LAI)

Previous results showed that vegetation plays a key role in the performance results of the SMOSL3 and AMSRM products. To analyze in more detail the effect of vegetation, we computed the distribution of the correlation values as a function of the LAI. We chose to focus our study on the R correlation indicator as correlation is of particular interest for many hydrologic and atmospheric applications (Koster et al., 2009). In Fig. 4.9a and b, the correlation values shown in Fig. 4.6a and b (for original and anomaly SSM data) were averaged according to the values of LAI illustrated in the global map shown in Fig. 4.3. The results for both original SSM data (Fig. 4.9a) and anomalies (Fig. 4.9b) show that the

performance of the remotely sensed SSM products (i.e., SMOSL3 and AMRSM) is strongly related to the distribution of the LAI values. In Fig. 4.9a, it can be seen that the values of the correlation coefficient (R) decrease almost linearly with the mean value of LAI for both SMOSL3 and AMSRM. The rate of the decrease is much larger for AMSRM than for SMOSL3. For AMSRM the value of R decreases from $R \approx 0.45$ to negative correlation values ($R \approx -0.1$) as LAI increased from about 1 to 7. For the same increase in LAI values, the decrease in R for SMOSL3 is more limited: from $R \approx 0.4$ to $R \approx 0.3$. However, it should be noted that AMSRM provides slightly better performances than SMOSL3 when LAI is lower than 1 (i.e. over sparse vegetation covers), which corresponds to almost 50% of the pixels considered in this global analysis.

In Fig. 4.9b, the same analysis is shown for anomalies. It can be seen that better performances were obtained for SMOSL3, whatever the range of LAI values. Moreover, for this latter product, the correlation values remain stable ($R \approx 0.3$) as LAI values increase. Conversely, the values of the R coefficient decrease rapidly and continuously for AMSMR as LAI values increase: $R \approx 0.25$ for $LAI \approx 1$ down to $R \approx 0.03$ for $LAI \approx 7$.

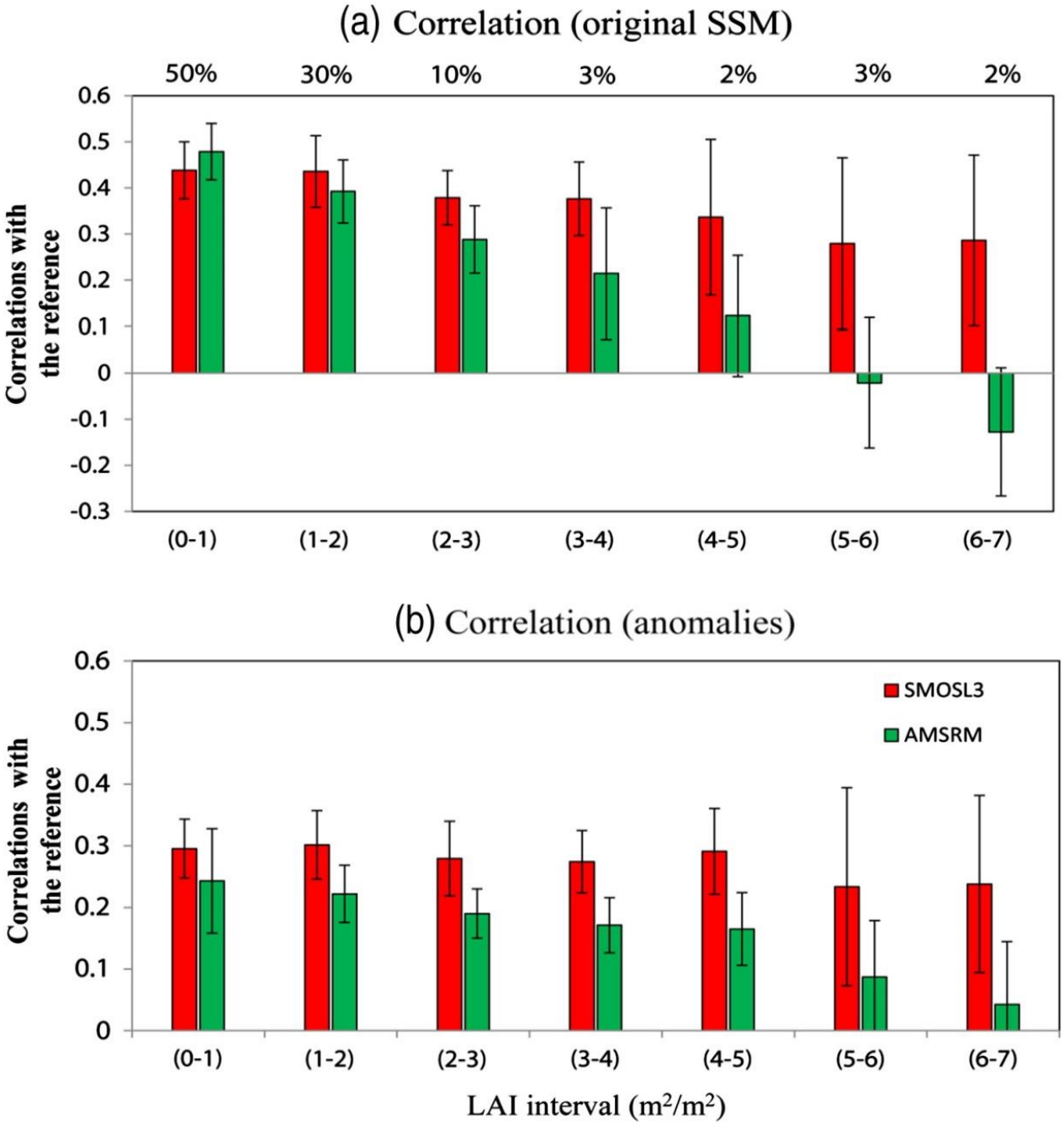

Fig. 4 - 9 *Distribution of the correlation coefficient (R) between SMOSL3 (red), AMSRM (green) and the reference dataset (DAS2) for the original SSM data (a) and anomalies (b) as a function of LAI for the period 03/2010–09/2011. Statistics are computed at each grid cell and then averaged by LAI intervals. The values of LAI were extracted from the map of (Dirmeyer et al., 2006) shown in Fig. 4.3. The percentage value (top of figure) provides the cover fraction (%) over continental surfaces corresponding to each LAI interval. Error bars represent mean ± standard deviation (SD) and only significant correlations (p-value < 0.05) are considered in the analysis.*

4.4 Discussion and conclusions

This study investigated the performances of two remotely sensed SSM products (SMOSL3 and AMSRM) with respect to a reference SSM product (DAS2) at global scale, with 0.25° spatial sampling and a daily time step. The study was made during the whole period of common availability of the SMOS and AMSR-E products, i.e. after the test periods during the commissioning phase of SMOS and before AMSR-E stopped producing data (03/2010–09/2011).

Both AMSRM and SMOSL3 generally showed a good agreement with the reference dataset and successfully captured the seasonal SSM variations present in the reference DAS2 product. For instance, SMOSL3 and AMSRM performed well (in terms of correlation) in the transition zones between wet and dry climates and over semi-arid regions (e.g., Indian subcontinent, Great Plains of North America, Sahel, Eastern Australia, and South-eastern regions of Brazil). It is particularly important that the two remotely sensed SSM products being compared give consistent and correct results in these areas, where SM has been recognized to exert a strong influence on the weather/climate (e.g., Koster et al., 2004a; Taylor et al., 2012; Teuling et al., 2010). Conversely, both SMOSL3 and AMSRM exhibited weak correlations with the reference data in dry regions (e.g. Sahara, Arabian Peninsula, and Central Australia). These results could be related to the low range of variations in SSM in these regions, which roughly corresponds to the expected retrieval accuracy of the remotely sensed products (~ 0.04 m^3/m^3).

We found quite opposite results in terms of bias for SMOSL3 and AMSRM: over all biomes, AMSRM overestimated SSM compared to the reference, while SMOSL3 underestimated SSM. The analysis of the SSM anomaly time series, obtained by removing the seasonal cycle, showed that the short-term SSM dynamics were better captured by SMOSL3 than by AMSRM at global scale. In addition, considering a variety of biomes, both SMOSL3

and AMSRM showed lowest performances in northern environments (“tundra”, “boreal semi-arid”, and “boreal humid”), while the best performances were found over biomes with relatively sparse vegetation covers (“Mediterranean warm”, “Mediterranean cold”, “temperate semi-arid”, “tropical semi-arid”, etc.). In the “tropical humid” biome, SMOSL3 was found to be much better correlated to DAS2 than AMSRM.

The results confirmed that vegetation plays a key role in the performance evaluation of the SMOSL3 and AMSRM SSM products. Over areas with sparse vegetation, with LAI values lower than 1, both SMOSL3 and AMSRM had relatively good and similar performances. However, for higher LAI values, SMOSL3 had a consistent performance, whereas the performance of AMSRM quickly deteriorated with the increase in foliar abundance.

The fact that better performances could be obtained with SMOS (operating at L-band) than with AMSR-E (operating at C-band) over vegetated areas is not surprising. However this study presents one of the first studies confirming this effect with observations from sensors in space. In the passive microwave domain, L-band has long been considered as an optimal frequency to monitor SSM. When a vegetation layer is present over the soil surface, it attenuates the soil emissions and adds its own contribution to the emitted radiation measured by passive microwave radiometers. The retrieval algorithm attempts to decouple the effects of soil and vegetation in order to provide an estimation of SSM. However, as vegetation effects increase with increasing frequency (Calvet et al., 2011), the correction for vegetation effects is more complex at C-band (~ 6.6 GHz for AMSR-E) than at L-band (~ 1.4 GHz for SMOS). Moreover, SMOS has multi-angular capabilities which make it, theoretically, more efficient for decoupling the soil and vegetation effects than mono-angular spatial radiometers such as AMSR-E (Wigneron et al., 2000). The combination of both a L-band system and multi-angular capabilities for SMOS compared to a C-band system and monoangular capabilities for

AMSR-E might explain the better performance of SMOS over biomes with dense vegetation cover (e.g., "tropical humid") in Fig. 4.8a and b or for LAI values larger than 1 in Fig. 4.9a and b. However, it should be noted that AMSRM had comparable performances to SMOSL3 (better performances if we consider the original SSM data and slightly lower performances if we consider anomalies) over sparse vegetation covers (with LAI $\leq$ 1), which represent more than 50% of the pixels considered in this global study. Future works will address in more depth the possibilities to exploit the complementary capabilities of both SMOS and AMRS-E to retrieve SSM over a gradient of vegetation density and to produce a coherent long term SSM product based on passive microwave sensors.

Some other aspects should be considered in this evaluation. As noted in the Introduction Section, the effective SM sampling depth at L-band (~ 0–3 cm) is larger than at C-band (~ 0–1 cm). Over a shallower soil layer (0–1 cm) SSM is more prone to quick time variations, especially during drying-out periods, due to weather events (rainfall, wind, high insolation, etc.) than over deeper soils. This effect may lead to lower correlations with SSM measurements or retrievals, which are not made at the exact same time or over larger soil sampling depth. Moreover, in the present study, the sampling depth corresponding to the SMOSL3 SSM product (~ 0–3 cm) is closer to that of the reference (0–7 cm for DAS2), than the sampling depth of AMRSM. Therefore, the mismatch between the sampling depths of the different products considered in this study is more detrimental for AMRSM, though it is present for both satellite data sets.

The effect due to the mismatch between the sampling depths of the different products may have an impact in the statistical indicators used in this study but it cannot fully explain the large and contrasting biases found between both the AMRSM and SMOSL3 products and the DAS2 reference. The positive bias in the AMSRM retrievals can be partially explained by the absence of correction in the NASA-VUA algorithm for open water bodies. It can also be

caused by a wrong estimation of the effective temperature in NASA-VUA algorithm over northern regions, leading to positive bias in satellite retrievals (Owe et al., 2008). In contrast, the negative bias found in SMOSL3 is consistent with the results obtained in previous studies (Al Bitar et al., 2012; Albergel et al., 2012; Dall'Amico et al., 2012; Jackson et al., 2012; Lacava et al., 2012; Sanchez et al., 2012) comparing SMOS retrievals with in situ measurement networks in different regions of the world which all relied on the first release of the SMOS retrieval algorithm. RFI may increase the brightness temperatures (TB) measured by SMOS, leading to smaller retrieved SSM values and, thus, to a negative bias (Oliva et al., 2012). However, Wigneron et al. (2012) showed that, even though no bias could be observed in the measured TB data over the VAS site in Spain, a strong negative bias could be noted in the SMOS SSM retrievals. Thus, the negative bias found in the SMOS SSM products (Fig. 4.8d) is likely to be related to some issues in the retrieval algorithm (e.g., accounting for pixel heterogeneity, use of auxiliary data, etc.) or in the L-MEB (L-band Microwave Emission of the Biosphere) forward modelling. For instance, recent results showed that the use of the dielectric soil model developed by Mironov et al. (2012), instead of the model of Dobson et al. (1985) led to improved results (the bias decreased by about 0.04 m^3/m^3 at global scale) and the New L2 SSM shows almost no negative bias. Moreover, improvements will be made by better accounting for the effects of litter, surface roughness, effective soil temperature, etc. (Grant et al., 2007; Saleh et al., 2009).

Finally, it should be noted that even though the reference product used in this study (SM-DAS-2 from ECMWF) was found to be very reliable according to some recent studies (Albergel et al., 2012), estimates of SSM from LDAS cannot be considered as “ground truth” (Albergel et al., 2013a). One must keep in mind that when using them to evaluate other SSM products, the interpretation of the results is hampered by their own accuracy (the accuracy of LDAS itself and its required inputs such as the atmospheric forcing, observations, etc.). For

instance, Albergel et al. (2012) pointed out some non-realistic representation of SM in ECMWF products in some regions of the world (e.g. the Tibetan plateau), due to shortcomings in the description of soil characteristics, in the pedotransfer functions employed, and the difficulty of representing soil spatial heterogeneity.

Chapter V

5. Global-scale comparison of passive (SMOS) and active (ASCAT) satellite based microwave soil moisture retrievals with soil moisture simulations (MERRA-Land)[2]

[2] This chapter has been published as: A. Al-Yaari, J.-P. Wigneron, A. Ducharne, Y.H. Kerr, W. Wagner, G. De Lannoy, R. Reichle, A. Al Bitar, W. Dorigo, P. Richaume, A. Mialon, Global-scale comparison of passive (SMOS) and active (ASCAT) satellite based microwave soil moisture retrievals with soil moisture simulations (MERRA-Land), Remote Sensing of Environment, Volume 152, September 2014, Pages 614-626, ISSN 0034-4257, http://dx.doi.org/10.1016/j.rse.2014.07.013.

5.1 Introduction

Soil moisture is a key variable in land surface and atmospheric systems, and has been identified as one of the "Essential Climate Variables" (Global Climate Observing System, 2010). It plays a fundamental role in the partitioning of precipitation into infiltration and runoff and the partitioning of incoming radiation into sensible and latent heat (Daly & Porporato, 2005; Koster et al., 2004b; Western et al., 2002). Knowledge about global spatial-temporal variability of soil moisture is thus fundamental to improve our understanding of the interactions between the hydrosphere, biosphere, and the atmosphere.

Until now, global-scale studies on this topic were mostly based on modeled data (Seneviratne et al., 2006; Taylor et al., 2012). With the recent advances in global soil moisture retrievals from satellites in the past decade, we are now in the position to study the related processes based on observations. Global surface soil moisture (SSM) datasets have been produced based on active and passive microwave satellite observations, including the Soil Moisture and Ocean Salinity (SMOS) and the Advanced Scatterometer (ASCAT) SSM products (Bartalis et al., 2007a; Kerr et al., 2010; Njoku et al., 2003; Owe et al., 2008). See also Kerr (2007) and Wagner et al. (2007) for a detailed review.

SMOS is the first passive satellite specifically designed to measure SSM (and sea surface salinity) on a global scale (Kerr et al., 2010; Kerr et al., 2012; Walker et al., 2001). Since its launch in November 2009, SMOS has been recording brightness temperatures at L-Band (1.4 GHz) with an average spatial resolution of 43 km. The SMOS SSM products are derived from the multi-angular and full-polarization brightness temperature observations, using multi-orbital retrieval techniques (Kerr et al., 2012). SMOS SSM is available either in global mode (referred here to as SMOSL3; Jacquette et al., 2010 and Kerr et al., 2013b) or in swath mode from the European Space Agency (ESA) at the Data Processing Ground Segment (DPGS) (Level 2) (Kerr et al., 2013a). In this study, we used the SMOS level 3 (SMOSL3) as

its projection (EASE grid) and format (NetCdf) simplified considerably the analysis while retaining all the level 2 characteristics. The ASCAT sensor is a C-band scatterometer (5.2 GHz) operating on-board the Metop since 2006. Wagner et al. (1999b) proposed a method to retrieve SSM from ERS-1/2 scatterometer backscatter measurements. Naeimi et al. (2009) later improved it and the method is now referred to as the Vienna University of Technology (TU-Wien) change detection algorithm, which is presently employed for ASCAT data.

Since these global SSM observations are relatively new, they have not yet been sufficiently evaluated and their accuracy is still unknown to some degree. It is therefore important (i) to investigate the consistency of the remote sensing products with independent SSM estimates, such as from land surface modelling, and (ii) to characterize their uncertainties. A better knowledge of the skill and uncertainties of the retrievals will help not only to improve the individual products, but also to optimize the fusion schemes adopted to create multi-sensor products, e.g. the essential climate variable (ECV) soil moisture product generated within ESA's Climate Change Initiative (Dorigo et al., 2012; Liu et al., 2011; Liu et al., 2012). This merged product has shown large potential for validating land surface models (Albergel et al., 2013a; Loew et al., 2013) and studying land–atmosphere–biosphere interactions (Barichivich et al., 2014; Miralles et al., 2014).

To date, the validation of the SMOS and ASCAT SSM products has been focused on different regions of the world, primarily by comparing to in situ observations, which are limited in space and time (e.g., Al Bitar et al., 2012; Albergel et al., 2009; Albergel et al., 2012; Brocca et al., 2010; Brocca et al., 2011; Leroux et al., 2011; Sanchez et al., 2012; Sinclair & Pegram, 2010; Su et al., 2011). A few studies compared microwave based SSM products to model simulations over larger domains (Al-Yaari et al., 2014; Dorigo et al., 2010; Draper et al., 2013; Parrens et al., 2012), thereby improving the knowledge of errors in the

satellite data across space and time. At the global scale, there is only, to date, one dedicated SM study that has been conducted to evaluate the SMOS level 2 (SMOSL2) against ASCAT SSM products. Leroux et al. (2013a) performed, at the global scale, a comparison between the SMOSL2 SSM products against the Advanced Microwave Scanning Radiometer for EOS (AMSR-E) and ASCAT SSM products taking the European Centre for Medium-Range Weather Forecasts (ECMWF) model simulations as a benchmark for the year 2010. This study showed that SMOS provided best results over Australia, North America, and Central Asia in terms of triple collocation errors.

Here, we investigate the consistency of the latest SMOS and ASCAT products, against each other and compared to an independent reference, based on land surface SSM simulations. The analysis is conducted at the global scale, using newly re-processed SSM products, and for the period 05/2010–12/2012. SSM data from the supplemental land surface analysis of the Modern-Era Retrospective analysis for Research and Applications (MERRA-Land) are used as the reference in this study. MERRA-Land data are suitable due to their global availability and their ability to capture the SSM spatial and temporal variability (Reichle et al., 2011). In addition, Albergel et al. (2013a) and Yi et al. (2011) showed very good performance of MERRA-Land in comparison with other reanalysis products and in situ data.

The objectives of this study are (i) to compare distinct SSM retrieval products derived from satellite-based microwave observations at two different frequency bands, L-band (~ 1.4 GHz) for the passive SMOSL3 product and C-band (~ 5 GHz) for the active ASCAT product, (ii) to characterize the global error structure of the SMOSL3 and ASCAT SSM products, and (iii) to understand the spatio-temporal variability of SSM over a variety of biomes and climate regimes at global scale. To achieve these objectives this paper presents (i) a classical time series analysis using a temporal correlation analysis of original SSM and

anomalies, unbiased root mean square difference (ubRMSD), and mean bias, (ii) a space–time analysis using Hovmöller diagrams, and (iii) a triple collocation error (TCE) estimation to characterize the spatial distribution of errors in the SMOS and ASCAT retrievals.

The three SSM datasets and the statistical methods used for the evaluation are presented in Section 5.2, results are presented in Section 5.3, and discussion and the main conclusions are presented in Section 5.4.

5.2 Materials and methods

5.2.1 Surface soil moisture datasets

Table 5.1 summarizes the main characteristics of the three SSM datasets (i.e. ASCAT, SMOSL3, and MERRA-Land) considered in this study. ASCAT and SMOSL3 were evaluated with respect to MERRA-Land during the period (05/2010–12/2012).

Table 5 - 1 The main characteristics of the ASCAT, SMOS, and MERRA-Land SSM products.

Soil moisture datasets	Incidence angle (°) of remotely-sensed observations	Data type and frequency	Sampling depth and unit	Temporal coverage	Reference
SMOS level 3 (SMOSL3)	0–55	Remotely sensed (L-band, passive)	~ 0–3 cm (m^3/m^3)	2010–present	Jacquette et al. (2010)
ASCAT	55	Remotely sensed (C-band, active)	~ 0–1 cm (m^3/m^3)	2006–present	Bartalis et al. (2007a)
MERRA-Land	–	Reanalysis	0–2 cm (m^3/m^3)	1980–present	Reichle et al. (2011)

5.2.1.1 SMOSL3

The SMOS mission was launched in November 2009 to monitor SSM at a depth of about 3 cm, with an accuracy of at least 0.04 m^3/m^3 at the global scale, and with a 3-day revisit at the equator (Kerr et al., 2001; Kerr et al., 2010). SMOS operates at L-band, with ascending overpasses at 06:00 Local Solar Time (LST) and descending overpasses at 18:00 LST (Kerr et al., 2012).

The SMOS level 3 (SMOSL3) SSM products, re-processed global maps of SSM at different temporal resolutions, 1-day, 3-day, 10-day, and monthly, have been recently released by the Centre Aval de Traitement des Données (CATDS; http://catds.ifremer.fr/). The daily SMOSL3 SSM products were used in this study. The main principle of the retrieval algorithm is the same as the one used by ESA for producing the operational level 2 SSM products (Kerr et al., 2012; Wigneron et al., 2007), that is, multi-angular observations are used to simultaneously retrieve SSM (directly quantified in m^3/m^3) and the vegetation optical depth at nadir (τ-NAD) based on a standard iterative minimization approach of a cost function (Wigneron et al., 2000). SMOSL3 ascending retrievals were selected in this study as they have generally been proven to be more accurate than SMOSL3 descending retrievals (Al-Yaari et al., 2014; Alyaari et al., 2014). The SMOSL3 datasets provide flags that can be used to screen out questionable SSM retrievals (Jacquette et al., 2010; Kerr et al., 2013b), in particular because of radio-frequency interferences (see Section 5.2.2 for more details).

It should be noted that, in the present study, we used the latest version available at CATDS. In the near future, new versions of the SMOSL3 products will be produced based on re-processing activities.

5.2.1.2 ASCAT

ASCAT is a real-aperture radar instrument that operates at C-band (5.255 GHz) on-board the Metop satellite since 2006, which crosses the equator at 21:30 LST for the ascending overpass and at 09:30 LST for the descending overpass.

In this study, we used SSM products generated with the WARP5.5 software provided by TU-Wien, which is the latest version of the algorithm used to produce this SSM dataset. As for SMOSL3, we only considered here morning overpasses, as previous findings indicated that the ascending ASCAT overpass retrievals are less accurate than the descending (i.e., morning) ones (e.g., Brocca et al., 2010).

ASCAT SSM data are provided in terms of degree of saturation, that is, in relative units ranging between 0 (dry) and 100 (saturated). These extremes correspond, respectively, to the lowest and highest values of the observed backscatter over the first few centimeters of soil (< 3 cm). As the two other SSM products (SMOSL3 and MERRA-Land) used in this study are expressed in volumetric units, the ASCAT SSM index was converted to volumetric units (m^3/m^3).

Multiplying the degree of saturation by the soil porosity (expressed in m^3/m^3) gives a direct estimate of the volumetric SSM content in m^3/m^3. The value of the soil porosity was estimated from global soil texture and hydraulic soil properties derived, as described by Balsamo et al. (2009), from the Food and Agriculture Organization digital (FAO) soil map (FAO, 2003; Su et al., 2011). The porosity map was provided at a resolution of $5' \times 5'$ and it was interpolated to 25 km, which is consistent with the ASCAT soil moisture resolution. In the ASCAT product, several flags are provided along with the SSM values, including a noise value (ERR) quantifying the uncertainty associated with the retrieved SSM value and a flag associated with the wetland fraction or to the topographic complexity. Readers are directed

to Wagner et al. (1999)and Naeimi et al. (2009) for more details on the TU-Wien algorithm and to Wagner et al. (2013) for a full review on the ASCAT SSM Product.

5.2.1.3 MERRA-Land

The Modern-Era Retrospective analysis for Research and Applications (MERRA) is a global atmospheric reanalysis data product that integrates information from a broad variety of in situ and remote sensing observations of the atmosphere (Rienecker et al., 2011). MERRA-Land is a supplemental data product of land surface hydrological fields (Reichle et al., 2011). The MERRA-Land product is a land-only, off-line, replay of a revised version of the MERRA land model component that benefits from (i) corrections to the precipitation forcing based on merging a gauge-based data product from the NOAA Climate Prediction Centre with MERRA precipitation and (ii) updated parameter values in the rainfall interception model. These changes correct known limitations in the MERRA surface meteorological forcing and yield improved estimates of land surface conditions (Reichle et al., 2011; Reichle, 2012). MERRA-Land SSM is associated with the 0–2 cm (topmost) soil layer and is available hourly at a spatial resolution of 2/3° longitude by 1/2° latitude. The MERRA-land SSM simulations at 6 am and 9 am were averaged and considered as a reference for both SMOS and ASCAT. We used the gridded SSM product expressed in volumetric units (m^3/m^3).

5.2.2 Pre-processing

Prior to the evaluation, SMOSL3 and ASCAT were filtered based on associated quality flags. Several values are associated with the ASCAT SSM retrievals, as described by (Naeimi et al., 2009): a noise error (ERR), which is based on Gaussian error propagation and which is related to the sensor characteristics and incidence angle uncertainty, an estimated standard deviation of the backscatter signal, etc. The ASCAT data were screened out to remove observations with a noise error (ERR) greater than 14% (Draper et al., 2012). The

SMOSL3 product provides a Data Quality indeX (DQX) and a probability of radio frequency interference (RFI). The DQX values, which are provided in volumetric SSM units, quantify the error in the SSM retrieval and the brightness temperature measurement accuracy. RFI originates, for example, from satellite transmissions, aircraft communications, radar, or TV radio-links and contaminates the passive microwave emissions from Earth (Njoku et al., 2005; Oliva et al., 2012). Fig. 5.1 shows the global spatial pattern of the probability of RFI occurrence in the SMOS observations, presented as average of the probability of RFI occurrences during the period (2010–2012). In the present study, RFI effects were filtered out, using RFI flags provided in the SMOSL3 product. SMOSL3 SSM values were excluded if one of the following conditions was fulfilled (i) DQX > 0.06, (ii) DQX is equal to fill value, or (iii) percentage of radio frequency interference (RFI_Per) > 30%.

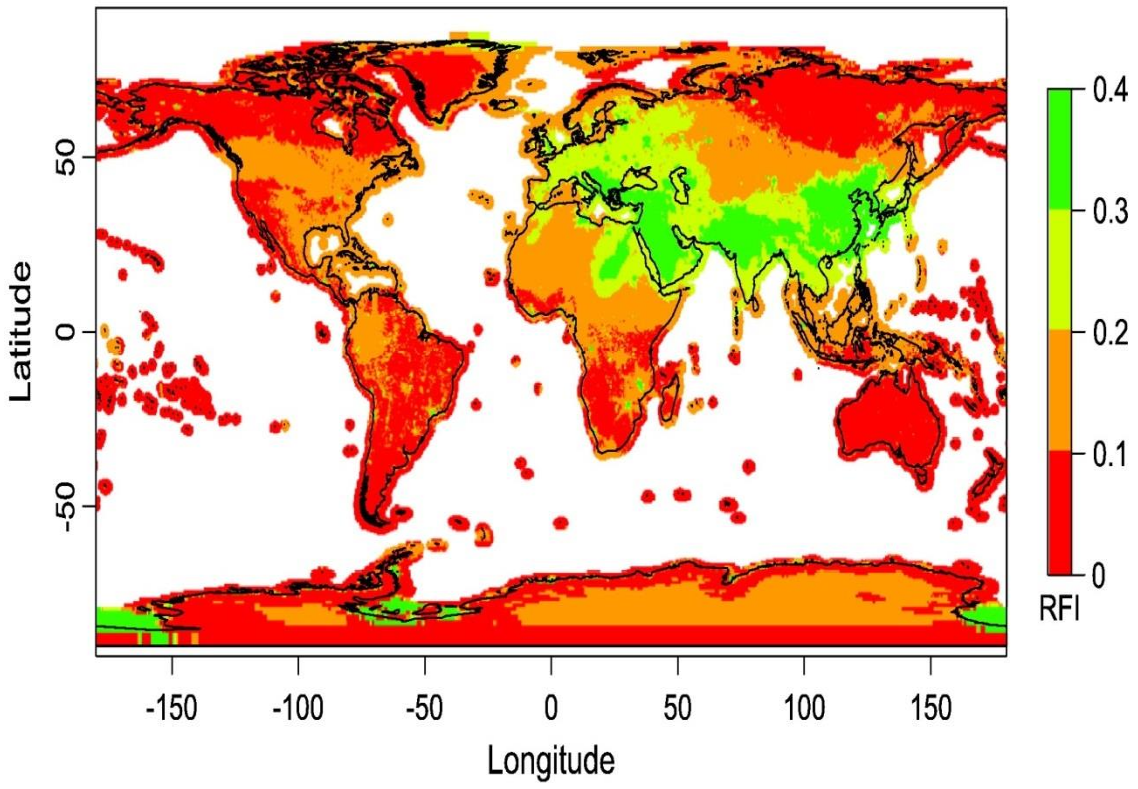

Fig. 5 - 1 *Three year average (2010–2012) of probability of radio frequency interference occurrences in the SMOS observations.*

ASCAT, SMOSL3, and the reference MERRA-Land dataset are distributed on different grids and formats. In this study, a nearest neighbor approach (e.g., Draper et al., 2011; Rüdiger et al., 2009) was used to re-project all the datasets onto a regular 0.25° × 0.25° grid. Finally, all the three SSM datasets were screened, applying additional static masks, to remove grid cells with (i) steep mountainous terrain, based on a topographic complexity flag (provided with the ASCAT data) greater than 10% (Draper et al., 2012), (ii) open water, identified as having a wetland fraction (provided with the ASCAT data) greater than 5%, and (iii) frozen soil conditions, identified as having soil temperatures (top layer) below 276 K, obtained from MERRA-Land.

It should be noted that all the statistical indicators were computed only when all the three SSM data were available from the different datasets and therefore the number of ASCAT and SMOSL3 SSM data used in the time series are identical, which is illustrated in Fig. 5.2.

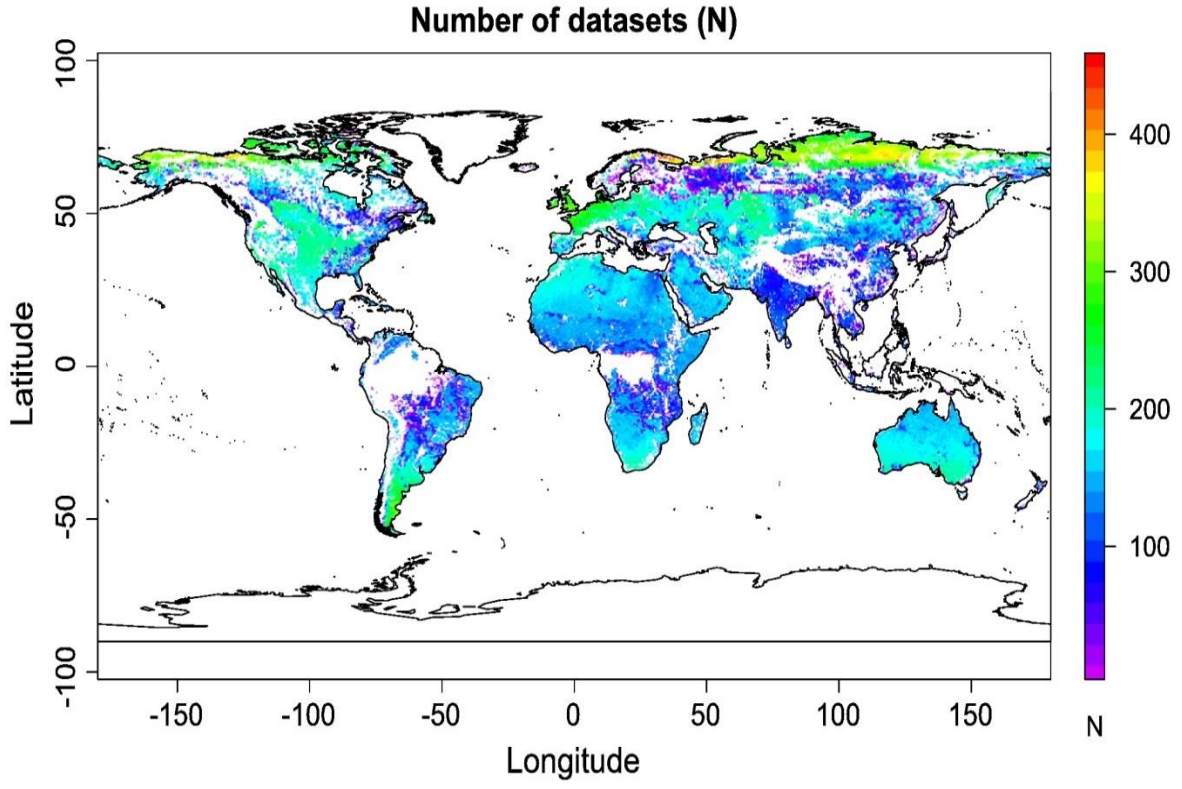

Fig. 5 - 2 *Number of data used to compare the SMOSL3 and ASCAT datasets.*

5.2.3 Comparison using classical metrics

Three classical metrics were calculated between pairs of the remotely sensed (SSM_{RS}) and reference SSM products(SSM_{REF}): (i) Pearson correlation coefficient (*R*), (ii) bias, and (iii) unbiased root mean squared difference (ubRMSD). The equations for the calculation of the three indicators are given as follows (Albergel et al., 2012; Brocca et al., 2011; CECR, 2012):

$$R = \frac{\sum_{i=1}^{n}(\mathrm{SSM_{REF(i)}} - \overline{\mathrm{SSM_{REF}}})(\mathrm{SSM_{RS(i)}} - \overline{\mathrm{SSM_{RS}}})}{\sqrt{\sum_{i=1}^{n}(\mathrm{SSM_{REF(i)}} - \overline{\mathrm{SSM_{REF}}})^2 \sum_{i=1}^{n}(\mathrm{SSM_{RS(i)}} - \overline{\mathrm{SSM_{RS}}})^2}} \qquad 5-1$$

$$\mathrm{Bias} = \overline{(\mathrm{SSM_{RS}} - \mathrm{SSM_{REF}})} \qquad 5-2$$

$$\mathrm{RMSD} = \sqrt{\overline{(\mathrm{SSM_{RS}} - \mathrm{SSM_{REF}})^2}} \qquad 5-3$$

$$\mathrm{unRMSD} = \sqrt{\mathrm{RMSD^2} - \mathrm{Bias^2}} \qquad 5-4$$

where *n* is the number of SSM data pairs, the overbar represents the mean operator, SSM_{REF} is the reference SSM (MERRA-Land), and SSM_{RS} is the satellite-based SSM product (SMOSL3 or ASCAT). We use the term ubRMSD rather than ubRMSE (root mean squared error) since the MERRA-Land SSM values also contain errors and cannot be considered as the "true" SSM values (Entekhabi et al., 2010).

All the above statistical indicators were computed for the original SSM values, expressed in volumetric units (m^3/m^3), and for SSM monthly anomalies for the correlation indicators only. The anomaly time-series are designed to assess the impact of seasonal effects that can unrealistically increase the degree of correlation between two time series (Scipal et al., 2008) and to explore the ability of the ASCAT/SMOSL3 SSM products to capture the short-term variability in the SSM time series. Following Albergel et al. (2009), the anomalies

$SSM_{anom}(t)$ were calculated as the difference from the mean for a sliding window of 5 weeks, the difference was further scaled to the standard deviation:

$$SSM_{anom}(t) = \frac{SSM_{or}(t) - \overline{SSM_{or}(t-17:t+17)}}{\sigma[SSM_{or}(t-17:t+17)]} \qquad 5-5$$

where the overbar and σ symbols denote the temporal mean and standard deviation operators, respectively, $SSM_{or}(t)$is the original remotely sensed/reference SSM value at time *t*; for a sliding window of 5 weeks corresponding to the time interval [*t* − 17 days, *t* + 17 days].

Global maps of *R* (original and monthly anomaly), ubRMSD, and bias were calculated for all common pixels on a daily basis between the reference and the SMOSL3 and ASCAT SSM time series. To investigate the effects of the vegetation and to simplify the interpretation of the correlation maps (original and anomalies), the metrics were also averaged according to the long-term mean leaf area index (LAI) values obtained from the Global Soil Wetness Project (Dirmeyer et al., 2006), displayed in Fig. 5.3.

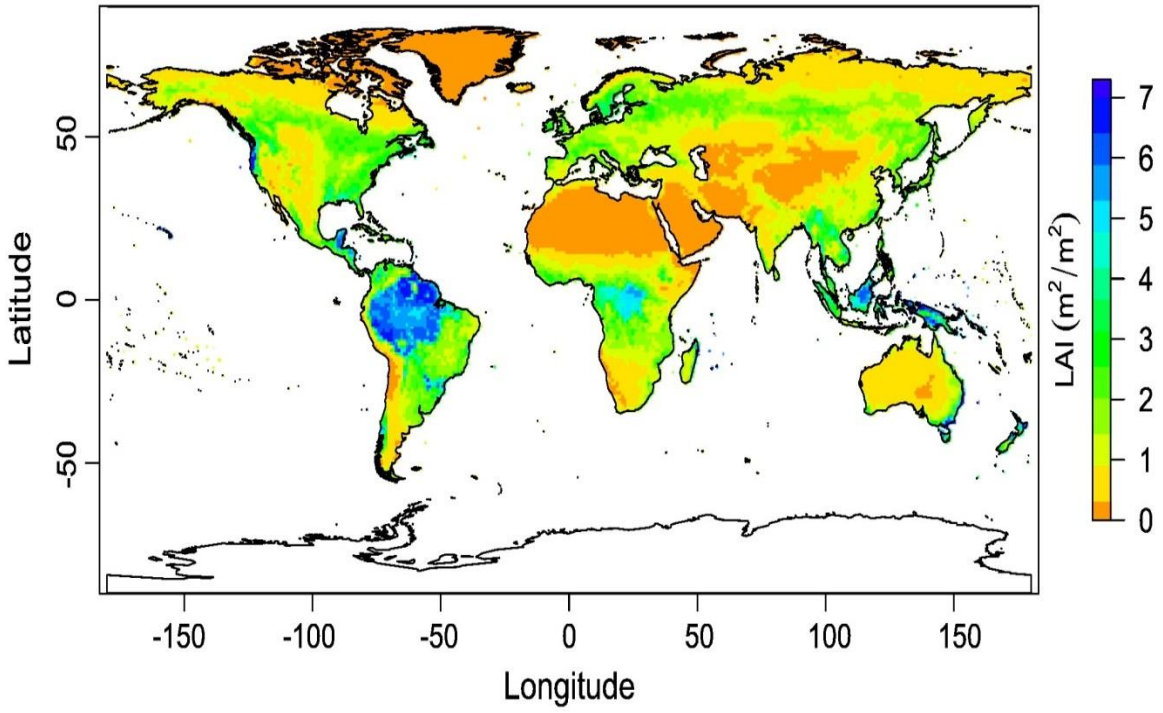

Fig. 5 - 3 *Global distribution of the long term mean leaf area index (LAI) (Dirmeyer et al., 2006).*

5.2.4 Comparison using Hovmöller diagrams (space–time distribution)

A Hovmöller diagram (HD) is a two-dimensional plot that shows the time–latitude variations of a longitudinally averaged variable (Hovmöller, 1949). Here, we used the HD method to compare the spatio-temporal patterns of SSM for SMOS, ASCAT and MERRA-Land at the global scale. The diagrams helped us to investigate the consistency and differences between the three SSM products.

5.2.5 Comparison using triple collocation error model

The triple collocation error model (TCE) is a powerful statistical tool to estimate the RMSD of a set of at least three linearly related data sources with uncorrelated errors. Stoffelen (1998) introduced the TCE model to evaluate wind vector datasets derived from a model, buoy measurements and scatterometer observations. Scipal et al. (2008) later

used the TCE to evaluate SSM datasets derived from models and satellites. Then, other authors (e.g., Dorigo et al., 2010; Draper et al., 2013; Loew & Schlenz, 2011; Miralles et al., 2010; Parinussa et al., 2011a) also used the TCE method to characterize the errors of SSM derived from models and remote sensing.

In this study, TCE was applied to the ASCAT, SMOS, and MERRA-Land SSM products, and specifically to their long-term anomalies, using 2010–2012 time series centered on its mean. The estimated SSM anomalies at time t from product i (denoted $\theta_i(t)$ in the following) are linked to the unknown true SSM $\theta(t)$ by a multiplicative bias term β_i together with an error ε_i:

$$\theta_1(t) = \beta_1 \theta(t) + \varepsilon_1 \qquad 5-6$$

$$\theta_2(t) = \beta_2 \theta(t) + \varepsilon_2 \qquad 5-7$$

$$\theta_3(t) = \beta_3 \theta(t) + \varepsilon_3 \qquad 5-8$$

Note that since centered time series (anomaly from Eq. (5.5) without normalization) are used here, a constant bias term is not needed in Eqs. (5.6), (5.7) and (5.8). One of the datasets has to be defined as the reference dataset, namely MERRA-Land in this study, with $\beta_1 = 1$. The other two datasets can then be calibrated using $\theta_i^* = \theta_i/\beta_i$ and $\varepsilon_i^* = \varepsilon_i/\beta_i$ in Eqs. (5.6), (5.7) and (5.8) to obtain:

$$\theta_1^* = \theta + \varepsilon_1^* \qquad 5-9$$

$$\theta_2^* = \theta + \varepsilon_2^* \qquad 5-10$$

$$\theta_3^* = \theta + \varepsilon_3^* \qquad 5-11$$

where θ_2^* and θ_3^* are the rescaled measurements, and ε_2^* and ε_3^* are the rescaled random errors (see, e.g. Draper et al., 2013). By pairwise subtraction of Eqs. (5.9), (5.10) and (5.11) and subsequent averaging over the cross-multiplied differences, we obtain:

$$\varepsilon_1^* = < (\theta_1^* - \theta_2^*)(\theta_1^* - \theta_3^*) > \qquad 5-12$$

$$\varepsilon_2^* = < (\theta_1^* - \theta_2^*)(\theta_2^* - \theta_3^*) > \quad 5-13$$

$$\varepsilon_3^* = < (\theta_1^* - \theta_3^*)(\theta_2^* - \theta_3^*) > \quad 5-14$$

where < > is the long-term mean, and the square root of the estimated ε_i^{2*} are the triple collocation errors estimates.

The above derivation, and hence the validity of the TCE analysis, is based on the assumptions that the errors ε_i of the three datasets are uncorrelated, and that the three datasets can be linearly modeled as in Eqs. (5.6), (5.7) and (5.8) (Dorigo et al., 2010; Janssen et al., 2007; Scipal et al., 2010). Because the three datasets are largely independent, TCE can be expected to perform well, but any residual error cross-correlations among the datasets would result in biased error estimates (Yilmaz & Crow, 2012). Finally, to obtain statistically reliable results we restricted our analysis to grid cells where at least 100 observations were available from each dataset.

5.3 Results

5.3.1 Spatial Analysis of SSM retrievals at the global scale

Fig. 5.4 shows global maps of the time series correlation coefficient *R* for original SSM values and monthly anomalies (with only significant correlations, i.e., $p < 0.05$), the ubRMSD, and the bias (Section 5.2.3). In these maps, SMOSL3 (right panels) and ASCAT (left panels) were evaluated against the MERRA-Land reference dataset at each pixel over the 05/2010–12/2012 period.

In general, the metrics for SMOSL3 and ASCAT show a similar spatial correspondence with the MERRA-Land SSM over most of the globe. Fig. 5.4a and b shows that strong correlations (*R* is generally greater than ~ 0.5) between the global remotely sensed and the reference SSM products are found in the transition zones between wet and dry climates (e.g., Sahel), in the Great Plains (USA), western Europe, Australia, India,

Kazakhstan, and south-eastern Brazil. This can be explained by the strong seasonal annual cycle of SSM in these regions (Koster et al., 2004b).

Conversely, remotely sensed datasets exhibited weak correlations (*R* is generally less than 0.15) against the reference in arid regions due to the small range of natural variation in the SSM values. The correlations can even be negative between the ASCAT and MERRA-Land data pairs in some arid sites (e.g., Saudi Arabia and North Africa; Fig. 5.4a). Low correlations for both SMOSL3 and ASCAT in high latitude regions can also be seen in Fig. 5.4a and b, where the *R* values drop below 0.20.

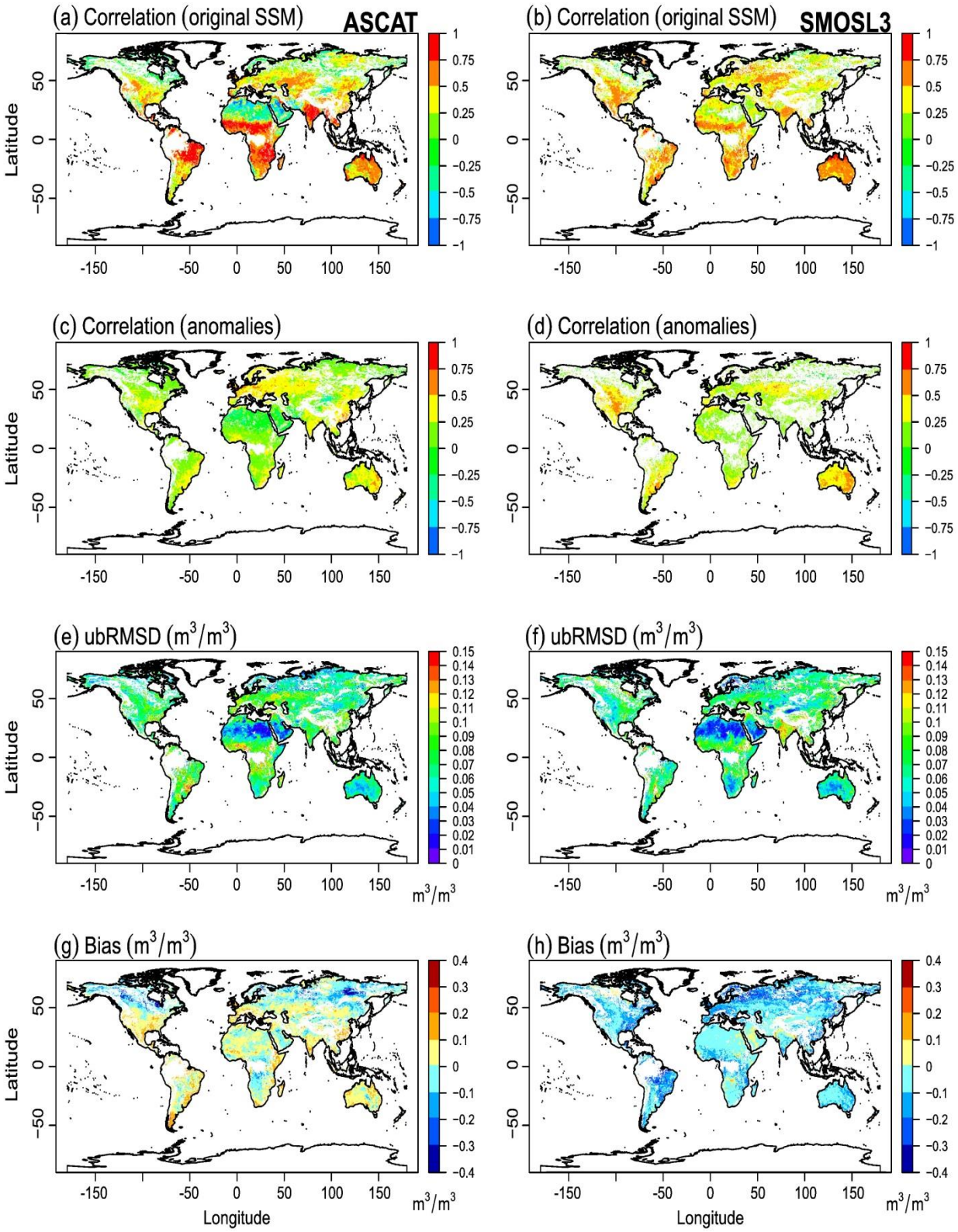

Fig. 5 - 4 *Pairwise comparison between the SMOSL3 (right panel) and the ASCAT (left panel) SSM datasets with respect to the reference MERRA-Land product in terms of the correlation coefficient (R) based on original SSM data (a and b), on SSM monthly anomalies (c and d), ubRMSD (m^3/m^3; e and f), and bias (m^3/m^3; g and h) during the 05/2010–12/2012 period. Only significant correlations ($p < 0.05$) were plotted.*

Time series correlation values (R) computed for seasonal anomalies, as described in Section 5.2.3, are shown in Fig. 5.4c and d. The global spatial patterns are again relatively similar for both SMOSL3 and ASCAT, with a slightly better ability of SMOSL3 to capture the short-term SSM variability of the reference than ASCAT in Central America and Australia, while ASCAT was found to be slightly better in Europe, India, and parts of China. For both datasets, rather high correlation values ($R > 0.5$) with the reference were found in eastern Australia, southern South Africa, Western Europe, and Central America, whereas low values were found in the northern Arabian Peninsula, North Africa, and tundra regions.

Fig. 5.4e–h shows a similar distribution of ubRMSD and bias values for both SMOSL3 and ASCAT products. The ubRMSD values show a clear spatial distribution: low ubRMSD and bias values were found in deserts (e.g., the Sahara, the Arabian Peninsula, southern South Africa, and Central Australia), whereas high values of ubRMSD and bias were found for both instruments in boreal regions, locations near the Equator, and India (only for SMOSL3 because of RFIs).

Due to the model-specific nature of the long-term mean values of soil moisture (Koster et al., 2009), large mean differences (biases) between the remotely sensed and the reference SSM products can be expected. Furthermore, bias may be caused by a wrong estimation of SSM when the satellite footprint includes small water bodies, as was found by (Bartsch et al., 2012; Gouttevin et al., 2013; Kerr et al., 2012). In Fig. 5.4g and h, relatively similar bias patterns can be noted for both SMOSL3 and ASCAT at global scale. However, the values of the biases are quite different: in comparison with the MERRA-Land SSM values, higher SSM values can be noted for ASCAT, especially in the boreal regions, whereas lower SSM values can be noted for SMOSL3. The positive bias, found mainly at high latitude regions, in the ASCAT retrievals which is associated to wetter months (i.e. summer periods) can be partially explained by errors in the FAO database used to convert the ASCAT degree

of saturation to volumetric water content where values for a few pixels in the northern hemisphere exceed 0.6 m^3/m^3.

Fig. 5.5a and b compares the areas where SMOSL3 correlates better with the reference than ASCAT (red), and where ASCAT correlates better with the reference than SMOSL3 (green). Looking at original datasets, it can be seen that better correlations with MERRA-Land were obtained with ASCAT over regions with high to moderate vegetation density and in regions where there is a strong seasonality in the SSM variability (e.g., India, Eastern Australia and the North-Central US, locations near the equator). On the other hand, SMOSL3 shows better correlations with MERRA-Land than ASCAT in areas with low to moderate vegetation density (e.g., Western Australia, Sahara, and North America). The latter regions are known to be slightly contaminated by RFI effects (see Fig. 5.1).

When looking at monthly anomalies (Fig. 5.5b), ASCAT shows higher correlations with the reference than with SMOSL3 over regions such as Central Europe, China and India, which are known to be highly contaminated by RFI effects (see Fig. 5.1). With the exception of these regions, SMOSL3 exhibits higher correlations with the reference over most of the grid cells.

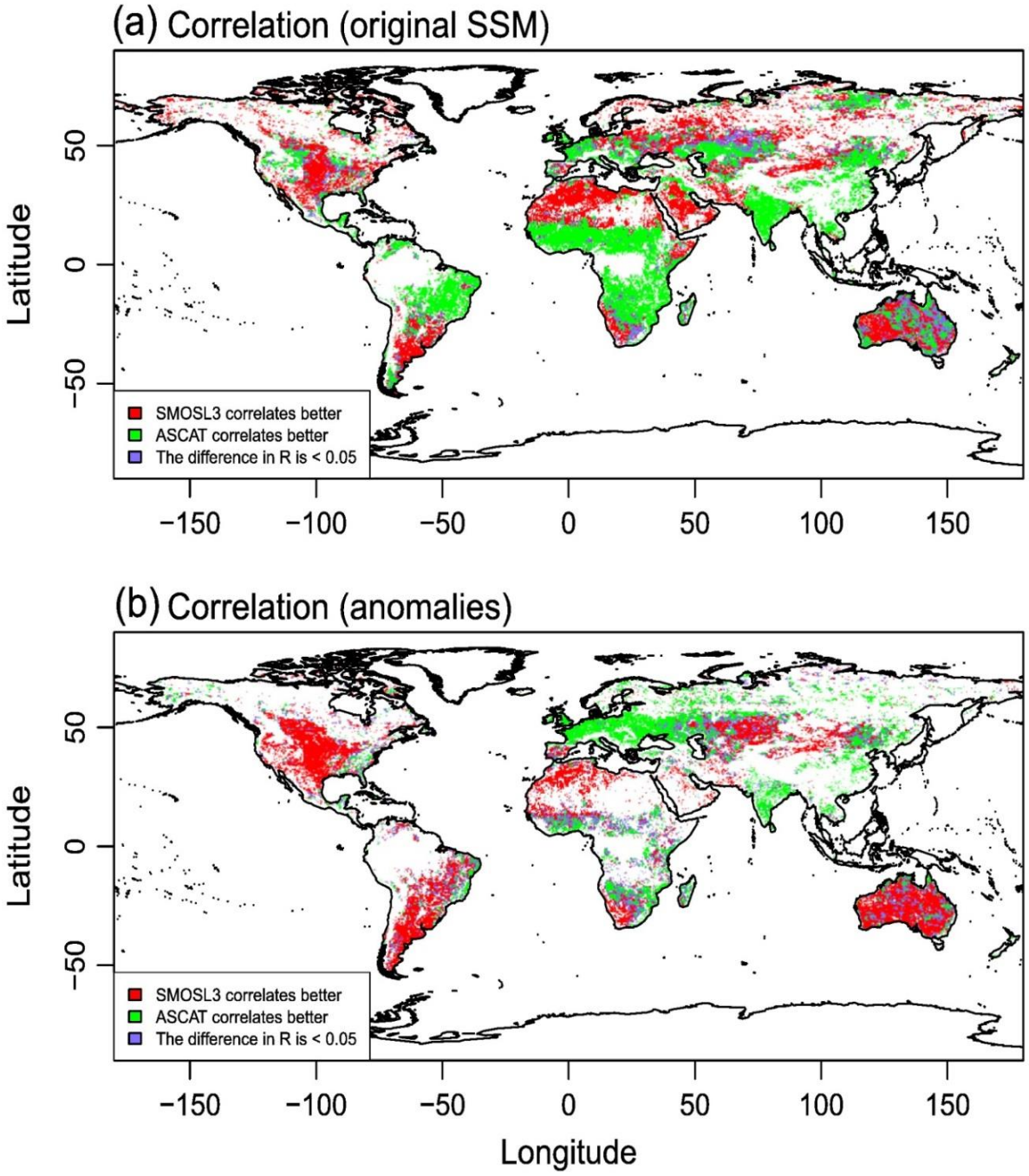

Fig. 5 - 5 *Pairwise comparison between the ASCAT and SMOSL3 SSM datasets with respect to the reference SSM product in terms of correlations based on the original SSM data (a) or on SSM monthly anomalies (b) during the 05/2010–2012 period. The maps show the areas where either ASCAT (green) or SMOSL3 (red) correlates better with the reference. Pixels where the difference in the values of R is lower than 0.05 appear in blue. Only significant correlations ($p < 0.05$) were plotted and white areas indicate that the correlation is not significant.*

5.3.2 Influence of leaf area index (LAI)

To analyze the effect of vegetation, we computed the average correlation coefficient as a function of the global long term mean LAI, using values of the Global Soil Wetness Project (Dirmeyer et al., 2006). Note that the MERRA-Land simulations use the monthly LAI climatology from the Global Soil Wetness Project 2 (GSWP-2). The results for both the original SSM data (Fig. 5.6a) and the anomalies (Fig. 5.6b) show that the consistency of the remotely sensed SSM products with the reference (MERRA-Land) is strongly related to LAI. In Fig. 5.6a, it can be seen that the values of R increase almost linearly with LAI for ASCAT, from $R \approx 0.18$ to $R \approx 0.55$ as LAI increases from about 1 to 7. For SMOSL3, on the other hand, R values remain relatively constant as LAI increases, with values between ~ 0.32 and 0.44. A decrease in R can be noted for SMOSL3 when LAI is higher than ~ 4, leading to higher correlation values to the reference with ASCAT, but this corresponds to a very low fraction of the total number of pixels considered here (less than 5%, after screening for uncertain retrievals). In contrast, SMOSL3 provides higher correlation values with the reference than ASCAT when LAI is lower than 1 (i.e. over sparse vegetation covers), which corresponds to almost 50% of the pixels considered in this global analysis, and similar correlation coefficients R are obtained for SMOSL3 and ASCAT for intermediate LAI values ($1 \leq \text{LAI} \leq 3$).

In Fig. 5.6b, the same analysis is shown for monthly anomalies. As noted above, they exhibit lower correlations to the reference data ($R \approx 0.25$) than the original data, for both SMOSL3 and ASCAT anomalies. The correlation differences between the two remotely sensed products are also much weaker than in Fig. 5.6a, even if SMOSL3/ASCAT remains better correlated to MERRA-Land for lower/higher values of the LAI.

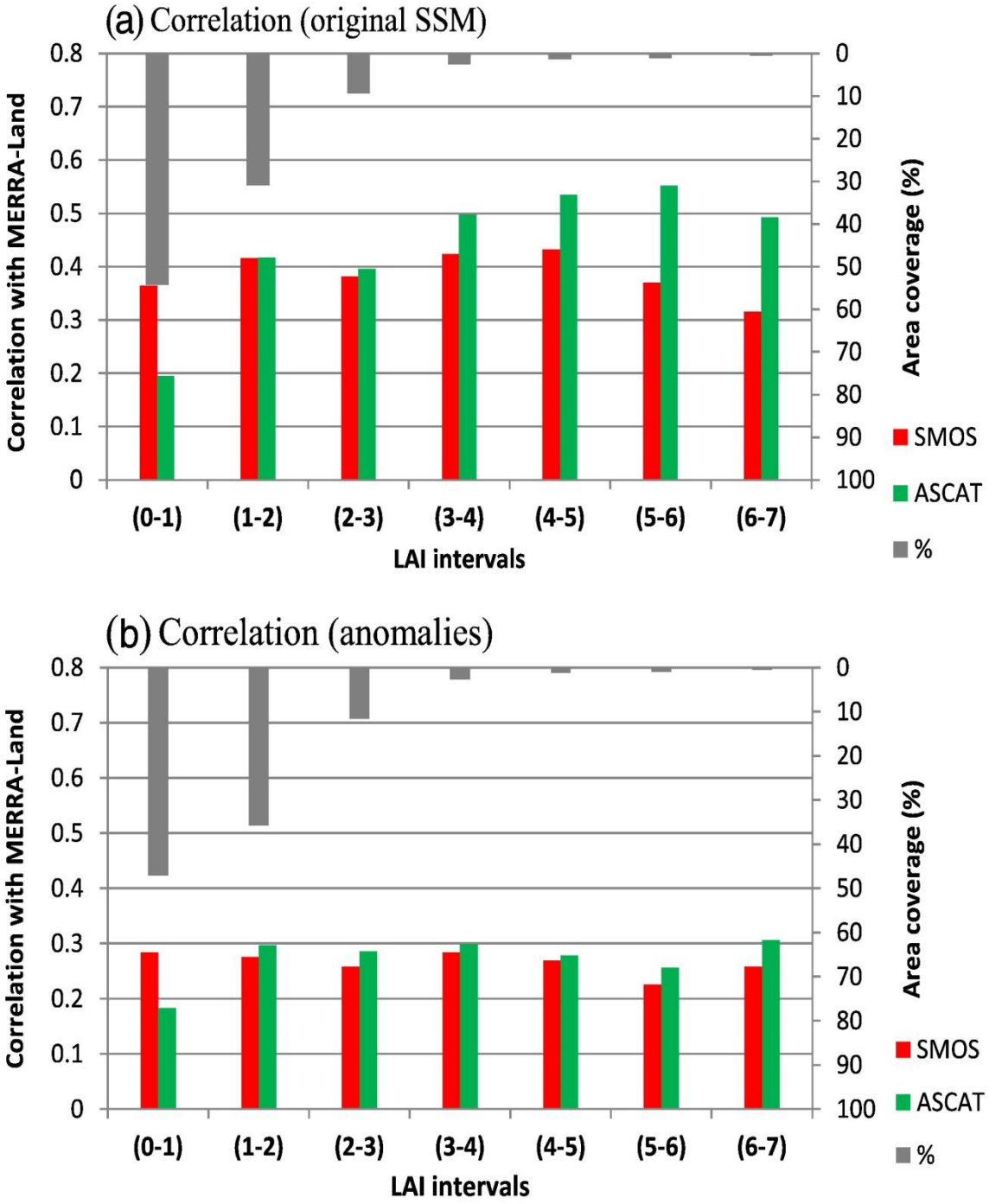

Fig. 5 - 6 *Distribution of the correlation coefficient (R) between ASCAT (green), SMOSL3 (red) and the reference product (MERRA-Land) for the original SSM data (a) and monthly anomalies (b) as a function of leaf area index (LAI) during the 05/2010–2012 period. Significant correlations ($p < 0.05$) were computed at each grid cell and then averaged by LAI intervals, which were extracted from the global distribution of LAI displayed in Fig. 5.3. The area coverage provides the cover fraction (%) over continental surfaces corresponding to each LAI interval.*

5.3.3 Hovmöller diagrams

SSM strongly varies spatially and temporally, and this variability depends mainly on latitude and season (Schlosser & Milly, 2002). It is therefore important to analyze the capability of both ASCAT and SMOSL3 to detect time evolution and spatial patterns of SSM simultaneously. To this end, we used Hovmöller diagrams to illustrate the seasonal variations of SSM for SMOSL3 and ASCAT. The time evolution of the SSM for SMOSL3, ASCAT, and MERRA-Land, averaged along the longitude range by latitude bands, is displayed in Fig. 5.7. Note that, for SMOSL3, many regions of Europe and Russia are screened out due to RFI contaminations (see Fig. 5.1), and so the values in the Northern Hemisphere are dominated by estimates from North America. Note also that frozen conditions were excluded from the analysis (see Section 5.2.2), so there is no-data at latitudes above 55°N in the winter time. The main difference between the three HDs is a difference in mean, with higher SSMs according to MERRA-Land. This is consistent with the negative biases of the remotely sensed SSM products with respect to the MERRA-Land reference shown in Fig. 5.4g–h. Moreover, Fig. 5.7 reveals a common periodical behavior with time and latitude: the lowest values are comprised in two "parallel" sinusoidal bands around the equator reaching the minima around April. Hence, ASCAT and SMOSL3 capture the SSM seasonal variations in the inter-tropical area as simulated by MERRA-Land. The meridional shift of the Intertropical Convergence Zone (ITCZ) is well detected by all three datasets, but MERRA-Land presents higher seasonal cycle variations.

The main differences in the SSM distribution are found in the Northern Hemisphere particularly related to the increase of SSM values during the summer period. Furthermore, very low SMOS SSM values (bright red color in Fig. 5.7c, i.e., SSM values close to 0.05 m^3/m^3) can be noted north of ~ 50°N during the winter. It is likely these very low values can be explained by the effect of soil freezing: the SMOS sensor cannot distinguish between

frozen and very dry soil conditions as the real part of the permittivity for both conditions are very close (values of permittivity ~ 5; Wigneron et al., 2007). So, it is likely that frozen soil conditions were not correctly flagged and excluded in the SMOSL3 products, and that the screening based on MERRA-Land soil temperatures may not be sufficient. For the same reasons, unrealistically drier winter-time SSM conditions were also retrieved by ASCAT in the same northern regions, albeit to a lower extent than for SMOS, with SSM values close to 0.2 m^3/m^3. Conversely, MERRA-Land SSM includes both liquid and frozen water and therefore shows a more realistic increase in SSM during the winter. These results show that correctly detecting and screening frost and snow is still a big challenge.

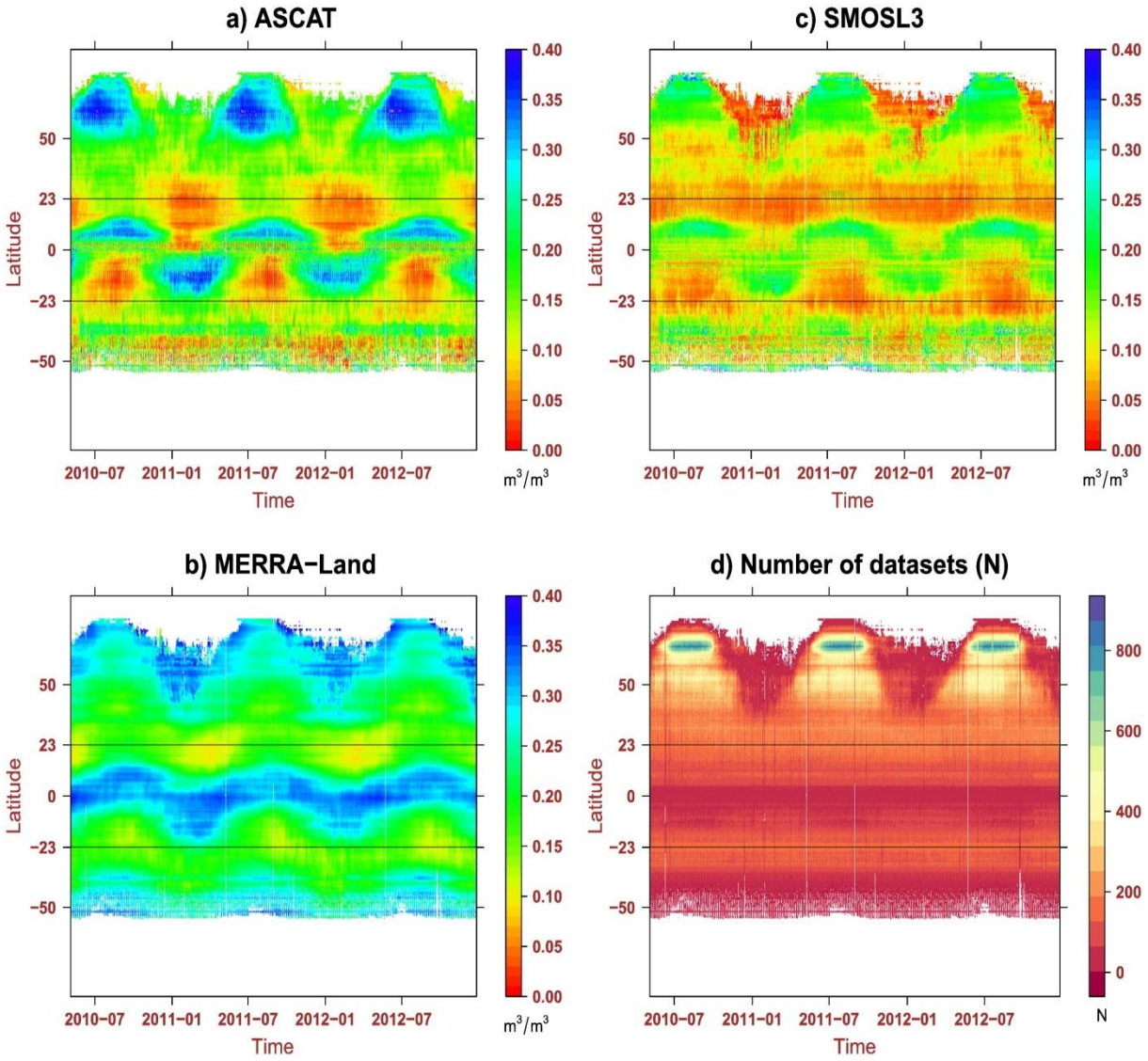

Fig. 5 - 7 *Time–latitude variations of original surface soil moisture data (m^3/m^3) for (a) ASCAT, (b) MERRA-L, (c) SMOSL3 and (d) number of data illustrated in Hovmöller diagrams.*

5.3.4 Triple collocation error model

Global error maps for the remotely sensed SSM long-term anomalies (excluding the effect of the biases) are derived using the TCE method over the 2010–2012 period. Fig. 5.8a

and b illustrates the TCE errors (i.e. the square-root of the values obtained from Eqs. (5.13) and (5.14)) of SMOSL3 and ASCAT.

In general, the spatial patterns of the TCE errors obtained with ASCAT and SMOS are similar with relatively low TCE errors, with a mean global error of 0.014 m^3/m^3 for SMOSL3, and 0.015 m^3/m^3 for ASCAT. Note that the mean global error found for SMOSL3 in our study is much lower than the one found by Leroux et al. (2011) (~ 0.06 m^3/m^3). The higher mean value obtained by Leroux et al. may be explained by the use of only one year (2010), while we used 3 years in the present analysis (2010–2012). Also, Leroux et al. (2011) did not exclude SSM data measured during the commissioning phase which might have increased the error for the SMOS dataset. Moreover, the way to handle data filtering using flags such as the data quality index and RFI percentage may be different in both studies.

As shown in Fig. 5.8a and b, the error estimates for both products are lowest in arid regions (e.g., Arabian Peninsula, Central Australia, and Egypt) due to low amounts of precipitation received leading to a low temporal variability of SSM in these regions. Higher TCE errors were found for both SMOSL3 and ASCAT over India and over locations near the Equator (e.g., South Sudan, Zambia) where MERRA-Land is much less reliable due to the paucity of precipitation gauges, particularly over most of the African continent.

Relatively high errors were obtained for ASCAT in some arid regions (e.g., Algeria, Libya, and Iran) which is a well-known phenomenon already noted in the previous Sections (5.3.1 and 5.3.2). Fig. 5.9 shows the areas where SMOSL3 provided lower errors than ASCAT (red), where ASCAT provided lower errors than SMOSL3 (green). Note that the absolute magnitude of the estimated error depends on the TCE reference. In general, it can be seen that lowest errors were obtained with ASCAT over regions with high to moderate vegetation density, and in regions where there is a strong seasonality in the SSM variability (e.g., India, in parts of Amazonia, Central Europe, Eastern Australia and the North-Eastern

USA). On the other hand lower errors were obtained with SMOSL3 in areas with low to moderate vegetation density (e.g., Western Australia, Sahara, and western US, Central Asia), confirming the results shown in the previous Section about the sensitivity to the vegetation effects.

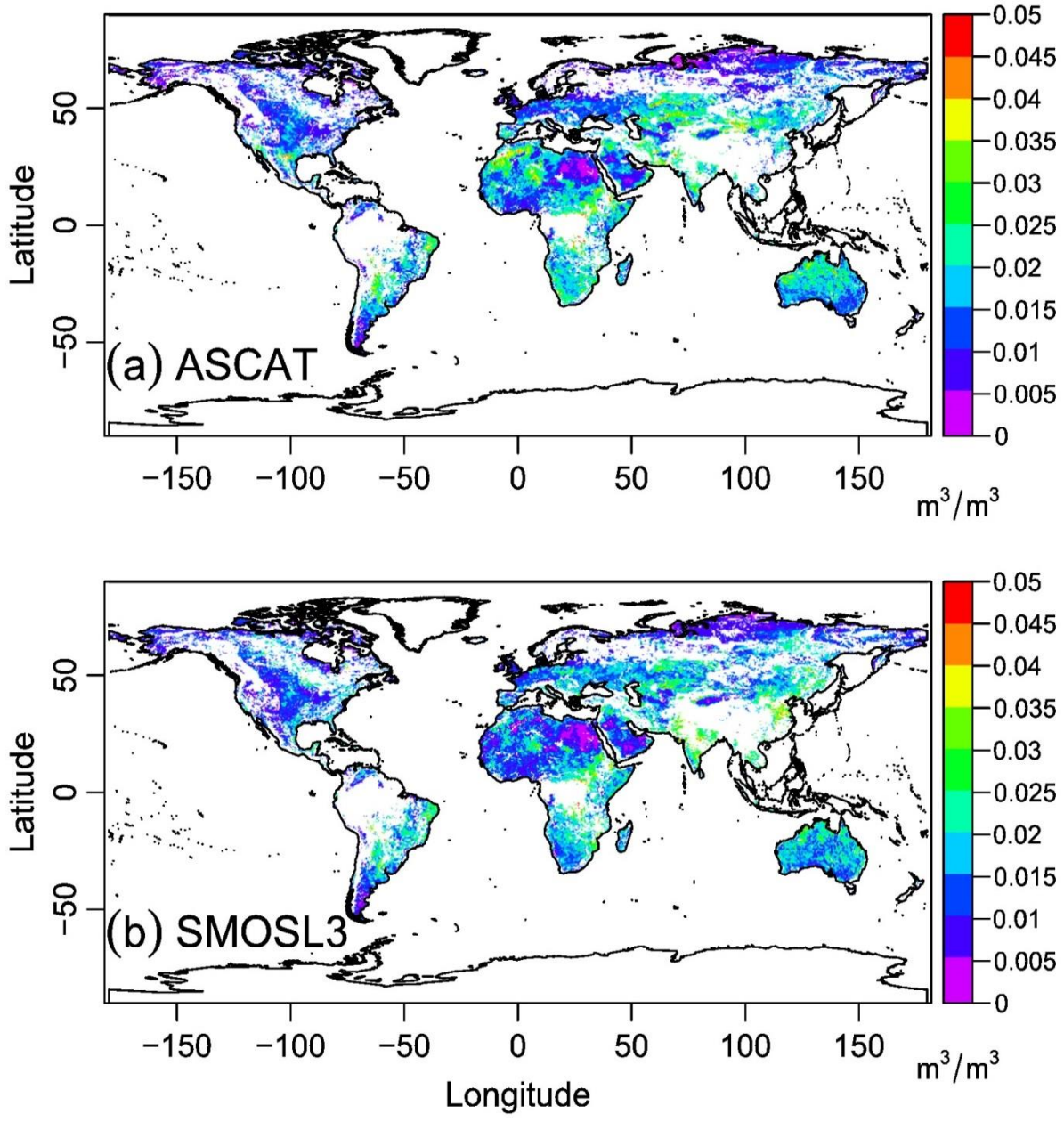

Fig. 5 - 8 *Spatial TCE errors of (a) ASCAT and (b) SMOSL3 SSM estimates expressed in volumetric water content. White areas indicate areas for which less than 100 common observations were available.*

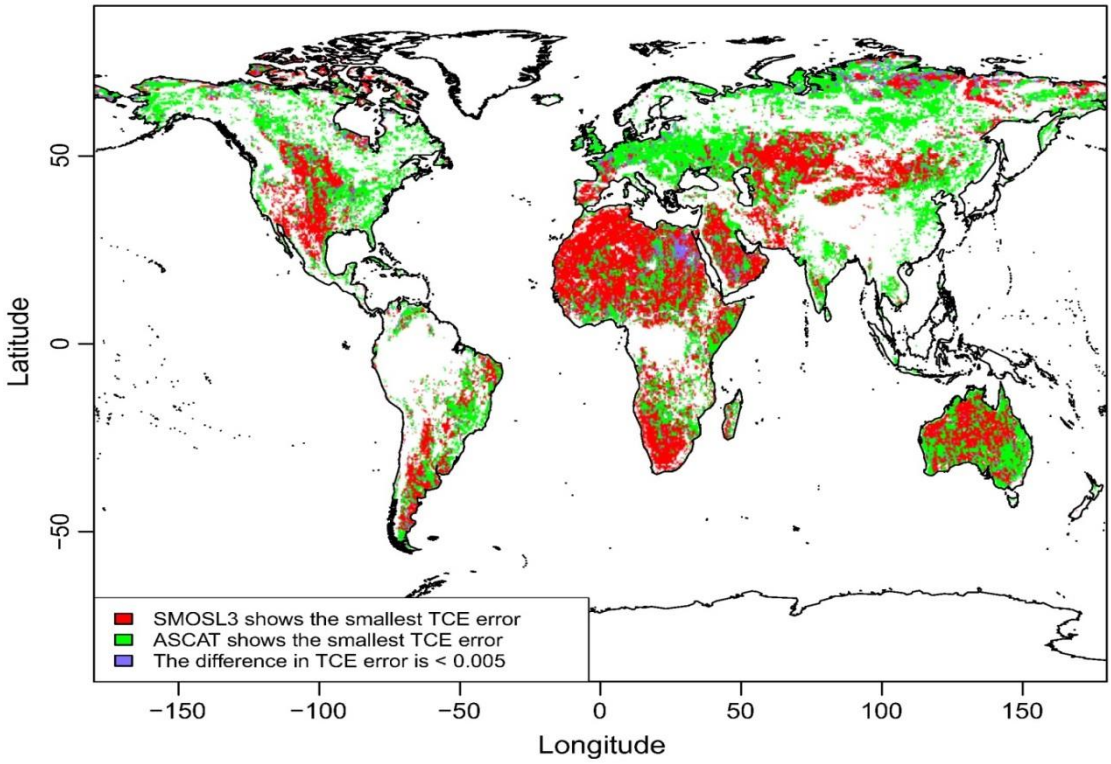

Fig. 5 - 9 *The areas in which either ASCAT (green) or SMOSL3 (red) shows the smallest TCE error value. Pixels where the difference in TCE error is less than 0.005 m^3/m^3 appear in blue. White areas indicate areas for which less than 100 common observations were available.*

5.4 Discussion and conclusions

5.4.1 Summary of the results

This study investigated the consistency of two microwave-based SSM products with respect to a reference SSM product, namely the MERRA-Land SSM product, derived from the MERRA reanalysis, for the period 05/2010–12/2012 at the global scale. The two remote sensing products are (i) the SMOSL3 SSM product, which is a microwave-based product derived from L-band passive brightness temperature measurements developed and supported by the CATDS, and (ii) the ASCAT SSM product, which is a microwave-based product

derived from C-band active backscatter measurements, developed and supported by TU-Wien.

The analysis of the original data shows, in general, a good correspondence between the SMOSL3 and ASCAT derived SSM products with the MERRA-Land reference. For instance, SMOSL3 and ASCAT successfully captured the spatio-temporal dynamics of the MERRA-Land SSM product, as seen in the correlation analyses, in the transition zones between wet and dry climates (e.g., Great Plains of North America, Sahel), Eastern Australia, and South-eastern regions of Brazil. It is worth noting that the regions of good agreement between SMOSL3, ASCAT, and MERRA-Land are also regions of strong coupling between soil moisture and precipitation as demonstrated by Koster et al. (2004b).

SMOSL3 and ASCAT exhibited weak correlations with the MERRA-Land reference data in tundra and arid regions (e.g., Sahara, Arabian Peninsula, and Central Australia). ASCAT even exhibited negative correlations over some of the dry deserts (e.g., Sahara). These low correlations may be explained by the small range of variation in the SSM values in these dry regions which corresponds roughly to the remotely sensed retrieval accuracy (~ 0.04 m^3/m^3, Kerr et al., 2001). Issues with the ASCAT SSM retrievals in dry regions may be explained by (i) systematic errors in the retrieval algorithm due to different scattering mechanisms in dry soils (Wagner et al., 2013) and (ii) changes in small-scale surface roughness, produced by wind-blown sand (Frison & Mougin, 1996). Anomaly time series correlations show, in general, similar spatial patterns compared to the correlations found using original datasets, but with lower *R* values, especially in the transition zones.

The global scale analysis of the bias and ubRMSD also confirmed these results. However, opposite patterns were generally obtained in terms of bias: ASCAT is generally wetter than MERRA-Land (positive bias), while SMOSL3 is generally drier than MERRA-Land (negative bias).

Additional insights were provided by the Hovmöller diagrams, which visualize the time changes in SSM as a function of latitude. It is found that even though strong correlations are found between all three products at global scale, the spatio-temporal patterns shown in the HD may be quite different for SMOSL3, ASCAT and MERRA-Land in some latitudinal bands. For instance, SMOSL3 presents consistently dry SSM conditions (less than ~ 0.10 m^3/m^3) at mid latitudes (between 10°N and 30°N). This could be partly explained by the impact of RFI as high RFI values increase the SMOS observed brightness temperatures (TB) resulting in lower SSM retrievals (Oliva et al., 2012). Wigneron et al. (2012) have interpreted the bias as an effect of the underestimation of the default contribution to TB of the forested areas in mixed pixels.

Finally, results from the TCE method generally confirmed the above results and the spatial error patterns were found to be consistent with known performance issues of SMOS and ASCAT (Leroux et al., 2013a). In particular, larger errors were found for SMOSL3 in the presence of moderate to dense vegetation in tropical and temperate regions and in regions known to be highly contaminated by RFI effects (Western Europe, India, Southern Asia). Higher errors were found for ASCAT over arid regions (North Africa, Central Australia, and Central Asia). Our findings are generally in agreement with the results obtained by previous studies analyzing spatial errors of ASCAT over 2007–2008 (e.g., Dorigo et al., 2010) and SMOS over 2010 (Leroux et al., 2011), using products based on earlier versions of the retrieval algorithms.

A more in-depth analysis, using LAI as a parameter to quantify the vegetation effects, revealed higher *R* values for SMOSL3 than for ASCAT when LAI is less than 1 (which corresponds to almost 50% of the pixels considered in this study), similar *R* values for both products for intermediate LAI values between 1 and 3, and higher *R* values for ASCAT than for SMOS when LAI exceeds 3. This implies that vegetation plays a key role in the

performance of the SMOSL3 and ASCAT SSM products, and that the two products have different sensitivities to vegetation. Generally, SMOS is more efficient at monitoring SSM than ASCAT over sparse vegetation, whereas ASCAT is more efficient over relatively dense vegetation (LAI > 3).

5.4.2 Discussion

These results may appear as surprising because microwave sensors should be more efficient to sense through moderate vegetation at L-band than at C-band (Al-Yaari et al., 2014): with increasing frequency (i) scattering and attenuation effects by vegetation elements (leaves, stems, trunks, branches, fruits, etc.) increase and (ii) the sampling depth in soil decreases. However, in this study, SMOS and ASCAT differ not only in terms of frequency but also in terms of microwave technology: SMOS is a radiometer (i.e. a passive microwave system), while ASCAT is a scatterometer (i.e. an active microwave system). Previous studies comparing SSM retrievals from radiometer and scatterometer systems (Brocca et al., 2011; Rüdiger et al., 2009) also found that SSM products retrieved from scatterometer data were less impacted by vegetation than those retrieved from radiometers data.

There are different ways of interpreting these results. First, the good performances of ASCAT over vegetation canopies could be due to higher-order surface-vegetation interaction effects (Crow et al., 2010), such as double bounce reflection (Karam et al., 1995) that may increase the sensitivity of active systems to SSM in comparison to passive systems. These higher-order effects are often neglected in the current models used for SSM retrievals from both active and passive systems. However, these interaction effects may become extremely important under some conditions and may, to a large extent, explain the sensitivity of ASCAT to soil moisture over vegetated regions even at high incidence angles (Crow et al., 2010).

Second, the scatterometer systems have been also found to be very sensitive to the seasonal vegetation dynamics. For instance, early studies which investigated signatures from ERS backscatter coefficients based on averaged observations on a monthly basis have shown that the time variations in the measured backscatter coefficient were in good agreement with the vegetation dynamics as monitored by optical vegetation indices (Frison & Mougin, 1996). It should be noted that, for some specific conditions, the increase in vegetation effects and the increase in SSM both lead to an increase in the backscatter coefficient (Wigneron et al., 1999a; Wigneron et al., 1999b), which may make the decoupling of the two effects difficult using an active system such as ASCAT. So, it is difficult to appreciate whether ASCAT is really monitoring the time variations in SSM or in the vegetation in regions where there is a natural high correlation between the vegetation dynamics and the increase in the SSM values. The hypothesis that ASCAT may have difficulties in decoupling vegetation and SSM effects at the seasonal scale may be used to interpret the fact that the performances of ASCAT become closer to those of SMOSL3 for LAI > 3 when anomalies (taking off seasonal effects) were used (Fig. 5.6a and b).

However, many results can be raised to contradict this hypothesis. For instance, in many climate regions (Mediterranean Climate regions for instance) where soil moisture and vegetation may be out of phase, ASCAT performed quite well. Moreover, the increase in vegetation density often leads to an increase in backscatter, but the opposite may also happen, depending on the soil moisture conditions. Eventually, considering anomalies, the performances of SMOS and ASCAT were very close (ASCAT slightly better) in terms of correlation values for LAI > 1. This latter result confirms the very good ability of active systems such as ASCAT in monitoring SSM over well-developed vegetation.

It is also important to keep in mind that MERRA-Land, although found to be very reliable in several instances (Albergel et al., 2013b; Yi et al., 2011), cannot be considered to

be “ground truth” (Albergel et al., 2013a). Consequently, the interpretation of the results depends on the accuracy of the MERRA-Land product itself. The skill of MERRA-Land soil moisture strongly depends on the accuracy of the precipitation forcing, which is derived by merging the MERRA reanalysis precipitation with measurements from a global network of gauges. The density of the gauge network varies tremendously, with good coverage in North America, Europe and many parts of Asia and South America. However, the gauge density is very sparse in Africa and at high latitudes. In these regions in particular, a lack of consistency between the remote sensing products and MERRA-Land SSM does not necessarily imply poor performance by the remote sensing estimates. Other factors that determine the skill of MERRA-Land soil moisture include the radiation forcing as well as the land model physics and associated model parameters, whose quality is similarly variable across the globe.

Looking ahead, improvements in the retrieval algorithms as well as in the LSM data can be expected. For the SMOSL3 product, this includes enhancements especially in terms of RFI filtering and dry bias correction. For ASCAT, the issues found over arid regions are currently under investigation. Finally, the next version of the MERRA reanalysis is currently in production and features improved precipitation forcing, the single most critical input to SSM estimates from models.

The results of the present study revealed that both the SMOSL3 and the ASCAT SSM products are largely consistent with the model-based SSM estimates from MERRA-Land, and that the two remote sensing products complement each other. Vegetation density and RFI contaminations of SMOSL3 were found to be the key factors in the interpretation of the consistency between the two remotely sensed products (SMOSL3 and ASCAT) with MERRA-Land. The potential synergy between the passive and active microwave systems at global scale is very promising for the development of improved, long-term SSM time series at

global scale, such as those pursued by the European Space Agency's Climate Change Initiative.

Chapter VI

6. Testing simple regression equations to derive long-term global soil moisture datasets from satellite-based brightness temperature observations[3]

[3] This chapter has been partially published as: Amen Al-Yaari, Jean-Pierre Wigneron, Agnes Ducharne, Yann H. Kerr, Patricia de Rosnay, Richard de Jeu, Ajit Govind, Ahmad Al Bitar, Clement Albergel, Joaquin Muñoz-Sabater, Philippe Richaume, Arnaud Mialon: Merging two passive microwave remote sensing (smos and amsr_e) datasets to produce a long term record of soil moisture. Geoscience and Remote Sensing Symposium (IGARSS), 2014 IEEE International 13-18 July 2014. The whole chapter is to be submitted.

6.1 Introduction

Soil moisture (SM) is one of the key variables in the environment and the climate system as it influences the exchange of heat and water between the land surface and atmospheric processes (Hupet & Vanclooster, 2002; Western et al., 2004; Wigneron et al., 1999a). In 2008, SM was recognized as an Essential Climate Variable (ECV) which is considered essential for IPCC (Intergovernmental Panel on Climate Change) requirements (Wagner et al., 2012). Complete and consistent record of SM, as an ECV, is required for hydrological applications, flood prediction, drought monitoring, climate forecasts, etc.

Active and passive microwave sensors offer the opportunity to retrieve surface SM (SSM) information from their surface backscatter and brightness temperatures (TB) signals, respectively, which are mainly determined by the soil dielectric constant (Njoku et al., 2002; Ulaby et al., 1996). Active and passive microwave remote sensing particularly at low frequencies have been shown to provide useful SSM retrievals (Bartalis et al., 2007a; Kerr et al., 2001; Njoku et al., 2003) with large spatial coverage and high temporal resolution and, hence, to be suitable for SSM monitoring at the global scale (Griend & Owe, 1994; Owe et al., 2001; Wigneron et al., 1995; Wigneron et al., 1998; Wigneron et al., 2000). Nevertheless, these microwave sensors provide individually inconsistent SSM datasets. Therefore, the ESA's Programme on Global Monitoring of ECV known as the Climate Change Initiative (CCI), and the European Space Agency's Water Cycle Multi-mission Observation Strategy (WACMOS) (Su et al., 2010), merged the different observations acquired by several microwave sensors in an attempt to produce the most complete and consistent long-term time series of SSM (1978-2010) (http://www.esa-cci.org/)(Liu et al., 2012). These include the Scanning Multichannel Microwave Radiometer (SMMR; 6.6, 10.7 , 18.0 21, and 37 GHz channels; (Wang, 1985)), the Special Sensor Microwave Imager (SSM/I; 19.4, 22.2, 37.0, and 85.0 GHz channels) of the Defense Meteorological Satellite Program, the Advanced

Microwave Scanning Radiometer on Earth Observing System (AMSR-E; from 6.9 to 89.0 GHz; (Njoku & Li, 1999)), and the Advanced Scatterometer (ASCAT) data (Liu et al., 2011). This product has been available since June 2012 and has been of interest for researchers to study the long-term trends of SSM (Albergel et al., 2013b; Seneviratne et al., 2010).

The second phase of the upcoming CCI project aims at including a new innovation in space technology, namely the SMOS (Soil Moisture and Ocean Salinity) SSM datasets, in the long term CCI SSM datasets. The SMOS satellite, launched in November 2009, is the first-ever satellite specifically dedicated to monitoring SSM with an accuracy of 0.04 m^3/m^3 from space over the continental surfaces (Kerr et al., 2010; Kerr et al., 2012). SMOS at L-band has been providing multi-angular microwave TB observations (Kerr et al., 2012) since 2010. Consequently, there is no prior record of SSM from SMOS. SSM is retrieved from the SMOS TB observations using several approaches such as the forward model inversion, neural networks, and statistical regressions, and readers are directed to (Wigneron et al., 2003) for a review. The operational retrieval method (i.e. forward model inversion) is time consuming and requires several auxiliary datasets (e.g., the land cover, soil texture, etc.). Besides, Wigneron et al. (2004) and Saleh et al. (2006) have developed and evaluated semi-empirical regression equations between the SSM and microwave reflectivity (i.e. one minus emissivity) based on the radiative transfer model (τ-ω model) (Mo et al., 1982; Wigneron et al., 1995), which simulates the L-band TB from soil underlying a vegetation canopy. More specifically, regression equations using multiple configurations of bipolarized and multi-angular microwave TB observations were shown to be efficient for retrieving SSM (Albergel et al., 2011; Calvet et al., 2011; Parrens et al., 2012; Saleh et al., 2006). These regression methods have been used in several studies based on in situ, airborne, or space-borne (SMOS) observations (Calvet et al., 2011; Parrens et al., 2012; Pellarin et al., 2003). For instance, Albergel et al. (2011) applied these methods successfully to SMOS data over some sites in

France, and the retrieval method was extended over the whole of France by Parrens et al. (2012).

To date, to our knowledge, no study has been performed to assess the potential of the statistical methods to retrieve SSM at the global scale. The objectives of this study are twofold (i) deriving a merged SSM product based on the AMSR-E TB observations over 2003-2009 which is coherent with the SMOS SSM products (2010-2014) in terms of absolute values and time variations and (ii) evaluating the quality of this merged product with respect to several global scale SSM.

The knowledge gained from this study is to be used to help the preparation of the upcoming CCI phase 2 SSM programme to provide guidelines for a seamless SSM record.

6.2 Materials and methods

6.2.1 Datasets

6.2.1.1 AMSR-E Level 3 brightness temperatures

The AMSR-E sensor measures dual-polarized TB at C-band (6.925 GHz) vertically and horizontally with a spatial resolution of ~ 56 km. In this study, the level 3 global daily gridded TB product, projected on a global (Equal Area Scalable Earth) EASE grid 25 km, provided by the National Snow and Ice Data Center (NSIDC) was used. C-band was preferred in our study for retrieving SSM, as it is more sensitive to SSM than higher frequency bands, and the closest to L-band.

Night-time surface temperatures are more stable than day-time, hence the vegetation temperature is closer to soil temperature as the temperature gradients between them is not strong (Kerr & Njoku, 1990), and therefore we limited our study to night-time data (corresponding to AMSR-E descending overpass-time 0130 hour local time)(e.g., Al-Yaari et al., 2014).

6.2.1.2 SMOS level 3 soil moisture products

The SMOS satellite provides SSM products with global coverage and a 3-day revisit at the equator with ascending and descending orbits at 0600 and 1800 hours local time, respectively, with a spatial resolution of 35–50 km (Kerr et al., 2010).

CATDS (Centre Aval de Traitement des Données) recently provided daily re-processed global gridded SSM products, projected on a global EASE grid 25 km, namely the SMOS level 3 (SMOSL3) products. SMOSL3 has an enhanced accuracy in the SSM data by using several revisits simultaneously and multi-orbit retrievals (Jacquette et al., 2010). SMOSL3 product is provided as volumetric soil water content (m^3/m^3) and can be freely obtained from the CATDS website (http://catds.fr).

SMOSL3 retrievals at dawn, corresponding to SMOS descending overpass-time 0600 hour local time, were selected in this study (Al-Yaari et al., 2014) for better consistency with AMSR-E night-time data.

6.2.1.3 ECMWF Soil temperature

Given the unavailability of real physical surface soil temperature through direct ground measurement at the global scale, we used soil temperature estimates produced by the European Center for Medium range Weather Forecasting (ECMWF). This surface soil temperature product (0-7cm) was re-projected and resampled to the same projection and spatial resolution of both SMOSL3 and AMSR-E SSM and TB products, respectively. ECMWF Soil temperature is available for the whole period concerned in this study (2003-2011).

6.2.1.4 MODIS NDVI

The NDVI (Normalized Difference Vegetation Index) products were obtained from MODIS (Moderate-resolution Imaging Spectroradiometer), which is an EOS sensor mounted

on the TERRA satellite launched (King & Greenstone, 1999) by NASA in 1999. The NDVI is produced globally over land at 1 km resolution and for 16-day composite periods. The NDVI was found to be sensitive to (a good estimator of) Leaf Area Index (LAI) (Chen & Cihlar, 1996; Colombo et al., 2003; Fan et al., 2009; Law & Waring, 1994; Potithep et al., 2010), which was shown to have a strong control on the skill of SSM retrieved by passive sensors (Al-Yaari et al., 2014).

6.2.2 Methods

In this study, we used simplified statistical regressions, which were analytically derived from the L-Band Emission of the Biosphere model (L-MEB, described in detail in Wigneron et al. (2007)), based on bi-polarization TB datasets (Saleh et al., 2006; Wigneron et al., 2004). More specifically, these methods have been numerically derived from the equations of the τ-ω model (a zero-order solution of the radiative transfer equations), which is a simple formulation derived from the general radiative transfer equation for non-scattering homogeneous media, assuming that the value of the single scattering albedo is negligible and that the values of optical depth are the same for both polarizations. So these methods are based on physical equations.

The equation developed by Saleh et al. (2006), which was also applied by (Albergel et al., 2011; Calvet et al., 2011) to bi-polarization TB observations made at an incidence angle θ, can be written as:

$$\ln(SSM) = b_2 \ln\left(\Gamma_H(\theta)\right) + b_1 \ln\left(\Gamma_V(\theta)\right) + b_0(\theta) \qquad 6-1$$

where Γ (θ) is the surface reflectivity at polarization V or H, defined as:

$$\Gamma_P(\theta) = 1 - \frac{T_{BP}(\theta)}{T_G} \qquad 6-2$$

where T_{BP} and T_G are the brightness temperature at polarization p (H or V) and surface soil temperature, respectively. In this study, T_G is obtained from ECMWF.

Mattar et al. (2012) have shown that vegetation effects may be accounted for by adding vegetation information such as the NDVI to the regression equation, which may in turn enhance the regressions analysis. According to Mattar et al. (2012), the regression equation can be rewritten as:

$$\ln(SSM) = b_3(NDVI) + b_2 \ln\left(\Gamma_H(\theta)\right) + b_1 \ln\left(\Gamma_V(\theta)\right) + b_0(\theta) \qquad 6-3$$

The coefficients b_0, b_1, b_2, and b_3 of the regression Eqs. (6.1) and (6.3) are assumed to be constant in time and have to be calibrated over each pixel.

6.2.2.1 Regression calibration

The coefficients b_0, b_1, b_2, and b_3 of the regression Eqs. (6.1) and (6.3) are calibrated using the AMSR-E T_{BP} at C-band (6.9 GHz) in both H and V polarizations. The calibration was made over the whole time period during which both AMSR-E TB observation and SMOSL3 products are simultaneously available (namely Jun. 2010 - Sept. 2011). In both equations (6.1 & 6.3), as a reference value for SSM, we used the most recent available re-processed SMOSL3 SSM products. The NDVI values used in Eq. (6.3) were taken from MODIS products. This bi-polarization approach was used here as AMSR-E provides TB measurements at only one angle 55° and two polarizations (H & V). In both equations (6.1 & 6.3), the regression coefficients were computed for each grid cell. They implicitly depend on the surface characteristics in terms of soil texture and surface roughness, vegetation types, topographic features, etc. (Saleh et al., 2006). Fig. 6.1 shows a flowchart representation of the regression calibration method (1&2), soil moisture retrieval (3), and the availability of the datasets used in time (bottom panel).

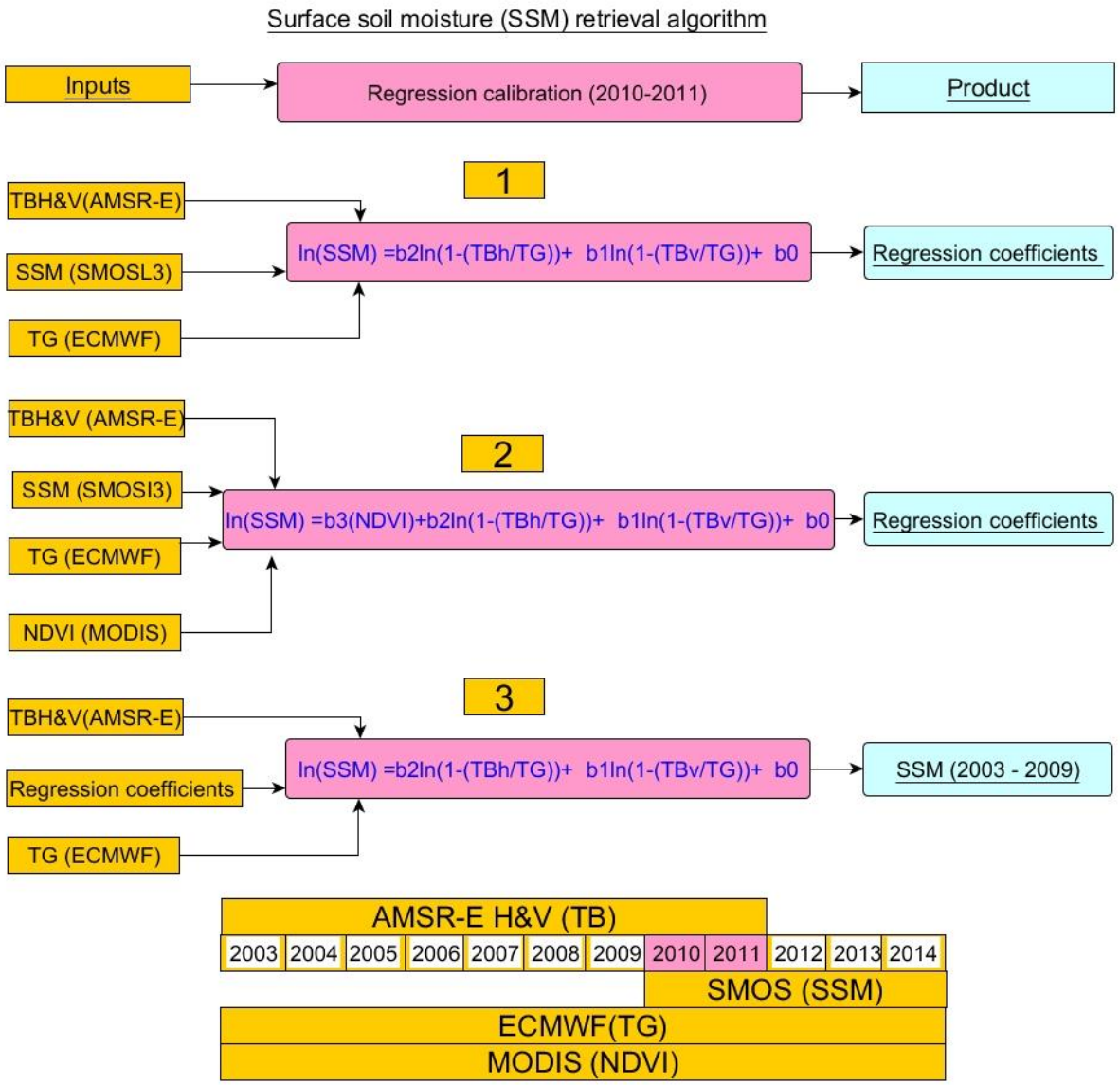

Fig. 6 - 1 *Flow chart of the regression calibration method using Eq. (6.1) (1) and Eq. (6.3) (2) and soil moisture retrievals using the computed regression coefficients (3). The bottom panel shows the dataset availability in time.*

6.2.2.2 Producing SSM data

The computed regression coefficients can then be used to derive a long SSM time series in all the pixels for the (2003-2009) period (see Fig. 6.1) using Eqs. (6.1) and (6.3). In this period, TB measurements are obtained from AMSR-E. During the calibration period, soil temperatures are obtained from ECMWF, NDVI are obtained from MODIS, and the

calibrated regression coefficients and thus all the parameters in the regression Eqs. (6.1) and (6.3) are known except the SSM which is our target to retrieve.

6.3 Results and discussion

6.3.1 Regression calibration

Using the above defined methodology, the regression coefficients b_0, b_1, and b_2 in Eq. (6.1) were derived from the AMSR-E V and H polarized TB, using the SMOSL3 SSM products as a reference. The corresponding calibration parameters b_2, b_1 (corresponding to H & V polarized TB, respectively), and b_0 (intercept coefficient) are displayed in Fig. 6.2, which shows, in general, that the spatial patterns of the coefficients are in agreement with land cover type. For instance, the intercept b_0 and the b_1 coefficient are somewhat similar with high values over regions with moderate vegetation (e.g., North Western Australia and equatorial regions) and low values over dry regions (e.g., Middle East).

Also, a difference in the spatial pattern of values between V (b_1) and H (b_2) polarizations can be seen in Figs. 6.2 (top and middle panel), especially over transition zones between wet and dry climates, including India. Over tundra areas, also, the coefficient b_1 for V polarization are low, whereas b_2 is high for H polarization. Looking at these two coefficient maps, a combination of low (high) coefficient values for V polarization and high (low) coefficient values for H polarization was selected to give the best predictions of SSM. The spatial patterns of the intercept (b_0) are relatively similar to the ones of b1.

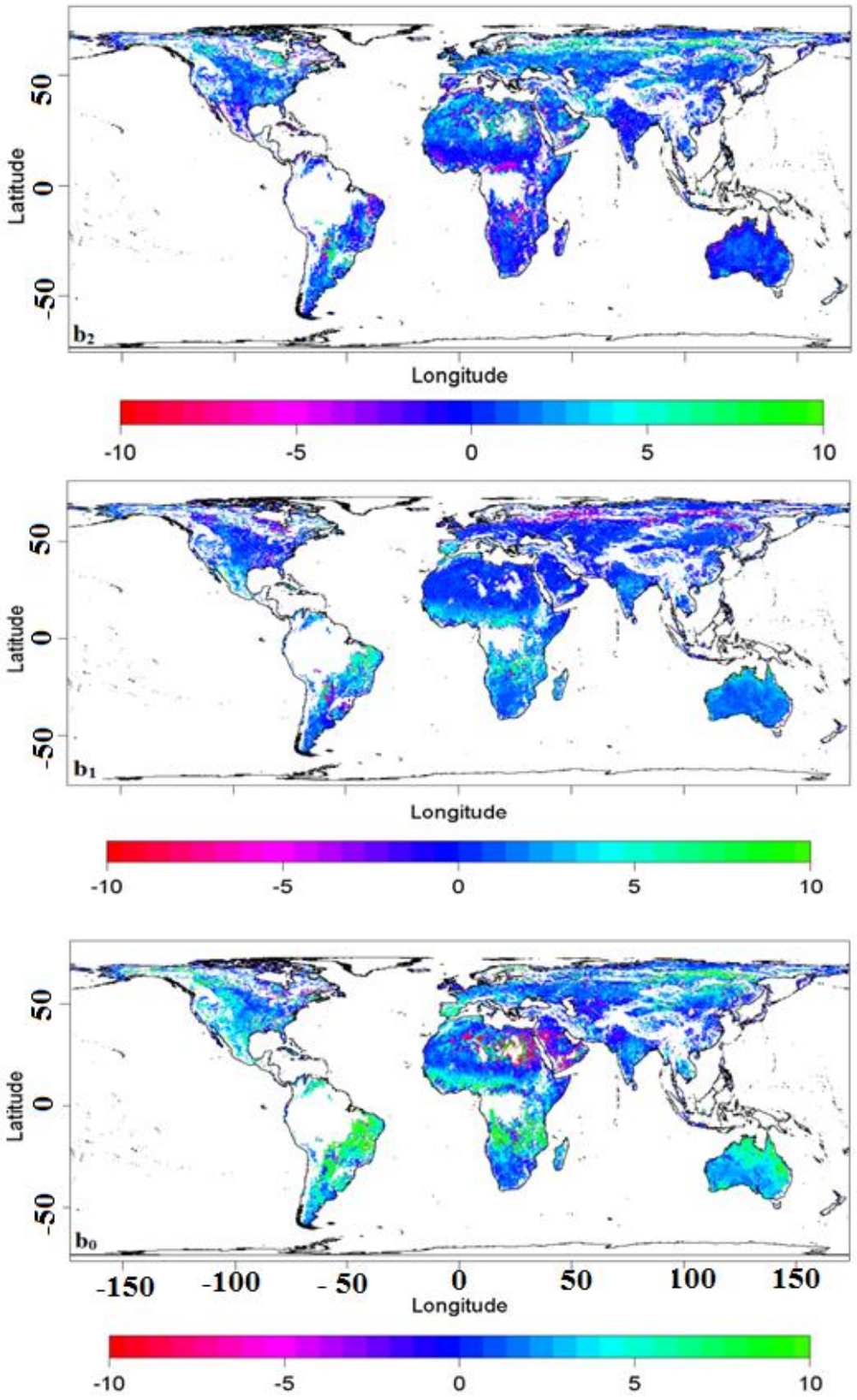

Fig. 6 - 2 *Regression coefficients of AMSR-E brightness temperature vs. SMOSL3 SSM in 2010-2011 with Eq. (6.1). b0 (bottom panel): intercept, b1 (middle panel): vertical polarization, and b2 (top panel): horizontal polarization. White areas over land indicate areas with dense vegetation, strong topography, or wetlands.*

A similar regression method using in addition the NDVI vegetation index (Eq. (6.3)), as proposed by Mattar et al. (2012), to account for vegetation effects was also investigated. The four calibration parameters b_3 (corresponding to the NDVI), b_2 and b_1 (corresponding to H & V polarized TB, respectively), and b_0 (intercept coefficient) are displayed in Fig. 6.3. It shows that the spatial patterns of the coefficients generally agree with the spatial patterns of the coefficients computed without NDVI. The NDVI coefficient (b_3) has distinguished spatial patterns with low values over moderate vegetation (e.g., the Sahel, India, West USA, etc.), whereas high values are found over arid regions (e.g., extreme South Africa, Central and Western Australia, the western United States, etc.).

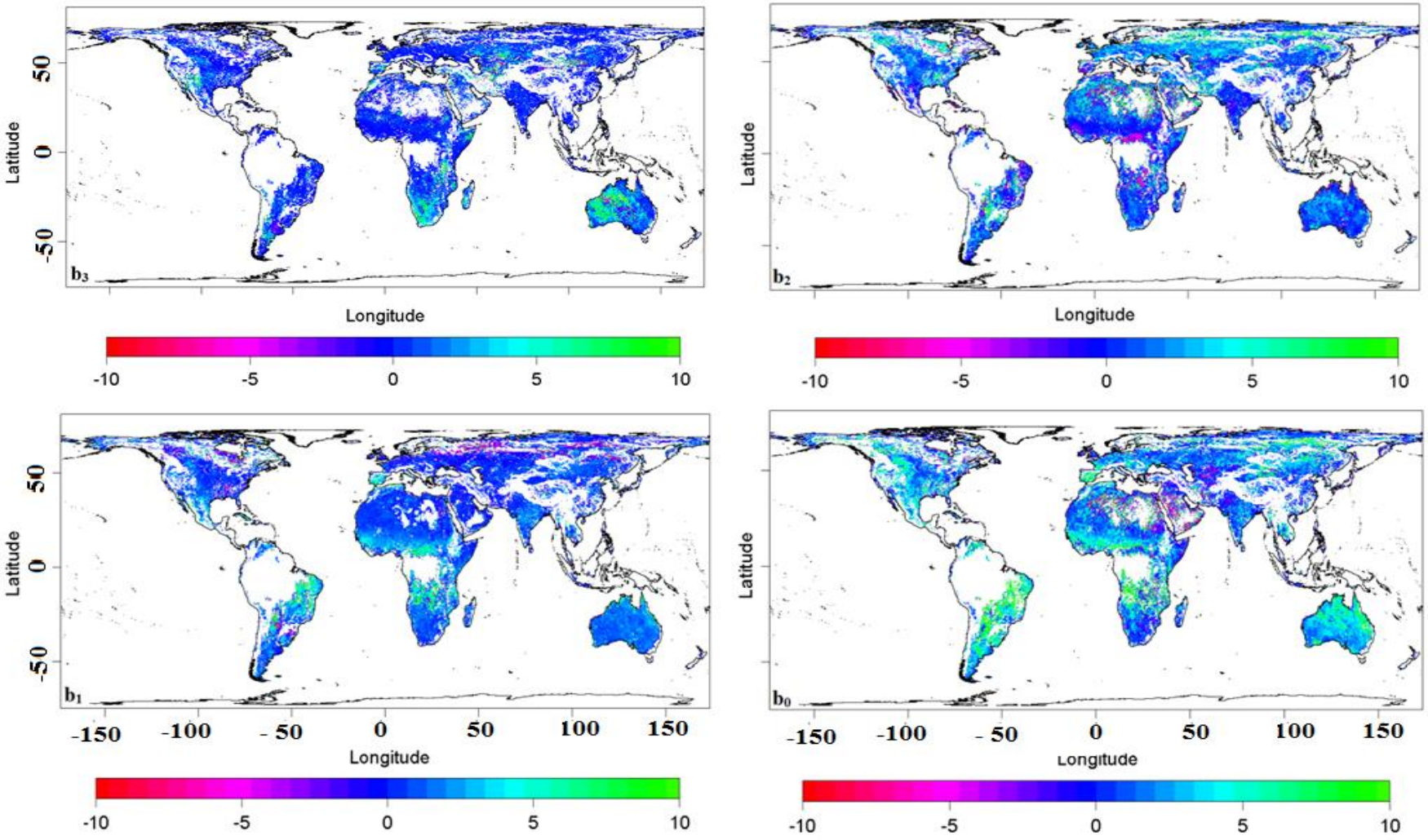

Fig. 6 - 3 *Regression coefficients of the AMSR-E TB vs. SMOSL3 SSM during the 2010-2011 period with Eq. (6.3). b_0: intercept, b_1: vertical polarization, b_2: horizontal polarization, and b_3: NDVI. White areas over land indicate areas with dense vegetation, strong topography, and wetlands.*

6.3.2 Regression's quality and new AMSR-E SSM products

The three regression coefficients from Eq. (6.1) obtained during the calibration period (2010-2011) were then used in the same empirical relationship equation (Eq. 6.1) to estimate SSM from AMSR-E TB data for the same period of calibration. Note that this step does not correspond to a validation exercise, as the comparison between the retrieved SSM values and the reference SSM values (SMOSL3) was made over the period of calibration (2010 - 2011). So, our objective here was merely to check whether realistic and coherent retrieved SSM values could be produced from the regression Eq. (6.1). The accuracy of the estimated SSM based on the bi-polarization approach (referred here to as AMSR-reg), in terms of the Root Mean Square Difference (RMSD; bottom panel) and correlation coefficient (R; top panel) values against SMOSL3, is shown in Fig. 6.4.

In Fig. 6.4 (b), the spatial patterns of the RMSD are similar to the vegetation distribution with a global mean of 0.05 and high RMSD (~ 0.1) over regions with high to moderate vegetation to low RMSD (< 0.04) over arid regions. In Fig. 6.4 (top panel), only the significant correlations between the reference and the retrieved SSM estimate obtained from Eq. (6.1) (p-value<0.05) are plotted. The reference generally correlates well with the AMSR-reg over most of the globe with a global mean of 0.60 with the highest R values (R > 0.75) over Australia, the United States, West Africa, etc.

Similarly, the four regression coefficients from Eq. (6.3) obtained during the calibration period (2010-2011) were then used in the same empirical relationship equation (Eq. 6.3) to estimate SSM from AMSR-E TB data for the same period of calibration. The accuracy of the estimated SSM based on the bi-polarization approach with the addition of NDVI vegetation index Eq. (6.3), in terms of the RMSD (bottom panel) and the correlation coefficient (top panel) values is illustrated in Figs. 6.5. It can be seen that the RMSD values

are higher than the ones computed with Eq. (6.1) without the inclusion of NDVI with a global mean of 0.10.

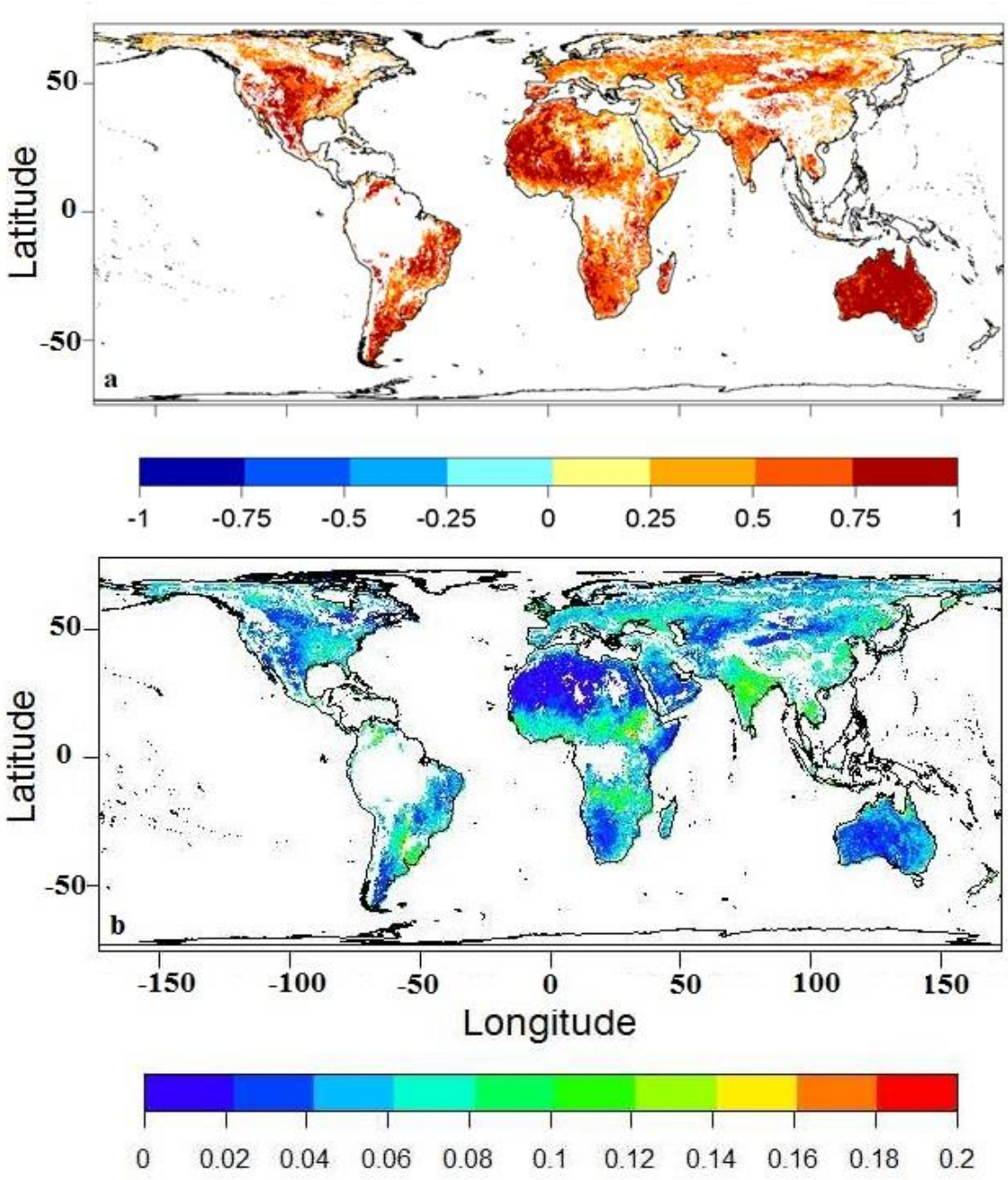

Fig. 6 - 4 *Regression statistics of AMSR-reg vs. SMOSL3 SSM in 2010-2011 with Eq. (6.1): a) R (a) and b) RMSD (m^3/m^3) (b). White areas over land indicate areas with dense vegetation, strong topography, and wetlands.*

This can be noted particularly over the extreme South Africa and the western and central of Australia, western USA, Central Asia, and the transition zones. These are areas

where the NDVI coefficient values are high and may explain these high RMSD values. Consequently, this means that the addition of NDVI leads to high values of SSM over these regions, hence, does not improve the SSM predictions in terms of absolute values. The spatial patterns of correlations are similar with Fig. 6.4 with a global mean of 0.57.

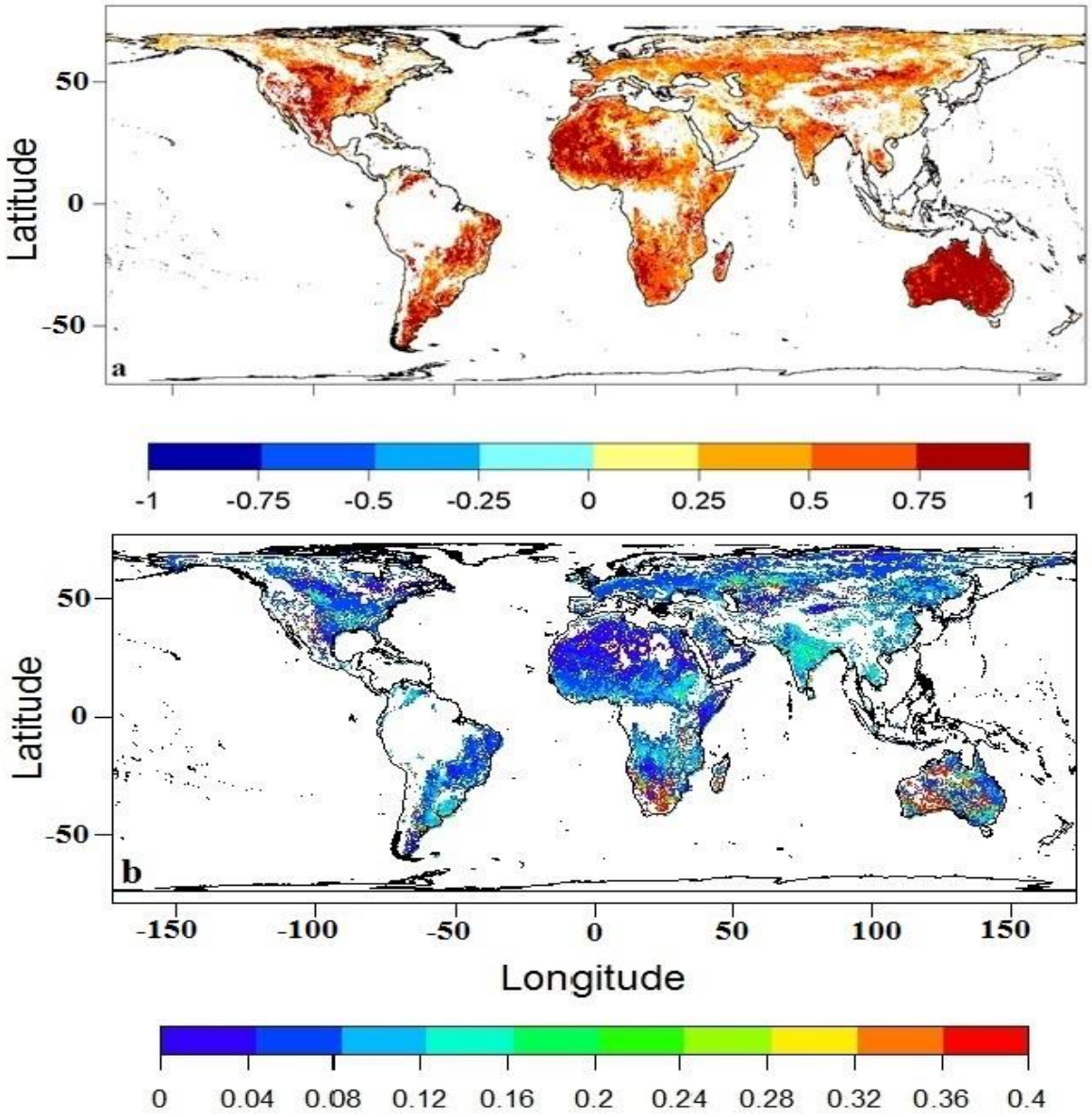

Fig. 6 - 5 *Regression statistics of AMSR-reg with inclusion of NDVI vs. SMOSL3 SSM in 2010-2011 with Eq. (6.3): a) R (top panel) and b) RMSD (bottom panel, m^3/m^3). Only significant correlations (p-value < 0.05) are presented. White areas over land indicate areas with dense vegetation, strong topography, and wetlands.*

Fig. 6.6 shows the areas where the correlation between the regressed data without NDVI and the reference SMOSL3 SSM products (in red) are higher than the correlation

between the regressed data with NDVI and the reference SMOSL3 SSM products (in blue), and the areas where the difference is lower than 0.05 (in green). In general, the green color is prevalent, several red points can be noted, and there is almost no blue color. This tells that the addition of NDVI did not improve the regression in terms of temporal dynamics, thus, neither in RMSD (m^3/m^3) nor in the correlation values. These results are consistent with a recent study (Miernecki et al., 2014), which concluded that including the NDVI variable in the regressions provided lower performances. Consequently, for retrieving the long record 2003-2009 SSM, the regression without the inclusion of the NDVI values is recommended to extend back the SMOSL3 SSM for the period 2003-2009.

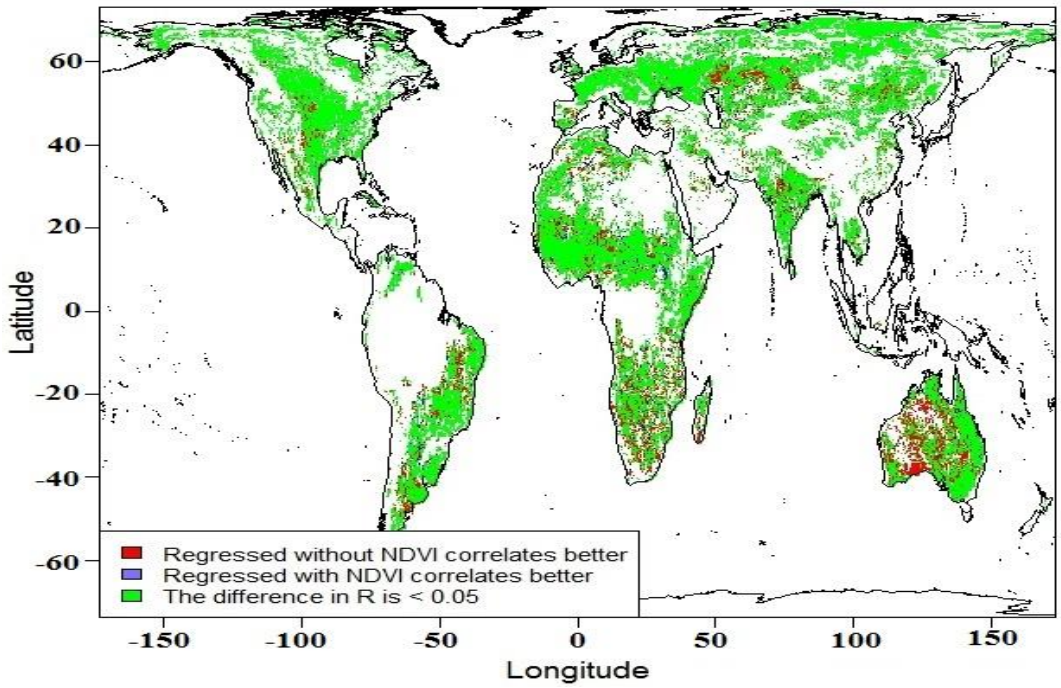

Fig. 6 - 6 Pairwise comparison between the AMSR-reg with NDVI and AMSR-reg without NDVI SSM products with respect to the reference SMOSL3 SSM product in terms of correlations based on the original SSM data during the 2010 – 2011 period. The map shows the areas where either AMSR-reg without NDVI (red) or AMSR-reg with NDVI (blue) correlates better with the reference. Pixels where the AMSR-reg with NDVI and AMSR-reg without NDVI have similar performances (differences in the values of R lower than 0.05) are shown in green. Only significant correlations (p-value < 0.05) are presented. White areas over land indicate areas with dense vegetation, strong topography, and wetlands.

6.3.3 Product comparison with original AMSR-E SSM product

A comparison between the SSM estimated from AMSR-E TB observations using the regression approach (referred to as AMSR-reg) and that retrieved from AMSR-E TB observations implementing the Land Parameter Retrieval Model (LPRM) model, developed at Vrije Universiteit Amsterdam in cooperation with the NASA (VU-NASA) (Owe et al., 2001) (referred to as AMSR-VUE), has been also carried out. The comparison was performed at the global scale considering the 2007- 2009 period. AMSR-VUE SSM products were used in this comparison, among other AMSR-E SSM retrievals, as they were shown to be the best (Brocca et al., 2011; Draper et al., 2009a; Gruhier et al., 2010). Correlation (R) and RMSD (m^3/m^3) indicators were selected to study the consistency of both SSM retrievals in time evolution and spatial patterns.

The temporal correlation between the AMSR-reg and AMSR-VUA is shown in Fig. 6.7a. High temporal correlations (R>0.75) are obtained over, particularly, the Sahel, central USA, and Europe regions, whereas a small correlation (even negative) is mainly obtained in the tundra regions, where the remotely-sensed retrievals are affected by the permanent snow cover and frozen soil. Except for the tundra regions, the results reveal that almost all over the world the AMSR-VUA and AMSR-reg are consistent. Consistently, Fig. 6.7b shows that high RMSD values are obtained over the tundra regions, but also over North-Eastern Australia, whereas small RMSD values have been mainly obtained over arid regions such as the Middle East, extreme South Africa, Western Australia, etc. High RMSD values over the Northern Australian region may be associated to the overestimation of the SSM values by the AMSR-reg as the intercept coefficient was high over these regions, hence leading to high retrieved SSM values.

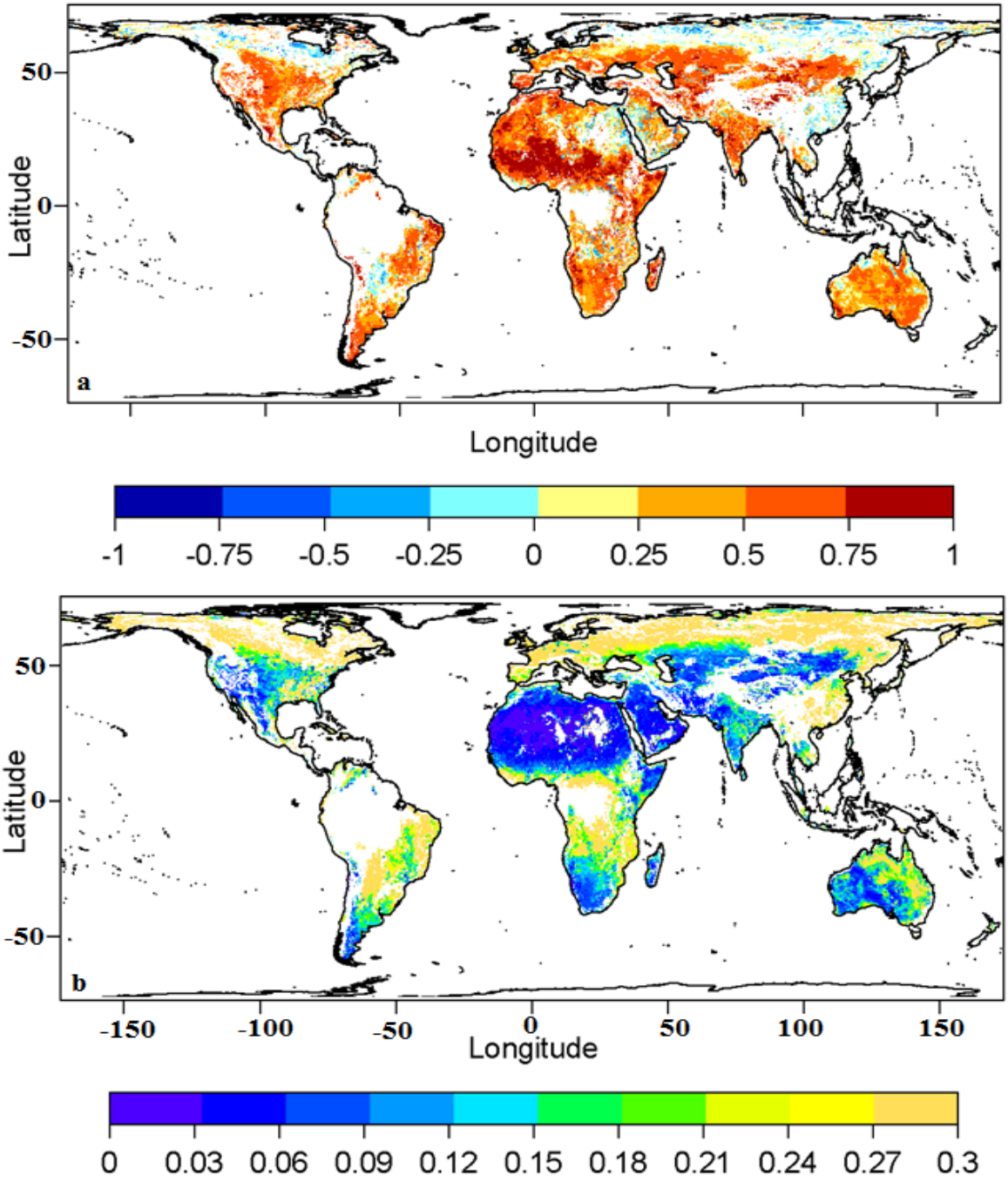

Fig. 6 - 7 *Maps of correlation between the AMSR-reg and the AMSR-VUA SSM products (top panel) and b) RMSD (m^3/m^3) between the AMSR-reg and the AMSR-VUA SSM products (bottom panel). Only significant correlations (p-value < 0.05) are presented. White areas over land indicate areas with dense vegetation, strong topography, and wetlands.*

6.3.4 Product evaluation against a reference (MERRA-Land)

As it is difficult to draw a concrete conclusion from the comparison between the AMSR-reg and AMSR-VUA about the performance of the regressed SSM data, both the AMSR-reg and AMSR-VUA retrievals were evaluated against independent land surface model simulations. To this end, we used the SSM product MERRA-Land obtained from the MERRA (Modern-Era Retrospective analysis for Research and Applications) reanalysis over the 2007-2009 period. MERRA-Land has been recently developed from MERRA as a supplemental and improved product of land surface hydrological fields (Reichle et al., 2011).

Figs. 6.8a-d show that the large-scale spatial patterns are relatively similar for both AMSR-reg and AMSR-VUA, with a slightly better ability of AMSR-VUA to capture the long-term MERRA-Land SSM variability than AMSR-reg. Figs. 6.8 a and b show that strong correlations between the global remotely sensed and the reference SSM products are found in the transition zones between wet and dry climates (e.g., Sahel), in the Great Plains (USA), and India with R greater than 0.5. This can be explained by the strong seasonal annual cycle of SSM in these regions (Koster et al., 2004b). However, AMSR-VUA datasets exhibit pronounced negative correlations against the reference over all the tundra (high latitude) regions, whereas AMSR-reg datasets exhibited moderate, and negative correlations over some parts, against the reference over the same regions.

Figs. 6.8c-d show a similar distribution of RMSD values for both AMSR-reg and AMSR-VUA products. For both products, the RMSD show a clear spatial distribution: low RMSD values were found over deserts (e.g., the Sahara, the Arabian Peninsula, extreme South Africa, and Central Australia), whereas high values of RMSD are found for both instruments over locations near the Equator, Southern Eastern Australia for only AMSR-reg, over boreal regions particularly for AMSR-VUA. Looking at the correlation and RMSD maps, AMSR-VUA have a serious problem over boreal and tundra regions as negative

correlations and very high RMSD values are found. The large differences between the AMSR-VUA and the reference SSM products, over tundra and boreal regions, may be caused by a wrong estimation of SSM when the satellite footprint includes water bodies, as AMSR-VUA does not account for water bodies. High RMSD values for AMSR-reg appear again over the North-Eastern Australia, as already noticed when compared with the AMSR-VUA for the same period. As explained before, the intercepts values (b_0 coefficient) over these regions are high which may explain the high values of RMSD.

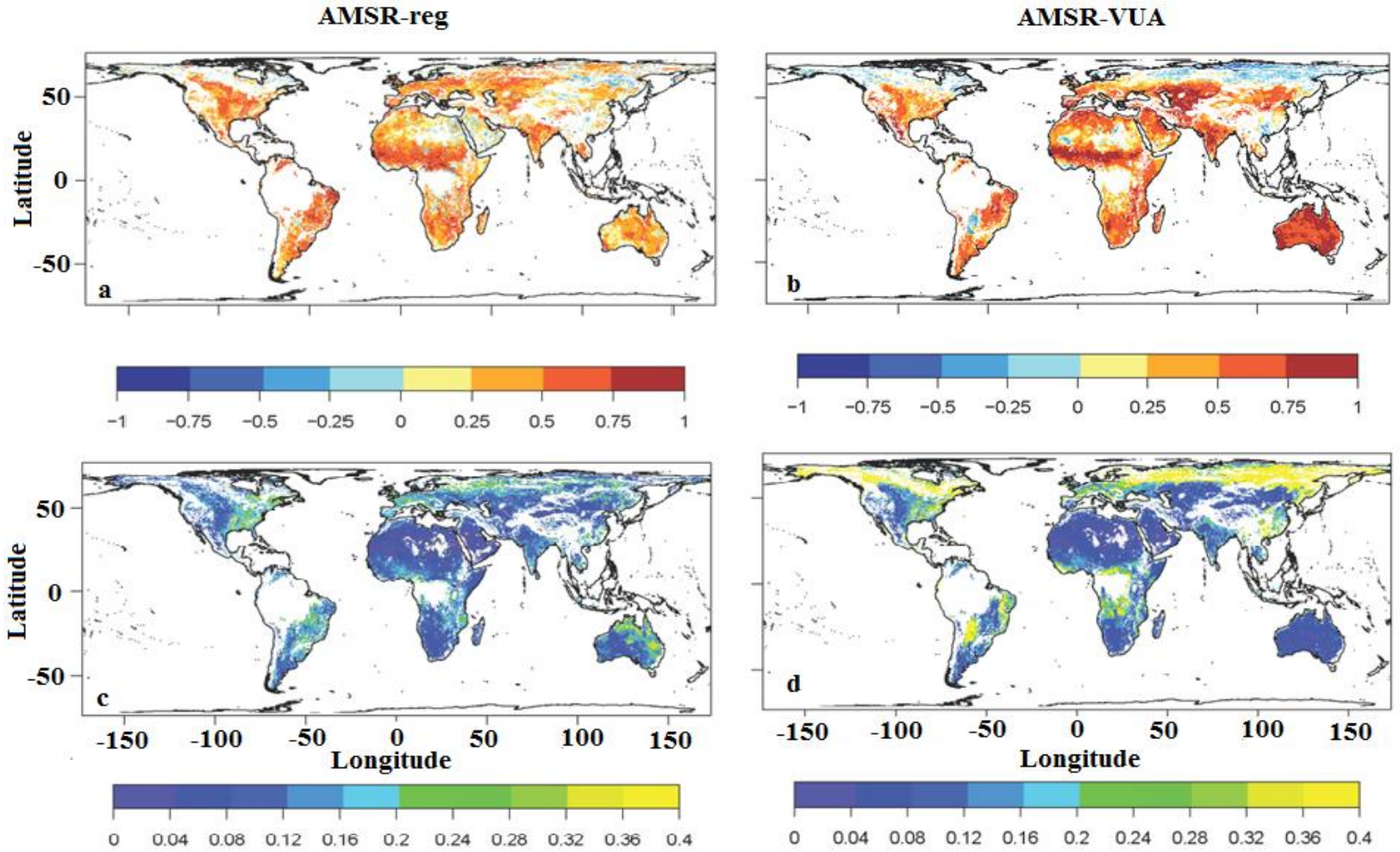

Fig. 6 - 8 *Pairwise comparison between the AMSR-reg (left panels) and AMSR-VUA (right panels) SSM products with respect to the MERRA-Land reference product in terms of the correlation coefficient (R) based on original SSM data (a and b), RMSD (m^3/m^3; c and d) during the 2007 – 2009 period. Only significant correlations (p-value < 0.05) are presented. White areas indicate areas with dense vegetation, strong topography, and wetlands.*

Fig. 6.9 confirms that AMSR-reg better captured the long-term variability of the reference SSM datasets over the Eastern USA, boreal and tundra regions, parts of the Sahel, northern Europe regions, and at some locations near the equator (in red). On the other hand, it can be seen that AMSR-VUA shows better correlations with the MERRA-Land SSM product in areas with low to moderate vegetation density (e.g., Australia, Arabian Peninsula, India, and Western USA, parts of South America (in blue). -

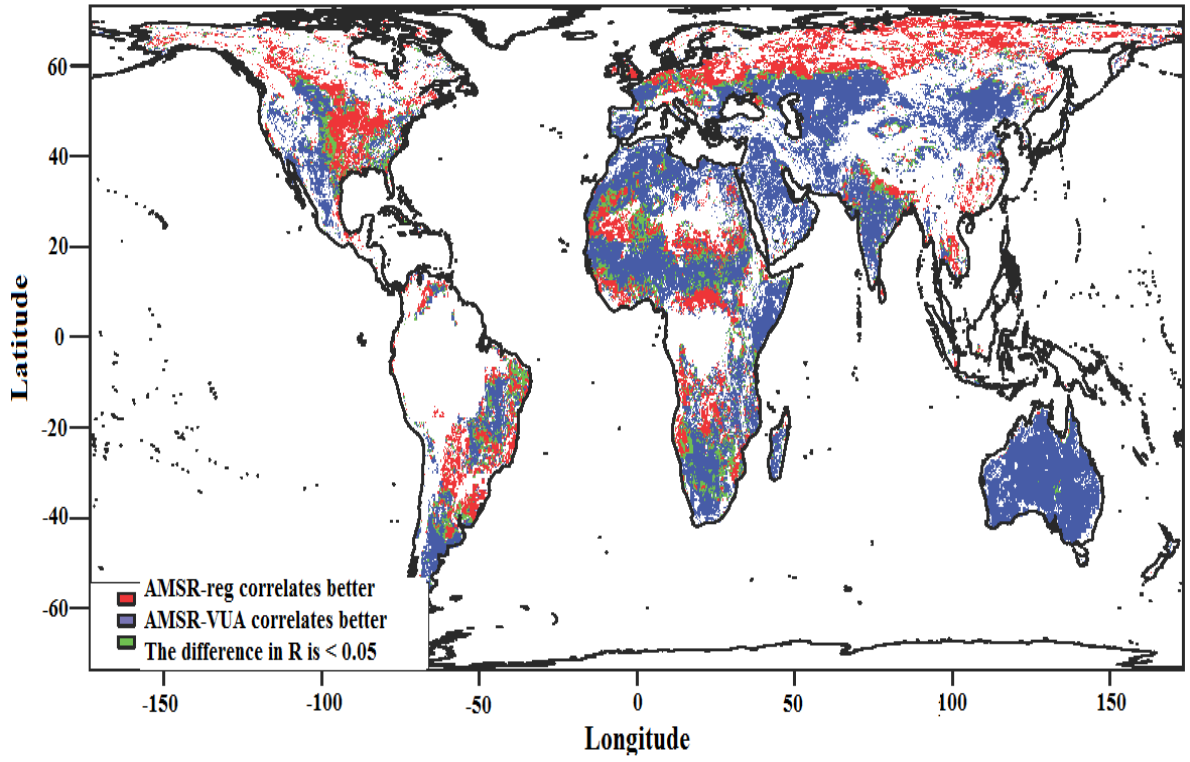

Fig. 6 - 9 *Pairwise comparison between the AMSR-reg and AMSR-VUA SSM products with respect to the reference MERRA-Land SSM product in terms of correlations based on the original SSM data during the 2007 – 2009 period. The map shows the areas where either AMSR-reg (red) or AMSR-VUA (blue) correlates better with the reference. Pixels where AMSR-reg and AMSR-VUA have similar performances (differences in the values of R lower than 0.05) are shown in green. Only significant correlations (p-value < 0.05) are presented and white areas indicate that the correlation is not significant.*

6.4 Summary and conclusions

The potential of a physically-based simple regression algorithm to retrieve SSM from space-borne TB observations was investigated in this study at the global scale. This regression algorithm has the advantage of requiring only surface temperature as an auxiliary dataset. In a first step, regression coefficients (with and without the inclusion of NDVI values) were computed for the period 2010-2011 using SMOSL3 SSM, as a reference, and the AMSR-E TB observations. The spatial patterns of the regression coefficients were, in general, in agreement with the land cover type. The use of NDVI information did not improve the regression quality in terms of correlation and RMSD. So regression coefficients without the NDVI information were used for the subsequent step of this work. As a second phase, the computed regression coefficients were used to produce a SSM product from the AMSR-E TB measurements for the 2003-2009 period (AMSR-reg). The AMSR-reg SSM retrievals were evaluated against the AMSR-VUA SSM products and against the MERRA-Land SSM simulations (considered here as a reference) for the 2007-2009 period. This first evaluation results showed that the regression approach is very promising as it produces realistic SSM climate record from the AMSR-E TB product in terms of absolute values and time variations.

Further studies are required to improve the regression approach, within the upcoming CCI programme phase 2 of the ESA, including (i) analyzing more in depth the link between the maps of the calibrated coefficients in relation to the soil physical properties (soil texture, structure, etc.), (ii) using other vegetation information such as the LAI or the other vegetation indices, (iii) evaluating AMSR-reg SSM retrievals against in situ sites at the local scale, (iv) investigating the temporal consistency of AMSR-reg (2003-2009) and SMOSL3 (2010-2014) SSM time series, and (v) doing a trend analysis using the developed time series (2003-2009) and the SMOS time series (2010-2014) with a purpose to depict which areas have become wetter or drier between 2003 and 2014.

Chapter VII

7. Conclusions and perspectives

7.1 Summary

A new level of the SMOS surface soil moisture (SSM) products has been released, namely the SMOS level 3 SSM products (SMOSL3). The SMOSL3 product is recent and thus currently subject to validation. In this context, the overall objective of this Ph.D. research work was investigating possible similarities and/or discrepancies and possible fusion of SMOSL3 SSM products with other existing microwave satellite datasets as an extension of preceding efforts to evaluate the SMOS SSM products.

In the first part of this Ph.D. thesis research (Chap. IV), a comparative analysis of SMOSL3, at L-band, with the AMSR-E SSM, at C-band, was presented. SM-DAS-2 SSM products were used to monitor both SMOSL3 and AMSR-E SSM from 03/2010 to 09/2011, a period during which both SMOS and AMSR-E products were available at the global scale. It was shown that both SMOSL3 and AMSR-E captured well the spatio-temporal variability of SM-DAS-2 for most of the biomes. In terms of correlation values, the SMOSL3 product was found to better capture the SSM temporal dynamics in highly vegetated biomes ("tropical humid", "temperate humid", etc.) while best results for AMSR-E were obtained over arid and semi-arid biomes ("desert temperate", "desert tropical", etc.). Finally, we showed that the accuracy of the remotely sensed SSM products is strongly related to the Leaf Area Index (LAI): (i) both the SMOSL3 and AMSR-E (marginally better) SSM products correlated well with the SM-DAS-2 product over regions with sparse vegetation for values of LAI ≤ 1, (ii) in regions where LAI >1, SMOSL3 showed better correlations with SM-DAS-2 than AMSR-E, and (iii) SMOSL3 had a consistent performance up to LAI = 6, whereas the AMSR-E performance deteriorated with increasing values of LAI. This section reveals that SMOS and AMSR-E complement one another in monitoring SSM over a wide range of conditions of vegetation density and that there are valuable satellite observed SSM data records over more than 10 years, which can be used to study land–atmosphere processes. This is one of the first

studies confirming the different effects of vegetation on L and C-bands signals with observations from sensors in space. In the passive microwave domain, L-band has long been considered as an optimal frequency to monitor SSM. When a vegetation layer is present over the soil surface, it attenuates the soil emissions and adds its own contribution to the emitted radiation measured by passive microwave radiometers. The retrieval algorithm attempts to decouple the effects of soil and vegetation in order to provide an estimation of SSM. However, as vegetation effects increase with increasing frequency, the correction for vegetation effects is more complex at C-band (~ 6.6 GHz for AMSR-E) than at L-band (~ 1.4 GHz for SMOS). Moreover, SMOS has multi-angular capabilities which make it, theoretically, more efficient for decoupling the soil and vegetation effects than mono-angular spatial radiometers such as AMSR-E. The combination of both a L-band system and multi-angular capabilities for SMOS compared to a C-band system and monoangular capabilities for AMSR-E explains the improved performance of SMOS over biomes with dense vegetation cover and for LAI values larger than 1.

The second part (Chap. V) investigated the consistency between the passive SMOSL3 and the active ASCAT SSM products with respect to land surface model SSM from the MERRA-Land product. It was found that the SMOSL3 and ASCAT SSM retrievals were consistent with the temporal dynamics of modelled SSM (correlation R>0.70) in the transition zones between wet and dry climates, including the Sahel, the Indian subcontinent, the Great Plains of North America, Eastern Australia, and South-Eastern Brazil. Over relatively dense vegetation covers, a better consistency with MERRA-Land was obtained with ASCAT than with SMOSL3. However, it was found that ASCAT retrievals exhibit negative correlation versus MERRA-Land in some arid regions (e.g., the Sahara and the Arabian Peninsula), most likely because of scattering effects in the soil that are not correctly accounted for over very dry surfaces. In terms of anomalies, SMOSL3 better captures the short term SSM variability

of the reference dataset (MERRA-Land) than ASCAT over regions with limited radio frequency interference (RFI) effects (e.g., North America, South America, and Australia). The seasonal and latitudinal variations of SSM, as revealed by Hovmöller diagrams, are relatively similar for the three products, although the MERRA-Land SSM values were generally higher and their seasonal amplitude is much lower than for SMOSL3 and ASCAT. Finally, both SMOSL3 and ASCAT had relatively comparable triple collocation errors with similar spatial error patterns: (i) lowest errors in arid regions (e.g., Sahara, and Arabian Peninsula) and Central America, and (ii) highest errors over most of the vegetated regions (e.g., northern Australia, India, Central Asia, and South America). However, the ASCAT SSM product is prone to larger random errors in some regions (e.g., North-Western Africa, Iran, and southern South Africa). As in the comparison of SMOS and AMSR-E, vegetation density was again found to be a key factor to interpret the consistency with MERRA-Land between the two remotely sensed products (SMOSL3 and ASCAT) which provides complementary information on SSM. The correlation (R) values increase almost linearly with LAI for ASCAT, from $R \approx 0.18$ to $R \approx 0.55$ as LAI increases from about 1 to 7. For SMOSL3, on the other hand, R values remain relatively constant as LAI increases, with values between ~ 0.32 and 0.44. SMOSL3 provides higher correlation values with the reference than ASCAT when LAI is lower than 1 (i.e. over sparse vegetation covers) and similar R values are obtained for SMOSL3 and ASCAT for intermediate LAI values ($1 \leq LAI \leq 3$).

The third part (Chap. VI) investigated the use of physically based multiple-linear regressions to retrieve a global and long term (e.g. 2003-2014) SSM record based on a combination of passive microwave remote sensing observations from the AMSR-E (2003 - 2011) and SMOS (2010 - 2014) sensors. The coefficients of these regression equations were calibrated using AMSR-E TB and SMOSL3 SSM (as a reference). This calibration process was carried out over the 2010- 2011 period, over which both SMOS and AMSR-E

observations coincide. Based on these calibrated coefficients, global SSM maps were computed from the AMSR-E TB observations over the whole 2003-2011 period (AMSR-reg). The AMSR-reg SSM retrievals were evaluated against the AMSR-VUA SSM products, for the 2010-2011 period, and the MERRA-Land SSM simulations (considered here as a reference) for the 2007-2009 period. The results showed that the regression approach is very promising as it produces realistic SSM climate record from the AMSR-E TB product in terms of absolute values and time variations. The R (mostly > 0.75) and RMSD (mostly < 0.04 m^3/m^3) maps showed a good agreement between the AMSR-reg SSM retrievals and the AMSR-VUA SSM retrievals as well as the MERRA-Land SSM simulations particularly over Australia, Central USA, Central Asia, and the Sahel.

7.2 Main conclusions

Based on the results of the three Chapters (IV, V, & VI) of this Ph.D. thesis research, joint conclusions can be drawn:

(i) There is, in general, a good correspondence between the SMOSL3 and ASCAT (AMSR-E) derived SSM products with the MERRA-Land (SM-DAS-2) reference in the transition zones between wet and dry climates (e.g., Great Plains of North America, Sahel), Eastern Australia, and South-eastern regions of Brazil. It is worth noting that these regions are regions of strong coupling between soil moisture and precipitation, where accurate soil moisture values are crucial to accurate weather, climate, and probably hydrological modelling.

(ii) The performance of SMOS satellite was the same whether it was compared with AMSR-E or ASCAT over the USA and Central Asia, as it correlated better to the reference datasets over these regions than AMSR-E and ASCAT.

(iii) Different performances of SMOS were noted when it was compared to AMSR-E and ASCAT over arid regions (e.g., the Arabian Peninsula) and regions with moderate vegetation (e.g., the Sahel). Over arid regions, for instance, SMOSL3 was closer to the reference than the ASCAT, whereas AMSR-E was closer to the reference than the SMOSL3. Over regions with moderate vegetation, SMOSL3 was closer to the reference than the AMSR-E, whereas ASCAT was closer to the reference than the SMOSL3. More specifically, higher (lower) correlations with the reference were obtained for SMOSL3 than for ASCAT (AMSR-E) when LAI is less than 1 (which corresponds to almost 50% of the pixels considered in this study). This implies that vegetation plays a key role in the performance of the SMOSL3 (as well as ASCAT and AMSR-E) SSM products, and the different satellite products have different sensitivities to vegetation. Generally, SMOS is more (less) efficient at monitoring SSM than ASCAT (AMSR-E) over sparse vegetation, whereas (AMSR-E) ASCAT is (less) more efficient over relatively dense vegetation (LAI >3). It should be noted that these conclusions are relative to the references used in these studies.

(iv) RFI contamination of SMOSL3 was found to be the key factor in the interpretation of the consistency between the SMOSL3 and the other two remotely sensed products (AMSR-E and ASCAT), with major issues over Europe, Middle East, and India, in particular.

(v) The complementary performances between SMOSL3 and the other two remotely sensed datasets revealed a potential synergy between the passive (SMOS) at L-band and passive (AMSR-E) and active (ASCAT) microwave systems at C-band, which is very promising for the development of improved, long-term SSM time

series at global scale, such as those pursued by the European Space Agency's (ESA) Climate Change Initiative (CCI).

(vi) Statistical regressions were proven, for the first time, capable of retrieving realistic SSM values in terms of temporal variations and absolute values from space-borne observations at the global scale.

7.3 Limitations

There are two main limitations that were encountered during this Ph.D. thesis research:

- The first limitation in our evaluation studies was that the SMOSL3, AMSR-E, and ASCAT remote sensing SSM products were provided with different spatial resolutions, acquisition times, sampling depths, techniques and limitations. This disparity among these different datasets might have influenced the statistical indicators used in the evaluation results, but it is difficult to say how much the impact was.
- The second limitation in our evaluation studies was the choice of land surface simulations and land data assimilation SSM estimates as references due to the limited availability of the in-situ observations at the global scale. We considered MERRA-Land and SM-DAS-2 SSM estimates, based on their reliability performances highlighted by previous studies, to perform the evaluations. But it is difficult to say which model is the best for this purpose and to determine which one is more reliable or 'true'. Therefore, MERRA-Land or SM-DAS-2 can be more detrimental for SMOS or the other two satellites. One must keep in mind that, when using them to evaluate other SSM products, the interpretation of the results is hampered by their own accuracy.

7.4 Perspectives

Researches on the exploitation and consolidation of the SMOS algorithm, products, and possible applications are far from complete. There are a number of possible ways to verify, refine, and develop the results analyzed in this Ph.D. thesis research, and also to continue the evaluations dealing particularly with issues left open at the end of this document. Further research may attempt to go further in the following tasks:

1. The evaluation of remote sensing products is a continuous task as datasets are continuously enlarged and new algorithms are available. We recommend investigating the performance of SMOS SSM products using longer datasets as the SMOS SSM product in this Ph.D. research work was evaluated for the period 2010-2011 and 2010-2012. It is expected that with the new processing campaign a 5 year coherent of SMOS dataset will be available in 2015. A continuous validation procedure can be imagined which automatically monitors SSM products at the global scale taking into account regional information and analysis as the ones presented in this Ph.D. research work.
2. The quality of the current SMOS SSM retrieval algorithm, used to translate observed TB into SSM, was recently enhanced by the substitution of the Dobson dielectric model with the Mironov dielectric mixing model, and the new retrieved SSM products will be released soon. An attempt will be made to perform a first assessment of the improvements of the most recent SMOS reprocessing: in particular the impact of introducing the Mironov model. Also, there is room for improvement in the SMOS retrieval algorithm by enhancing the RFI filtering. Some regions such as Europe, China, India, etc. are severely contaminated by the RFI at L-band, which led to unreliable SMOS SSM retrievals over these regions. The RFI problems are common issues for most

radiometers, and efforts should be pursued on international level to minimize them. Furthermore, alternative soil moisture algorithms in particular the use of neural networks and statistical regression analyses proposed in Chapter VI, should be considered, especially over regions where the forward algorithm fails to accurately retrieve the SSM. Using these methods will also help in retrieving SSM in real time as using the standard algorithm (forward modelling) takes one month to retrieve SSM for one year whereas the other methods take roughly no more than a few hours. Furthermore, the SMOS SSM algorithm should account for changes in vegetation optical thickness (τ) and roughness of the soil surface caused by farming practices (e.g. tillage) and planting activities, which may confuse the satellites (Patton & Hornbuckle, 2013). For instance, new approaches such as the one combining vegetation and roughness effects within one parameter (TR) (Fernández-Morán et al., 2014; Parrens et al., 2014), which is retrieved simultaneously to SSM, may improve the SMOS SSM products. The evaluation procedure of these products can benefit from the analyses presented in the PhD and can be a common benchmark for them.

3. Unfortunately, in the highly vegetated regions, in situ data are almost completely unavailable so that it was unfeasible at the moment to investigate in detail the quite surprising finding of SMOS performance against ASCAT data over these regions, where ASCAT was closer to the model in terms of correlation. However, in-situ measurements stations are growing and this issue can be further investigated. More generally, the validation of the SMOS SSM products will significantly benefit from the increasing number of in-situ soil moisture networks thanks to efforts like the International Soil Moisture Network initiative (http://www.ipf.tuwien.ac.at/insitu/) (Dorigo et al., 2011). In

this Ph.D. research work we also found that passive L-band microwave (e.g. SMOS) proved to be performant in semi-arid areas, where RFI is low, compared to active C-band sensors (e.g. ASCAT). These areas are subject to high stress in terms of water resources and satellite based SSM datasets are very useful to monitor this stress. For instance, specific studies need to be developed in semi-arid areas (like Yemen). The combination of multi-sensors (SMOS, the upcoming SMAP mission, AMSR-E) supported by in-situ monitoring station, to be installed in Yemen, is envisioned in the near future.

4. As said previously, one of the limitations of this Ph.D. research was using Land Surface Models simulations as benchmarks, which are commonly used for evaluating the remotely sensed SSM at larges scales. Much less attention has been paid to the use of other space-borne datasets such as the Gravity Recovery and Climate Experiment (GRACE) satellite, which has been providing information on total water storage change (TWS) since 2002. This limitation can be overcome, in the future, by integration of GRACE data, for instance, into the validation of SMOS SSM datasets. Possibilities and benefits of relating the SMOS SSM products to TWS provided by the GRACE should be investigated. Abelen & Seitz (2013) compared GRACE data, for instance, against ASCAT SSM products using correlation analysis between change in SSM from ASCAT and change in TWS from GRACE. This can be done using also SMOS SSM products to identify regions where the change of TWS is in agreement with SSM, thus, the regions where SMOS datasets may be useful for the understanding of TWS and vice-versa. On the other hand, GRACE is only able to provide the TWS but not to determine the individual contribution of each variable in the observed TWS integral signal. Further research shall focus

on incorporating SMOS SSM datasets with GRACE products, which may be of help to separate the GRACE TWS datasets. In addition, GRACE and other remotely sensed products for all components (i.e. precipitation, evapotranspiration, runoff, and water storage) of the water budget have been recently used to compute and evaluate the potential of water budget closure. Sheffield et al. (2009), for instance, used the stream flow component as the water balance closure and was evaluated over the Mississippi River basin against stream flow measurements. Including SMOS datasets in these analyses by, for instance, closing the water budget using SSM and evaluating errors using the SMOS SSM datasets can be investigated in the near future.

5. Many studies suggest the use of multi-sensors data to disaggregate SSM from microwave data (Merlin et al., 2008; Merlin et al., 2010; Merlin et al., 2012; Merlin et al., 2013; Piles et al., 2011). Those methods deliver high spatial resolution soil moisture. Analyses similar to the ones done in this Ph.D. need to be done to compare those approaches over different climatic conditions.

6. The SMOS, AMSR-E, and ASCAT missions have their own advantages and limitations as was shown throughout this Ph.D. research work. Some perform better over arid regions; others can be better for vegetated areas. It is recommended to make a product from these different sensors where spatially each sensor has a different weight. This will be achieved by, for instance, taking advantage of each sensor on different places while conserving spatial and temporal coherence. The integration procedures (simple weighting, the constrained linear method, the optimal interpolation method, and the neural network technique) developed by Aires (2014) can be applied to optimally combine the multiple observation datasets to obtain a coherent dataset.

7. Further analyses are to be focused on the extraction of long-term trends from the 11 year time series (i.e. 2003-2010 from AMSR-reg and 2010-2014 from SMOS) SSM with a purpose to depict which areas have become wetter or drier between 2003 and 2014. Before doing the trend analyses, the homogeneities of the developed long-term SSM time series should be examined over the full period i.e. 2003 -2014. There are special algorithms/ways that could be used to detect the discontinuities, which may cause misinterpretation of the trends, in the SSM time series for the whole period (e.g., Easterling & Peterson, 1995; Loew et al., 2013; Moisselin J-M & O, 2002).

8. The upcoming SMAP mission will provide continuity for L-band measurements of SMOS. At the end of this year (2014), the SMOS mission will have been in the space for 5 years, and the SMAP satellite would be just launched. A consolidated SSM product, that is suitable to fill climate change research gaps, can be obtained through data fusion between SMOS and SMAP SSM products. How to build seamless data record of SSM from SMOS to SMAP should be envisaged, with insights from the analyses performed in this Ph.D. research work.

References

Abelen, S. & Seitz, F. (2013). Relating satellite gravimetry data to global soil moisture products via data harmonization and correlation analysis. *Remote Sensing of Environment, 136*, 89-98

Aires, F. (2014). Combining Datasets of Satellite-Retrieved Products. Part I: Methodology and Water Budget Closure. *Journal of Hydrometeorology, 15*, 1677-1691

Al-Yaari, A., Wigneron, J.P., Ducharne, A., Kerr, Y., de Rosnay, P., de Jeu, R., Govind, A., Al Bitar, A., Albergel, C., Muñoz-Sabater, J., Richaume, P. & Mialon, A. (2014). Global-scale evaluation of two satellite-based passive microwave soil moisture datasets (SMOS and AMSR-E) with respect to Land Data Assimilation System estimates. *Remote Sensing of Environment, 149*, 181-195

Al Bitar, A., Leroux, D., Kerr, Y.H., Merlin, O., Richaume, P., Sahoo, A. & Wood, E.F. (2012). Evaluation of SMOS Soil Moisture Products Over Continental U.S. Using the SCAN/SNOTEL Network. *Geoscience and Remote Sensing, IEEE Transactions on, 50*, 1572-1586

Albergel, C., Rüdiger, C., Carrer, D., Calvet, J.-C., Fritz, N., Naeimi, V., Bartalis, Z. & Hasenauer, S. (2009). An evaluation of ASCAT surface soil moisture products with in-situ observations in Southwestern France. *Hydrology and Earth System Sciences, 13*

Albergel, C., Zakharova, E., Calvet, J.C., Zribi, M., Parde, M., Wigneron, J.P., Novello, N., Kerr, Y., Mialon, A. & Fritz, N.E.D. (2011). A first assessment of the SMOS data in southwestern France using in situ and airborne soil moisture estimates : the CAROLS airborne campaign. *Remote Sensing of Environment, 115*, 2718-2728

Albergel, C., de Rosnay, P., Gruhier, C., Munoz-Sabater, J., Hasenauer, S., Isaksen, L., Kerr, Y. & Wagner, W. (2012). Evaluation of remotely sensed and modelled soil moisture products using global ground-based in situ observations. *Remote Sensing of Environment, 118*, 215-226

Albergel, C., Dorigo, W., Balsamo, G., Muñoz-Sabater, J., de Rosnay, P., Isaksen, L., Brocca, L., de Jeu, R. & Wagner, W. (2013a). Monitoring multi-decadal satellite earth observation of soil moisture products through land surface reanalyses. *Remote Sensing of Environment, 138*, 77-89

Albergel, C., Dorigo, W., Reichle, R.H., Balsamo, G., de Rosnay, P., Muñoz-Sabater, J., Isaksen, L., de Jeu, R. & Wagner, W. (2013b). Skill and Global Trend Analysis of Soil Moisture from Reanalyses and Microwave Remote Sensing. *Journal of Hydrometeorology, 14*, 1259-1277

Alyaari, A., Wigneron, J., Ducharne, A., Kerr, Y., Al Bitar, A., de Jeu, R., Govind, A., de Rosnay, P., Albergel, C. & Munoz-Sabater, J. (2014). Performances of SMOS and AMSR-E soil moisture retrievals against Land Data Assimilation system estimates. In,

Microwave Radiometry and Remote Sensing of the Environment (MicroRad), 2014 13th Specialist Meeting on (pp. 19-24)

Arora, V.K. & Boer, G.J. (2006). The Temporal Variability of Soil Moisture and Surface Hydrological Quantities in a Climate Model. *Journal of Climate, 19*, 5875-5888

Balsamo, G., Viterbo, P., Beljaars, A.C.M., van den Hurk, B.J.J.M., Hirschi, M., Betts, A.K. & K., S. (2009). A revised hydrology for the ECMWF model: Verification from field site to terrestrial water storage and impact in the ECMWF-IFS. *J. Hydrometeor, 10*

Balsamo, G., Boussetta, S., Dutra, E., Beljaars, A., Viterbo, P. & Van de Hurk, B. (2011). Evolution of land surface processes in the IFS. *ECMWF Newsletter, 127*, 17–22

Barella-Ortiz, A., Polcher, J., Tuzet, A. & Laval, K. (2013). Potential evaporation estimation through an unstressed surface-energy balance and its sensitivity to climate change. *Hydrol. Earth Syst. Sci., 17*, 4625-4639

Barichivich, J., Briffa, K., Myneni, R., Schrier, G., Dorigo, W., Tucker, C., Osborn, T. & Melvin, T. (2014). Temperature and Snow-Mediated Moisture Controls of Summer Photosynthetic Activity in Northern Terrestrial Ecosystems between 1982 and 2011. *Remote Sensing, 6*, 1390-1431

Bartalis, Z., Wagner, W., Naeimi, V., Hasenauer, S., Scipal, K., Bonekamp, H., Figa, J. & Anderson, C. (2007a). Initial soil moisture retrievals from the METOP-A Advanced Scatterometer (ASCAT). *Geophysical Research Letters, 34*, L20401

Bartalis, Z., Hasenauer, S., Naeimi, V. & Wagner, W. (2007b). WARP-NRT 2.0 Reference Manual. ASCAT Soil Moisture Report Series, No. 14. *Institute of Photogrammetry and Remote Sensing, Vienna University of Technology, Austria*

Bartalis, Z., V. Naeimi, S. Hasenauer & Wagner, W. (2008). ASCAT Soil Moisture Product Handbook. ASCAT Soil Moisture Report Series, No. 15. *Institute of Photogrammetry and Remote Sensing, Vienna University of Technology.*

Bartalis, Z., Naeimi, V. & Wagner, W. (2009). Metop ASCAT Soil Moisture. *GMSM Kick-Off Meeting Conference*

Bartsch, A., Melzer, T., Elger, K. & Heim, B. (2012). Soil Moisture from Metop ASCAT Data at High Latitudes. In K. Hinckel (Ed.), *Tenth International Conference on Permafrost (TICOP)* (pp. 33-38)

Beljaars, A.C.M., Viterbo, P., Miller, M.J. & Betts, A.K. (1996). The Anomalous Rainfall over the United States during July 1993: Sensitivity to Land Surface Parameterization and Soil Moisture Anomalies. *Monthly Weather Review, 124*, 362-383

Beven, K.J. & Kirkby, M.J. (1979). A physically based, variable contributing area model of basin hydrology / Un modèle à base physique de zone d'appel variable de l'hydrologie du bassin versant. *Hydrological Sciences Bulletin, 24*, 43-69

Bindlish, R., Jackson, T.J., Wood, E., Gao, H., Starks, P., Bosch, D. & Lakshmi, V. (2003). Soil moisture estimates from TRMM Microwave Imager observations over the Southern United States. *Remote Sensing of Environment, 85*, 507-515

Blöschl , G., Komma, J. & Hasenauer, S. (2009). Hydrological downscaling of soil moisture (2009): Report for Final report of the Visiting Scientist Activity to the Satellite Application Facility on Support to Operational Hydrology and Water Management (H-SAF); 64 pages

Bolten, J.D., Crow, W.T., Xiwu, Z., Jackson, T.J. & Reynolds, C.A. (2010). Evaluating the Utility of Remotely Sensed Soil Moisture Retrievals for Operational Agricultural Drought Monitoring. *Selected Topics in Applied Earth Observations and Remote Sensing, IEEE Journal of, 3*, 57-66

Briggs, L.J. & Shantz, H.L. (1912). The Wilting Coefficient and Its Indirect Determination. *Botanical Gazette, 53*, 20-37

Brocca, L., Melone, F., Moramarco, T., Wagner, W. & Hasenauer, S. (2010). ASCAT soil wetness index validation through in situ and modeled soil moisture data in central Italy. *Remote Sensing of Environment, 114*, 2745-2755

Brocca, L., Hasenauer, S., Lacava, T., Melone, F., Moramarco, T., Wagner, W., Dorigo, W., Matgen, P., Martínez-Fernández, J., Llorens, P., Latron, J., Martin, C. & Bittelli, M. (2011). Soil moisture estimation through ASCAT and AMSR-E sensors: An intercomparison and validation study across Europe. *Remote Sensing of Environment, 115*, 3390-3408

Budyko, M.I. (1956). Heat Balance of the Earth's Surface. *Translated by Nine A. Stepanova Washington, D.C 1958.*

Calvet, J.C., Wigneron, J.P., Walker, J., Karbou, F., Chanzy, A. & Albergel, C. (2011). Sensitivity of Passive Microwave Observations to Soil Moisture and Vegetation Water Content: L-Band to W-Band. *Geoscience and Remote Sensing, IEEE Transactions on, 49*, 1190-1199

Campbell, J.B. (1996). Introduction to Remote Sensing. *The Guilford Press*

Camps, A., Bara, J., Sanahuja, I.C. & Torres, F. (1997). The processing of hexagonally sampled signals with standard rectangular techniques: application to 2-D large aperture synthesis interferometric radiometers. *Geoscience and Remote Sensing, IEEE Transactions on, 35*, 183-190

Camps, A., Vall-llossera, M., Batres, L., Torres, F., Duffo, N. & Corbella, I. (2005). Retrieving sea surface salinity with multiangular L-band brightness temperatures: Improvement by spatiotemporal averaging. *Radio Science, 40*, RS2003

Camps, A., Gourrion, J., Tarongi, J.M., Gutie, x, rrez, A., Barbosa, J. & Castro, R. (2010). Rfianalysis in smos imagery. In, *Geoscience and Remote Sensing Symposium (IGARSS), 2010 IEEE International* (pp. 2007-2010)

CECR (2012). Comprehensive Error Characterisation Report, Version 0.7. *ESA Climate Change Initiative Phase 1 Soil Moisture Project*

Chen, J.M. & Cihlar, J. (1996). Retrieving leaf area index of boreal conifer forests using Landsat TM images. *Remote Sensing of Environment, 55*, 153-162

Cheruy, F., Dufresne, J. & Ducharne, A. Role of the land-atmosphere coupling in systematic mid-latitude summer warm biases and climate change amplification in CMIP5 simulations. *Geophysical Research Letters (Submitted for publication)*

Cheruy, F., Campoy, A., Dupont, J.C., Ducharne, A., Hourdin, F., Haeffelin, M., Chiriaco, M. & Idelkadi, A. (2013). Combined influence of atmospheric physics and soil hydrology on the simulated meteorology at the SIRTA atmospheric observatory. *Climate Dynamics, 40*, 2251-2269

Chesworth, W. (2008). Biomes and their Soils. In W. Chesworth (Ed.), *Encyclopedia of Soil Science* (pp. 61-68): Springer Netherlands

Choudhury, B.J., Schmugge, T.J., Chang, A. & Newton, R.W. (1979). Effect of surface roughness on the microwave emission from soils. *Journal of Geophysical Research: Oceans, 84*, 5699-5706

Choudhury, B.J., Schmugge, T.J. & Mo, T. (1982). A parameterization of effective soil temperature for microwave emission. *Journal of Geophysical Research: Oceans, 87*, 1301-1304

Choudhury, B.J. (1993). Reflectivities of selected land-surface types at 19 and 37 GHz from ssm/i observations. *Remote Sens. Environ, 46*

Chung, D., R.A.M de Jeu, W. Dorigo, Hahn, S., Melzer, T., R.M. Parinussa, C.Paulik., C. Reimer, M. Vreugdenhil & Wagner, W. (2013). Algorithm Theoretical Baseline Document (ATDB) Version 1, Climate Change Initiative
Phase 1 Soil Moisture Project

Collow, T.W., Robock, A., Basara, J.B. & Illston, B.G. (2012). Evaluation of SMOS retrievals of soil moisture over the central United States with currently available in situ observations. *Journal of Geophysical Research: Atmospheres, 117*, D09113

Colombo, R., Bellingeri, D., Fasolini, D. & Marino, C.M. (2003). Retrieval of leaf area index in different vegetation types using high resolution satellite data. *Remote Sensing of Environment, 86*, 120-131

Crosson, W.L., Laymon, C.A., Inguva, R. & Schamschula, M.P. (2002). Assimilating remote sensing data in a surface flux–soil moisture model. *Hydrological Processes, 16*, 1645-1662

Crow, W.T. & Wood, E.F. (2003). The assimilation of remotely sensed soil brightness temperature imagery into a land surface model using Ensemble Kalman filtering: a case study based on ESTAR measurements during SGP97. *Advances in Water Resources, 26*, 137-149

Crow, W.T., Wagner, W. & Naeimi, V. (2010). The Impact of Radar Incidence Angle on Soil-Moisture-Retrieval Skill. *Geoscience and Remote Sensing Letters, IEEE, 7*, 501-505

Curran, P.J. (1985). Principles of Remote Sensing. *Longman Scientific and Technical, UK, pp: 282*

D'Odorico, P. & Porporato, A. (2004). Preferential states in soil moisture and climate dynamics. *Proceedings of the National Academy of Sciences of the United States of America, 101*, 8848-8851

Daganzo-Eusebio, E., Oliva, R., Kerr, Y.H., Nieto, S., Richaume, P. & Mecklenburg, S.M. (2013). SMOS Radiometer in the 1400–1427-MHz Passive Band: Impact of the RFI Environment and Approach to Its Mitigation and Cancellation. *Geoscience and Remote Sensing, IEEE Transactions on, 51*, 4999-5007

Dall'Amico, J.T., Schlenz, F., Loew, A. & Mauser, W. (2012). First Results of SMOS Soil Moisture Validation in the Upper Danube Catchment. *Geoscience and Remote Sensing, IEEE Transactions on, 50*, 1507-1516

Daly, E. & Porporato, A. (2005). A review of soil moisture dynamics: from rainfall infiltration to ecosystem response. *Environ Eng Sci 22(1)*, 9-24

de Jeu, R.A.M., Wagner, W., Holmes, T.R.H., Dolman, A.J., Giesen, N.C. & Friesen, J. (2008). Global Soil Moisture Patterns Observed by Space Borne Microwave Radiometers and Scatterometers. *Surveys in Geophysics, 29*, 399-420

De Lannoy, G.J.M., Reichle, R.H. & Pauwels, V.R.N. (2013). Global Calibration of the GEOS-5 L-Band Microwave Radiative Transfer Model over Nonfrozen Land Using SMOS Observations. *Journal of Hydrometeorology, 14*, 765-785

de Rosnay, P. & Polcher, J. (1998). Modelling root water uptake in a complex land surface scheme coupled to a GCM. *Hydrol. Earth Syst. Sci., 2*, 239-255

de Rosnay, P., Calvet, J.-C., Kerr, Y., Wigneron, J.-P., Lemaître, F., Escorihuela, M.J., Sabater, J.M., Saleh, K., Barrié, J., Bouhours, G., Coret, L., Cherel, G., Dedieu, G., Durbe, R., Fritz, N.E.D., Froissard, F., Hoedjes, J., Kruszewski, A., Lavenu, F., Suquia, D. & Waldteufel, P. (2006). SMOSREX: A long term field campaign experiment for soil moisture and land surface processes remote sensing. *Remote Sensing of Environment, 102*, 377-389

de Rosnay, P., Drusch, M., Balsamo, G., Isaksen, L. & Albergel, C. (2011). Extended Kalman Filter soil moisture analysis in the IFS. *ECMWF Spring Newsletter n127*

de Rosnay, P., Balsamo, G., Albergel, C., Muñoz-Sabater, J. & Isaksen, L. (2012). Initialisation of Land Surface Variables for Numerical Weather Prediction. *Surveys in Geophysics*, 1-15

de Rosnay, P., Drusch, M., Vasiljevic, D., Balsamo, G., Albergel, C. & Isaksen, L. (2013). A simplified Extended Kalman Filter for the global operational soil moisture analysis at ECMWF. *Quarterly Journal of the Royal Meteorological Society, 139*, 1199-1213

Demarest, P., Good, S. & Rand, D. (2001). Ascent plan for Aqua (EOS-PM1) including phasing with Terra (EOS-AM1). *Proceedings of 16th International Symposium on Space Flight Dynamics, Pasadena*

Dente, L., Su, Z. & Wen, J. (2012). Validation of SMOS Soil Moisture Products over the Maqu and Twente Regions. *Sensors, 12*, 9965-9986

Dingman, L.S. (2002). Physical Hydrology. Upper Saddle River: Prentice- Hall

Dirmeyer, P.A., X. Gao & Oki, T. (2002). The Second Global Soil Wetness Project, GSWP-2. *IGPO Publication Series No. 37, 65 pp*

Dirmeyer, P.A., Gao, X., Zhao, M., Zhichang, G., Oki, T. & Hanasaki, N. (2006). GSWP 2: Multimodel analysis and implications for our perception of the land surface. *B. Am. Meteorol, 87*

Dobriyal, P., Qureshi, A., Badola, R. & Hussain, S.A. (2012). A review of the methods available for estimating soil moisture and its implications for water resource management. *Journal of Hydrology, 458–459,* 110-117

Dobson, M.C., Ulaby, F.T., Hallikainen, M.T. & El-Rayes, M.A. (1985). Microwave Dielectric Behavior of Wet Soil-Part II: Dielectric Mixing Models. *Geoscience and Remote Sensing, IEEE Transactions on, GE-23,* 35-46

Dorigo, W., de Jeu, R., Chung, D., Parinussa, R., Liu, Y., Wagner, W. & Fernández-Prieto, D. (2012). Evaluating global trends (1988–2010) in harmonized multi-satellite surface soil moisture. *Geophysical Research Letters, 39,* L18405

Dorigo, W.A., Scipal, K., Parinussa, R.M., Liu, Y.Y., Wagner, W., de Jeu, R.A.M. & Naeimi, V. (2010). Error characterisation of global active and passive microwave soil moisture datasets. *Hydrology and Earth System Sciences, 14,* 2605-2616

Dorigo, W.A., Wagner, W., Hohensinn, R., Hahn, S., Paulik, C., Drusch, M., Mecklenburg, S., van Oevelen, P., Robock, A. & Jackson, T. (2011). The International Soil Moisture Network: a data hosting facility for global in situ soil moisture measurements. *Hydrol. Earth Syst. Sci. Discuss., 8*

Draper, C., Mahfouf, J.F., Calvet, J.C., Martin, E. & Wagner, W. (2011). Assimilation of ASCAT near-surface soil moisture into the SIM hydrological model over France. *Hydrol. Earth Syst. Sci., 15,* 3829-3841

Draper, C., Reichle, R., de Jeu, R., Naeimi, V., Parinussa, R. & Wagner, W. (2013). Estimating root mean square errors in remotely sensed soil moisture over continental scale domains. *Remote Sensing of Environment, 137,* 288-298

Draper, C.S., Walker, J.P., Steinle, P.J., de Jeu, R.A.M. & Holmes, T.R.H. (2009a). An evaluation of AMSR–E derived soil moisture over Australia. *Remote Sensing of Environment, 113,* 703-710

Draper, C.S., Mahfouf, J.F. & Walker, J.P. (2009b). An EKF assimilation of AMSR-E soil moisture into the ISBA land surface scheme. *Journal of Geophysical Research: Atmospheres, 114,* D20104

Draper, C.S., Reichle, R.H., De Lannoy, G.J.M. & Liu, Q. (2012). Assimilation of passive and active microwave soil moisture retrievals. *Geophysical Research Letters, 39,* L04401

Drusch, M. (2007). Initializing numerical weather prediction models with satellite-derived surface soil moisture: Data assimilation experiments with ECMWF's Integrated

Forecast System and the TMI soil moisture data set. *Journal of Geophysical Research: Atmospheres, 112*, D03102

Drusch, M. & Viterbo, P. (2007). Assimilation of Screen-Level Variables in ECMWF's Integrated Forecast System: A Study on the Impact on the Forecast Quality and Analyzed Soil Moisture. *Monthly Weather Review, 135*, 300-314

Drusch, M., Scipal, K., de Rosnay, P., Balsamo, G., Andersson, E., Bougeault, P. & Viterbo, P. (2009). Towards a Kalman Filter based soil moisture analysis system for the operational ECMWF Integrated Forecast System. *Geophysical Research Letters, 36*, L10401

Ducharne, A., Koster, R.D., Suarez, M.J., Stieglitz, M. & Kumar, P. (2000). A catchment-based approach to modeling land surface processes in a general circulation model: 2. Parameter estimation and model demonstration. *Journal of Geophysical Research: Atmospheres, 105*, 24823-24838

Easterling, D.R. & Peterson, T.C. (1995). A new method for detecting undocumented discontinuities in climatological time series. *International Journal of Climatology, 15*, 369-377

English, N.B., Weltzin, J.F., Fravolini, A., Thomas, L. & Williams, D.G. (2005). The influence of soil texture and vegetation on soil moisture under rainout shelters in a semi-desert grassland. *Journal of Arid Environments, 63*, 324-343

Entekhabi, D., Rodriguez-Iturbe, I. & Castelli, F. (1996). Mutual interaction of soil moisture state and atmospheric processes. *Journal of Hydrology, 184*, 3-17

Entekhabi, D., Njoku, E.G., O'Neill, P.E., Kellogg, K.H., Crow, W.T., Edelstein, W.N., Entin, J.K., Goodman, S.D., Jackson, T.J., Johnson, J., Kimball, J., Piepmeier, J.R., Koster, R.D., Martin, N., McDonald, K.C., Moghaddam, M., Moran, S., Reichle, R., Shi, J.C., Spencer, M.W., Thurman, S.W., Leung, T. & Van Zyl, J. (2010). The Soil Moisture Active Passive (SMAP) Mission. *Proceedings of the IEEE, 98*, 704-716

Escorihuela, M.J., Chanzy, A., Wigneron, J.P. & Kerr, Y.H. (2010). Effective soil moisture sampling depth of L-band radiometry: A case study. *Remote Sensing of Environment, 114*, 995-1001

Fan, L., Gao, Y., Brück, H. & Bernhofer, C. (2009). Investigating the relationship between NDVI and LAI in semi-arid grassland in Inner Mongolia using in-situ measurements. *Theoretical and Applied Climatology, 95*, 151-156

FAO (2003). Digital soil map of the world (DSMW). *Tech. rep., Food and Agriculture Organization of the United Nations. Re-issued version*

Fernández-Morán, R., Wigneron., J.-P., Lopez-Baeza., E., Sgado-Hernanz., P., Mialon., A., Miernecki., M., Al-Yaari., A., Parrens., M., Swchank., M., Wang., S., Coll-Pajaron., A., Lawrence., H. & Kerr, Y. (2014). Evaluating the impact of roughness in soil moisture and optical thickness retrievals over the VAS area. *International Geoscience and Remote Sensing Symposium (IGARSS 2014), Québec, Canada*

Ferrazzoli, P., Paloscia, S., Pampaloni, P., Schiavon, G., Solimini, D. & Coppo, P. (1992). Sensitivity to microwave measurements to vegetation biomass and soil moisture content: a case study. *Geoscience and Remote Sensing, IEEE Transactions on, 30*, 750-756

Ferrazzoli, P., Guerriero, L. & Wigneron, J.P. (2002). Simulating L-band emission of forests in view of future satellite applications. *Geoscience and Remote Sensing, IEEE Transactions on, 40*, 2700-2708

Findell, K.L. & Eltahir, E.A.B. (2003). Atmospheric Controls on Soil Moisture–Boundary Layer Interactions. Part I: Framework Development. *Journal of Hydrometeorology, 4*, 552-569

Frison, P.L. & Mougin, E. (1996). Monitoring global vegetation dynamics with ERS-1 wind scatterometer data. *International Journal of Remote Sensing, 17*, 3201-3218

Fu, B., Chen, L., Ma, K., Zhou, H. & Wang, J. (2000). The relationships between land use and soil conditions in the hilly area of the loess plateau in northern Shaanxi, China. *CATENA, 39*, 69-78

Gao, H., Wood, E.F., Jackson, T.J., Drusch, M. & Bindlish, R. (2006). Using TRMM/TMI to Retrieve Surface Soil Moisture over the Southern United States from 1998 to 2002. *Journal of Hydrometeorology, 7*, 23-38

Gascoin, S., Ducharne, A., Ribstein, P., Lejeune, Y. & Wagnon, P. (2009a). Dependence of bare soil albedo on soil moisture on the moraine of the Zongo glacier (Bolivia): Implications for land surface modeling. *Journal of Geophysical Research: Atmospheres, 114*, D19102

Gascoin, S., Ducharne, A., Ribstein, P., Perroy, E. & Wagnon, P. (2009b). Sensitivity of bare soil albedo to surface soil moisture on the moraine of the Zongo glacier (Bolivia). *Geophysical Research Letters, 36*, L02405

Georgakakos, K.P. & Carpenter, T.M. (2006). Potential value of operationally available and spatially distributed ensemble soil water estimates for agriculture. *Journal of Hydrology, 328*, 177-191

Gillies, R.R., Kustas, W.P. & Humes, K.S. (1997). A verification of the 'triangle' method for obtaining surface soil water content and energy fluxes from remote measurements of the Normalized Difference Vegetation Index (NDVI) and surface e. *International Journal of Remote Sensing, 18*, 3145-3166

Global Climate Observing System (2010). Implementation plan for the Global Observing System for climate in support of the UNFCC (2010 Update), 180 pp.

Gouttevin, I., Bartsch, A., Krinner, G. & Naeimi, V. (2013). A comparison between remotely-sensed and modelled surface soil moisture (and frozen status) at high latitudes. *Hydrol. Earth Syst. Sci. Discuss., 10*, 11241-11291

Grant, J.P., Wigneron, J.P., Van de Griend, A.A., Kruszewski, A., Søbjærg, S.S. & Skou, N. (2007). A field experiment on microwave forest radiometry: L-band signal behaviour for varying conditions of surface wetness. *Remote Sensing of Environment, 109*, 10-19

Griend, A.A. & Owe, M. (1994). Microwave vegetation optical depth and inverse modelling of soil emissivity using Nimbus/SMMR satellite observations. *Meteorology and Atmospheric Physics, 54*, 225-239

Gruhier, C., de Rosnay, P., Hasenauer, S., Holmes, T., de Jeu, R., Kerr, Y., Mougin, E., Njoku, E., Timouk, F., Wagner, W. & Zribi, M. (2010). Soil moisture active and passive microwave products: intercomparison and evaluation over a Sahelian site. *Hydrol. Earth Syst. Sci., 14*, 141-156

Hain, C.R., Mecikalski, J.R. & Anderson, M.C. (2009). Retrieval of an Available Water-Based Soil Moisture Proxy from Thermal Infrared Remote Sensing. Part I: Methodology and Validation. *Journal of Hydrometeorology, 10*, 665-683

Hain, C.R., Crow, W.T., Mecikalski, J.R., Anderson, M.C. & Holmes, T. (2011). An intercomparison of available soil moisture estimates from thermal infrared and passive microwave remote sensing and land surface modeling. *Journal of Geophysical Research: Atmospheres, 116*, D15107

Hanson, B.R., Orloff, S. & Peters, D. (2000). Monitoring Soil Moisture Helps Refine Irrigation Management. California Agriculture, 54(3), 38-42

Heathman, G.C., Starks, P.J., Ahuja, L.R. & Jackson, T.J. (2003). Assimilation of surface soil moisture to estimate profile soil water content. *Journal of Hydrology, 279*, 1-17

Hillel, D. (1982). Introduction to Soil Physics. In. San Diego: Academic Press

Hillel, D.J. (1980). *Aggregate stability. In: Fundamentals of soil physics*.

Hoeben, R. & Troch, P.A. (2000). Assimilation of active microwave observation data for soil moisture profile estimation. *Water Resources Research, 36*, 2805-2819

Hollinger, S.E. & Isard, S.A. (1994). A Soil Moisture Climatology of Illinois. *Journal of Climate, 7*

Houser , J.K., Schiffer, R.A., Schlosser, A.C., Lapenta, W.M. & Rossow, W.B., et al. (2007). Predicting Energy and Water Cycle Consequences of Earth System Variability and Change. *National Aeronautics and Space Administration (NASA)*

Hovmöller, E. (1949). The Trough-and-Ridge diagram. *Tellus, 1*, 62-66

Hupet, F. & Vanclooster, M. (2002). Intraseasonal dynamics of soil moisture variability within a small agricultural maize cropped field. *Journal of Hydrology, 261*, 86-101

Jackson, T.J. (1980). Profile soil moisture from surface measurements. *Journal of the Irrigation and Drainage Division of the ASCE, 106*

Jackson, T.J., Cosh, M.H., Bindlish, R., Starks, P.J., Bosch, D.D., Seyfried, M., Goodrich, D.C., Moran, M.S. & Jinyang, D. (2010). Validation of Advanced Microwave Scanning Radiometer Soil Moisture Products. *Geoscience and Remote Sensing, IEEE Transactions on, 48*, 4256-4272

Jackson, T.J., Bindlish, R., Cosh, M.H., Tianjie, Z., Starks, P.J., Bosch, D.D., Seyfried, M., Moran, M.S., Goodrich, D.C., Kerr, Y.H. & Leroux, D. (2012). Validation of Soil

Moisture and Ocean Salinity (SMOS) Soil Moisture Over Watershed Networks in the U.S. *Geoscience and Remote Sensing, IEEE Transactions on, 50*, 1530-1543

Jacquette, E., Al Bitar, A., Mialon, A., Kerr, Y., Quesney, A., Cabot, F. & Richaume, P. (2010). SMOS CATDS level 3 global products over land. *Proc.SPIE, Remote Sensing for Agriculture, Ecosystems, and Hydrology XII, 78240K, 7824*

Janssen, P.A.E.M., Abdalla, S., Hersbach, H. & Bidlot, J.-R. (2007). Error Estimation of Buoy, Satellite, and Model Wave Height Data. *Journal of Atmospheric and Oceanic Technology, 24*, 1665-1677

JAXA (2006). AMSR-E Data Users Handbook, 4th Edition. *Japan Aerospace Exploration Agency (JAXA) NCX-030021, URL:http://www.eorc.jaxa.jp/en/hatoyama/amsr-e/amsr-e_handbook_e.pdf*

Jeyaseelan, A.T. (2004). Droughts & floods assessment and monitoring using Remote Sensing and GIS. *Satellite Remote Sensing and GIS Applications in Agricultural Meteorology*, 291–313

Kaihotsu, I., Imaoka, K., Fujii, H., Oyunbaatar, D., Yamanaka, T., Shiraishi, K. & Koike, T. (2013). First evaluation of SMOS L2 soil moisture products using in situ observation data of MAVEX on the Mongolian Plateau in 2010 and 2011. *Hydrological Research Letters, 7*, 30-35

Kaleita, A.L., Tian, L.F. & Hirschi, M.C. (2005). Relationship Between Soil Moisture Content and Soil Surface Reflectance. *Transactions of the ASAE, 48*

Karam, M.A., Amar, F., Fung, A.K., Mougin, E., Lopes, A., Le Vine, D.M. & Beaudoin, A. (1995). A microwave polarimetric scattering model for forest canopies based on vector radiative transfer theory. *Remote Sensing of Environment, 53*, 16-30

Kerr, Y. (2007). Soil moisture from space: Where are we? *Hydrogeology Journal, 15*, 117-120

Kerr, Y., Richaume , P., Waldteufel, P., Wigneron, J.P., Ferrazzoli, P. & Mahmoodi, A. (2013a). SMOS level 2 Processor for Soil Moisture - (Algorithm Theoretical Basis Document) ATBD. Available at:http://www.cesbio.ups-tlse.fr/SMOS_blog/wp-content/uploads/DOCS/SO-TN-ARR-L2PP-0037_ATBD_v3.6.pdf. *ESA No: SO-TN-ESL-SM-GS-0001*

Kerr, Y., Jacquette, E., Al Bitar, A., Cabot, F., Mialon, A., Richaume , P., Quesney, A., Berthon, L. & Wigneron, J. (2013b). The CATDS SMOS L3 soil moisture retrieval processor, Algorithm Theoretical Baseline Document (ATBD). *SO-TN-CBSA-GS-0029*

Kerr, Y.H. & Njoku, E.G. (1990). A semiempirical model for interpreting microwave emission from semiarid land surfaces as seen from space. *Geoscience and Remote Sensing, IEEE Transactions on, 28*, 384-393

Kerr, Y.H., Waldteufel, P., Wigneron, J.P., Martinuzzi, J., Font, J. & Berger, M. (2001). Soil moisture retrieval from space: the Soil Moisture and Ocean Salinity (SMOS) mission. *Geoscience and Remote Sensing, IEEE Transactions on, 39*, 1729-1735

Kerr, Y.H., Vergely, J.L., Waldteufel, P., Richaume , P., Anterrieu, E. & Moreno, R. (2008). CATDS SMOS L3 processor: Algorithm Theoretical Baseline Document for the soil moisture retrieval (ATBD). *CNES-CESBIO, Toulouse, France, CATDS-ATBD-SM-L3, V1.1*

Kerr, Y.H., Waldteufel, P., Wigneron, J.P., Delwart, S., Cabot, F., Boutin, J., Escorihuela, M.J., Font, J., Reul, N., Gruhier, C., Juglea, S.E., Drinkwater, M.R., Hahne, A., Martin-Neira, M. & Mecklenburg, S. (2010). The SMOS Mission: New Tool for Monitoring Key Elements ofthe Global Water Cycle. *Proceedings of the IEEE, 98*, 666-687

Kerr, Y.H., Waldteufel, P., Richaume, P., Wigneron, J.P., Ferrazzoli, P., Mahmoodi, A., Al Bitar, A., Cabot, F., Gruhier, C., Juglea, S.E., Leroux, D., Mialon, A. & Delwart, S. (2012). The SMOS Soil Moisture Retrieval Algorithm. *Geoscience and Remote Sensing, IEEE Transactions on, 50*, 1384-1403

Kidd, C. (2006). Radio frequency interference at passive microwave earth observation frequencies. *International Journal of Remote Sensing, 27*, 3853-3865

King, M.D. & Greenstone, R. (1999). *EOS Reference Handbook: A Guide to NASA's Earth Science Enterprise and the Earth Observing System*. NASA Doc

Kiome, R.M. (1992). Soil and water conservation for improved soil moisture and crop production: an empirical and modelling study in semi arid Kenya. *PhD Thesis, University of East Anglia, Norwich, pp: 1-20*

Koike, T., Nakamura, Y., Kaihotsu, I., Davva, G., Matsuura, N., Tamagawa, K. & Fujii, H. (2004). Development of an advanced microwave scanning radiometer (AMSR–E) algorithm of soil moisture and vegetation water content. *Annual Journal of Hydraulic Engineering, JSCE, 48*

Kong, X. (2006). near-surface soil moisture retrieval at field and regional scales in the UK. *School of Environmental Sciences, University of East Anglia, Norwich, NR4 7TJ, UK*

Koster, R.D., Suarez, M.J., Ducharne, A., Stieglitz, M. & Kumar, P. (2000). A catchment-based approach to modeling land surface processes in a general circulation model: 1. Model structure. *Journal of Geophysical Research: Atmospheres, 105*, 24809-24822

Koster, R.D., Suarez, M.J., Higgins, R.W. & Van den Dool, H.M. (2003). Observational evidence that soil moisture variations affect precipitation. *Geophysical Research Letters, 30*, 1241

Koster, R.D., Suarez, M.J., Liu, P., Jambor, U., Berg, A., Kistler, M., Reichle, R., Rodell, M. & Famiglietti, J. (2004a). Realistic Initialization of Land Surface States: Impacts on Subseasonal Forecast Skill. *Journal of Hydrometeorology, 5*, 1049-1063

Koster, R.D., Dirmeyer, P.A., Guo, Z., Bonan, G., Chan, E., Cox, P., Gordon, C.T., Kanae, S., Kowalczyk, E., Lawrence, D., Liu, P., Lu, C.-H., Malyshev, S., McAvaney, B., Mitchell, K., Mocko, D., Oki, T., Oleson, K., Pitman, A., Sud, Y.C., Taylor, C.M., Verseghy, D., Vasic, R., Xue, Y. & Yamada, T. (2004b). Regions of Strong Coupling Between Soil Moisture and Precipitation. *Science, 305*, 1138-1140

Koster, R.D., Sud, Y.C., Guo, Z., Dirmeyer, P.A., Bonan, G., Oleson, K.W., Chan, E., Verseghy, D., Cox, P., Davies, H., Kowalczyk, E., Gordon, C.T., Kanae, S., Lawrence, D., Liu, P., Mocko, D., Lu, C.-H., Mitchell, K., Malyshev, S., McAvaney, B., Oki, T., Yamada, T., Pitman, A., Taylor, C.M., Vasic, R. & Xue, Y. (2006). GLACE: The Global Land–Atmosphere Coupling Experiment. Part I: Overview. *Journal of Hydrometeorology, 7*, 590-610

Koster, R.D., Guo, Z., Yang, R., Dirmeyer, P.A., Mitchell, K. & Puma, M.J. (2009). On the Nature of Soil Moisture in Land Surface Models. *Journal of Climate, 22*, 4322-4335

Koster, R.D., Mahanama, S.P.P., Livneh, B., Lettenmaier, D.P. & Reichle, R.H. (2010). Skill in streamflow forecasts derived from large-scale estimates of soil moisture and snow. *Nature Geosci, 3*, 613-616

Krinner, G., Viovy, N., de Noblet-Ducoudré, N., Ogée, J., Polcher, J., Friedlingstein, P., Ciais, P., Sitch, S. & Prentice, I.C. (2005). A dynamic global vegetation model for studies of the coupled atmosphere-biosphere system. *Global Biogeochemical Cycles, 19*, GB1015

Lacava, T., Matgen, P., Brocca, L., Bittelli, M., Pergola, N., Moramarco, T. & Tramutoli, V. (2012). A First Assessment of the SMOS Soil Moisture Product With In Situ and Modeled Data in Italy and Luxembourg. *Geoscience and Remote Sensing, IEEE Transactions on, 50*, 1612-1622

Lacava, T., Coviello, I., Faruolo, M., Mazzeo, G., Pergola, N. & Tramutoli, V. (2013). A Multitemporal Investigation of AMSR-E C-Band Radio-Frequency Interference. *Geoscience and Remote Sensing, IEEE Transactions on, 51*, 2007-2015

Law, B.E. & Waring, R.H. (1994). Remote Sensing of Leaf Area Index and Radiation Intercepted by Understory Vegetation. *Ecological Applications, 4*, 272-279

Leese, J., Jackson, T., Pitman, A. & Dirmeyer, P. (2001). GEWEX/BAHC international workshop on soil moisture monitoring analysis and prediction for hydrometeorological and hydroclimatological applications. *Bulletin of the American Meteorological Society;Jul2001, Vol. 82 Issue 7*

Leroux, D.J., Kerr, Y.H., Richaume, P. & Berthelot, B. (2011). Estimating SMOS error structure using triple collocation. In, *Geoscience and Remote Sensing Symposium (IGARSS), 2011 IEEE International* (pp. 24-27)

Leroux, D.J., Kerr, Y.H., Richaume, P. & Fieuzal, R. (2013a). Spatial distribution and possible sources of SMOS errors at the global scale. *Remote Sensing of Environment, 133*, 240-250

Leroux, D.J., Kerr, Y.H., Al Bitar, A., Bindlish, R., Jackson, T.J., Berthelot, B. & Portet, G. (2013b). Comparison Between SMOS, VUA, ASCAT, and ECMWF Soil Moisture Products Over Four Watersheds in U.S. *IEEE Transactions on Geoscience and Remote Sensing, 52*, 1562-1571

Li, L., Njoku, E.G., Im, E., Chang, P.S. & Germain, K.S. (2004). A preliminary survey of radio-frequency interference over the U.S. in Aqua AMSR-E data. *Geoscience and Remote Sensing, IEEE Transactions on, 42*, 380-390

Liu, Y.Y., Parinussa, R.M., Dorigo, W.A., De Jeu, R.A.M., Wagner, W., van Dijk, A.I.J.M., McCabe, M.F. & Evans, J.P. (2011). Developing an improved soil moisture dataset by blending passive and active microwave satellite-based retrievals. *Hydrol. Earth Syst. Sci., 15*

Liu, Y.Y., Dorigo, W.A., Parinussa, R.M., de Jeu, R.A.M., Wagner, W., McCabe, M.F., Evans, J.P. & van Dijk, A.I.J.M. (2012). Trend-preserving blending of passive and active microwave soil moisture retrievals. *Remote Sensing of Environment, 123*, 280-297

Loew, A. & Schlenz, F. (2011). A dynamic approach for evaluating coarse scale satellite soil moisture products. *Hydrol. Earth Syst. Sci., 15*, 75-90

Loew, A., Stacke, T., Dorigo, W., de Jeu, R. & Hagemann, S. (2013). Potential and limitations of multidecadal satellite soil moisture observations for selected climate model evaluation studies. *Hydrol. Earth Syst. Sci., 17*, 3523-3542

Luk, S.-h. (1985). Effect of antecedent soil moisture content on rainwash erosion. *CATENA, 12*, 129-139

Maaß, N., Kaleschke, L., Tian-Kunze, X. & Drusch, M. (2013). Snow thickness retrieval over thick Arctic sea ice using SMOS satellite data. *The Cryosphere Discuss., 7*, 3627-3674

Marshall, T.J. & Holmes, J.W. (1988). Soil Physics, second edition. *Cambrige University Press, pp: 57.*

Mattar, C., Wigneron, J.P., Sobrino, J.A., Novello, N., Calvet, J.C., Albergel, C., Richaume, P., Mialon, A., Guyon, D., Jimenez-Munoz, J.C. & Kerr, Y. (2012). A Combined Optical&Microwave Method to Retrieve Soil Moisture Over Vegetated Areas. *Geoscience and Remote Sensing, IEEE Transactions on, 50*, 1404-1413

McMullan, K.D., Brown, M.A., Martin-Neira, M., Rits, W., Ekholm, S., Marti, J. & Lemanczyk, J. (2008). SMOS: The Payload. *Geoscience and Remote Sensing, IEEE Transactions on, 46*, 594-605

Merlin, O., Walker, J.P., Chehbouni, A. & Kerr, Y. (2008). Towards deterministic downscaling of SMOS soil moisture using MODIS derived soil evaporative efficiency. *Remote Sensing of Environment, 112*, 3935-3946

Merlin, O., Al Bitar, A., Walker, J.P. & Kerr, Y. (2010). An improved algorithm for disaggregating microwave-derived soil moisture based on red, near-infrared and thermal-infrared data. *Remote Sensing of Environment, 114*, 2305-2316

Merlin, O., Rudiger, C., Al Bitar, A., Richaume, P., Walker, J.P. & Kerr, Y.H. (2012). Disaggregation of SMOS Soil Moisture in Southeastern Australia. *Geoscience and Remote Sensing, IEEE Transactions on, 50*, 1556-1571

Merlin, O., Escorihuela, M.J., Mayoral, M.A., Hagolle, O., Al Bitar, A. & Kerr, Y. (2013). Self-calibrated evaporation-based disaggregation of SMOS soil moisture: An evaluation study at 3 km and 100 m resolution in Catalunya, Spain. *Remote Sensing of Environment, 130*, 25-38

Mialon, A., Coret, L., Kerr, Y.H., Secherre, F. & Wigneron, J.P. (2008). Flagging the Topographic Impact on the SMOS Signal. *Geoscience and Remote Sensing, IEEE Transactions on, 46*, 689-694

Mialon, A., Richaume , P., Leroux, D., bircher, S., Al Bitar, A., Pellarin, T., Wigneron, J.P. & Kerr, Y. (2014). Comparison of Dobson and Mironov dielectric models in the SMOS soil moisture retrieval algorithm. *IEEE transactions on Geoscience and Remote Sensing (submitted)*

Michele, C.D. & Salvadori, G. (2002). On the derived flood frequency distribution: analytical formulation and the influence of antecedent soil moisture condition. *Journal of Hydrology, 262*, 245-258

Miernecki, M., Wigneron, J.-P., Lopez-Baeza, E., Kerr, Y., De Jeu, R., De Lannoy, G.J.M., Jackson, T.J., O'Neill, P.E., Schwank, M., Moran, R.F., Bircher, S., Lawrence, H., Mialon, A., Al Bitar, A. & Richaume, P. (2014). Comparison of SMOS and SMAP soil moisture retrieval approaches using tower-based radiometer data over a vineyard field. *Remote Sensing of Environment, 154*, 89-101

Miralles, D.G., Crow, W.T. & Cosh, M.H. (2010). Estimating Spatial Sampling Errors in Coarse-Scale Soil Moisture Estimates Derived from Point-Scale Observations. *Journal of Hydrometeorology, 11*, 1423-1429

Miralles, D.G., van den Berg, M.J., Gash, J.H., Parinussa, R.M., de Jeu, R.A.M., Beck, H.E., Holmes, T.R.H., Jiménez, C., Verhoest, N.E.C., Dorigo, W.A., Teuling, A.J. & Johannes Dolman, A. (2014). El Niño–La Niña cycle and recent trends in continental evaporation. *Nature Clim. Change, 4*, 122-126

Mironov, V., Kerr, Y., Wigneron, J.P., Kosolapova, L. & Demontoux, F. (2012). Temperature- and Texture-Dependent Dielectric Model for Moist Soils at 1.4 GHz. *Geoscience and Remote Sensing Letters, IEEE, 10*, 419-423

Mironov, V.L., Kosolapova, L.G. & Fomin, S.V. (2009). Physically and Mineralogically Based Spectroscopic Dielectric Model for Moist Soils. *Geoscience and Remote Sensing, IEEE Transactions on, 47*, 2059-2070

Mladenova, I., Lakshmi, V., Jackson, T.J., Walker, J.P., Merlin, O. & de Jeu, R.A.M. (2011). Validation of AMSR-E soil moisture using L-band airborne radiometer data from National Airborne Field Experiment 2006. *Remote Sensing of Environment, 115*, 2096-2103

Mo, T., Choudhury, B.J., Schmugge, T.J., Wang, J.R. & Jackson, T.J. (1982). A model for microwave emission from vegetation-covered fields. *Journal of Geophysical Research: Oceans, 87*, 11229-11237

Mohanty, B.P. & Skaggs, T.H. (2001). Spatio-temporal evolution and time-stable characteristics of soil moisture within remote sensing footprints with varying soil, slope, and vegetation. *Advances in Water Resources, 24(9-10): 1051-1067*

Moisselin J-M & O, M. (2002). Research, digitization and homogenization of long-term data series. *Actes du Colloque ‘‘La Perennisation et la Valorisation des donnees*

scientifiques et techniques'' (Ensuring Long-Term Preservation and adding Value to scientific and technical data) organise par le CNES du 5 au 7=11=2002.Toulouse

Monteith, J.L. (1965). Evaporation and Environment. In:The state and movement of water in living organism. *19th Symp. Soc. Exptl. Biol. P. 205-234*

Montpetit, B., Royer, A., Wigneron, J.-P., Chanzy, A. & Mialon, A. (2014). Multi-frequency bare soil reflectivity models evaluations. *Remote Sensing of Environment (submitted)*

Muller, E. & Decamps, H. (2001). Modelling soil moisture-reflectance. *Remote Sensing of Environment, 76(2): 173-180.*

Muñoz-Sabater, J., Jarlan, L., Calvet, J.-C., Bouyssel, F. & De Rosnay, P. (2007). From Near-Surface to Root-Zone Soil Moisture Using Different Assimilation Techniques. *Journal of Hydrometeorology, 8,* 194-206

Naeimi, V., Scipal, K., Bartalis, Z., Hasenauer, S. & Wagner, W. (2009). An Improved Soil Moisture Retrieval Algorithm for ERS and METOP Scatterometer Observations. *Geoscience and Remote Sensing, IEEE Transactions on, 47,* 1999-2013

Ni-Meister, W. (2008). Recent Advances On Soil Moisture Data Assimilation. *Physical Geography, 29,* 19-37

Nichols, S., Zhang, Y. & Ahmad, A. (2011). Review and evaluation of remote sensing methods for soil-moisture estimation. *Journal of Photonics for Energy,* 028001-028001-028017

Njoku, E.G. & O'Neill, P.E. (1982). Multifrequency Microwave Radiometer Measurements of Soil Moisture. *Geoscience and Remote Sensing, IEEE Transactions on, GE-20,* 468-475

Njoku, E.G. & Entekhabi, D. (1996). Passive microwave remote sensing of soil moisture. *Journal of Hydrology, 184,* 101-129

Njoku, E.G. & Li, L. (1999). Retrieval of land surface parameters using passive microwave measurements at 6-18 GHz. *Geoscience and Remote Sensing, IEEE Transactions on, 37,* 79-93

Njoku, E.G., Wilson, W.J., Yueh, S.H., Dinardo, S.J., Fuk, K.L., Jackson, T.J., Lakshmi, V. & Bolten, J. (2002). Observations of soil moisture using a passive and active low-frequency microwave airborne sensor during SGP99. *Geoscience and Remote Sensing, IEEE Transactions on, 40,* 2659-2673

Njoku, E.G., Jackson, T.J., Lakshmi, V., Chan, T.K. & Nghiem, S.V. (2003). Soil moisture retrieval from AMSR-E. *Geoscience and Remote Sensing, IEEE Transactions on, 41,* 215-229

Njoku, E.G., Ashcroft, P., Chan, T.K. & Li, L. (2005). Global Survey and Statistics of Radio-Frequency Interference in AMSR-E Land Observations. *IEEE Transactions on Geoscience and Remote Sensing,, 46*

Njoku, E.G. & Chan, S.K. (2006). Vegetation and surface roughness effects on AMSR-E land observations. *Remote Sensing of Environment, 100*, 190-199

Noilhan, J. & Planton, S. (1989). A Simple Parameterization of Land Surface Processes for Meteorological Models. *Monthly Weather Review, 117*, 536-549

O'Geen, A.T. (2012). Soil Water Dynamics. . *Nature Education Knowledge 3(6):12*

Ochsner, T.E., Cosh, M.H., Cuenca, R.H., Dorigo, W.A., Draper, C.S., Hagimoto, Y., Kerr, Y.H., Njoku, E.G., Small, E.E. & Zreda, M. (2013). State of the Art in Large-Scale Soil Moisture Monitoring. *Soil Sci. Soc. Am. J.*, 1888-1919

Oki , T. (1999). The global water cycle. In Global Energy and Water Cycles, Browning K. and Gurney R. (Eds.), . *Cambridge University Press: pp. 10–27*

Oliva, R., Daganzo, E., Kerr, Y.H., Mecklenburg, S., Nieto, S., Richaume, P. & Gruhier, C. (2012). SMOS Radio Frequency Interference Scenario: Status and Actions Taken to Improve the RFI Environment in the 1400–1427-MHz Passive Band. *Geoscience and Remote Sensing, IEEE Transactions on, 50*, 1427-1439

Owe, M., de Jeu, R. & Walker, J. (2001). A methodology for surface soil moisture and vegetation optical depth retrieval using the microwave polarization difference index. *IEEE Transactions on Geoscience and Remote Sensing, 39*, 1643-1654

Owe, M., de Jeu, R. & Holmes, T. (2008). Multisensor historical climatology of satellite-derived global land surface moisture. *Journal of Geophysical Research: Earth Surface, 113*, F01002

Panegrossi, G., Ferretti, R., Pulvirenti, L. & Pierdicca, N. (2001). Impact of ASAR soil moisture data on the MM5 precipitation forecast for the Tanaro flood event of April 2009. *Nat. Hazards Earth Syst. Sci., 11*

Parajka, J., Naeimi, V., Blöschl, G., Wagner, W., Merz, R. & Scipal, K. (2006). Assimilating scatterometer soil moisture data into conceptual hydrologic models at the regional scale. *Hydrol. Earth Syst. Sci., 10*, 353-368

Parinussa, R., Meesters, A., Liu, Y., Dorigo, W., Wagner, W. & de Jeu, R. (2011a). An Analytical Solution to Estimate the Error Structure of a Global Soil Moisture Dataset. *IEEE Geoscience and remote sensing letters, 8*, 779-783

Parinussa, R.M., Holmes, T.R.H., Yilmaz, M.T. & Crow, W.T. (2011b). The impact of land surface temperature on soil moisture anomaly detection from passive microwave observations. *Hydrology and Earth System Sciences, 15*, 3135-3151

Parinussa, R.M., Meesters, A.G.C.A., Liu, Y.Y., Dorigo, W., Wagner, W. & de Jeu, R.A.M. (2011c). Error Estimates for Near-Real-Time Satellite Soil Moisture as Derived From the Land Parameter Retrieval Model. *Geoscience and Remote Sensing Letters, IEEE, 8*, 779-783

Parrens, M., Zakharova, E., Lafont, S., Calvet, J.C., Kerr, Y., Wagner, W. & Wigneron, J.P. (2012). Comparing soil moisture retrievals from SMOS and ASCAT over France. *Hydrology and Earth System Sciences, 16*, 423-440

Parrens, M., Wigneron., J.-P., Richaume., P., Kerr., Y., Wang., S., Al-Yaari., A., Fernández-Morán., R., Mialon., A., Escorihuela., M.-J. & Grant, J. (2014). Global maps of roughness parameters from l-band SMOS observations. *International Geoscience and Remote Sensing Symposium (IGARSS 2014), Québec, Canada*

Patton, J. & Hornbuckle, B. (2013). Initial Validation of SMOS Vegetation Optical Thickness in Iowa. *Geoscience and Remote Sensing Letters, IEEE, 10*, 647-651

Peischl, S., Walker, J.P., Rüdiger, C., Ye, N., Kerr, Y.H., Kim, E., Bandara, R. & Allahmoradi, M. (2012). The AACES field experiments: SMOS calibration and validation across the Murrumbidgee River catchment. *Hydrol. Earth Syst. Sci., 16*, 1697-1708

Pellarin, T., Calvet, J.C. & Wigneron, J.P. (2003). Surface soil moisture retrieval from L-band radiometry: a global regression study. *Geoscience and Remote Sensing, IEEE Transactions on, 41*, 2037-2051

Peplinski, N.R., Ulaby, F.T. & Dobson, M.C. (1995). Dielectric properties of soils in the 0.3-1.3-GHz range. *Geoscience and Remote Sensing, IEEE Transactions on, 33*, 803-807

Pielke, R., Sr. & Niyogi, D. (2010). The Role of Landscape Processes within the Climate System. In J.-C. Otto, & R. Dikau (Eds.), *Landform - Structure, Evolution, Process Control* (pp. 67-85): Springer Berlin Heidelberg

Pierdicca, N., Luca, P., Fabio, F., Raffaele, C. & Marco, T. (2013). Analysis of two years of ASCAT- and SMOS-derived soil moisture estimates over Europe and North Africa. *EUROPEAN JOURNAL OF REMOTE SENSING, 46*, 759-773

Piles, M., Camps, A., Vall-llossera, M., Corbella, I., Panciera, R., Rudiger, C., Kerr, Y.H. & Walker, J. (2011). Downscaling SMOS-Derived Soil Moisture Using MODIS Visible/Infrared Data. *Geoscience and Remote Sensing, IEEE Transactions on, 49*, 3156-3166

Pitman, A.J. (2003). The evolution of, and revolution in, land surface schemes designed for climate models. *International Journal of Climatology 23*, 479–510

Planet, W.G. (1970). Some comments on reflectance measurements of wet soils. *Remote Sensing of Environment, 1*, 127-129

Potithep, S., Nasahara, N., Muraoka, H., Nagai, S. & Suzuki, R. (2010). What is the actual relationship between LAI and VI in a deciduous broadleaf forest? International Archives of the Photogrammetry. *Remote Sensing and Spatial Information Science, 38 (2010)*

PUM (2012). Product User Manual (PUM): for product H14 – SM-DAS-2, Soil Moisture Profile Index in the roots region by scatterometer data assimilation. *SAF/HSAF/PUM-14*

Quesada, B., Vautard, R., Yiou, P., Hirschi, M. & Seneviratne, S.I. (2012). Asymmetric European summer heat predictability from wet and dry southern winters and springs. *Nature Clim. Change, 2*, 736-741

Rahimzadeh-Bajgiran, P., Berg, A.A., Champagne, C. & Omasa, K. (2013). Estimation of soil moisture using optical/thermal infrared remote sensing in the Canadian Prairies. *ISPRS Journal of Photogrammetry and Remote Sensing, 83*, 94-103

Raju, S., Chanzy, A., Wigneron, J.-P., Calvet, J.-C., Kerr, Y. & Laguerre, L. (1995). Soil moisture and temperature profile effects on microwave emission at low frequencies. *Remote Sensing of Environment, 54*, 85-97

Reichle, R.H., Walker, J.P., Koster, R.D. & Houser, P.R. (2002a). Extended versus Ensemble Kalman Filtering for Land Data Assimilation. *Journal of Hydrometeorology, 3*, 728-740

Reichle, R.H., McLaughlin, D.B. & Entekhabi, D. (2002b). Hydrologic Data Assimilation with the Ensemble Kalman Filter. *Monthly Weather Review, 130*, 103-114

Reichle, R.H., Koster, R.D., Liu, P., Mahanama, S.P.P., Njoku, E.G. & Owe, M. (2007). Comparison and assimilation of global soil moisture retrievals from the Advanced Microwave Scanning Radiometer for the Earth Observing System (AMSR-E) and the Scanning Multichannel Microwave Radiometer (SMMR). *Journal of Geophysical Research: Atmospheres, 112*, D09108

Reichle, R.H., Crow, W.T. & Keppenne, C.L. (2008). An adaptive ensemble Kalman filter for soil moisture data assimilation. *Water Resources Research, 44*, W03423

Reichle, R.H., Koster, R.D., De Lannoy, G.J.M., Forman, B.A., Liu, Q., Mahanama, S.P.P. & Touré, A. (2011). Assessment and Enhancement of MERRA Land Surface Hydrology Estimates. *Journal of Climate, 24*, 6322-6338

Reichle, R.H. (2012). The MERRA-Land Data Product. *GMAO Office Note No. 3 (Version 1.2)*, 38 pp

Richter, G.M. & Semenov, M.A. (2005). Modelling impacts of climate change on wheat yields in England and Wales: assessing drought risks. *Agricultural Systems, 84*, 77-97

Rienecker, M.M., Suarez, M.J., Gelaro, R., Todling, R., Bacmeister, J., Liu, E., Bosilovich, M.G., Schubert, S.D., Takacs, L., Kim, G.-K., Bloom, S., Chen, J., Collins, D., Conaty, A., da Silva, A., Gu, W., Joiner, J., Koster, R.D., Lucchesi, R., Molod, A., Owens, T., Pawson, S., Pegion, P., Redder, C.R., Reichle, R., Robertson, F.R., Ruddick, A.G., Sienkiewicz, M. & Woollen, J. (2011). MERRA: NASA's Modern-Era Retrospective Analysis for Research and Applications. *Journal of Climate, 24*, 3624-3648

Robock, A., Schlosser, C.A., Vinnikov, K.Y., Speranskaya, N.A., Entin, J.K. & Qiu, S. (1998). Evaluation of the AMIP soil moisture simulations. *Global and Planetary Change, 19*, 181-208

Robock, A., Konstantin, V., Govindarajalu, S., Jared, E., Steven, H., Nina, S., Suxia, L. & Namkhai, A. (2000). The Global Soil Moisture Data Bank. *Bulletin of the American Meteorological Society;Jul2001, Vol. 82 Issue 7, 81*, 1281-1299

Rowntree, P.R. & Bolton, J.A. (1983). Simulation of the atmospheric response to soil moisture anomalies over Europe. *Quarterly Journal of the Royal Meteorological Society, 109*, 501-526

Rüdiger, C., Calvet, J.-C., Gruhier, C., Holmes, T.R.H., de Jeu, R.A.M. & Wagner, W. (2009). An Intercomparison of ERS-Scat and AMSR-E Soil Moisture Observations with Model Simulations over France. *Journal of Hydrometeorology, 10*

Sabater, J.M., Jarlan, L., Calvet, J.-C., Bouyssel, F. & De Rosnay, P. (2007). From Near-Surface to Root-Zone Soil Moisture Using Different Assimilation Techniques. *Journal of Hydrometeorology, 8*, 194-206

Sahoo, A.K., Houser, P.R., Ferguson, C., Wood, E.F., Dirmeyer, P.A. & Kafatos, M. (2008). Evaluation of AMSR-E soil moisture results using the in-situ data over the Little River Experimental Watershed, Georgia. *Remote Sensing of Environment, 112*, 3142-3152

Saleh, K., Wigneron, J.-P., de Rosnay, P., Calvet, J.-C. & Kerr, Y. (2006). Semi-empirical regressions at L-band applied to surface soil moisture retrievals over grass. *Remote Sensing of Environment, 101*, 415-426

Saleh, K., Kerr, Y.H., Richaume, P., Escorihuela, M.J., Panciera, R., Delwart, S., Boulet, G., Maisongrande, P., Walker, J.P., Wursteisen, P. & Wigneron, J.P. (2009). Soil moisture retrievals at L-band using a two-step inversion approach (COSMOS/NAFE'05 Experiment). *Remote Sensing of Environment, 113*, 1304-1312

Sanchez, N., Martinez-Fernandez, J., Scaini, A. & Perez-Gutierrez, C. (2012). Validation of the SMOS L2 Soil Moisture Data in the REMEDHUS Network (Spain). *Geoscience and Remote Sensing, IEEE Transactions on, 50*, 1602-1611

Sandholt, I., Rasmussen, K. & Andersen, J. (2002). A simple interpretation of the surface temperature/vegetation index space for assessment of surface moisture status. *Remote Sensing of Environment, 79*, 213-224

Schanda, E. (1986). Physical fundamentals of remote sensing. *Berlin Heidelberg New York Tokyo: Springer Verlag*

Schlosser, C.A. & Milly, P.C.D. (2002). A Model-Based Investigation of Soil Moisture Predictability and Associated Climate Predictability. *Journal of Hydrometeorology, 3*, 483-501

Schmugge, T., O'Neill, P.E. & Wang, J.R. (1986). Passive Microwave Soil Moisture Research. *Geoscience and Remote Sensing, IEEE Transactions on, GE-24*, 12-22

Schmugge, T.J., Jackson, T.J. & McKim, H.L. (1980). Survey of methods for soil moisture determination. *Water Resources Research, 16*, 961-979

Schmugge, T.J. (1985). Remote Sensing of Soil Moisture. *In: Anderson, M.G., Burt, T.P. (Eds.), Hydrological Forecasting.Wiley, New York,*, 101–124

Schmugge, T.J., Kustas, W.P., Ritchie, J.C., Jackson, T.J. & Rango, A. (2002). Remote sensing in hydrology. *Advances in Water Resources, 25(8-12): 1367-1385.*

Scipal, K., Drusch, M. & Wagner, W. (2008). Assimilation of a ERS scatterometer derived soil moisture index in the ECMWF numerical weather prediction system. *Advances in Water Resources, 31*, 1101-1112

Scipal, K., Dorigo, W. & de Jeu, R. (2010). Triple collocation - A new tool to determine the error structure of global soil moisture products. In, *Geoscience and Remote Sensing Symposium (IGARSS), 2010 IEEE International* (pp. 4426-4429)

Seneviratne, S., Wilhelm M, Stanelle T, van den Hurk B, Hagemann S, Berg A, Cheruy F, Higgins ME, Meier A, Brovkin V, Claussen M, Ducharne A, Dufresne JL, Findell K, Ghattas J, Lawrence DM, Malyshev S, Rumukainen M & B, S. (2013). Impact of soil moisture-climate feedbacks on CMIP5 projections: First results from the GLACE-CMIP5 experiment. *Geophys. Res. Lett.,, 40*

Seneviratne, S.I., Luthi, D., Litschi, M. & Schar, C. (2006). Land-atmosphere coupling and climate change in Europe. *Nature, 443*, 205-209

Seneviratne, S.I., Corti, T., Davin, E.L., Hirschi, M., Jaeger, E.B., Lehner, I., Orlowsky, B. & Teuling, A.J. (2010). Investigating soil moisture–climate interactions in a changing climate: A review. *Earth-Science Reviews, 99*, 125-161

Sheffield, J., Ferguson, C.R., Troy, T.J., Wood, E.F. & McCabe, M.F. (2009). Closing the terrestrial water budget from satellite remote sensing. *Geophysical Research Letters, 36*, L07403

Sinclair, S. & Pegram, G.G.S. (2010). A comparison of ASCAT and modelled soil moisture over South Africa, using TOPKAPI in land surface mode. *Hydrol. Earth Syst. Sci., 14*

Singh, V. & Woolhiser, D. (2002). Mathematical Modeling of Watershed Hydrology. *Journal of Hydrologic Engineering, 7*, 270-292

Smith, A. & Mullins, E. (2000). *Soil and Environmental Analysis - Physical Methods -Second Edition:Revised and Expanded*.

Stoffelen, A. (1998). Toward the true near-surface wind speed: Error modeling and calibration using triple collocation. *Journal of Geophysical Research: Oceans, 103*, 7755-7766

Strangeways, I. (2000). *"Water", Measuring the Natural Environment*.

Su, C.-H., Ryu, D., Young, R.I., Western, A.W. & Wagner, W. (2013). Inter-comparison of microwave satellite soil moisture retrievals over the Murrumbidgee Basin, southeast Australia. *Remote Sensing of Environment, 134*, 1-11

Su, Z., Dorigo, W., Fernández-Prieto, D., Van Helvoirt, M., Hungershoefer, K., de Jeu, R., Parinussa, R., Timmermans, J., Roebeling, R., Schröder, M., Schulz, J., Van der Tol, C., Stammes, P., Wagner, W., Wang, L., Wang, P. & Wolters, E. (2010). Earth observation Water Cycle Multi-Mission Observation Strategy (WACMOS). *Hydrol. Earth Syst. Sci. Discuss., 7*, 7899-7956

Su, Z., Wen, J., Dente, L., van der Velde, R., Wang, L., Ma, Y., Yang, K. & Hu, Z. (2011). The Tibetan Plateau observatory of plateau scale soil moisture and soil temperature

(Tibet-Obs) for quantifying uncertainties in coarse resolution satellite and model products *Hydrol. Earth Syst. Sci., 15*

Svetlitchnyi, A.A., Plotnitskiy, S.V. & Stepovaya, O.Y. (2003). Spatial distribution of soil moisture content within catchments and its modelling on the basis of topographic data. *Journal of Hydrology, 277*, 50-60

Tao, F., Yokozawa, M., Hayashi, Y. & Lin, E. (2003). Changes in agricultural water demands and soil moisture in China over the last half-century and their effects on agricultural production. *Agricultural and Forest Meteorology, 118*, 251-261

Taylor, C.M., de Jeu, R.A.M., Guichard, F., Harris, P.P. & Dorigo, W.A. (2012). Afternoon rain more likely over drier soils. *Nature, 489*, 423-426

Teuling, A.J., Seneviratne, S.I., Stockli, R., Reichstein, M., Moors, E., Ciais, P., Luyssaert, S., van den Hurk, B., Ammann, C., Bernhofer, C., Dellwik, E., Gianelle, D., Gielen, B., Grunwald, T., Klumpp, K., Montagnani, L., Moureaux, C., Sottocornola, M. & Wohlfahrt, G. (2010). Contrasting response of European forest and grassland energy exchange to heatwaves. *Nature Geosci, 3*, 722-727

Twarakavi, N.K.C., Sakai, M. & Šimůnek, J. (2009). An objective analysis of the dynamic nature of field capacity. *Water Resources Research, 45*, W10410

Ulaby, F., Moore, r. & Fung AK (1981). Microwave remote sensing fundamentals and radiometry. Microwave remote sensing: active and passive. *Artech House, Boston, MA, 1–456*

Ulaby, F., Moore, K. & Fung, K. (1986). Microwave Remote Sensing, Active and Passive, vol.III: From Theory to Applications. *Artech House, Massachusettes.*

Ulaby, F.T., Dubois, P.C. & van Zyl, J. (1996). Radar mapping of surface soil moisture. *Journal of Hydrology, 184*, 57-84

van de Griend, A.A. & Engman, E.T. (1985). Partial area hydrology and remote sensing. *Journal of Hydrology, 81: 211-251*

van den Hurk, B. & Viterbo, P. (2003). The Torne-Kalix PILPS 2(e) experiment as a test bed for modifications to the ECMWF land surface scheme. *Global and Planetary Change, 38*, 165-173

Veihmeyer, F.J. & Hendrickson, A.H. (1931). The moisture equivalent as a measure of the field capacity of soils. *Soil Sci, 32*, 181-193

Veihmeyer, f.j. & Hendrickson, a.h. (1950). Soil Moisture in Relation to Plant Growth. . *Annual Review of Plant Physiology 1950 Vol. 1 pp. 285-304*

Verstraeten, W.W., Veroustraete, F., Wagner, W., Van Roey, T., Heyns, W., Verbeiren, S., van der Sande, C.J. & Feyen, J. (2007). Impact assessment of remotely sensed soil moisture on ecosystem carbon fluxes across Europe. 2nd International Workshop on Uncertainty in Greenhouse Gas Inventories, IIASA, Austria, 27-28 Sep., 2007

Vivoni, E.R., Gebremichael, M., Watts, C.J., Bindlish, R. & Jackson, T.J. (2008). Comparison of ground-based and remotely-sensed surface soil moisture estimates over complex terrain during SMEX04. *Remote Sensing of Environment, 112*, 314-325

Wagner, W., Lemoine, G., Borgeaud, M. & Rott, H. (1999a). A study of vegetation cover effects on ERS scatterometer data. *Geoscience and Remote Sensing, IEEE Transactions on, 37*, 938-948

Wagner, W., Lemoine, G. & Rott, H. (1999b). A Method for Estimating Soil Moisture from ERS Scatterometer and Soil Data. *Remote Sensing of Environment, 70*, 191-207

Wagner, W., Bloeschl, G., Pampaloni, P., Calvet, J.-C., Bizzarri, B., Wigneron, J.-P. & Kerr, Y. (2007). Operational readiness of microwave remote sensing of soil moisture for hydrologic applications. *Nordic Hydrology, 38*, 1-20

Wagner, W., Dorigo, W., Richard de Jeu, Diego Fernandez, Jerome Benveniste, Eva Haas & Ertl, M. (2012). Fusion of Active and Passive Microwave Observations to Create an Essential Climate Variable Data Record on Soil Moisture. *XII Congress of the International Society for Photogrammetry and Remote Sensing-Melbourne, Australia*

Wagner, W., Hahn, S., Kidd, R., Melzer, T., Bartalis, Z., Hasenauer, S., Figa-Saldaña, J., de Rosnay, P., Jann, A., Schneider, S., Komma, J., Kubu, G., Brugger, K., Aubrecht, C., Züger, J., Gangkofner, U., Kienberger, S., Brocca, L., Wang, Y., Blöschl, G., Eitzinger, J. & Steinnocher, K. (2013). The ASCAT Soil Moisture Product: A Review of its Specifications, Validation Results, and Emerging Applications. *Meteorologische Zeitschrift, 22*, 5-33

Walker, J.P., Willgoose, G.R. & Kalma, J.D. (2001). One-Dimensional Soil Moisture Profile Retrieval by Assimilation of Near-Surface Measurements: A Simplified Soil Moisture Model and Field Application. *Journal of Hydrometeorology, 2*, 356-373

Walker, J.P. & Houser, P.R. (2004). Requirements of a global near-surface soil moisture satellite mission: accuracy, repeat time, and spatial resolution. *Advances in Water Resources, 27*, 785-801

Walker, J.P., Willgoose, G.R. & Kalma, J.D. (2004). In situ measurement of soil moisture: a comparison of techniques. *Journal of Hydrology, 293*, 85-99

Wang, J.R. & Schmugge, T.J. (1980). An Empirical Model for the Complex Dielectric Permittivity of Soils as a Function of Water Content. *Geoscience and Remote Sensing, IEEE Transactions on, GE-18*, 288-295

Wang, J.R. & Choudhury, B.J. (1981). Remote sensing of soil moisture content, over bare field at 1.4 GHz frequency. *Journal of Geophysical Research: Oceans, 86*, 5277-5282

Wang, J.R., O'Neill, P.E., Jackson, T.J. & Engman, E.T. (1983). Multifrequency Measurements of the Effects of Soil Moisture, Soil Texture, And Surface Roughness. *Geoscience and Remote Sensing, IEEE Transactions on, GE-21*, 44-51

Wang, J.R. (1985). Effect of vegetation on soil moisture sensing observed from orbiting microwave radiometers. *Remote Sensing of Environment, 17*, 141-151

Wang, L. & Qu, J. (2009). Satellite remote sensing applications for surface soil moisture monitoring: A review. *Frontiers of Earth Science in China, 3*, 237-247

Wang, X. & Zhang, Z. (2005). A review: theories, methods and development of soil moisture monitoring by remote sensing. In, *Geoscience and Remote Sensing Symposium, 2005. IGARSS '05. Proceedings. 2005 IEEE International* (pp. 4505-4507)

Ward, A.D. & Trimble, S.W. (2004). Environmental Hydrology, 2nd edn. *Lewis Publishers*

Weidong, L., Baret, F., Xingfa, G., Qingxi, T., Lanfen, Z. & Bing, Z. (2002). Relating soil surface moisture to reflectance. *Remote Sensing of Environment, 81*, 238-246

Western, A.W., Grayson, R.B. & Blöschl, G. (2002). Scaling of soil moisture: a hydrologic perspective. *Annual Review of Earth and Planetary Sciences, 30, 149-180*

Western, A.W., Zhou, S.-L., Grayson, R.B., McMahon, T.A., Blöschl, G. & Wilson, D.J. (2004). Spatial correlation of soil moisture in small catchments and its relationship to dominant spatial hydrological processes. *Journal of Hydrology, 286*, 113-134

Wetzel, P.J. & Woodward, R.H. (1986). Soil moisture estimation using GOESVISSR infrared data: a case study with a simple statistical method. *Journal of Applied Meteorology, 26(1): 107-117*

Whiting, M.L., Li, L. & Ustin, S.L. (2004). Predicting water content using Gaussian model on soil spectra. *Remote Sensing of Environment, 89*, 535-552

Wigneron, J.-P., Chanzy, A., Calvet, J.-C. & Bruguier, N. (1995). A simple algorithm to retrieve soil moisture and vegetation biomass using passive microwave measurements over crop fields. *Remote Sensing of Environment, 51*, 331-341

Wigneron, J.-P., Olioso, A., Calvet, J.-C. & Bertuzzi, P. (1999a). Estimating root zone soil moisture from surface soil moisture data and soil-vegetation-atmosphere transfer modeling. *Water Resources Research, 35*, 3735-3745

Wigneron, J.-P., Schwank, M., Baeza, E.L., Kerr, Y., Novello, N., Millan, C., Moisy, C., Richaume, P., Mialon, A., Al Bitar, A., Cabot, F., Lawrence, H., Guyon, D., Calvet, J.-C., Grant, J.P., Casal, T., de Rosnay, P., Saleh, K., Mahmoodi, A., Delwart, S. & Mecklenburg, S. (2012). First evaluation of the simultaneous SMOS and ELBARA-II observations in the Mediterranean region. *Remote Sensing of Environment, 124*, 26-37

Wigneron, J.P., Calvet, J.C., Kerr, Y., Chanzy, A. & Lopes, A. (1993). Microwave emission of vegetation: sensitivity to leaf characteristics. *Geoscience and Remote Sensing, IEEE Transactions on, 31*, 716-726

Wigneron, J.P., Schmugge, T., Chanzy, A., Calvet, J.C. & Kerr, Y. (1998). Use of passive microwave remote sensing to monitor soil moisture. *Agronomie, 18*, 27-43

Wigneron, J.P., Ferrazzoli, P., Olioso, A., Bertuzzi, P. & Chanzy, A. (1999b). A Simple Approach To Monitor Crop Biomass from C-Band Radar Data. *Remote Sensing of Environment, 69*, 179-188

Wigneron, J.P., Waldteufel, P., Chanzy, A., Calvet, J.C. & Kerr, Y. (2000). Two-Dimensional Microwave Interferometer Retrieval Capabilities over Land Surfaces (SMOS Mission). *Remote Sensing of Environment, 73*, 270-282

Wigneron, J.P., Laguerre, L. & Kerr, Y.H. (2001). A simple parameterization of the L-band microwave emission from rough agricultural soils. *Geoscience and Remote Sensing, IEEE Transactions on, 39*, 1697-1707

Wigneron, J.P., Calvet, J.C., Pellarin, T., Van de Griend, A.A., Berger, M. & Ferrazzoli, P. (2003). Retrieving near-surface soil moisture from microwave radiometric observations: current status and future plans. *Remote Sensing of Environment, 85*, 489-506

Wigneron, J.P., Calvet, J.C., De Rosnay, P., Kerr, Y., Waldteufel, P., Saleh, K., Escorihuela, M.J. & Kruszewski, A. (2004). Soil moisture retrievals from biangular L-band passive microwave observations. *Geoscience and Remote Sensing Letters, IEEE, 1*, 277-281

Wigneron, J.P., Kerr, Y., Waldteufel, P., Saleh, K., Escorihuela, M.J., Richaume, P., Ferrazzoli, P., de Rosnay, P., Gurney, R., Calvet, J.C., Grant, J.P., Guglielmetti, M., Hornbuckle, B., Mätzler, C., Pellarin, T. & Schwank, M. (2007). L-band Microwave Emission of the Biosphere (L-MEB) Model: Description and calibration against experimental data sets over crop fields. *Remote Sensing of Environment, 107*, 639-655

Wigneron, J.P., Chanzy, A., De Rosnay, P., Rudiger, C. & Calvet, J.C. (2008). Estimating the Effective Soil Temperature at L-Band as a Function of Soil Properties. *Geoscience and Remote Sensing, IEEE Transactions on, 46*, 797-807

wigneron, J.P., Kerr, Y., mailon, A., Novello, N., Cabot, F. & delwart, S.e.a. (2010). First evaluation of SMOS observations and Level-2 products over agricultural sites in temperate regions. *Proceedings of the 3rd International Symposium on Recent Advances in Quantitative Remote Sensing: RAQRS'III, 27 Sept.–1Oct., Torrent, Valencia, Spain*, 678–681

Wipfler, E.L., Metselaar, K., van Dam, J.C., Feddes, R.A., van Meijgaard, E., van Ulft, L.H., van den Hurk, B., Zwart, S.J. & Bastiaanssen, W.G.M. (2011). Seasonal evaluation of the land surface scheme HTESSEL against remote sensing derived energy fluxes of the Transdanubian region in Hungary. *Hydrol. Earth Syst. Sci., 15*, 1257-1271

Yi, Y., Kimball, J.S., Jones, L.A., Reichle, R.H. & McDonald, K.C. (2011). Evaluation of MERRA Land Surface Estimates in Preparation for the Soil Moisture Active Passive Mission. *Journal of Climate, 24*, 3797-3816

Yilmaz, M.T. & Crow, W.T. (2012). The Optimality of Potential Rescaling Approaches in Land Data Assimilation. *Journal of Hydrometeorology, 14*, 650-660

Zazueta, F.S. & Xin, J. (1994). Soil Moisture Sensors. *Florida Cooperative Extension Service, Institute of Food and Agriculture Sciences, University of Florida, Buletin 292*

List of figures

List of tables

Statement of Co- Authorship

The manuscripts for chapters 4 and 5 have been published in the journal Remote Sensing of Environment. The research was conducted by the lead author. The co-authors for the two manuscripts provided some of the datasets used in the analyses and scientific advices in the use of the remotely sensed and modelled data as detailed below:

For the manuscript entitled "Global-scale evaluation of two satellite-based passive microwave soil moisture datasets (SMOS and AMSR-E) with respect to Land Data Assimilation System estimates", J.-P. Wigneron and A. Ducharne provided direction and important ideas and considerations. P. de Rosnay, C. Albergel, and J. Muñoz-Sabater provided the SM-DAS-2 assimilation soil moisture, used as a reference in the analyses, and scientific advices on the performance of this assimilation product. R. de Jeu provided the AMSR-E passive microwave soil moisture datasets for evaluation and scientific advices on the performance of this retrieval model. Y. Kerr, A. Al Bitar, P. Richaume, and A. Mialon provided the SMOSL3 datasets, helped in selecting the thresholds used in the pre-processing step, and provided scientific advices on the comparison of the three soil moisture datasets. In a final step, all co-authors helped the lead author, who carried out the whole analysis and wrote the whole paper, in the interpretation of the inter-comparison results and statistical analysis based on a variety of remotely sensed and modelled data.

For the manuscript entitled "Global-scale comparison of passive (SMOS) and active (ASCAT) satellite based microwave soil moisture retrievals with soil moisture simulations (MERRA-Land)", J.-P. Wigneron and A. Ducharne provided direction and important ideas and considerations. W. Wagner and W. Dorigo provided the ASCAT datasets and helped with

the data pre-processing step. G. De Lannoy and R. Reichle provided the MERRA-Land soil moisture used, as a reference, in the analyses and provided scientific advice on the use of the triple collocation method. Y. Kerr, A. Al Bitar, P. Richaume, and A. Mialon provided the SMOSL3 datasets and scientific advices on the performance of this retrieval product, as well as provided scientific advices on the comparison of the three soil moisture datasets. In a final step, all co-authors helped the lead author, who carried out the whole analysis and wrote the whole paper, in the interpretation of the inter-comparison results and statistical analysis based on a variety of remotely sensed and modelled data.

List of publications

Journal papers (Peer reviewed)

A. Al-Yaari, J.-P. Wigneron, A. Ducharne, Y.H. Kerr, W. Wagner, G. De Lannoy, R. Reichle, A. Al Bitar, W. Dorigo, P. Richaume, A. Mialon, Global-scale comparison of passive (SMOS) and active (ASCAT) satellite based microwave soil moisture retrievals with soil moisture simulations (MERRA-Land), Remote Sensing of Environment, Volume 152, September 2014, Pages 614-626, ISSN 0034-4257, http://dx.doi.org/10.1016/j.rse.2014.07.013.

A. Al-Yaari, J.-P. Wigneron, A. Ducharne, Y. Kerr, P. de Rosnay, R. de Jeu, A. Govind, A. Al Bitar, C. Albergel, J. Muñoz-Sabater, P. Richaume, A. Mialon, Global-scale evaluation of two satellite-based passive microwave soil moisture datasets (SMOS and AMSR-E) with respect to Land Data Assimilation System estimates, Remote Sensing of Environment, Volume 149, June 2014, Pages 181-195, ISSN 0034-4257, http://dx.doi.org/10.1016/j.rse.2014.04.006.

Marie Parrens, Jean-Pierre Wigneron, Philippe Richaume, Ahmad Albitar, Arnaud Mialon, Shu Wang,Roberto Fernandez-Moran, **Amen Al-Yaari**, Peggy O'Neill, and Yann Kerr, Considering Combined or Separated Roughness and Vegetation Effects in Soil Moisture Retrievals (Submitted to IEEE transactions on Geoscience and remote sensing).

Conference proceedings (peer reviewed)

Al-Yaari, A.; Wigneron, J.-P.; Ducharne, A.; Kerr, Y.; Wagner, W.; Reichle, R.; De Lannoy, G.; Al Bitar, A.; Dorigo, W.; Parrens, M.; Fernandez, R.; Richaume, P.; Mialon, A., "Compared performances of microwave passive soil moisture retrievals (SMOS) and active soil moisture retrievals (ASCAT) using land surface model estimates (MERRA-LAND)," Geoscience and Remote Sensing Symposium (IGARSS), 2014 IEEE International , vol., no., pp.2463,2466, 13-18 July 2014. doi: 10.1109/IGARSS.2014.6946971. URL: http://ieeexplore.ieee.org/stamp/stamp.jsp?tp=&arnumber=6946971&isnumber=6946328

Al-Yaari, A.; Wigneron, J.-P.; Ducharne, A.; Kerr, Y.; de Rosnay, P.; de Jeu, R.; Govind, A.; Al Bitar, A.; Albergel, C.; Munoz-Sabater, J.; Richaume, P.; Mialon, A., "Merging two passive microwave remote sensing (SMOS and AMSR_E) datasets to produce a long term record of Soil Moisture," Geoscience and Remote Sensing Symposium (IGARSS), 2014 IEEE International , vol., no., pp.2269,2272, 13-18 July 2014 doi: 10.1109/IGARSS.2014.6946922.
URL: http://ieeexplore.ieee.org/stamp/stamp.jsp?tp=&arnumber=6946922&isnumber=6946328

Parrens, M.; Wigneron, J.-P.; Richaume, P.; Kerr, Y.; Wang, S.; **Alyaari, A**.; Fernandez-Moran, R.; Mialon, A.; Escorihuela, M.J.; Grant, J.-P., "Global maps of roughness parameters from L-band SMOS observations," Geoscience and Remote Sensing Symposium (IGARSS), 2014 IEEE International , vol., no., pp.4675,4678, 13-18 July 2014.
URL: http://ieeexplore.ieee.org/stamp/stamp.jsp?tp=&arnumber=6947536&isnumber=6946328

Fernandez-Moran, R.; Wigneron, J.-P.; Lopez-Baeza, E.; Salgado-Hernanz, P.M.; Mialon, A.; Miernecki, M.; **Alyaari, A**.; Parrens, M.; Schwank, M.; Wang, S.; Coll-Pajaron, A.; Lawrence, H.; Kerr, Y.H., "Evaluating the impact of roughness in soil moisture and optical thickness retrievals over the VAS area," *Geoscience and Remote Sensing Symposium (IGARSS), 2014 IEEE International* , vol., no., pp.1947,1950, 13-18 July 2014 doi:10.1109/IGARSS.2014.6946841.
URL: http://ieeexplore.ieee.org/stamp/stamp.jsp?tp=&arnumber=6946841&isnumber=6946328

Wang, S.; Wigneron, J.-P.; Parrens, M.; **Al-Yaari, A.;** Fernandez-Moran, R.; Jiang, L.-M.; Zeng, J.-Y.; Kerr, Y., "Evaluating roughness effects on C-band AMSR-E observations," Geoscience and Remote Sensing Symposium (IGARSS), 2014 IEEE International , vol., no., pp.3311,3314, 13-18 July 2014. doi: 10.1109/IGARSS.2014.6947188.

URL:http://ieeexplore.ieee.org/stamp/stamp.jsp?tp=&arnumber=6947188&isnumber=6946328

Al-Yaari, A; Wigneron, JP.; Ducharne, A; Kerr, Y.; Al Bitar, A; de Jeu, R.; Govind, A; de Rosnay, P.; Albergel, C.; Munoz-Sabater, J., "Performances of SMOS and AMSR-E soil moisture retrievals against Land Data Assimilation system estimates," Microwave Radiometry and Remote Sensing of the Environment (MicroRad), 2014 13th Specialist Meeting on , vol., no., pp.19,24, 24-27 March 2014. doi:10.1109/MicroRad.2014.6878900http://ieeexplore.ieee.org/stamp/stamp.jsp?tp=&arnumber=6878900&isnumber=6878887

Conference Abstracts

De Jeu, R. ; Wigneron, J.-P. ; Kerr, Y. ; Drusch, M. ; van der Schalie, R. ; **Al-Yaari, A.** ; Rodriguez, N. A study towards the integration of SMOS soil moisture in a consistent climate record [Présentation orale]. Satellite Soil Moisture Validation & Application Workshop 2014 (2014-07-10-2014-07-11) Amsterdam (NLD). 2014.

Al-Yaari, A. ; Wigneron, J.-P. ; Ducharne, A. ; Govind, A. ; Kerr, Y. ; Al Bitar, A. ; De Jeu, R. ; Albergel, C. ; Sabater, J. M. ; Moisy, C. Global-scale evaluation of two satellite-based passive microwave soil moisture data sets (SMOS and AMSR-E) with respect to modelled estimates [Poster]. EGU 2014, European Geosciences Union General Assembly (2014-04-27-2014-05-02) Vienne (AUT). 2014.

Al-Yaari, A. ; Wigneron, J.-P. ; Ducharne, A. ; Govind, A. ; Moisy, C. ; De Rosnay, P. ; De Jeu, R. ; Albergel, C. ; Balsamo, G. ; Kerr, Y. Evaluation and intercomparison of SMOSL3, AMSR E-LPRM, SM-DAS-2, and ERA-Interim/land soil moisture products [Poster]. ESA Living Planet Symposium (2013-09-09-2013-09-13) Edinburgh (Royaume Uni). 2013.

Al-Yaari, A. ; Wigneron, J.-P. ; Govind, A. ; Ducharne, A. ; Moisy, C. ; De Rosnay, P. ; De Jeu, R. ; Albergel, C. ; Balsamo, G. ; Kerr, Y. Evaluation and intercomparison of SMOSL3, CCI, AMSR E-LPRM, SM-DAS-2, and ERA-Interim/Land soil moisture products [Poster]. SMOS Land Application Workshop (2013-02-25-2013-02-27) Frascati (ITA). 2013.

Kerr, Y. ; Leroux, D. ; Pellarin, T. ; **Al-Yaari, A.** ; Wigneron, J.-P. ; Mialon, A. ; Drusch, M. ; Munoz-Sabater, J. ; Bircher, S. Suggestion on the validation of remote sensing products, ntercomparison of sensors and rules to establish a long term data set [Présentation orale]. Satellite Soil Moisture Validation and Application Workshop (2013-07-01-2013-07-03) Frascati (ITA). 2013.

Al-Yaari, A. ; Wigneron, J.-P. ; Ducharne, A. ; Govind, A. ; Moisy ; De Rosnay, P. ; De Jeu, R. ; Albergel, C. ; Balsamo, G. ; Kerr, Y. Evaluation and intercomparison of SMOSL3, CCI, AMSRE-LPRM, SM-DAS-2, and ERA-Interim/Land soil moisture products [Poster]. ESA Satellite Soil Moisture Validation and Application Workshop (2013-07-01-2013-07-03) Frascati (ITA). 2013.

Y. H. Kerr, J.-P. Wigneron, P. Ferrazzoli, P. Richaume, P. Waldteufel, A. Mialon, A.AlBitar, S. Bircher, F. Cabot, A. Choné, D. Leroux, B. Molero, M. Parrens, N.Rodriguez, **A. Al-Yaari**, J. Grant, S. Delwart, M. Drusch, S. Mecklenburg, A review of the latest improvements in the L-MEB Model (SMOS mission)[oral]. The 4th International Symposium on Recent Advances in Quantitative Remote Sensing: RAQRS'IV, 22-26th September 2014.

J. P. Wigneron, Y. Kerr, M. Schwank, E. Lopez Baeza, M. Parrens, R. Fernandez, **Amen Al-Yaari**, S. Wang, P. Richaume, S. Bircher, A. Mialon, A. Al Bitar, H.Lawrence, J. P. Grant, M. Miernecki, A. Mahmoodi, S. Delwart, M. Drusch, S. Mecklenburg, A review of the latest improvements in the L-MEB Model (SMOS mission) . The 4th International Symposium on Recent Advances in Quantitative Remote Sensing: RAQRS'IV, 22-26th September 2014.

R. Fernandez-Moran, J.-P. Wigneron, E. Lopez-Baeza, P.M. Salgado-Hernanz, Y. Kerr, A. Mialon, M. Parrens, M. Miernecki, A. Coll-Pajaron, **A. Al-Yaari**, S. Wang, M. Schwank, Roughness parameterization for soil moisture optimum retrieval over the Valencia anchor station. The 4th International Symposium on Recent Advances in Quantitative Remote Sensing: RAQRS'IV, 22-26th September 2014.